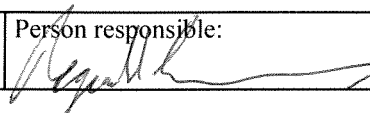


NGU Report 2011.026

Mannen unstable rock slope (Møre & Romsdal):
Logging of borehole and drill core KH-01-10,
geomorphologic digital elevation model
interpretation & displacement analysis by
terrestrial laser scanning

Report no.: 2011.026		ISSN 0800-3416	Grading: Open	
Title: Mannen unstable rock slope (Møre & Romsdal): Logging of borehole and drill core KH-01-10, geomorphologic digital elevation model interpretation & displacement analysis by terrestrial laser scanning				
Authors: Aline Saintot, Harald Elvebakk, Thierry Oppikofer, Guri V. Ganerød & Tor Ø. Farsund		Client: Åknes/Tafjord Beredskapscenter IKS		
County: Møre & Romsdal		Commune: Rauma		
Map-sheet name (M=1:250.000) Ålesund		Map-sheet no. and -name (M=1:50.000) 1319 II Romsdalen		
Deposit name and grid-reference: Mannen		Number of pages: 130		Price (NOK): 530
		Map enclosures: 0		
Fieldwork carried out: 2010	Date of report: 1 September 2011	Project no.: 336700	Person responsible: 	
Summary: Mannen is an unstable rock slope located in Romsdalen in Møre og Romsdal County. The most active part is located in the uppermost part of the slope and has an estimated volume of 2.5–3 Mm ³ and moves with a velocity of approximately 4–5 cm/year. Since 2009, the unstable rock slope at Mannen is under continuous monitoring by the Åknes/Tafjord Beredskapscenter IKS. A 138 m deep, vertical cored borehole has been drilled in 2010 in the uppermost part of the Mannen rock slope. The aim of this coring was to characterize weakness zones that may explain the active deformation. This report presents the geological logging of the drill core and the geophysical logging of the borehole by an optical televiewer, which gives orientation of fractures and structures, as well as fracture frequency. Both the geological core logging and geophysical borehole logging resulted in the observation of many highly deformed and even crushed levels at several depths. Among them, the core interval between 57 and 81 m depth shows the highest density of severely crushed zones associated with fine-grained products, such as breccias or even clay-rich gouges. This interval is interpreted to be the subsurface expression of the main basal sliding surface. The geomorphologic analysis of a high-resolution digital elevation model in combination with photographs allowed delimiting different scenarios for the Mannen rock slope instability. Based on the orientations of the structures forming the basal failure surface, a wedge failure mechanism is proposed for the most active block (scenario A). The orientation of the wedge intersection line formed by the two basal surfaces is consistent with the displacement vector obtained by dGPS measurements and repetitive terrestrial laser scans, which are also presented in this report. Moreover, the analysis of the terrestrial laser scanning datasets reveals toppling movements of the uppermost part of the instability. These might be related to toppling of shallow, free-standing blocks. At the location of the borehole, the basal failure surface inferred from the digital elevation model is at approximately 70 m depth. This coincides well with the heavily crushed zone logged in the drill core and borehole.				
Keywords:	Drill core logging	Borehole logging		
Fractures	Damage zones	Televiewer		
Digital elevation model	Terrestrial laser scanning	Unstable rock slope		

CONTENTS

1.	INTRODUCTION.....	10
2.	GEOLOGICAL AND STRUCTURAL CORE LOGGING	13
2.1	THE BEDROCK AND ITS MECHANICAL PROPERTIES	13
2.2	DUCTILE FOLDS	14
2.3	FRACTURING, CRUSHED ZONES AND FAULT ROCKS	39
2.3.1	Large intervals of poor rock mass quality	39
2.3.2	Discrete intervals of poor rock mass quality	39
2.3.3	Clay-rich intervals	41
2.4	SUMMARY OF OBSERVATIONS AND INTERPRETATION	41
3.	TELEVIEWER LOGGING OF THE BOREHOLE	43
3.1	INSTRUMENTATION, DATA ACQUISITION AND PROCESSING	43
3.2	STRUCTURAL DATA ALONG THE BOREHOLE.....	44
3.2.1	Overview of the attitude of the structural data along the entire borehole	44
3.2.2	Structural data in the c. 3.1–31.7 m depth interval	46
3.2.3	Structural data in the 32–58 m depth interval	60
3.2.4	Structural data in depth interval: 57–77 m	74
3.2.5	Structural data in depth interval: 89–133 m	84
3.3	SUMMARY OF THE ATTITUDE OF THE METAMORPHIC FOLIATION AND FRACTURES ALONG THE ENTIRE BOREHOLE OF MANNEN.....	102
4.	GEOMORPHOLOGIC ANALYSIS OF DIGITAL ELEVATION MODEL AND COMBINAISON WITH DRILL CORE AND BOREHOLE DATA.....	106
5.	MAP OF DISPLACEMENT BY TERRESTRIAL LASER SCAN ANALYSIS	108
5.1	METHODOLOGY	108
5.1.1	TLS data acquisition.....	108
5.1.2	Error assessment.....	109
5.2	TLS DISPLACEMENT ANALYSIS	111
5.2.1	Shortest distance comparison	111
5.2.2	Roto-translation matrix analysis.....	113
6.	CONCLUSION AND PERSPECTIVES	115
7.	REFERENCES.....	116
8.	APPENDIX	117

FIGURES

Figure 1. Mannen unstable rock slope on the southern side of Romsdalen (Western Norway).	11
Figure 2. Location of drilling site at the top of Mannen unstable rock slope (UTM32 coordinates: 436618.5E; 6925616N). Possible limits of the different unstable volumes, i.e. scenarios labelled A, B and C on figure, and as explained in Chapter 4.	12
Figure 3. Photograph of the drilling site on the top of the moving block. The main back-crack (black wall) is on the right side.	12
Figure 4. Structural and geological core logging from 0 to 7 m depth. Pictures of the 1 m long bits of the dry (left) and wet (right) core.	16
Figure 5. Structural and geological core logging from 7 to 13 m depth (see Figure 4).	17
Figure 6. Structural and geological core logging from 13 to 19 m depth (see Figure 4).	18
Figure 7. Structural and geological core logging from 19 to 25 m depth (see Figure 4).	19
Figure 8. Structural and geological core logging from 25 to 31 m depth (see Figure 4).	20
Figure 9. Structural and geological core logging from 31 to 37 m depth (see Figure 4).	21
Figure 10. Structural and geological core logging from 37 to 43 m depth (see Figure 4).	22
Figure 11. Structural and geological core logging from 43 to 49 m depth (see Figure 4).	23
Figure 12. Structural and geological core logging from 49 to 55 m depth (see Figure 4).	24
Figure 13. Structural and geological core logging from 55 to 61 m depth (see Figure 4).	25
Figure 14. Structural and geological core logging from 61 to 67 m depth (see Figure 4).	26
Figure 15. Structural and geological core logging from 67 to 73 m depth (see Figure 4).	27
Figure 16. Structural and geological core logging from 73 to 79 m depth (see Figure 4).	28
Figure 17. Structural and geological core logging from 79 to 85 m depth (see Figure 4).	29
Figure 18. Structural and geological core logging from 85 to 91 m depth (see Figure 4).	30
Figure 19. Structural and geological core logging from 91 to 97 m depth (see Figure 4).	31
Figure 20. Structural and geological core logging from 97 to 103 m depth (see Figure 4).	32
Figure 21. Structural and geological core logging from 103 to 109 m depth (see Figure 4). ...	33
Figure 22. Structural and geological core logging from 109 to 115 m depth (see Figure 4). ...	34
Figure 23. Structural and geological core logging from 115 to 121 m depth (see Figure 4). ...	35
Figure 24. Structural and geological core logging from 121 to 127 m depth (see Figure 4). ...	36
Figure 25. Structural and geological core logging from 127 to 133 m depth (see Figure 4). ...	37
Figure 26. Structural and geological core logging from 133 to 138 m depth (see Figure 4). ...	38
Figure 27. Mannen borehole deviation: north and east components (left) on the vertical section and direction viewed from the top (right).	43
Figure 28. Stereoplots (lower hemisphere, Schmidt's projection) of the foliation planes measured along the borehole by televiwer imaging.	45
Figure 29. Stereoplots (lower hemisphere, Schmidt's projection) of the fractures measured along the borehole by optical televiwer imaging.	45
Figure 30. Unwrapped optical images of the wall of Mannen borehole with digitised foliation planes in the 4–16 m depth interval (left). Dip angle and dip direction of each plane are displayed on the arrow plot (N up; centre). Attitude of foliation plane is seen from two different angles (to N315 and N045 or to N290 and N020) with strike (right hand rule) and dip angle of the plane (right).	47
Figure 31. Unwrapped optical images of the wall of Mannen borehole with digitised foliation planes in the 16–28 m depth interval (caption as in Figure 30).	48
Figure 32. Unwrapped optical images of the wall of Mannen borehole with digitised foliation planes in the 28–31.7 m depth interval (caption as in Figure 30) and stereoplots of the metamorphic foliation (planes and poles) in the 4–11 and 11–31.7 m depth intervals (data listed in Appendix 1).	49

Figure 33. Contour plots with poles of fractures providing four main fracture sets (marked by different colours) in the c. 3–32 m depth interval. The prominent fracture set is the blue coloured set with dip direction/dip angle $019^{\circ}/36^{\circ}$	50
Figure 34. Rose diagram of the fractures in the 3–32 m depth interval.....	50
Figure 35. Arrow plots (N up) of the 128 fractures in the c. 3–32 m depth interval, frequency histograms of the four fractures sets as defined by the statistical analysis (see Figure 33; with identical colours representing the fracture sets). The deviation of the borehole (arrow plot; N up) is shown in the right.....	51
Figure 36. Optical televiewer synthetic images with digitised planar fractures in the 3.1–7.6 m depth interval (left); arrow plots of the fracture orientation (N up; centre); attitude of the fracture from two different view angles (to N290 and N020 herein) and strike/dip angle of the fracture with main characteristics (right).....	53
Figure 37. Optical televiewer synthetic images with digitised planar fractures in the 8–12 m depth interval (caption as on Figure 36).....	54
Figure 38. Optical televiewer synthetic images with digitised planar fractures in the 12–16 m depth interval (caption as on Figure 36).....	55
Figure 39. Optical televiewer synthetic images with digitised planar fractures in the 16–20 m depth interval (caption as on Figure 36).....	56
Figure 40. Optical televiewer synthetic images with digitised planar fractures in the 20–24 m depth interval (caption as on Figure 36).....	57
Figure 41. Optical televiewer synthetic images with digitised planar fractures in the 24–28.2 m depth interval (caption as on Figure 36).....	58
Figure 42. Optical televiewer synthetic images with digitised planar fractures in the 28.2–31.7 m depth interval (caption as on Figure 36).....	59
Figure 43. Optical televiewer images showing crushed zones in the two 23–24.5 m (left) and 27–29 m (right) depth intervals. The two layers of clay-rich gouges are well observed in the 27–29 m depth interval.....	60
Figure 44. Unwrapped optical images of the wall of Mannen borehole with digitised foliation planes in the 32–44 m depth interval (caption as in Figure 30).....	61
Figure 45. Unwrapped optical images of the wall of Mannen borehole with digitised foliation planes in the 44–56 m depth interval (caption as in Figure 30).....	62
Figure 46. Unwrapped optical images of the wall of Mannen borehole with digitised foliation planes in the 56–58 m depth interval (caption as in Figure 30) and stereoplot of the metamorphic foliation (planes and poles) in the 33.5–38, 38–42, 42–47, 47–55, 55–57 and 57–58 m depth intervals (data listed in Appendix 1).....	63
Figure 47. Contour plots, with poles of fractures, providing four main fracture sets in the c. 32–58 m depth interval.....	64
Figure 48. Rose diagram of the fractures in the 32–58 m depth interval.....	64
Figure 49. Arrow plots (N up) of the 71 fractures in the c. 32–58 m depth interval, frequency histograms of the five fractures sets as defined by the statistical analysis (see Figure 47). The deviation of the borehole (arrow plot; N up) is shown in the right.....	65
Figure 50. Optical televiewer synthetic images with digitised planar fractures in the 32–36 m depth interval (caption as on Figure 36).....	67
Figure 51. Optical televiewer synthetic images with digitised planar fractures in the 36–40 m depth interval (caption as on Figure 36).....	68
Figure 52. Optical televiewer synthetic images with digitised planar fractures in the 40–44 m depth interval (caption as on Figure 36).....	69
Figure 53. Optical televiewer synthetic images with digitised planar fractures in the 44–48 m depth interval (caption as on Figure 36).....	70
Figure 54. Optical televiewer synthetic images with digitised planar fractures in the 48–52 m depth interval (caption as on Figure 36).....	71

Figure 55. Optical televiewer synthetic images with digitised planar fractures in the 52–56 m depth interval (caption as on Figure 36).....	72
Figure 56. Optical televiewer synthetic images with digitised planar fractures in the 56–58 m depth interval (caption as on Figure 36).....	73
Figure 57. Optical televiewer images showing crushed zones at 46.7 m (left) and 56.3 m (right) depths.	74
Figure 58. Unwrapped optical images of the wall of Mannen borehole with digitised foliation planes in the 57.4–69 m depth interval (caption as in Figure 30).	75
Figure 59. Unwrapped optical images of the wall of Mannen borehole with digitised foliation planes in the 69–77.6 m depth interval (caption as in Figure 30) and stereoplot of the metamorphic foliation (planes and poles) in the 58–59.5, 61–64.5, 64.5–71 and 71–77 m depth interval (data listed in Appendix 1).	76
Figure 60. Contour plots, with poles of fractures, providing one main fracture set in the c. 57–77 m depth interval. Note that the strong dispersion of the 18 fractures provides a statistic analysis of low significance.	77
Figure 61. Rose diagram of the fractures in the 57–77 m depth interval.	77
Figure 62. Arrow plots (N up) of the 18 fractures in the c. 57–77 m depth interval, frequency histograms of the single fracture set as defined by the statistical analysis (see Figure 60). The deviation of the borehole (arrow plot; N up) is shown in the right.	78
Figure 63. Optical televiewer synthetic images with digitised planar fractures in the 57.4–61.5 m depth interval (caption as on Figure 36).	79
Figure 64. Optical televiewer synthetic images with digitised planar fractures in the 61.5–65.5 m depth interval (caption as on Figure 36).	80
Figure 65. Optical televiewer synthetic images with digitised planar fractures in the 65.5–69.5 m depth interval (caption as on Figure 36).	81
Figure 66. Optical televiewer synthetic images with digitised planar fractures in the 69.5–73.5 m depth interval (caption as on Figure 36).	82
Figure 67. Optical televiewer synthetic images with digitised planar fractures in the 73.0–77.6 m depth interval (caption as on Figure 36).	83
Figure 68. Optical televiewer images showing crushed zones at 59.4 m (left) and 73.2 m (right) depths. The filling of the fractures is partly cement, which was injected to stabilise the borehole. The cement is especially visible in the picture to the right as a grey mass.	84
Figure 69. Unwrapped optical images of the wall of Mannen borehole with digitised foliation planes in the 89–101 m depth interval (caption as in Figure 30).	85
Figure 70. Unwrapped optical images of the wall of Mannen borehole with digitised foliation planes in the 101–113 m depth interval (caption as in Figure 30).	86
Figure 71. Unwrapped optical images of the wall of Mannen borehole with digitised foliation planes in the 113–126 m depth interval (caption as in Figure 30).	87
Figure 72. Unwrapped optical images of the wall of Mannen borehole with digitised foliation planes in the 126–132 m depth interval (caption as in Figure 30) and stereoplot of the metamorphic foliation (planes and poles) in the 90–110.2, 110.9–112, 113.5–116.2, 116.4–122.3, 124–126.6 and 127–133 m depth interval (data listed in Appendix 1).	88
Figure 73. Contour plots, with poles of fractures, providing four main fracture sets in the c. 89–133 m depth interval.	89
Figure 74. Rose diagram of the fractures in the 90–131 m depth interval.	89
Figure 75. Arrow plots (N up) of the 90 fractures in the c. 89–133 m depth interval, frequency histograms of the four fractures sets as defined by the statistical analysis (see Figure 73). The deviation of the borehole (arrow plot; N up) is shown in the right.	91
Figure 76. Optical televiewer synthetic images with digitised planar fractures in the 89–93 m depth interval (caption as on Figure 36).....	92

Figure 77. Optical televiewer synthetic images with digitised planar fractures in the 93–97 m depth interval (caption as on Figure 36).....	93
Figure 78. Optical televiewer synthetic images with digitised planar fractures in the 97–101 m depth interval (caption as on Figure 36).....	94
Figure 79. Optical televiewer synthetic images with digitised planar fractures in the 105–109 m depth interval (caption as on Figure 36).	95
Figure 80. Optical televiewer synthetic images with digitised planar fractures in the 110–114 m depth interval (caption as on Figure 36).	96
Figure 81. Optical televiewer synthetic images with digitised planar fractures in the 114–118 m depth interval (caption as on Figure 36).	97
Figure 82. Optical televiewer synthetic images with digitised planar fractures in the 118–122 m depth interval (caption as on Figure 36).	98
Figure 83. Optical televiewer synthetic images with digitised planar fractures in the 122–126 m depth interval (caption as on Figure 36).	99
Figure 84. Optical televiewer synthetic images with digitised planar fractures in the 126–130 m depth interval (caption as on Figure 36).	100
Figure 85. Optical televiewer synthetic images with digitised planar fractures in the 130–133 m depth interval (caption as on Figure 36).	101
Figure 86. Optical televiewer images showing a crushed zone in the 112–114 m depth interval.....	102
Figure 87. Dip direction of fractures and foliation in function to depth.	103
Figure 88. Arrow plots of the foliation and fractures planes in the 4–58 m depth interval. ..	104
Figure 89. Arrow plots of the foliation and fractures planes in the 58–133 m depth interval.	105
Figure 90. (a), Aerial photograph draped on a meter-scale resolution DEM of the Mannen rock slope with the inferred limits of scenarios A, B and C (yellow lines); red pins mark the location of the dGPS antennas. (b), Photograph from helicopter of the unstable rock slope of Mannen (scenario A) with an important set of N–S trending opened fractures, a bulge at the front and a sliding surface underlined by rockfall events. The red cone is the location of the drilling site on the top of the unstable slope. (c), determination of a wedge failure on two outcropping surfaces at the limits of scenario A. Note the good fit between the wedge intersection line and the displacement vector obtained from dGPS measurements (the red arrow on the map indicates the direction of the vector displacement).....	106
Figure 91: Pictures of the scan extents in a) August 2008 from viewpoint A; b) June 2010 from viewpoint A; c) and d) June 2010 from viewpoint B.	109
Figure 92: Hillshade maps of 25 cm cell size DEMs created on the TLS point clouds from 2008 (in green) and 2010 (in red). The scan positions and directions are shown. The inset shows a map of the blocks used for the roto-translation matrix technique.	110
Figure 93: Shortest distance comparison between the 2008 and 2010 TLS point clouds (view to the W). Positive differences up to +25 cm are shown in yellow to red colours and negative differences up to –25 cm in blue to violet colours. The 6 compartments on the instability and 4 blocks along the back-crack used for the detailed displacement analysis using the roto-translation matrix technique are outlined. A major rockfall occurred at the foot of the investigated area. Snow covered areas in 2010 and areas not covered by the 2008 dataset were excluded from the shortest distance comparison (grey areas).....	111
Figure 94: Shortest distance comparison of the Mannen instability (view to the WNW): a) eastern part with blocks 1 and 2 sliding towards the SSE by 10–12 cm and block 3 and loose blocks in the graben essentially showing subsidence by 5–12 cm; b) western part with blocks 4 and 5 that also move downward by 5–10 cm. The computed translation vectors of each block are indicated by the displacement length and the trend and plunge of the vector orientation.....	112

Figure 95: Shortest distance comparison for the 4 blocks along the back-crack (view to the W). The three columns are detached from the stable rock mass behind. The middle column can be divided into two parts BC2a and BC2b with high displacement rates (25 cm) for the latter..... 112

TABLES

Table 1. Results of rock mechanical laboratory analysis.	15
Table 2. Fracture frequency along the core. The length of the bars for the fracture frequency is proportional to the maximum number of 13 fractures found in the interval 67–68 m. The length of the bars for the thickness of crush zones is proportional to 100 cm length of the core interval, i.e. a percentage like for the RQD (Rock Quality Designation) values. The symbol * indicates core loss along the interval.	40
Table 3. Samples for XRD analysis and grain size distribution.	41
Table 4. Observation in the 3.4–31.7 m depth interval of crushed and fractured zones, open fractures, orientation and stereoplot. Mean dip angles and dip angles at the bottom of the fractured zone are shown.	52
Table 5. Observation in the 39.8–56.3 m depth interval of crushed and fractured zones, open fractures, orientation and stereoplot. Mean dip angles and dip angles at the bottom of the fractured zone are shown.	66
Table 6. Observation in the 57.4–77.6 m depth interval of crushed and fractured zones, open fractures, orientation and stereoplot. Mean dip angles and dip angles at the bottom of the fractured zone are shown. (* = uncertain dip direction).	78
Table 7. Observation in the 89–133 m depth interval of crushed and fractured zones, open fractures, orientation and stereoplot. Mean dip angles and dip angles at the bottom of the fractured zone are shown.	90
Table 8: Accuracy assessment of the roto-translation matrix technique for 5 stable reference blocks at Mannen.	110
Table 9: Displacement analysis of the Mannen instability using the roto-translation matrix technique for 4 unstable blocks along the back-crack and 6 compartments in the uppermost part of the unstable area. Grey-shaded values are not significant given the mean errors measured on the stable reference compartments (Table 8). Errors on the translation orientation and the toppling azimuth depend on the translation length and toppling angle, respectively.	113

APPENDIX

Appendix 1	117
Appendix 2	121
Appendix 3	129

1. INTRODUCTION

The locality of Mannen is a large rock slope instability, which developed in Proterozoic gneisses at the edge of the elevated plateau south of Romsdalen Valley (Møre og Romsdal County, Western Norway; Figure 1). Detailed surveys of Mannen began in 2006 with geological surface mapping (Henderson and Saintot, 2007) and risk analysis (Dahle et al., 2008, 2010). Large open cracks are conspicuous far inward the plateau but the largest gravity-induced deformation occurred at the edge of the plateau, where a several Mm^3 large block already moved down-slope by approximately 20 m (Figure 2). Displacement rates measured by yearly differential Global Positioning System (dGPS) reach 4–5 cm/year for the upper part of the unstable rock slope. Based on these displacement measurements, the past slope displacement and the high potential consequences of a rock avalanche from Mannen (see Dahle et al., 2008, 2010), the instability has been classified as a high-risk object in 2009. From that time, instrumentation for permanent monitoring is set out under the authority of the Åknes-Tafjord Early-Warning Centre (Stranda, Møre og Romsdal). In parallel, further geological investigations were performed in order to better constrain the gravitational deformation. They comprise the geological logging of a 138 m long core vertically drilled in the unstable rock slope, the borehole logging by an optical televiewer, the analysis of a 1 m resolution digital elevation model acquired by NGU in 2009 (cf. Farsund, 2010, 2011) and a displacement analysis by terrestrial laser scanning. These investigations made in 2010 and 2011 are presented in this report.

Following structural and geological analysis of the surrounding areas, Henderson and Saintot (2007) deduced a translational sliding as mechanism of deformation. A several meter wide opened, steep crack is obvious at the back of the collapsing block and leads to detach the unstable block from the edge of the plateau. However, a basal sliding surface that would accommodate its downward motion is not identified so far. Based on a structural and morphological interpretation, Dahle et al. (2008) proposed the occurrence of two parallel north-dipping sliding surfaces that both developed from the main back-crack but at different depths. The model is refined in Dahle et al. (2010) with the implementation of steps along both sliding surfaces. These steps are inferred from steep tensile structures observed on the topographic surface. The main issue of such a model is that the instability is not considered any longer as a single volume, but as an assemblage of smaller blocks that may fail independently each other.

The bedrock consists of Proterozoic sillimanite-bearing gneiss units. In a first attempt, they may be assumed strong in terms of rheology and therefore difficult to deform under gravity. However, the numerous structures inherited from a protracted tectonic history that encompassed both the ductile and brittle domains of deformation lead to an important weakening ('tectonic weakening') of the rock mass (cf. Saintot et al. 2011). Specifically, the metamorphic foliation surfaces are prone to be reactivated where favourably orientated in regards to the gravitational forces. Many rockslides in the gneisses of Western Norway have basal sliding surfaces that developed along the metamorphic foliation ideally dipping toward the fjords or valleys (see in Henderson et al. 2006). At Mannen, the lack of access due to the steepness of the slope does not permit to measure the foliation elsewhere than on the plateau and the top of the unstable rock slope. On the plateau the foliation strikes approximately E–W and steeply dips towards either the south or the north. A recumbent fold is identified along the southern wall of the main back-crack, and even, shapes the wall. In addition, Henderson and Saintot (2007) identified that a large N–S epidote-rich cataclastic vertical fault zone forms the western border of the instability. Anyhow, pre-existing planar structures on which north-dipping sliding surfaces may develop are not (yet) observed at Mannen.

The vertical drilling of the unstable rock slope from its top surface in 2010 was principally carried out in order to establish the existence of sliding surface(s) and to characterise them

structurally and geologically (Figure 2 and Figure 3). A description of the geological logging of the 138 m long drill core is reported in detail in Chapter 2 (Figure 4–Figure 26). It includes an attempt to quantify the rock mass quality by using the fracture frequency and the RQD (rock quality designation) (Deere, 1964) value in addition to a qualitative description of fractures, crushed zones and fault rocks. Four samples of intact rocks were taken from the core and mechanical tests provided their rheological properties. Clayey intervals encountered along the core are generally associated to crushed zones and probably mark the location of sliding planes; the clays were sampled for XRD and grain size distribution analyses.

Structural measurements of fractures and foliation planes are obtained through the analysis of orientated images of the borehole taken by an optical televiewer (Chapter 3). Televiewer data are analysed together with the core logging data in the aim to enhance the location and orientation of the gravity-induced structures. The structural data from the drill core and borehole are also compared with existing field data obtained inward the plateau (Henderson and Saintot, 2007).

A geomorphologic analysis of a 1 m resolution digital elevation model (DEM) yields the detection of the possible limits of three different unstable volumes that roughly match the three scenarios, A, B and C, reported by Dahle et al. (2010; Figure 2) (Chapter 4). The planar surfaces that formed these limits are cross-examined with the structures observed in the field and along the drill core and in the borehole. Repetitive terrestrial laser scans provides a map of displacement vectors and toppling movements for the uppermost part of the slope (Chapter 5). The combination of this 3D displacement analysis with the structural analysis enhances the understanding of the gravity-induced deformation at Mannen.



Figure 1. Mannen unstable rock slope on the southern side of Romsdalen (Western Norway).

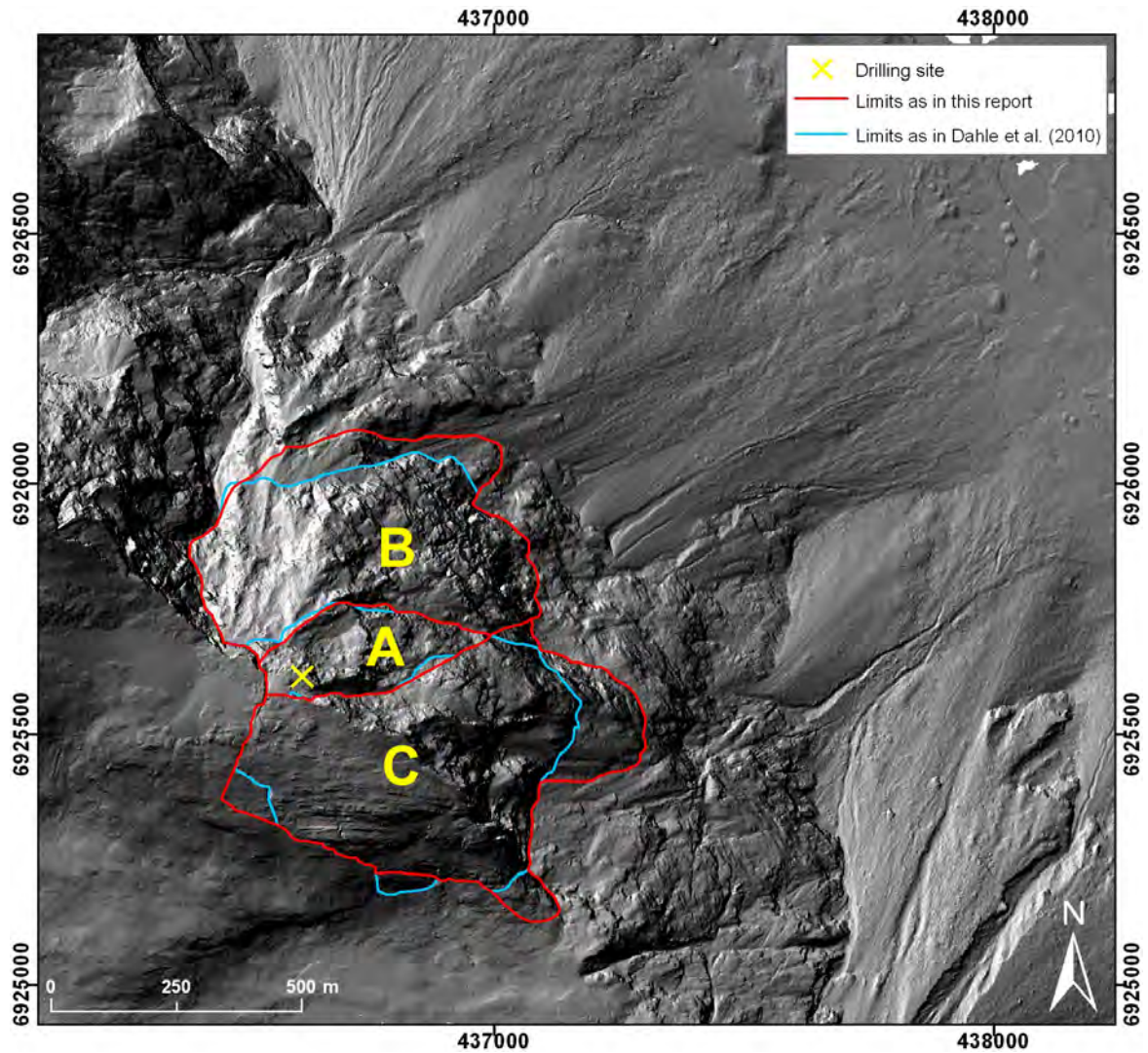


Figure 2. Location of drilling site at the top of Mannen unstable rock slope (UTM32 coordinates: 436618.5E; 6925616N). Possible limits of the different unstable volumes, i.e. scenarios labelled A, B and C on figure, and as explained in Chapter 4.



Figure 3. Photograph of the drilling site on the top of the moving block. The main back-crack (black wall) is on the right side.

2. GEOLOGICAL AND STRUCTURAL CORE LOGGING

The locations of the geological features that are identified during the core logging are according to the depth indicated on the boxes containing the drill core. However, it should be noticed that until 47.9 m depth, the depths recorded by the optical televiewer are from 30 to 50 cm lower than the depth indicated on the drill core boxes. This shift in depth value is due to the presence of severely damaged zones and core loss that renders difficult the depth marking on the core bits. At 47.9 m depth, the optical televiewer image shows a 50 cm thick crushed zone which is not present along the core, likely due to core loss. Underneath, the optical televiewer depths fit relatively well with the depths indicated along the core.

2.1 THE BEDROCK AND ITS MECHANICAL PROPERTIES

All the gneiss units along the 138 m-long core contain in various amount sillimanite and garnet that testifies for an episode of high-grade metamorphism (in the granulite facies).

The gneisses are fine- to medium-grained in general and well to strongly foliated along the entire core. The dip angle of the metamorphic foliation can be estimated to be gentle to shallow. Televiewer analysis provided more precise orientation measurements of the foliation and fractures (Chapter 3).

Muscovite-rich gneiss is prominent in the first 11 meters and in the last meters of the core. This indicates the paragenetic nature of some of the gneisses. Orthogneisses are also observed with a prominent biotite and K-feldspar content. Augengneiss is abundant between 20 m and 85 m depth in the orthogneisses (Figure 7–Figure 17). These gneisses are often banded.

Amphibolites and amphibole-rich gneiss units are also abundant in the first 35 meters and between 100–135 m depth (Figure 4–Figure 9 and Figure 20–Figure 26). Garnets are frequent in the amphibolites and are commonly chloritised. The amphibolites are often associated with calcite-vein networks. Foliation is poorly developed in the amphibolites.

Quartz-K-feldspar pegmatites are abundant in the 43–47 m and 92–106 m intervals (Figure 11, Figure 19–Figure 21).

Finally six rock types characterize the core:

- 1) Pegmatite
- 2) Amphibolite
- 3) Garnet and sillimanite bearing, fine-grained, strongly foliated gneiss
- 4) Garnet and sillimanite bearing, fine-grained, strongly foliated augen gneiss
- 5) Garnet, sillimanite and muscovite bearing, medium- to coarse-grained gneiss
- 6) Garnet, sillimanite and muscovite bearing, medium- to coarse-grained augen gneiss

Four of these rocks were sampled by the Norwegian University of Science and Technology (NTNU) and tested at the Foundation for Scientific and Industrial Research (SINTEF) for their rock mechanical properties (Table 1) (Farsund, 2011). Sample 1 corresponds to a garnet-bearing amphibolite (Figure 5 and Figure 6); sample 2 to a fine-grained strongly foliated augengneiss (Figure 7), sample 3 to a medium- to coarse-grained augengneiss (Figure 14 and Figure 15) and sample 4 to a muscovite-rich medium-grained gneiss (Figure 26). The resulting rock mass properties has been implemented as parameters in numerical stability modelling of the Mannen unstable rock slope in the framework of Tor Farsund's master thesis at NTNU (Farsund, 2011).

The results from the Brazilian test (Table 1) show that the tensile strength of samples 1–4 is classified as very high according to Bieniawski (1975) with regards to the estimated point load index. Based on the calculated uniaxial compressive strength, the strength is respectively extremely high for sample 1–3 and high for sample 4 according to ISRM (1978). The average uniaxial tensile strength of all samples is estimated to $\sigma_t = 15.1 \pm 3.2$ MPa.

The results of uniaxial compressive tests show that the strength of sample 1, 3 and 4 is very high and that the one of sample 2 is medium to very high (ISRM 1978). The average uniaxial compressive strength of all samples is estimated to be $\sigma_c = 136 \pm 37$ MPa; this strength is classified as very high according to ISRM (1978). The average angle of fracture in the uniaxial compressive tests is $\beta = 26^\circ \pm 5^\circ$ and the resulting average friction angle is $\phi = 39^\circ \pm 11^\circ$.

The results of tilt tests on all samples provides an average basic friction angle of $\phi_b = 25.9 \pm 2.0^\circ$.

The two deformability parameters, the Young's modulus and Poisson's ratio of all samples have average values of $E = 51 \pm 20$ GPa and $\nu = 0.14 \pm 0.03$, respectively. The amphibolite (sample 1) is characterised by remarkably high Young's modulus values ranging from 78 to 92 GPa.

The sonic velocity and density of each sample is presented in Table 1. The average sonic velocity is estimated to $V_p = 5155 \pm 765$ m/s. The average density is 2812 ± 149 kg/m³ with however, a value of density for the amphibolite ($\rho > 3000$ kg/m³; Table 1) well above the other rocks ($2696 < \rho < 2796$ kg/m³; Table 1).

With regards of all the values obtained by mechanical tests (Table 1), the amphibolite is certainly the strongest rock among the four types of rocks which, however, can be all assumed to be very strong.

2.2 DUCTILE FOLDS

Folds hinges were observed at several intervals and mainly in amphibolite layers. Most of them correspond to recumbent folds and are conspicuous at c. 8 m (Figure 5), 87–88 m (Figure 18), 92 m (Figure 19), 100.5–101 m (Figure 20), 105m (Figure 21), 116–116.5 m (Figure 23), 131.8 m (Figure 25) and 133.6 m (Figure 26) depth. Gently to moderately inclined folds with horizontal to gently plunging hinges are also observed at c. 5 m (Figure 4), 18.5 m (Figure 6), 19.5 m (Figure 7), 89.4 m (Figure 18), 91.5 m (Figure 19), 117 m (Figure 23), 121.4 m (Figure 24) and 130.5–132.5 m (Figure 25) depth.

Table 1. Results of rock mechanical laboratory analysis.

Depth of sampling [m]	Sample number- Rock type	Results of Brazilian test and empirical calculation			Results of uniaxial compressive test			Results of tilt test	Deformability parameters		Sonic velocity V_p [m/s]	Density ρ [kg/m ³]
		Uniaxial tensile strength, σ_t [MPa]	Point load index, $I_{s(50)} = \sigma_t \cdot 0.80$ [MPa]	Uniaxial compressive strength, $\sigma_c = k_{50} \cdot I_{s(50)}$ [MPa]	Uniaxial compressive strength, σ_c [MPa]	Angle of fracture, β [°]	Friction angle, $\phi = 2(45 - \beta)$ [°]		Basic friction angle ϕ_b [°]	Young's modulus, E [GPa]		
12.5–14.5	1- Garnet-bearing amphibolite (Figure 5 and Figure 6)	15.8–19.2	12.6–15.4	316–384 with $k_{50}=25$	112–212	16–22	46–58	25.9–27.9	78–92	0.10–0.18	6391–6613	3022–3122
22.2–24.0	2- Fine-grained strongly foliated augen gneiss (Figure 7)	16.1–17.7	12.9–14.2	322–354 with $k_{50}=25$	111–161	25–30	30–40	22.6–27.6	40–44	0.15–0.19	4549–4913	2696–2734
64.4–70.0	3- Medium- to coarse-grained augen gneiss (Figure 14 and Figure 15)	12.7–17.9	10.2–14.3	254–358 with $k_{50}=25$	109–181	25–33	24–40	24.2–28.0	34–41	0.09–0.15	4501–4851	2708–2726
136.0–137.5	4- Muscovite-rich medium-grained gneiss (Figure 26)	9.7–11.9	7.8–9.5	155–190 with $k_{50}=20$	101–104	25–28	34–40	24.4–28.4	37–47	0.10–0.16	4795–4989	2760–2796

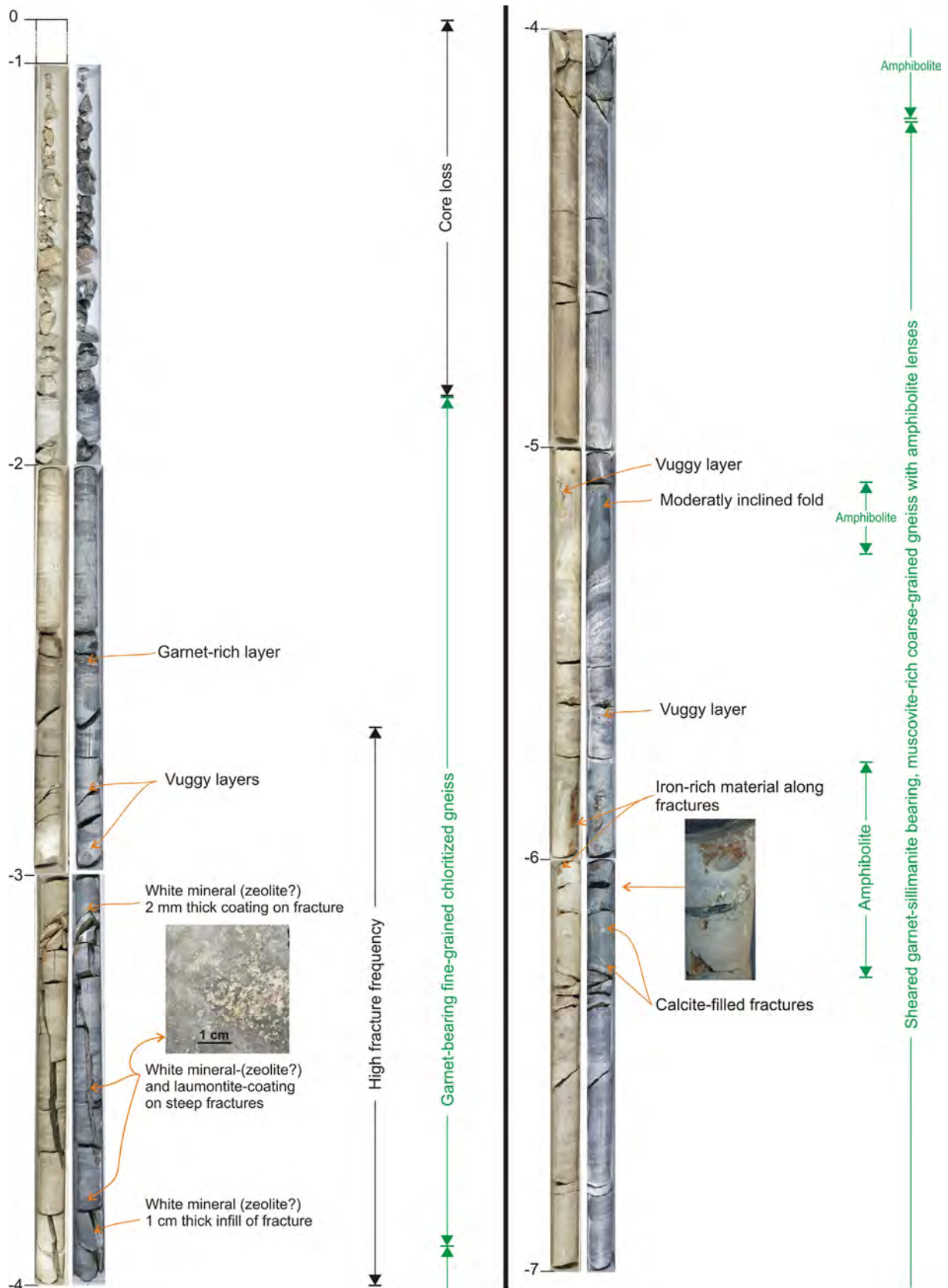
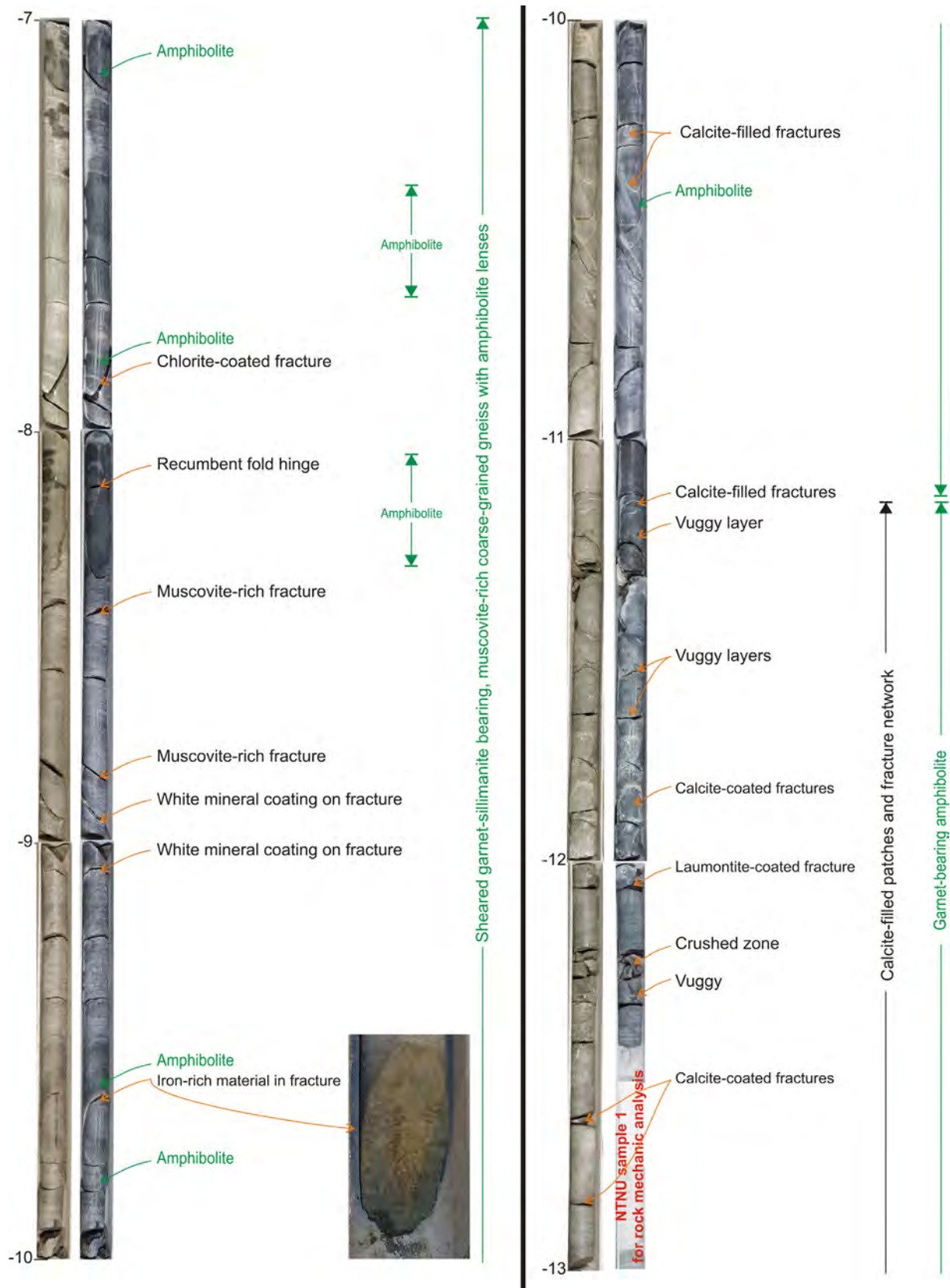


Figure 4. Structural and geological core logging from 0 to 7 m depth. Pictures of the 1 m long bits of the dry (left) and wet (right) core.



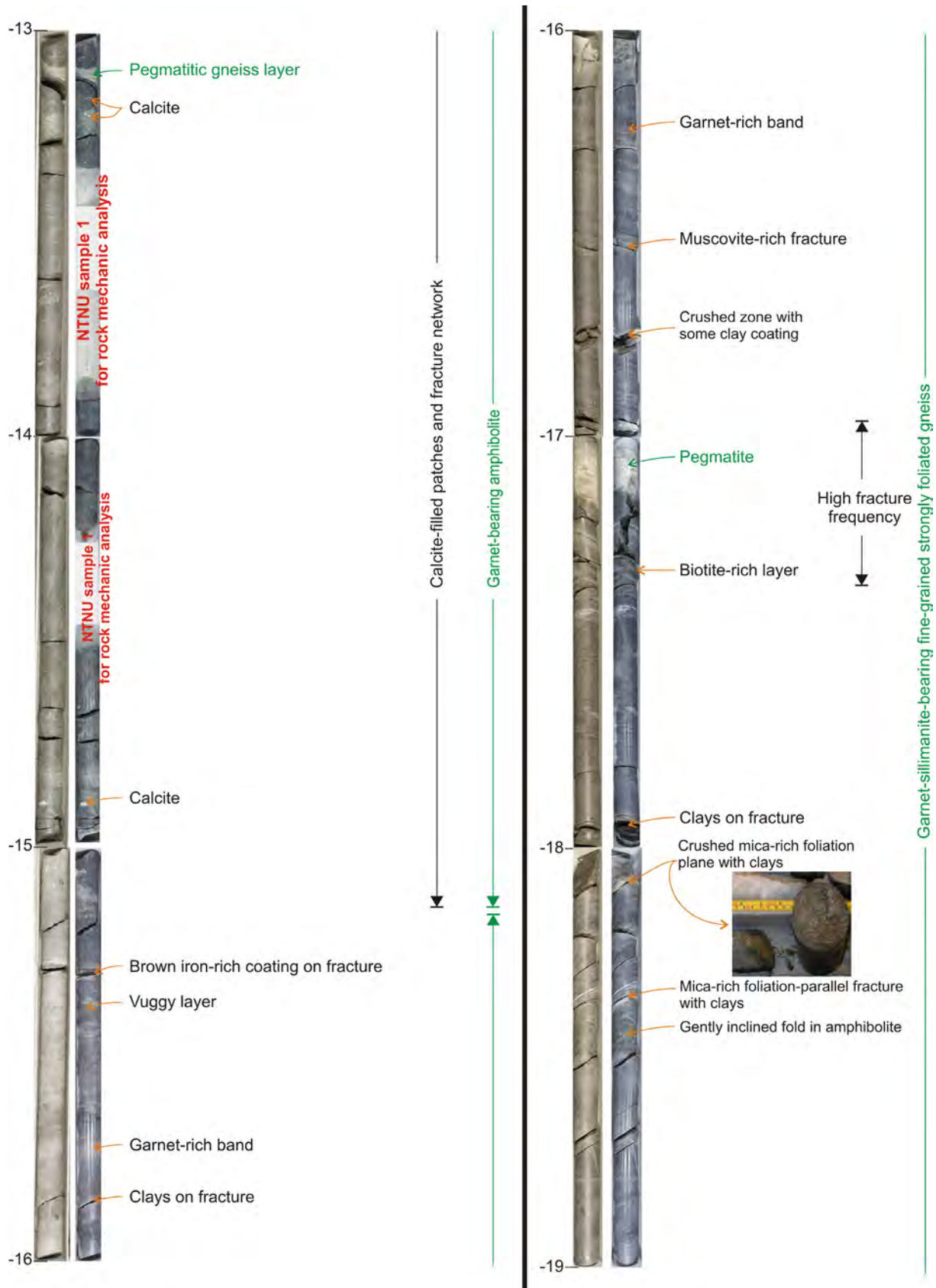


Figure 6. Structural and geological core logging from 13 to 19 m depth (see Figure 4).

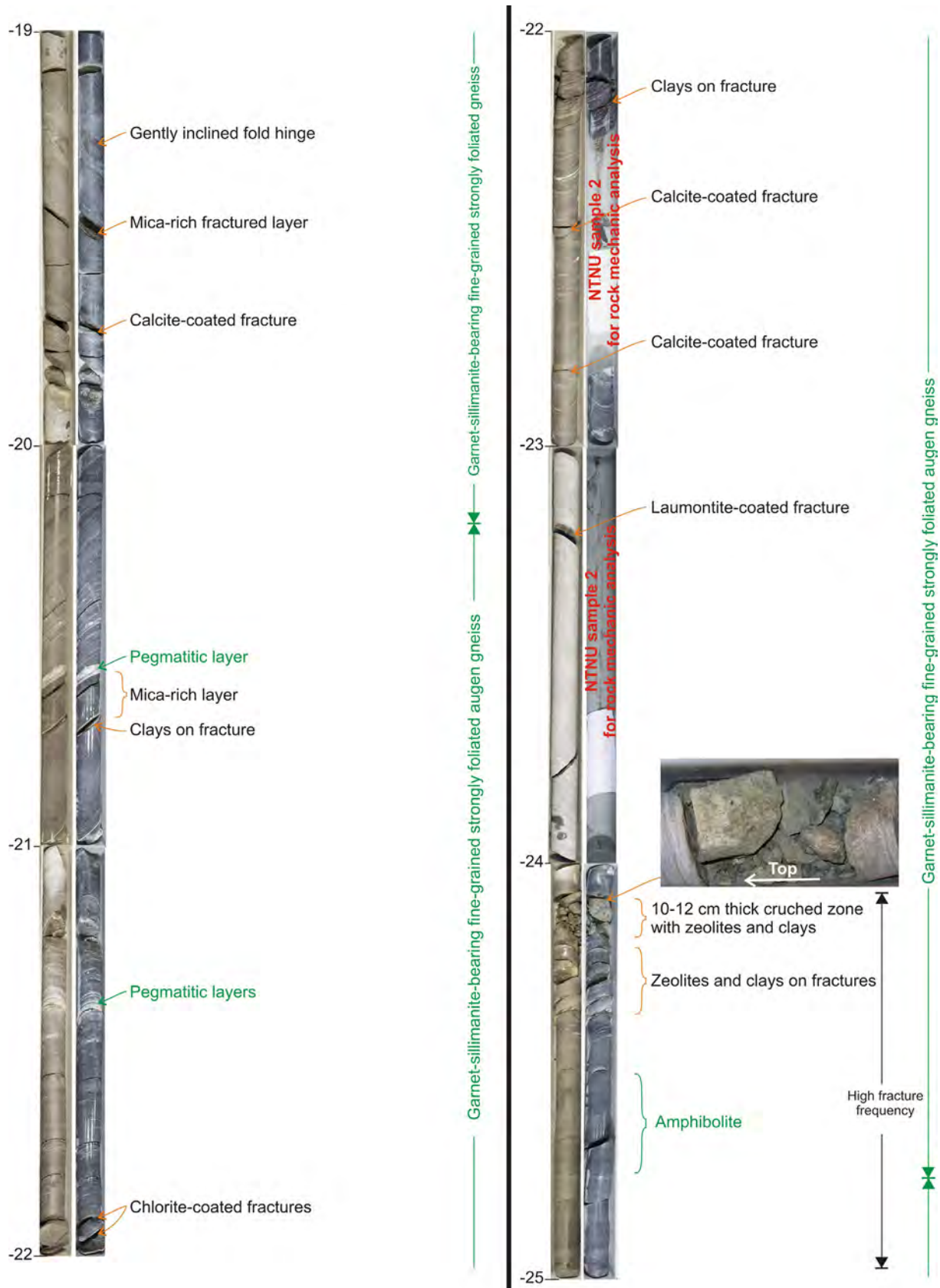


Figure 7. Structural and geological core logging from 19 to 25 m depth (see Figure 4).

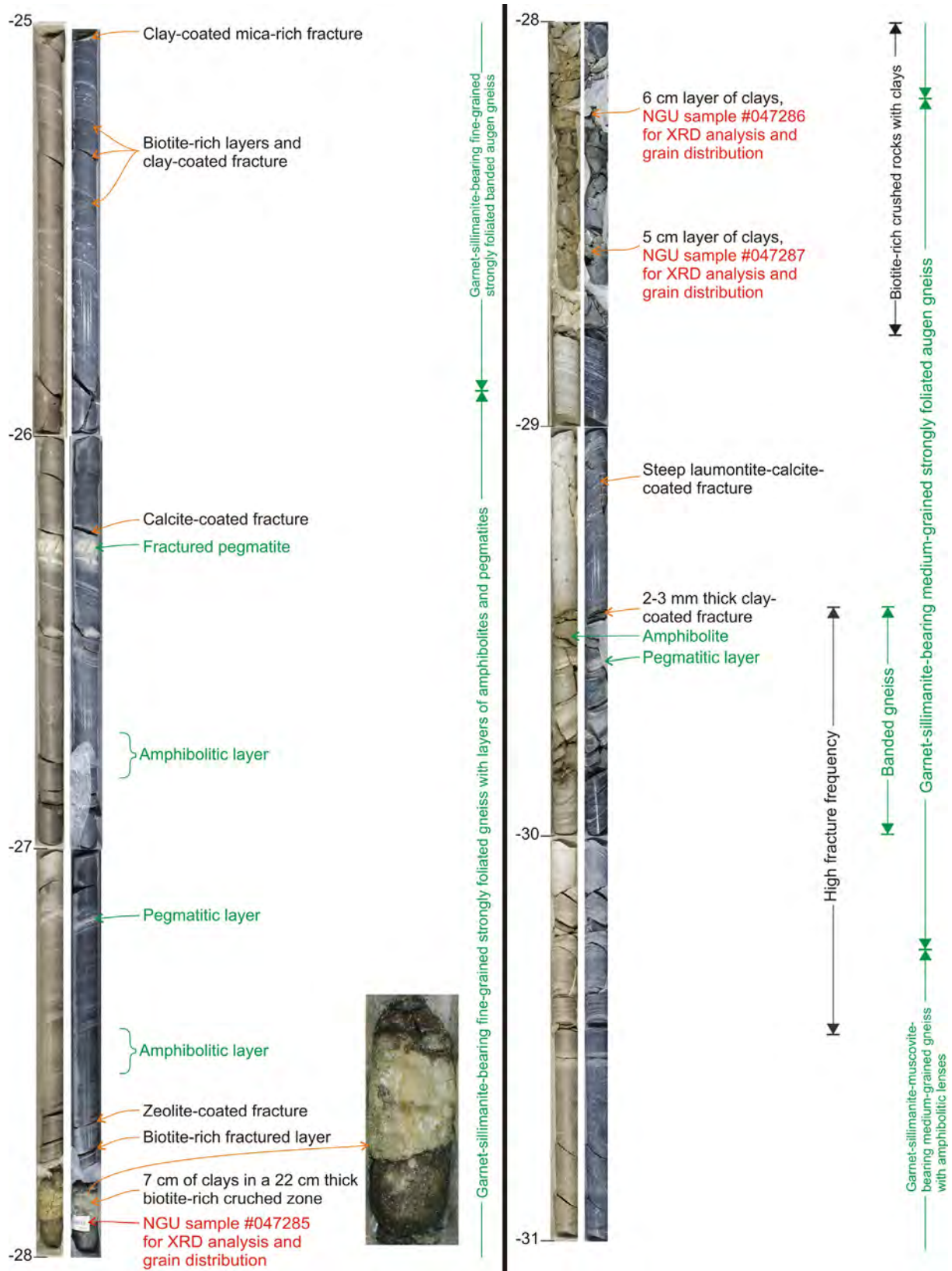


Figure 8. Structural and geological core logging from 25 to 31 m depth (see Figure 4).

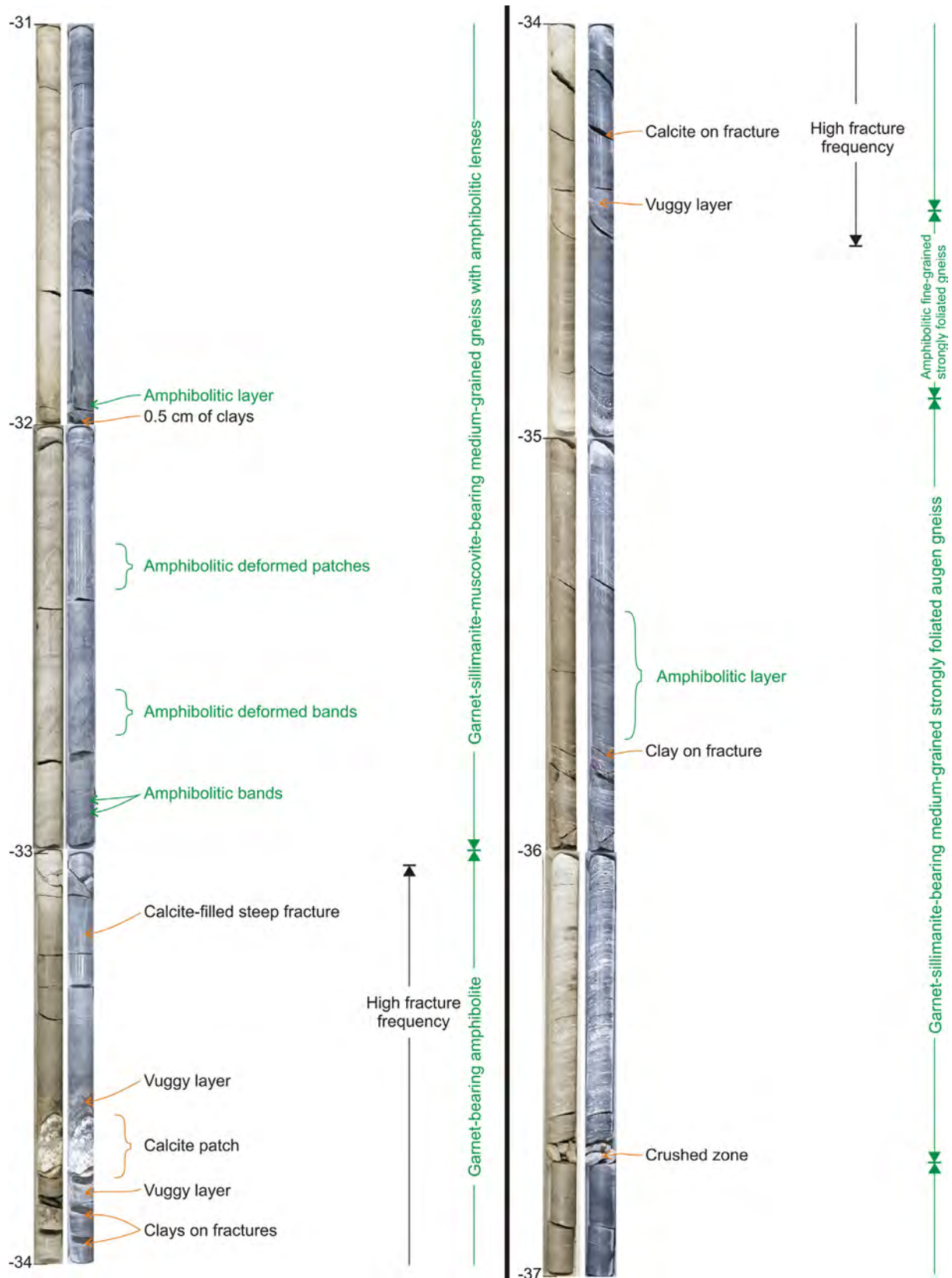


Figure 9. Structural and geological core logging from 31 to 37 m depth (see Figure 4).

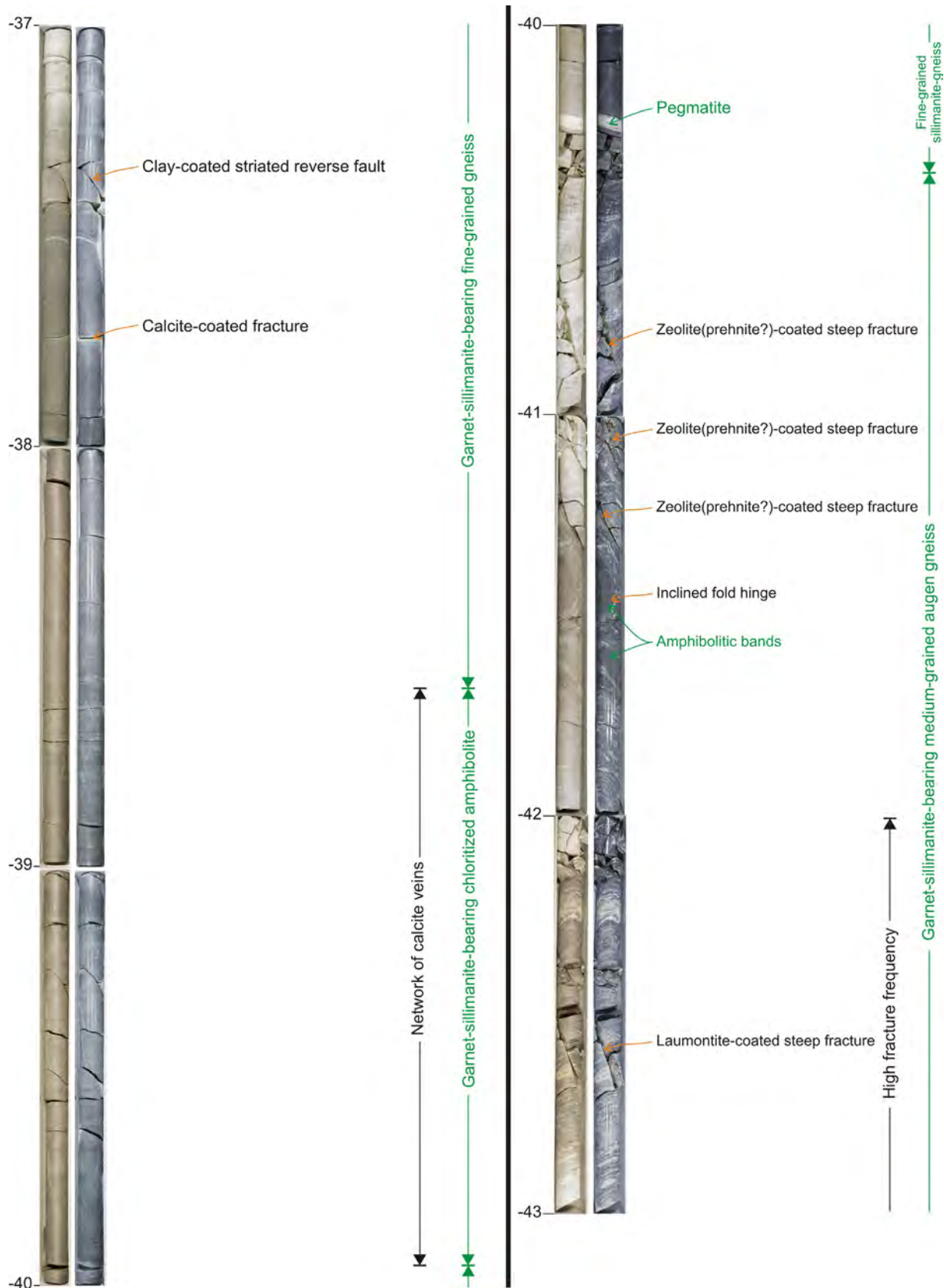
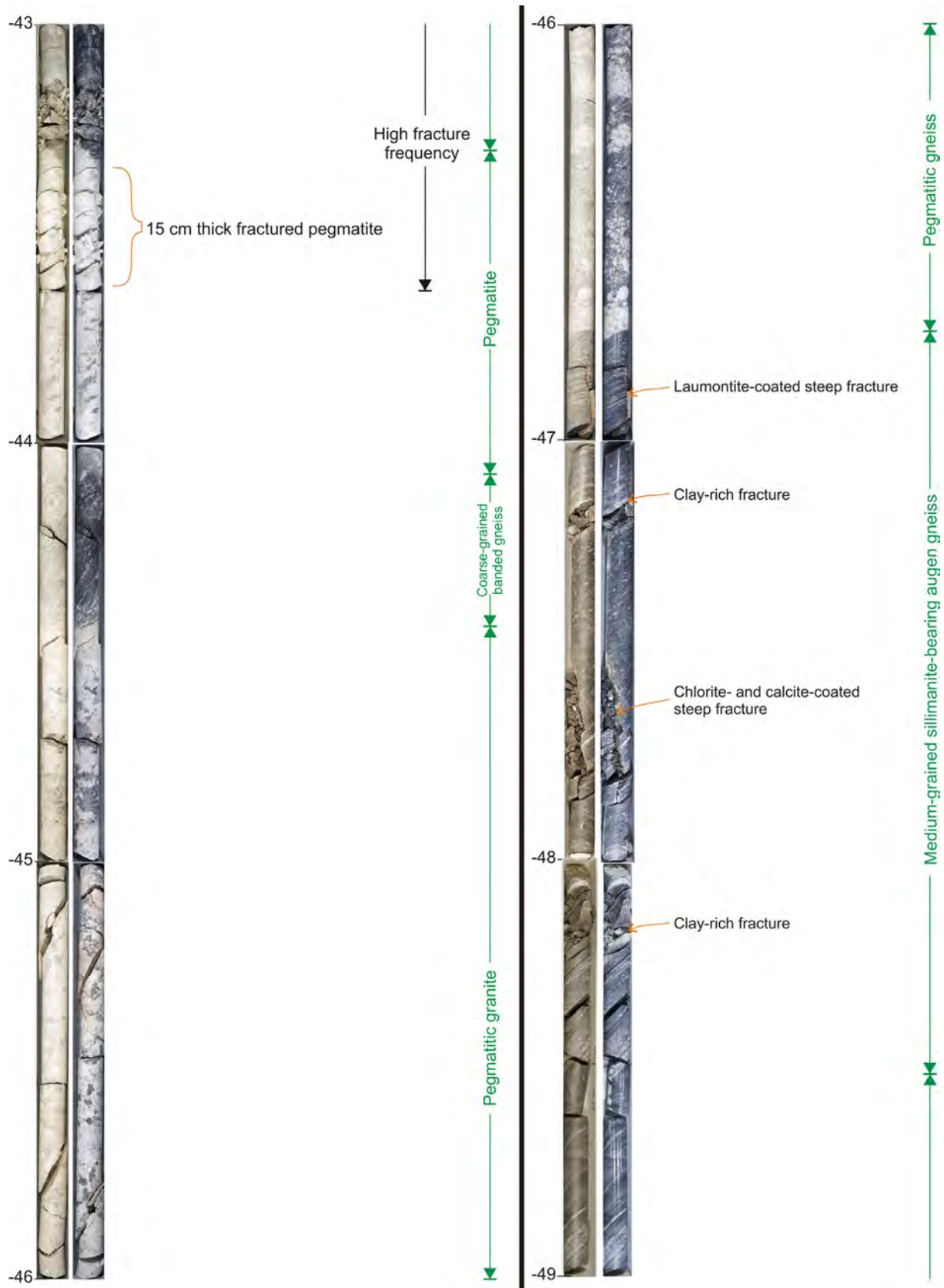


Figure 10. Structural and geological core logging from 37 to 43 m depth (see Figure 4).



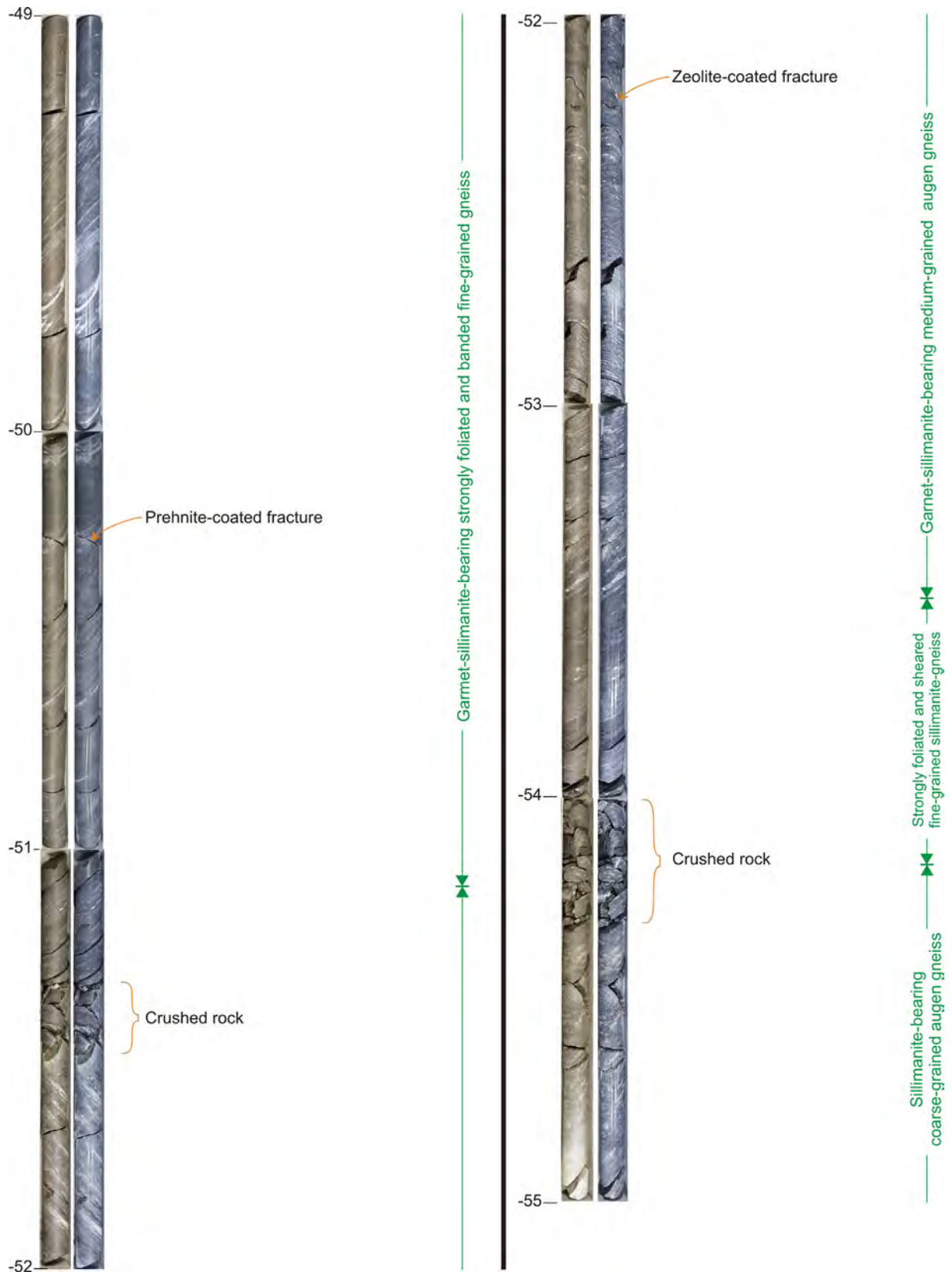


Figure 12. Structural and geological core logging from 49 to 55 m depth (see Figure 4).

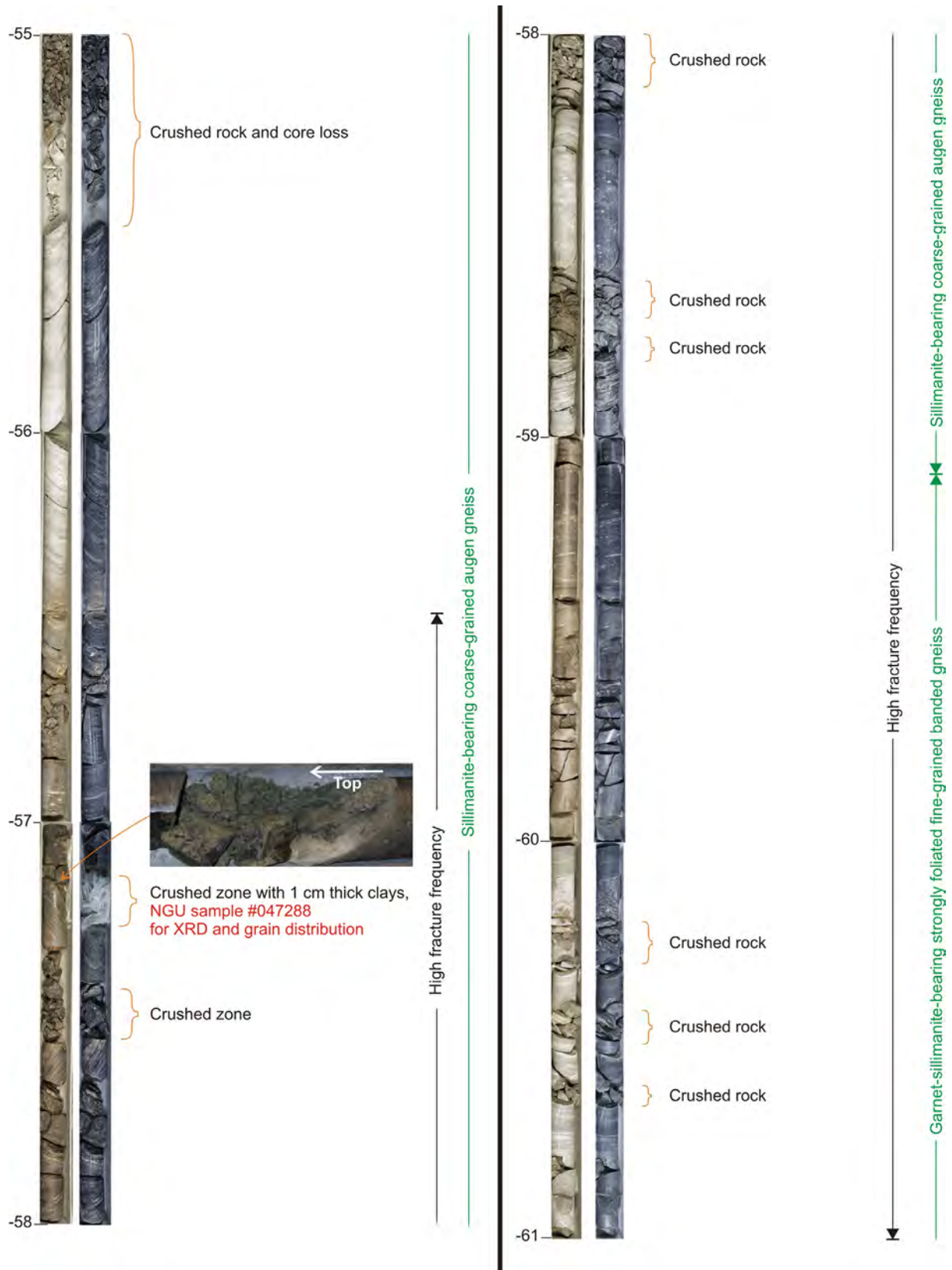


Figure 13. Structural and geological core logging from 55 to 61 m depth (see Figure 4).

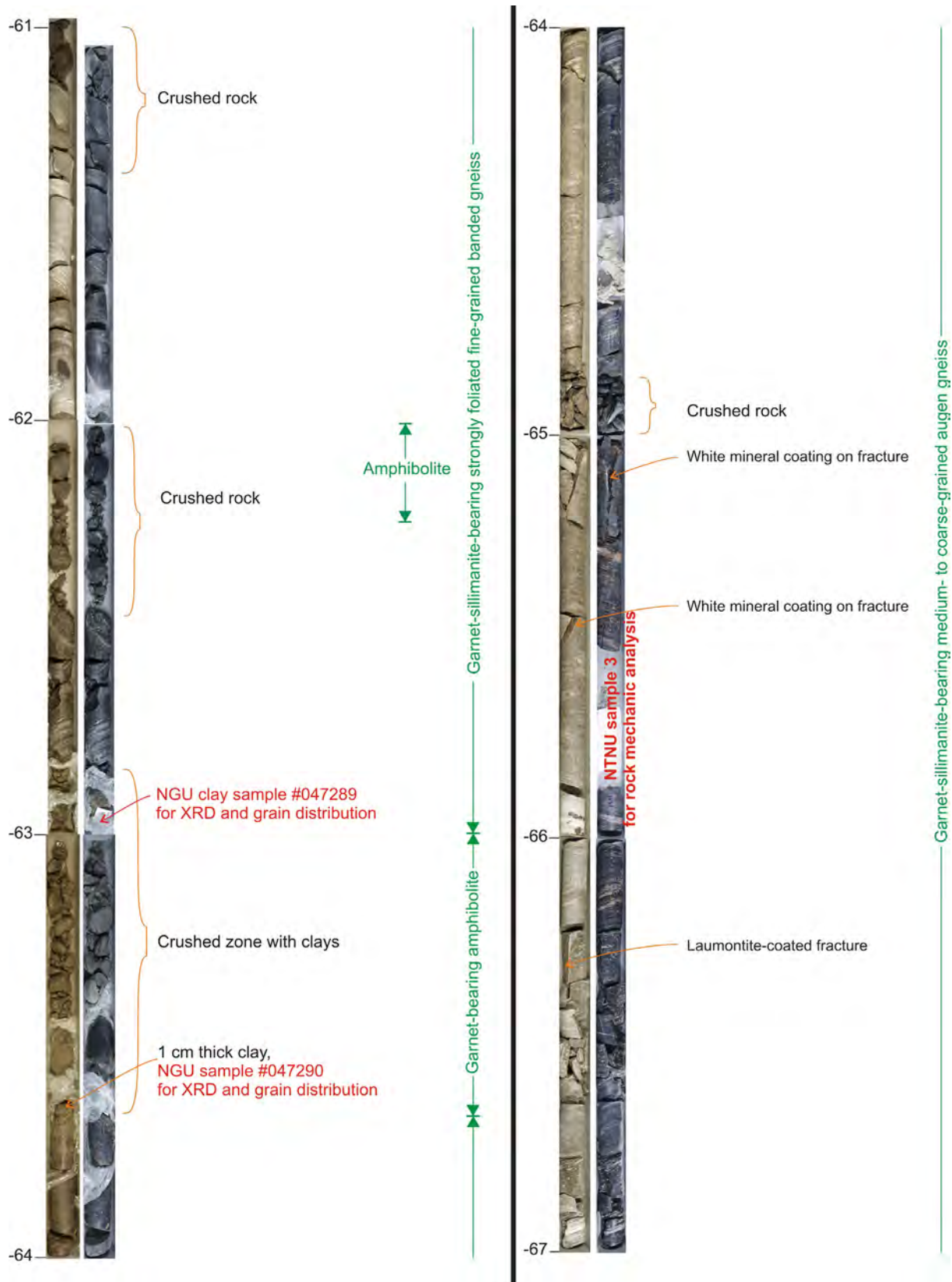
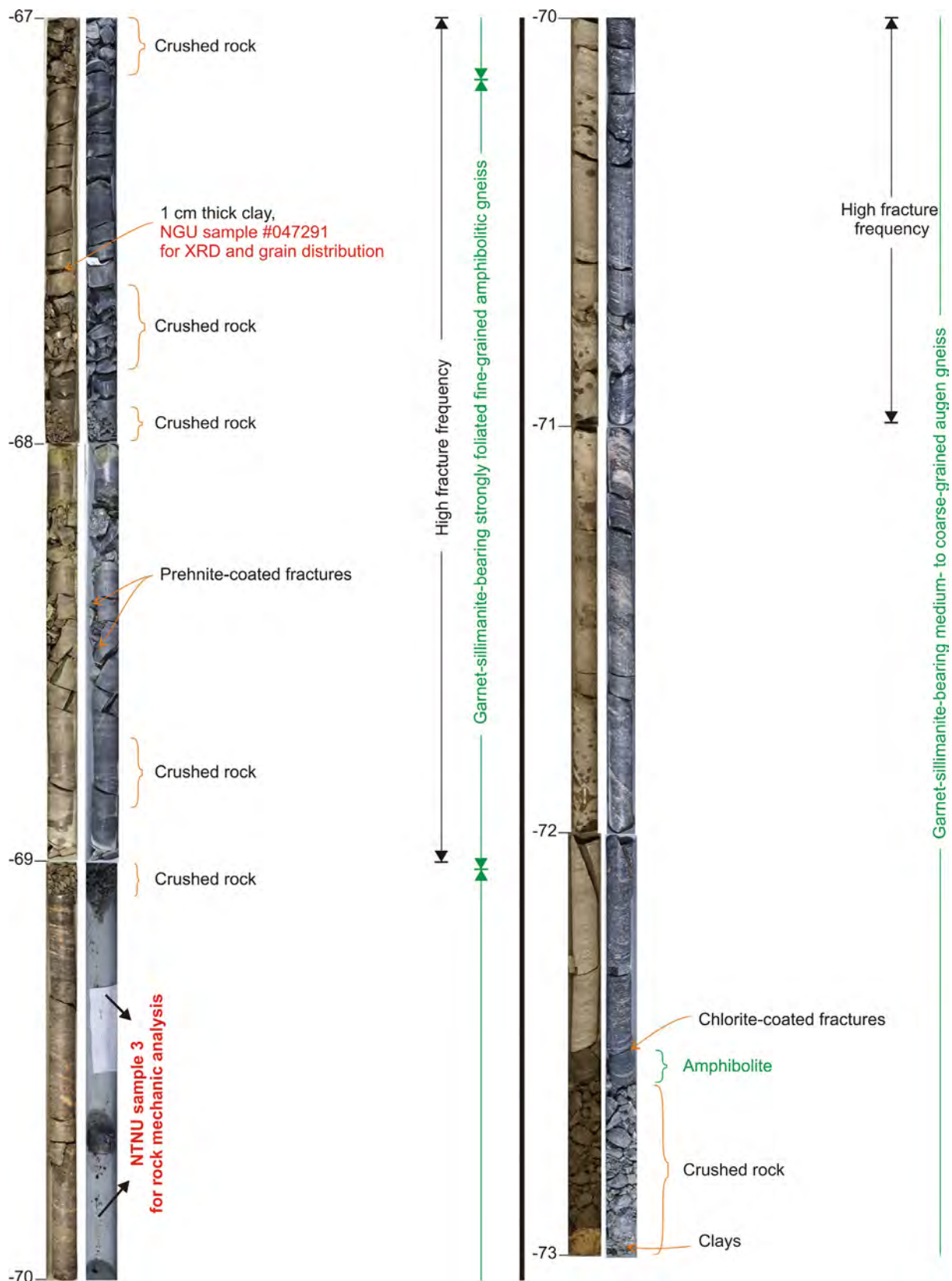


Figure 14. Structural and geological core logging from 61 to 67 m depth (see Figure 4).



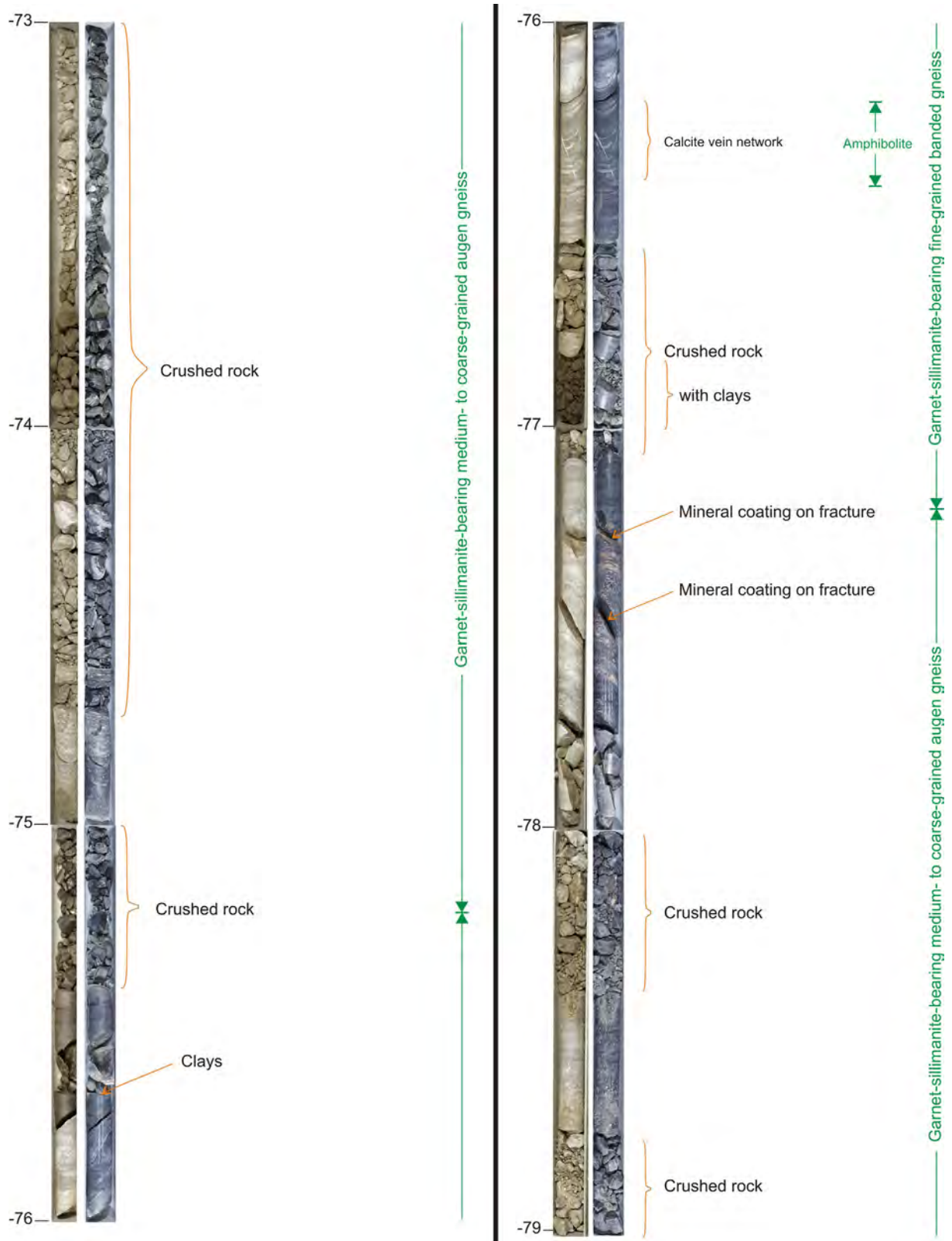


Figure 16. Structural and geological core logging from 73 to 79 m depth (see Figure 4).

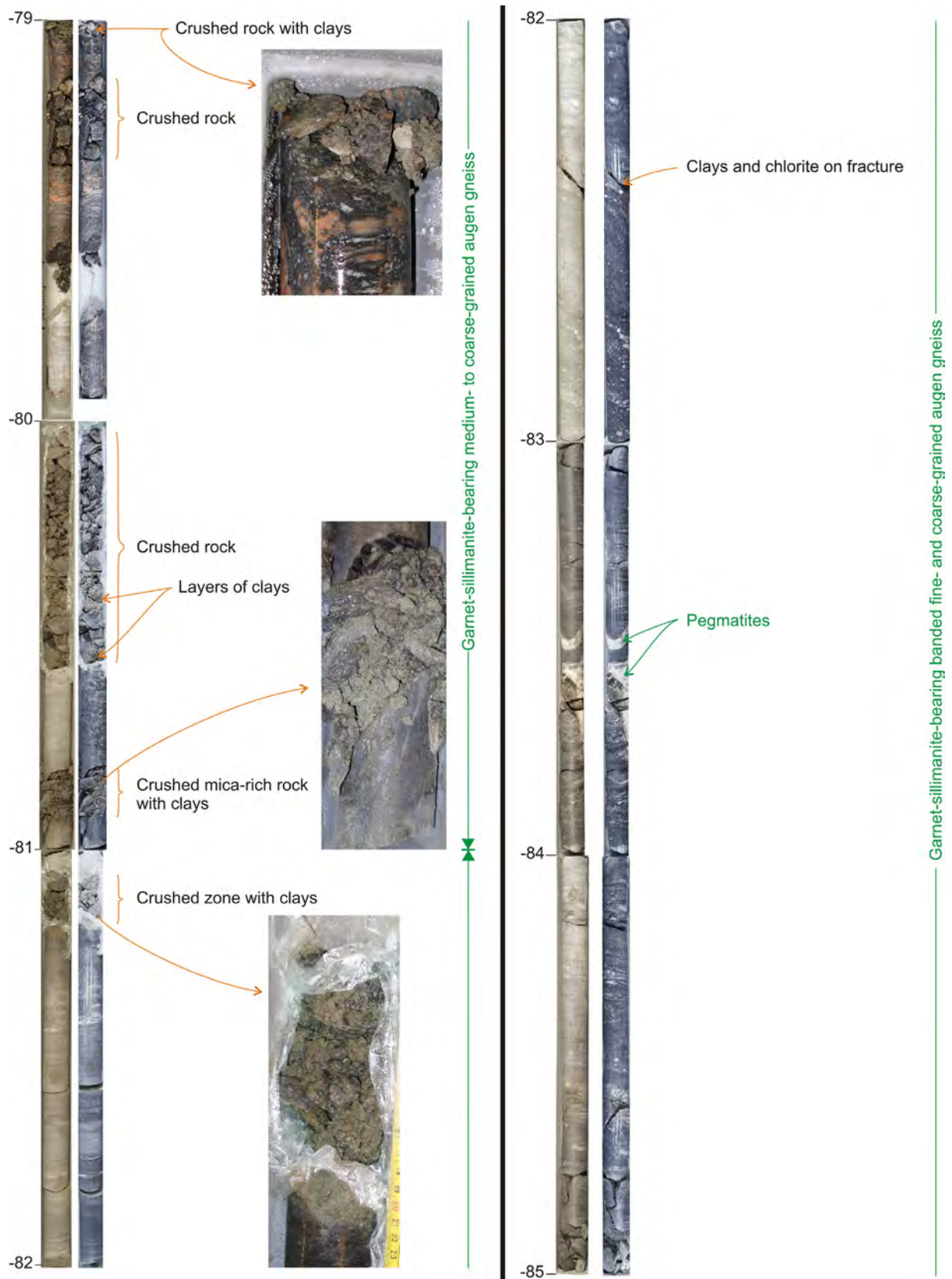


Figure 17. Structural and geological core logging from 79 to 85 m depth (see Figure 4).

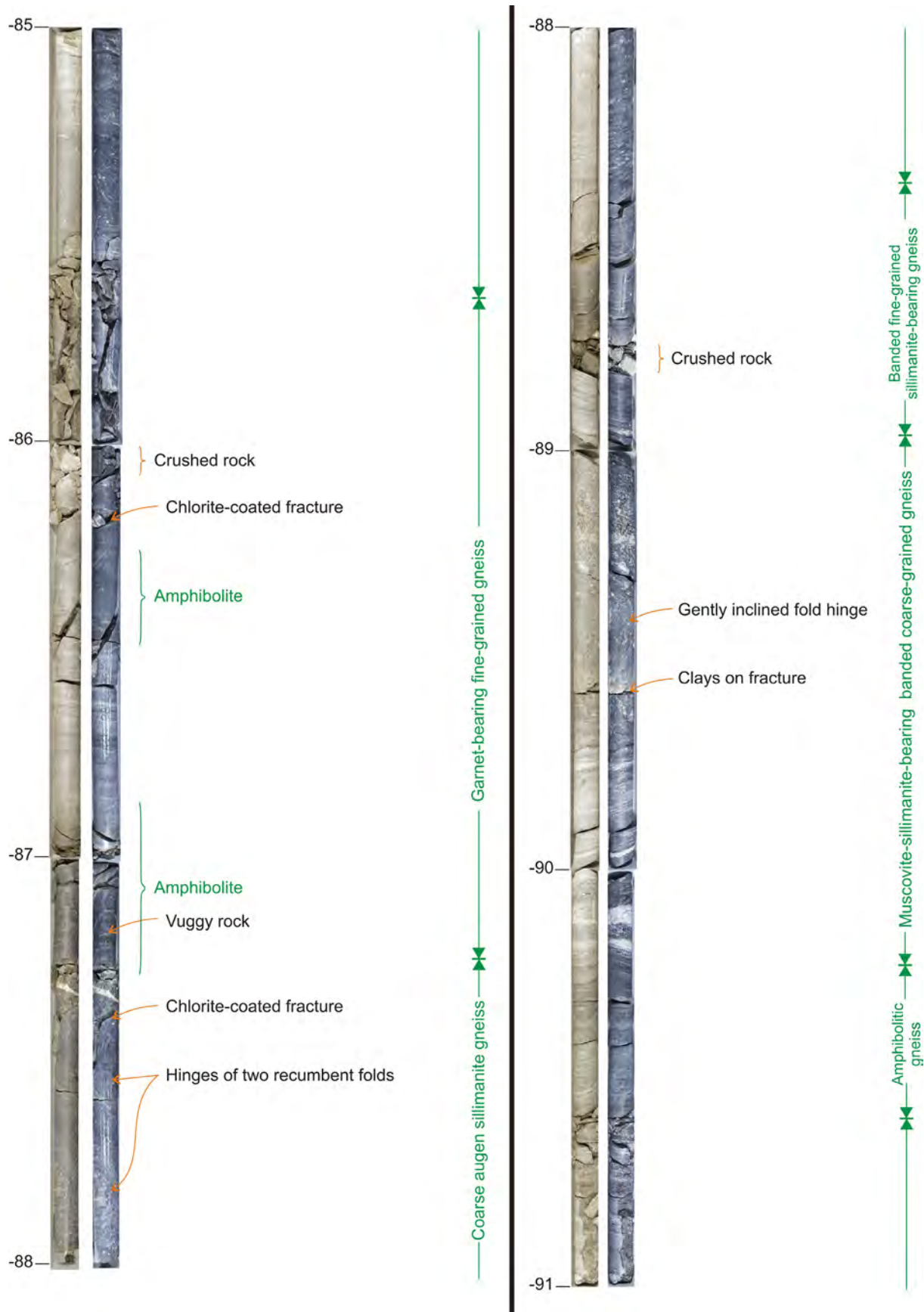


Figure 18. Structural and geological core logging from 85 to 91 m depth (see Figure 4).

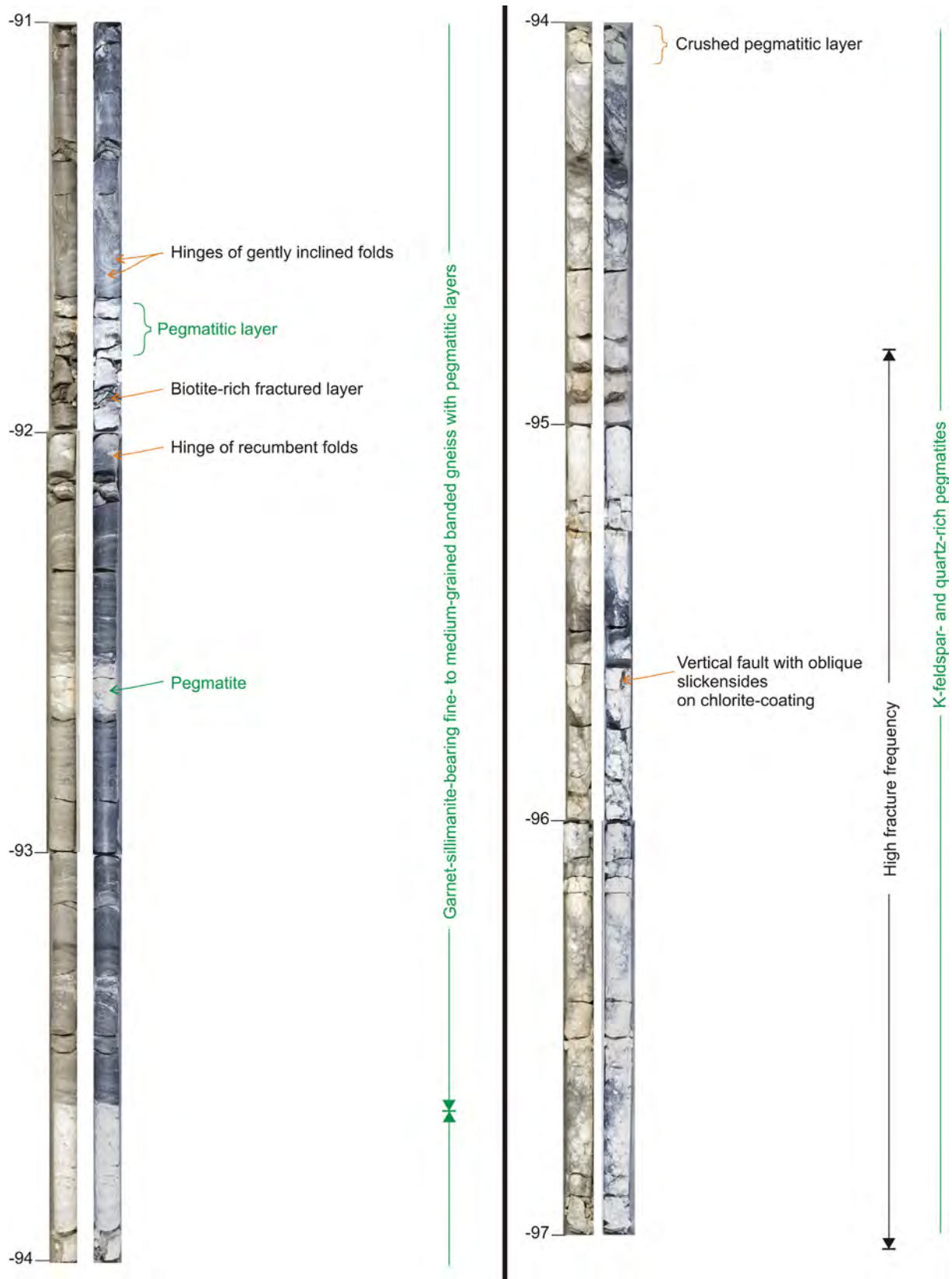


Figure 19. Structural and geological core logging from 91 to 97 m depth (see Figure 4).

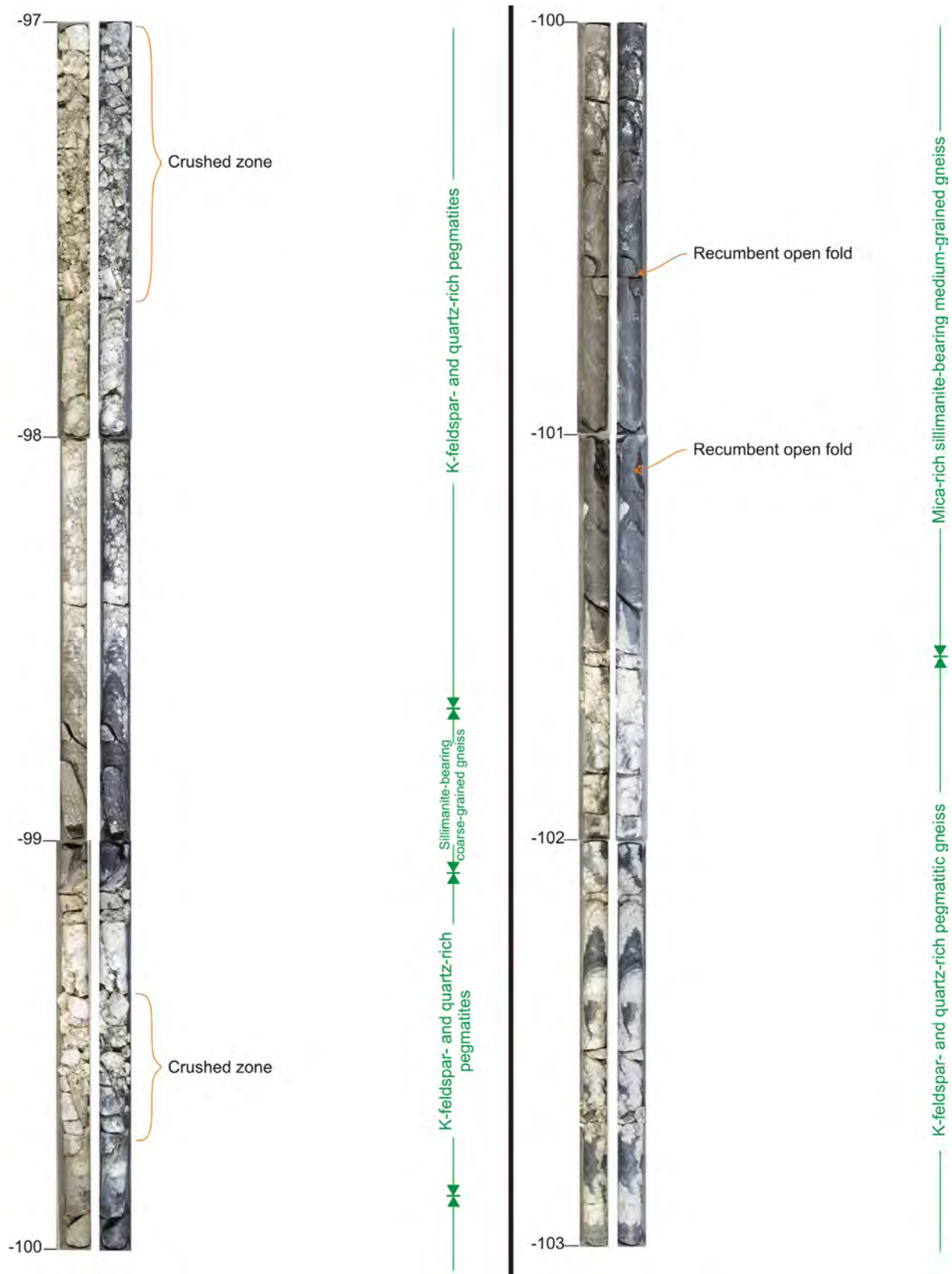


Figure 20. Structural and geological core logging from 97 to 103 m depth (see Figure 4).

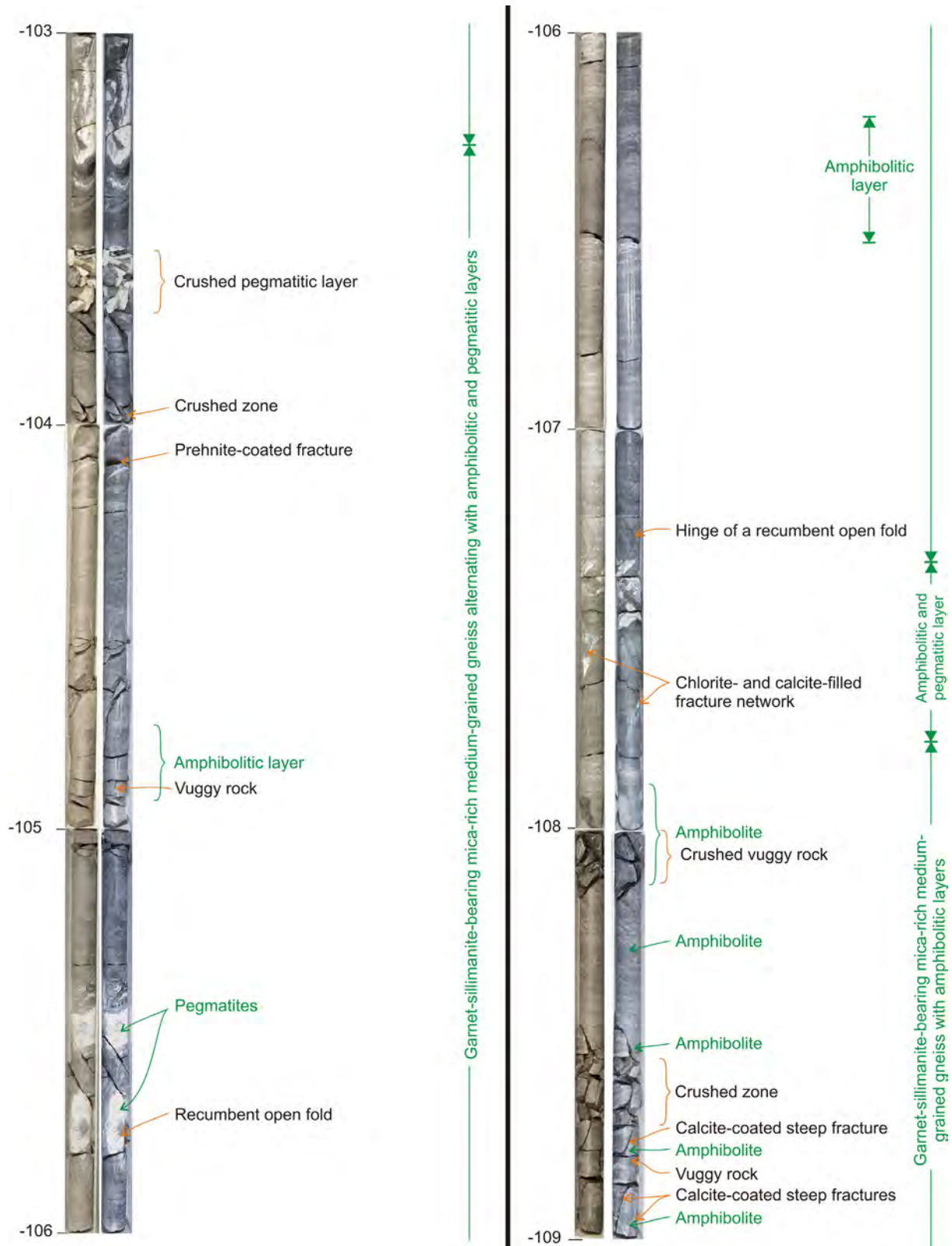


Figure 21. Structural and geological core logging from 103 to 109 m depth (see Figure 4).

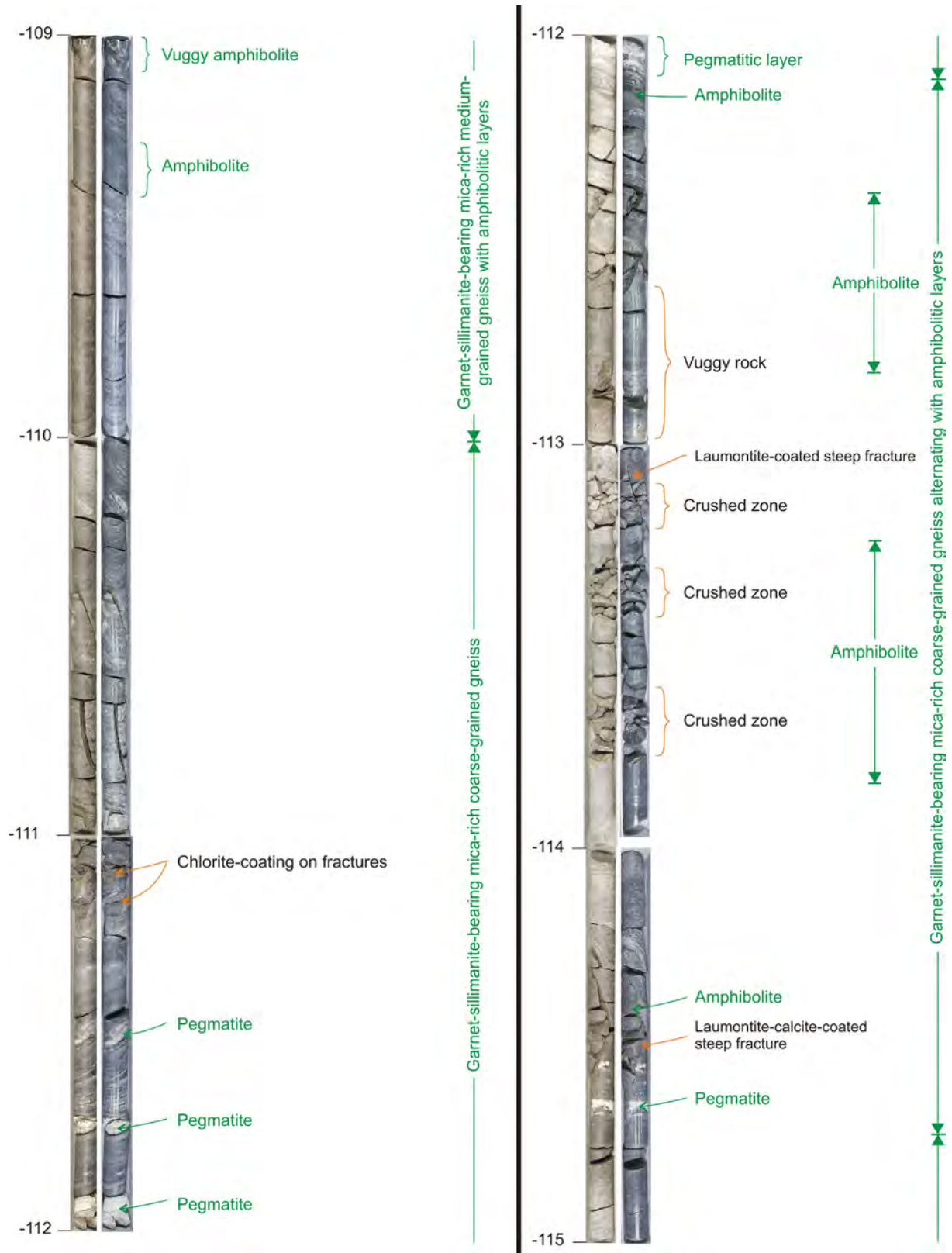


Figure 22. Structural and geological core logging from 109 to 115 m depth (see Figure 4).

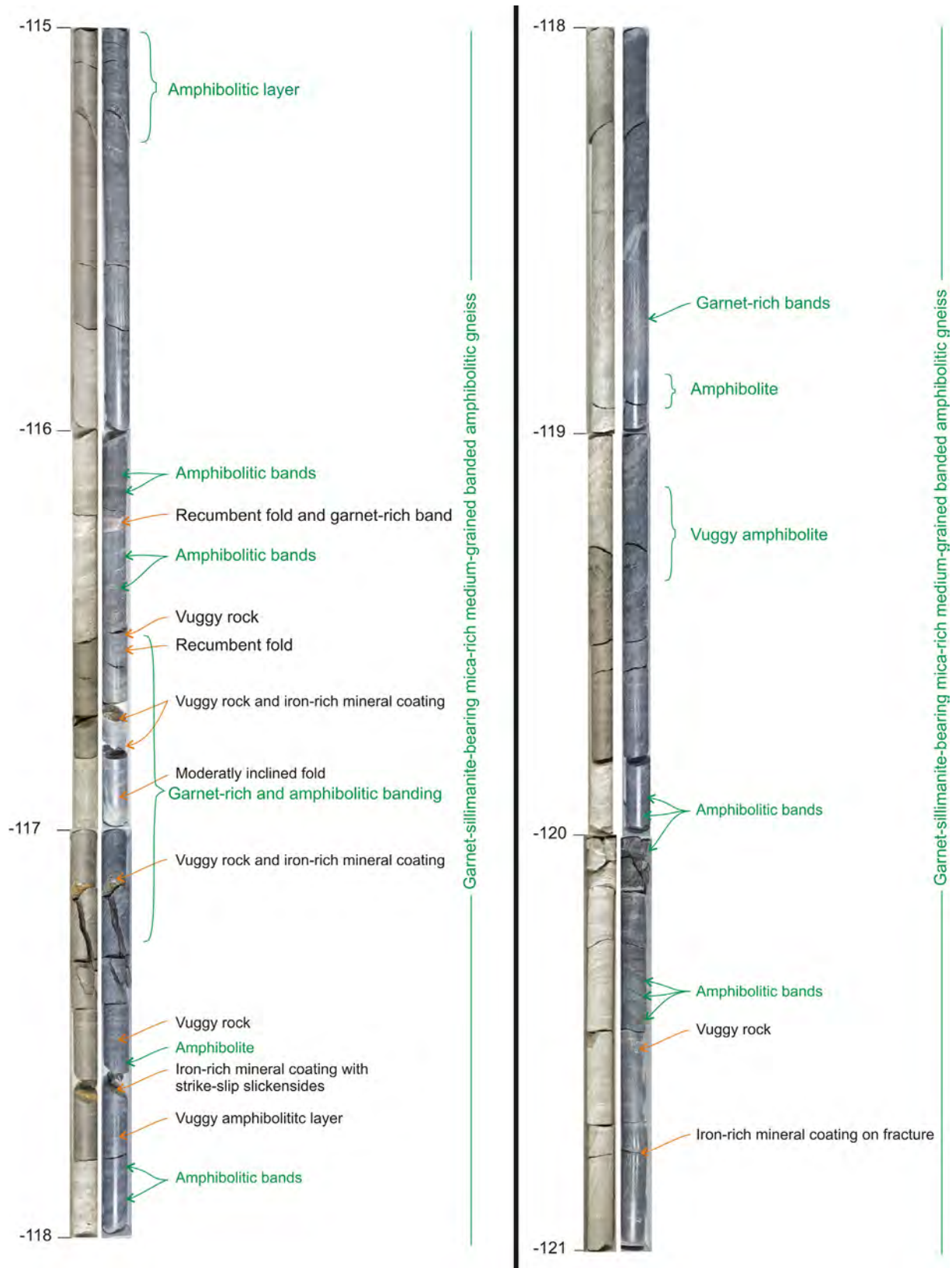


Figure 23. Structural and geological core logging from 115 to 121 m depth (see Figure 4).

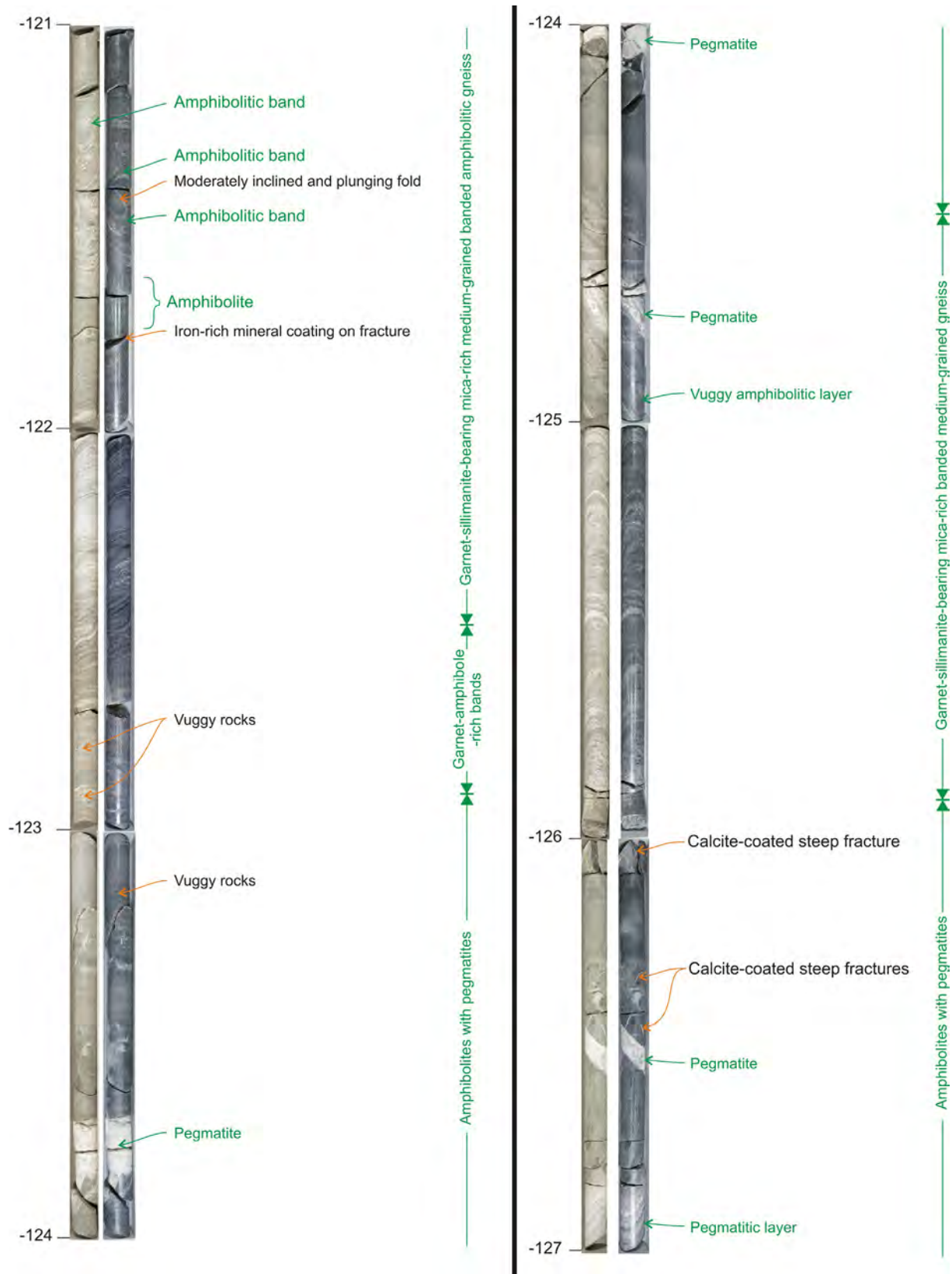
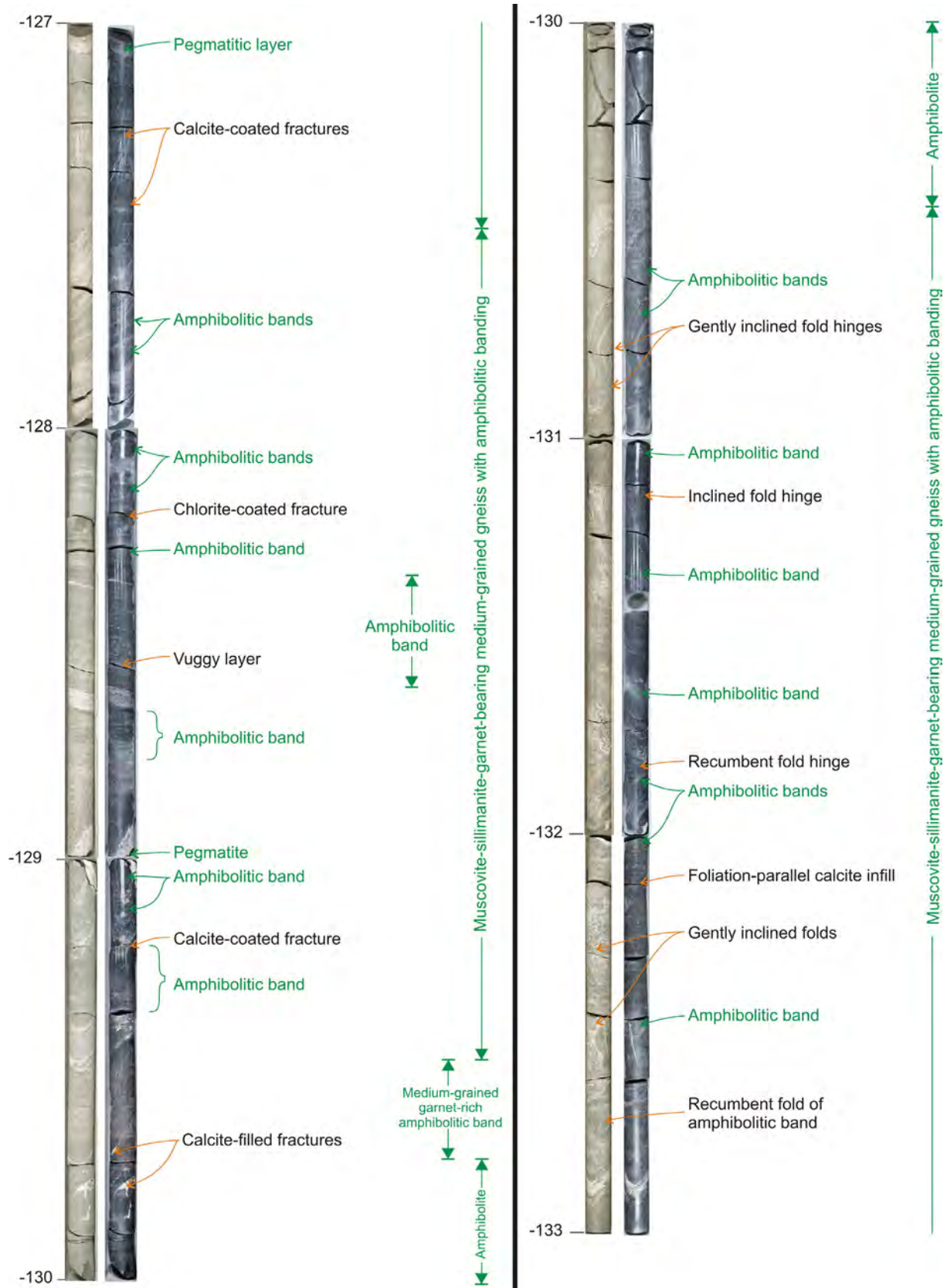


Figure 24. Structural and geological core logging from 121 to 127 m depth (see Figure 4).



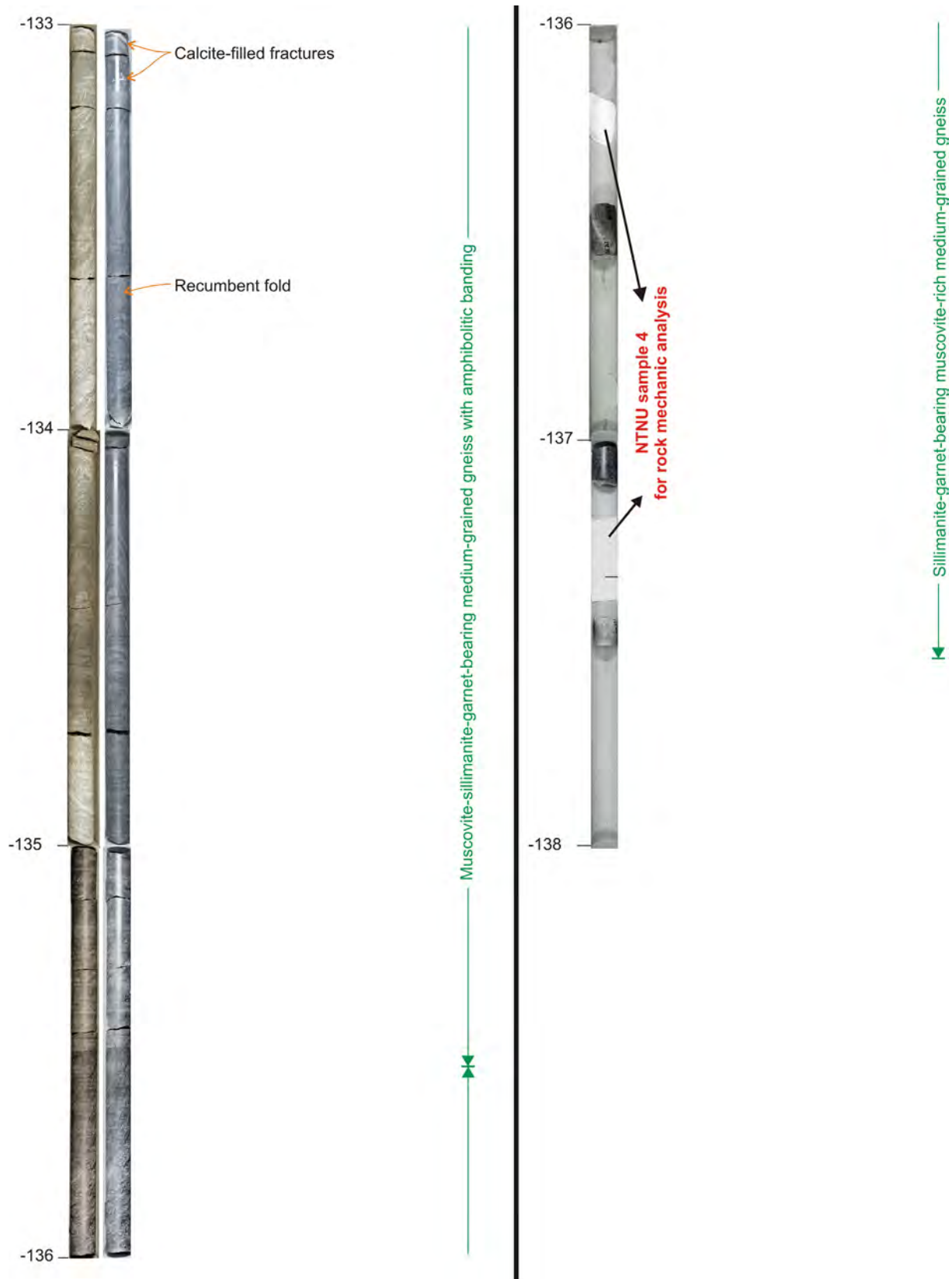


Figure 26. Structural and geological core logging from 133 to 138 m depth (see Figure 4).

2.3 FRACTURING, CRUSHED ZONES AND FAULT ROCKS

Fractures are generally mineral-coated (mainly with zeolites) and especially the steep fractures. It should be noted that the latter are underrepresented due to the verticality of the borehole. Fractures occur along the metamorphic foliation and at the contact between amphibolites and gneiss units. In intervals with high fracture frequency, the fractures are generally not found along the foliation. Therefore, the fracturing along the metamorphic foliation does not represent in general the main process of failure, except in the 24–25 m core interval where fractures follow the metamorphic foliation (see Table 2).

2.3.1 Large intervals of poor rock mass quality

The 28–31 m depth interval (Figure 8) is characterised by a low RQD value. It corresponds to 80 cm of crushed rocks in the 28–29 m interval and to a high fracture frequency in the 29–31 m interval (Table 2). Clay-rich zones varying in thickness from mm to c. 8 cm are encountered and sampled at 27.90–27.92 m, 28.21–28.25 m and 28.55–28.61 m (Table 3).

The 57–64 m depth interval (Figure 13 and Figure 14) comprises rock with poor quality. In the intervals 57–59 and 61–64 m, the low RQD values are due to important thicknesses of crushed rocks with up to 60–70% of crushed rocks at 62–64 m depth. A 1 cm thick clayey interval was sampled at 57.20 m depth (Table 3). In the 59–61 m depth interval, the RQD value is slightly higher due to the absence of crushed zones, but the fracture frequency remains very high (Table 2). The 61–64 m depth interval is also characterised by thin (mm-scale) clayey zones. Two of them were sampled at 63.00 m and 63.66 m (Table 3).

The 72–81 m depth interval (is distinguished by zones of crushed rocks (Table 2, Figure 15 and Figure 16). These zones can be more than 1 m thick, and clays are present within some of the zones.

2.3.2 Discrete intervals of poor rock mass quality

The 67–68 m depth interval (Figure 15) includes several zones of crushed rock (Table 2) and a c. 1 cm thick clayey zone at 67.60 m that was sampled (Table 3). The maximum value of fracture frequency is found in this depth interval and reaches a value of 13 fractures/m (Table 2).

The 97–98 m depth interval consists almost entirely of crushed rock (Table 2 and Figure 20).

The 108–109 m depth interval comprises several small (dm-scale) zones with crushed rocks (Table 2 and Figure 21).

The 99–100 m depth interval contains a c. 40 cm thick crushed zone (Table 2 and Figure 20).

The 113–114 m depth interval has three distinct zones of crushed rocks; two of them are located within an amphibolite layer (Table 2 and Figure 22).

Table 2. Fracture frequency along the core. The length of the bars for the fracture frequency is proportional to the maximum number of 13 fractures found in the interval 67–68 m. The length of the bars for the thickness of crush zones is proportional to 100 cm length of the core interval, i.e. a percentage like for the RQD (Rock Quality Designation) values. The symbol * indicates core loss along the interval.

Depth interval (m)	Fracture frequency	Foliation-parallel fracture frequency	Frequency of other fractures	Total thickness (cm) of crush zones	RQD	Depth interval (m)	Fracture frequency	Foliation-parallel fracture frequency	Frequency of other fractures	Total thickness (cm) of crush zones	RQD
2 - 3	5	1	4		77	70 - 71	9	4	5		48
3 - 4	12	3	9		15	71 - 72	5	1	4		86
4 - 5	7	2	5		77	72 - 73	3	1	2	40	52
5 - 6	3	2	1		83	73 - 74			100		0
6 - 7	7	2	5		78	74 - 75	3		3	75	32
7 - 8	5	3	2		87	75 - 76	6	2	4	50	39
8 - 9	6	2	4		70	76 - 77	1	1	1	55	56
9 - 10	7	3	4		61	77 - 78	8	1	7	5	63
10 - 11	7		7		71	78 - 79	2		2	60	34
11 - 12	8	4	4		70	79 - 80*	5		5	23	64
12 - 13	6	4	2	5	73	80 - 81	3		3	70	24
13 - 14	6		6		82	81 - 82	4	2	2	20	80
14 - 15	6		6		79	82 - 83	2	1	1		100
15 - 16	4	1	3		90	83 - 84	5		5		85
16 - 17	6	2	4	3	95	84 - 85	5	1	4		78
17 - 18	10	5	5		76	85 - 86	4		4		56
18 - 19	8	6	2		82	86 - 87	5	1	4	5	61
19 - 20	7	4	3		72	87 - 88	5	3	2		81
20 - 21	5	4	1		91	88 - 89	5	5		10	83
21 - 22	5	4	1		84	89 - 90	4	2	2		91
22 - 23	6	3	3		79	90 - 91	7	6	1		81
23 - 24	4	3	1		100	91 - 92	8	3	5		61
24 - 25	12	9	3	12	64	92 - 93	5	3	2		85
25 - 26	4	2	2		84	93 - 94	6	3	3		88
26 - 27	8	7	1		72	94 - 95	6		6	5	66
27 - 28	5	4	1	20	58	95 - 96	9		9		70
28 - 29	2	2		80	20	96 - 97	9		9		68
29 - 30	11	5	6		15	97 - 98	1	1	1	75	36
30 - 31	12	4	8		36	98 - 99	3	2	1		85
31 - 32	6	3	3		90	99 - 100	5		5	40	22
32 - 33	3	1	2		97	100 - 101	5	1	4		85
33 - 34	11	2	9		55	101 - 102	7	1	6		70
34 - 35	5	2	3		90	102 - 103	6		6		100
35 - 36	6	4	2		75	103 - 104	5	2	3	20	60
36 - 37	7	1	6	5	82	104 - 105	9	1	8		45
37 - 38	8	5	3		51	105 - 106	5		5		89
38 - 39	7	4	3		68	106 - 107	4	1	3		91
39 - 40	7	2	5		70	107 - 108	5		5		94
40 - 41	8	5	3		28	108 - 109	5		5	35	41
41 - 42	5		5		68	109 - 110	4	1	3		100
42 - 43	9	3	6		48	110 - 111	8		8		86
43 - 44	10	1	9	15	47	111 - 112	8	3	5		64
44 - 45	3		3		100	112 - 113	8	4	4		42
45 - 46	6		6		50	113 - 114	8		8	58	17
46 - 47	4	1	3		84	114 - 115	8		8		65
47 - 48	5	3	2		76	115 - 116	5	3	2		91
48 - 49	7	5	2		40	116 - 117	5	1	4		67
49 - 50	3	1	2		100	117 - 118	6	1	5		100
50 - 51	4	2	2		100	118 - 119	3	1	2		95
51 - 52*	4	3	1	20	34	119 - 120	4		4		93
52 - 53	5	3	2		84	120 - 121	7	2	5		80
53 - 54	5	5			77	121 - 122	4	2	2		86
54 - 55	6	4	2	30	52	122 - 123	1		1		100
55 - 56*	3	3		20	50	123 - 124	4		4		80
56 - 57	9	4	5		77	124 - 125	6	1	5		80
57 - 58	8	3	5	40	30	125 - 126	3	1	2		90
58 - 59	10	3	7	37	35	126 - 127	8	1	7		82
59 - 60	10		10		54	127 - 128	5	1	4		85
60 - 61	12	1	11	23	43	128 - 129	5	4	1		93
61 - 62	5	2	3	40	37	129 - 130	7		7		100
62 - 63	2		2	60	18	130 - 131	8	1	7		94
63 - 64	4	2	2	70	26	131 - 132	4		4		95
64 - 65	5	1	4	10	68	132 - 133	4	1	3		99
65 - 66	6	1	5		86	133 - 134	3		3		92
66 - 67	7	1	6		47	134 - 135	4		4		97
67 - 68	13	2	11	42	11	135 - 136	3		3		100
68 - 69	10	4	6	15	45	136 - 137	3	2	1		100
69 - 70	6	5	1	7	88	137 - 138	2		2		

2.3.3 Clay-rich intervals

Clay-rich zones were sampled during the core logging for XRD analysis and grain size distribution (see above for the description of sampled zones, Table 3). The results of laboratory analysis were not yet available at the time of the finalization of this present report. They will be fully described and interpreted in a separate report.

Table 3. Samples for XRD analysis and grain size distribution

Sample number	Depth of sampling - material
47285	27.90–27.92 m - gouge / clays (see Figure 8)
47286	28.21–28.25 m - gouge / clays (see Figure 8)
47287	28.55–28.61 m - gouge / clays (see Figure 8)
47288	57.20 m - gouge / clays (see Figure 13)
47289	63.00 m - gouge / clays (see Figure 14)
47290	63.66 m - gouge / clays (see Figure 14)
47291	67.60 m - gouge / clays (see Figure 15)

The clays are typically the products of the chemical weathering of gneissic minerals. Because (1) angular fragments of the host rock are preserved in the clayey matrix and (2) severely fractured and crushed zones commonly surround the clay-rich intervals, it is inferred that they also derive from the weathering of frictional products and characterise the gouge infill of fault cores. This assertion is supported by the fact that the clayey zones are generally surrounded by crushed zones, which correspond to the typical damaged zone of shear zones.

The three several cm thick clay-rich shear zones at 27 or 28 m depth cannot be explained by only gravity-induced forces. Indeed, we assume that at this shallow depth it will require more than the 10 000 years to form such thickness of weathered products only by gravity-induced forces and slow creep. It is thus likely that the gouge-filled zones are of tectonic origin and that, after the ice sheet melting, these intrinsically weak zones localized the gravitational deformation leading to the development of sliding surfaces.

Whatever their origin and formation the clayey zones locally contribute to lower the stability of the rock mass. For stability assessments it is important to better characterise the content of swelling clays.

2.4 SUMMARY OF OBSERVATIONS AND INTERPRETATION

The bedrock types near the surface reappear further down in the drill core. This is likely due to the occurrence of recumbent folding, which is observed both on surface outcrops (i.e. along the back-crack) and in the drill core.

- 0–24 m: In this interval, the rock is fractured, but the rock mass quality is generally good.
- 24–40 m: From 24 m depth and downwards, crushed zones occur and specifically in the 28–31 m depth interval. At c. 27.8–28.0 m, a major shear plane is observed. It consists of a 8–10 cm thick fault core filled by a clay-rich gouge, bordered by two zones of c. 10 cm crushed biotite-rich gneiss. This main shear zone is succeeded by a crushed zone containing two narrow zones with 3–4 cm thick gouge infill. Below these zones, the rock is heavily fractured.
- 40–54 m: Crushed zones occur regularly from 40 m and downwards, with occasional core loss.
- 54–56 m: Two 20–30 cm thick zones of severely fractured rocks with interlayered clays, but without a distinct clay/gouge fault core, are present in this interval.

56–82 m: Rocks are either crushed or strongly fractured and several zones are so distinguished between 57–59m, 59–61 m, 61–64 m and 67–68 m. Gouges in fault cores surrounded by damaged rocks are abundant in these zones. The interval between 72.5 and 81.2 m depth consists of zones of crushed rock and narrow zones with a clay-rich gouge.

This high frequency of weak zones in the 56–82 m depth interval (see Table 2) may indicate the location of the potential sliding surfaces of the Mannen rock slope instability.

82–92 m: There are fewer occurrences of zones with crushed rock below 81.2 m, and the frequency of such zones as well as fracturing decrease with depth.

92–138 m: The fracturing decreases and rock mass quality improves with depth, except in a few zones of crushed rocks. A 6–7 m wide zone of heavily fractured pegmatite occurs at c. 93.6–99.9 m, which is crushed in the interval 97–98 m. Other remarkable crushed zones are in the 99–100 m, 108–109 m and 113–114 m depth intervals. At c. 115 m and below the rock in the core is more intact.

Below 92 m, fewer foliation parallel fractures appear compared to above 92 m. This might be due to the frequent changes in the attitude of the foliation due to the folding of the bedrock. In this lower part, the fractures are concentrated in zones where amphibolites occur.

3. TELEVIEWER LOGGING OF THE BOREHOLE

An optical televiewer was used to map in-situ the attitude of the metamorphic foliation, of fractures and damage zones along the borehole down to a depth of 133 m.

3.1 INSTRUMENTATION, DATA ACQUISITION AND PROCESSING

The borehole optical televiewer probe is manufactured by Robertson Geologging Ltd. (<http://www.geologging.com>) and comprises a conventional light source, a camera with a 360° circle view lens and an orientation device. The high-technology optical system of the camera allows a 360° simultaneous imaging of the wall of the borehole in mm steps downward. The pixel resolution of the images is of 1 by 1 mm. In real time, the images of the walls are taken orientated relatively to the magnetic north and unwrapped. The orientation device also provides the borehole deviation from its vertical axis, which is at Mannen of 7.3 m to the west at 133 m depth (Figure 27). The borehole deviation is measured every 1 m during the logging and the velocity of the logging was of 1 m/min.

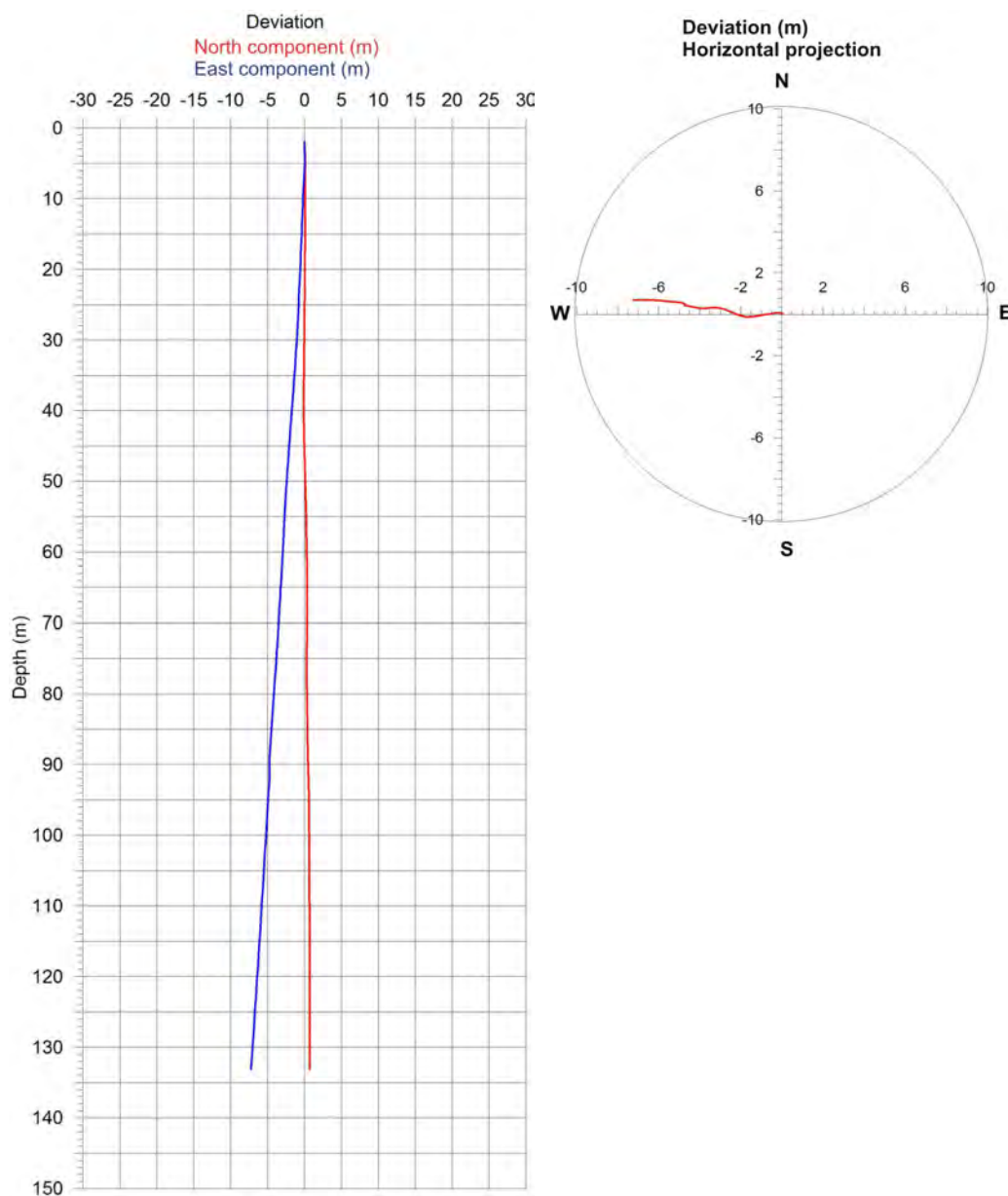


Figure 27. Mannen borehole deviation: north and east components (left) on the vertical section and direction viewed from the top (right).

The digitalisation of specific geological features, as fractures, crushed zones that are observed along the images allows to gather their characteristics (thickness, opening, infill...) and orientation (dip direction and angle) relatively to the magnetic north and corrected from the borehole deviation. The magnetic deviation at Mannen is 0.6° eastward and can thus be neglected. The orientations of planar structures given by the instrumentation are so considered relative to the geographic north. Hence, these measurements are afterwards processed like classical structural data.

The interpretation software RG-DIP from Robertson Geologging Ltd. allows to display the core images and the planar data orientations (with conventional arrow plots, stereoplots, rose diagrams) (see in Appendix 1).

The drilling was interrupted two times due to collapse of the hole. This was where crushed rocks were encountered at c. 32 m and 59 m depth. Drilling went on after stabilization and casing of the borehole. The logging by the optical televiewer was made before the casing of the borehole and thus followed the steps of drilling. The televiewer logging had also to be interrupted between 77 and 89 m because of the high risk of jamming the probe in an unstable severely damaged rock. The logging continued to the bottom of the hole after the installation of a drill string.

The method of logging by a borehole optical televiewer is described in detail in <http://www.ngu.no/no/hm/Norges-geologi/Geofysikk/Borehullsgeofysikk/> (in Norwegian).

3.2 STRUCTURAL DATA ALONG THE BOREHOLE

The data from the optical televiewer are presented according to this four logged depth intervals which are, from the top to the bottom, 3.1–31.7 m (in Chapter 3.2.2), 32–58 m (in Chapter 3.2.3), 57–77 m (in Chapter 3.2.4) and 89–133 m (in Chapter 3.2.5). The hole was dry down to 123.9 m depth.

In each interval, the digitised metamorphic foliation planes are visible and measured (see tables in Appendix 1). All the measurement of fractures and fractured zones are listed in Appendix 2 with characterisation of the thickness and/or aperture of fractures. The fracture frequency is also analysed (parameters for the fracture frequency calculation is given in Appendix 3).

3.2.1 Overview of the attitude of the structural data along the entire borehole

Before presenting in detail the structural analysis in the four logged intervals, a general view of the attitude of all the 196 foliation and 287 fracture planes collected along the borehole is given in Figure 28 and Figure 29. The foliation appears to be moderately to gently dipping towards the NNE with average orientations of $011^\circ/20^\circ$ and $015^\circ/33^\circ$ (dip direction/dip angle) depending on the statistical method used (Figure 28). 96% of the data plots in a cone of c. 25° aperture around the pole of the average orientation. Even if a bias is due to the verticality of the borehole, a qualitative inspection of the wall of the borehole (Appendix 1) coupled with the direct observation of the core (see Chapter 2) allows to confirm the shallow dip angles of the foliation planes. In turn, the measurement of fractures is likely biased and steep fractures are underrepresented in the dataset. It results that the mean value of the fracture orientation is the one of the foliation (Figure 29). However, few steep fractures have been measured (Figure 29) and their attitude is of importance in terms of stability analysis of Mannen rock slope. The contour plots of the fractures, and specifically the Gauss counting method, allows obtaining four subsets of steep fractures with average values of dip directions/dip angles of $118^\circ/76^\circ$, $206^\circ/59^\circ$, $251^\circ/52^\circ$ and $350^\circ/73^\circ$.

Datasets: 196

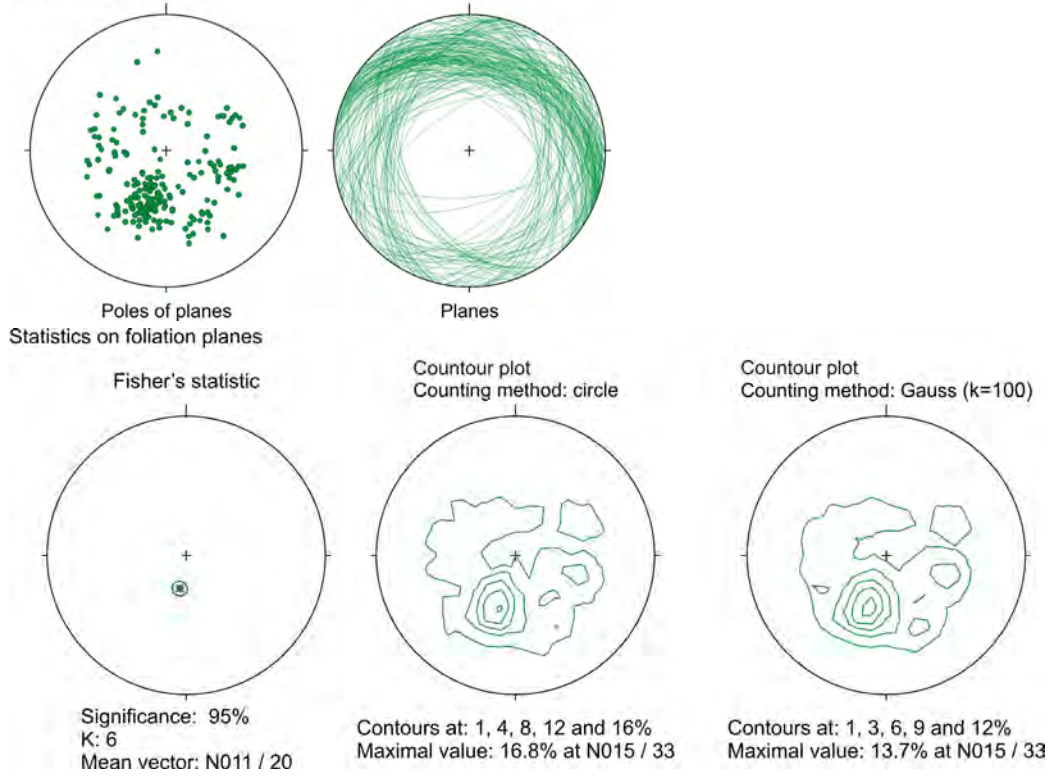


Figure 28. Stereoplots (lower hemisphere, Schmidt's projection) of the foliation planes measured along the borehole by televiwer imaging.

Datasets: 287

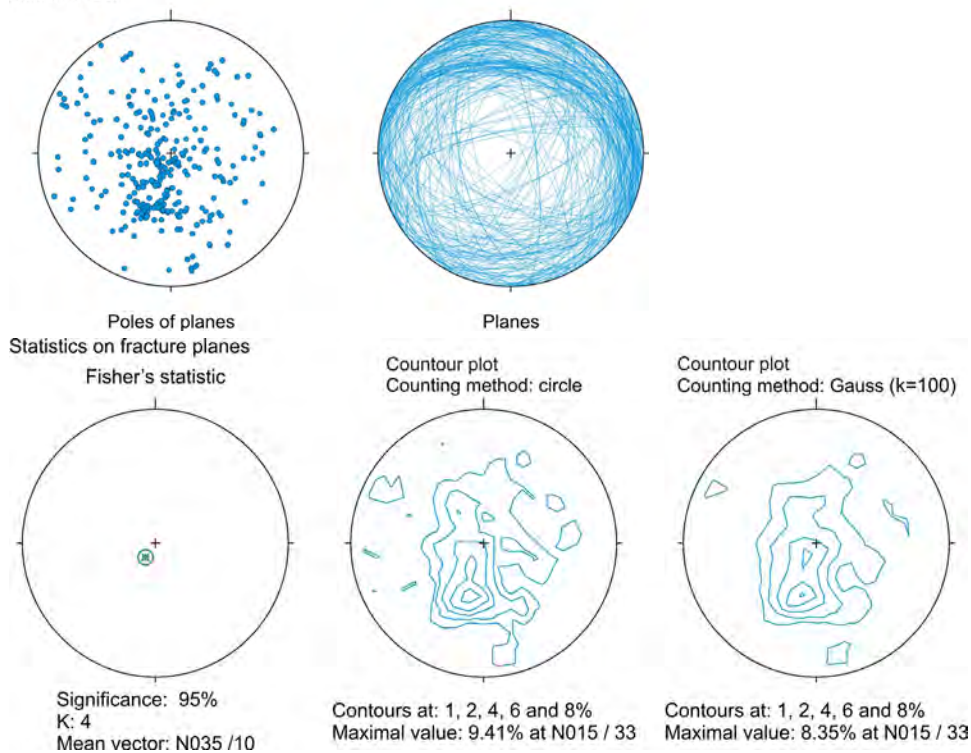


Figure 29. Stereoplots (lower hemisphere, Schmidt's projection) of the fractures measured along the borehole by optical televiwer imaging.

3.2.2 Structural data in the c. 3.1–31.7 m depth interval

3.2.2.1 Metamorphic foliation in the 4–31.7 m depth interval

The foliation was measured at 54 different depths along the 4–31.7 m interval (Figure 30–Figure 32 and Appendix 1). In the first 11 m depth of the hole, the foliation dips to the NW (dip direction: 304°) and the dip angle varies from 20° to 64° (Figure 30, Figure 32). From 15 m depth to the bottom of the studied interval at 31.7 m, the foliation dips towards the NNE (dip direction: 025°), i.e. towards the valley, with an average angle of 25° (Figure 30–Figure 32).

3.2.2.2 Fractures in the c. 3–32 m depth interval

Figure 33 shows the four main fractures sets out of the 128 fractures encountered in the 3–32 m depth interval. The majority of mapped fractures is parallel to the foliation and the main set corresponds to fractures dipping toward the NNE, directly to the valley with a dip angle of 36°. This main set is also well displayed on the rose diagram of all fractures (Figure 34).

The frequency histogram of the four fracture sets detected in the c. 3–32 m depth interval shows clearly the spatial distribution of the fractures (Figure 35). Very shallow fractures are prominent in the first 15 m of the depth interval (in red on Figure 35). The major fracture set of the interval (dip direction and angle: N019/36; in blue on Figure 35) is nearly present in the entire interval and largely prevails in the c. 15–29.5 m depth with frequency reaching 10–12 fractures/m. From 29 to 32 m depth, interestingly, a set of steep fractures (dip direction and angle: N210/53; in pink on Figure 35) becomes predominant.

The c. 3–32 m depth interval was divided in 7 zones with regards to the fracture frequency (Figure 35) during the numerical calculation and according to the results listed in Appendix 3.

Figure 36–Figure 42 give the detailed pictures of the fractures in the 3.1–31.7 m depth interval. Foliation-parallel fractures are conspicuous from 20 m downward 31.7 m depth as well as the occurrence of 10–50 cm thick crushed zones (Table 4). The thickest crushed zone occurs between 28.2 and 28.7 m and corresponds to a zone reported from the core logging (Chapter 2). The clay-rich gouges sampled during the core logging (see Chapter 2.3.3) are well observed on the optical televiewer images (Figure 43). In general, it is in the 21–29 m depth interval that the crushed zones, accompanied or not by clays, and opened fractures are abundant. It also fits with the increase of the fracture frequency (see Figure 35). The digitalisation of the borders of these crushed zones allows to determine their orientations (Table 4), which clearly correspond to the main set of fractures dipping moderately towards the valley (dip direction/dip angle: 019°/36°; in blue on Figure 35). It may be assumed that the gravity-induced destabilisation of the overriding blocks may have produced the crushed zones by sliding along these favourably orientated surfaces. The thick clay-rich fault rocks are more difficult to explain at such shallow depth as only the results of gravity forces and may be probably the witness of the tectonic origin of the main set of NNE-dipping fractures (see also discussion in Chapter 2.3.3).

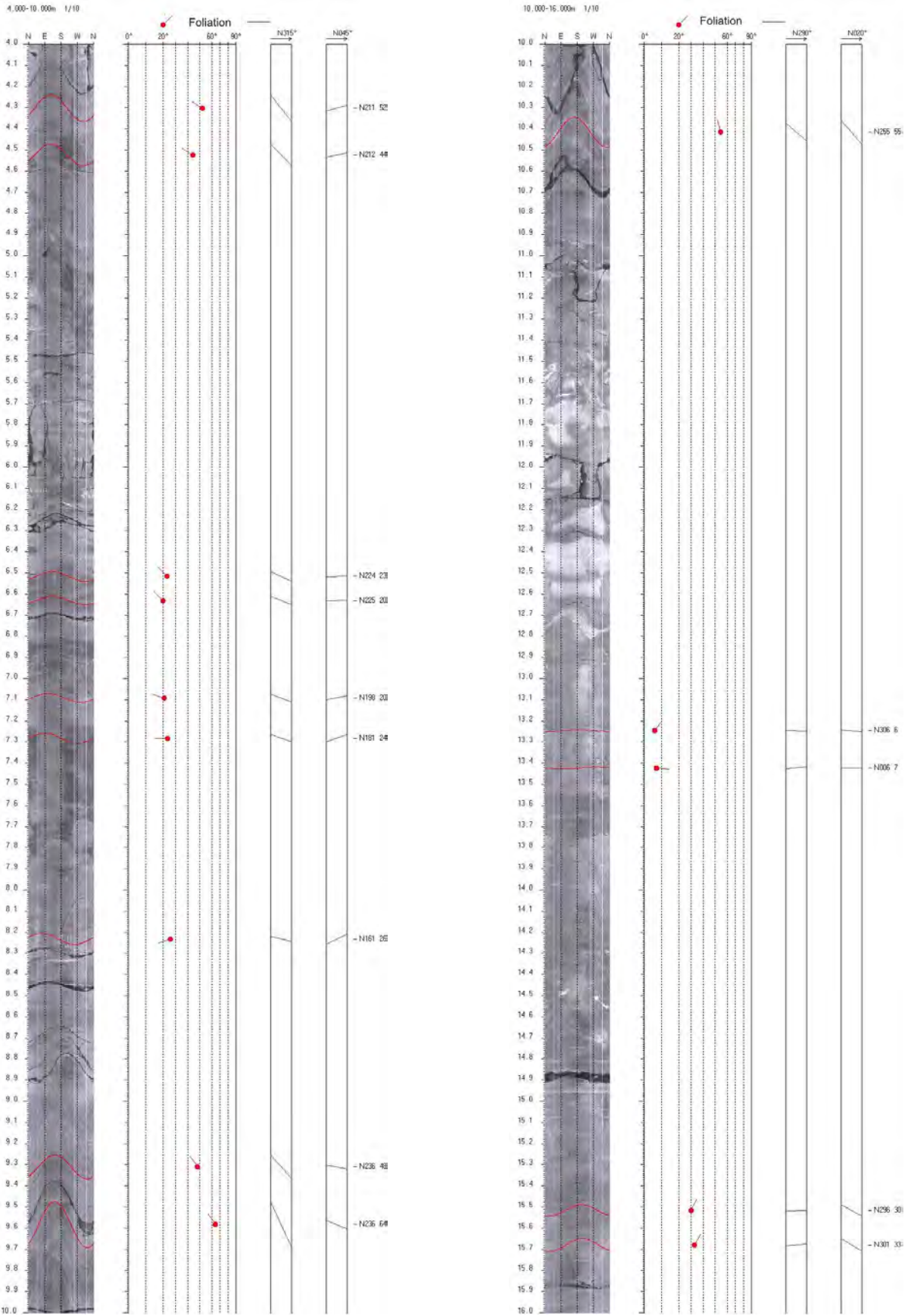


Figure 30. Unwrapped optical images of the wall of Mannen borehole with digitised foliation planes in the 4–16 m depth interval (left). Dip angle and dip direction of each plane are displayed on the arrow plot (N up; centre). Attitude of foliation plane is seen from two different angles (to N315 and N045 or to N290 and N020) with strike (right hand rule) and dip angle of the plane (right).

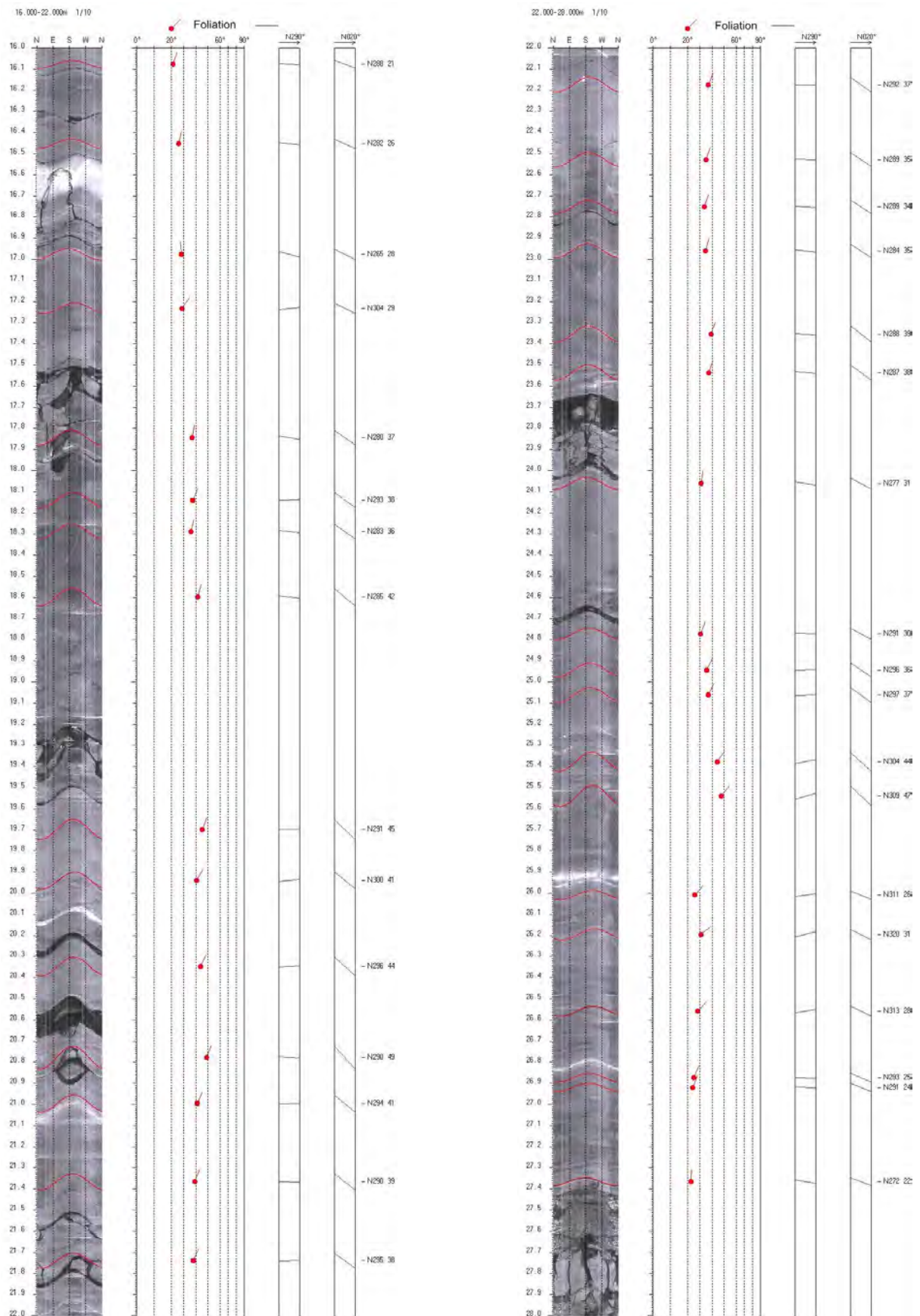


Figure 31. Unwrapped optical images of the wall of Mannen borehole with digitised foliation planes in the 16–28 m depth interval (caption as in Figure 30).

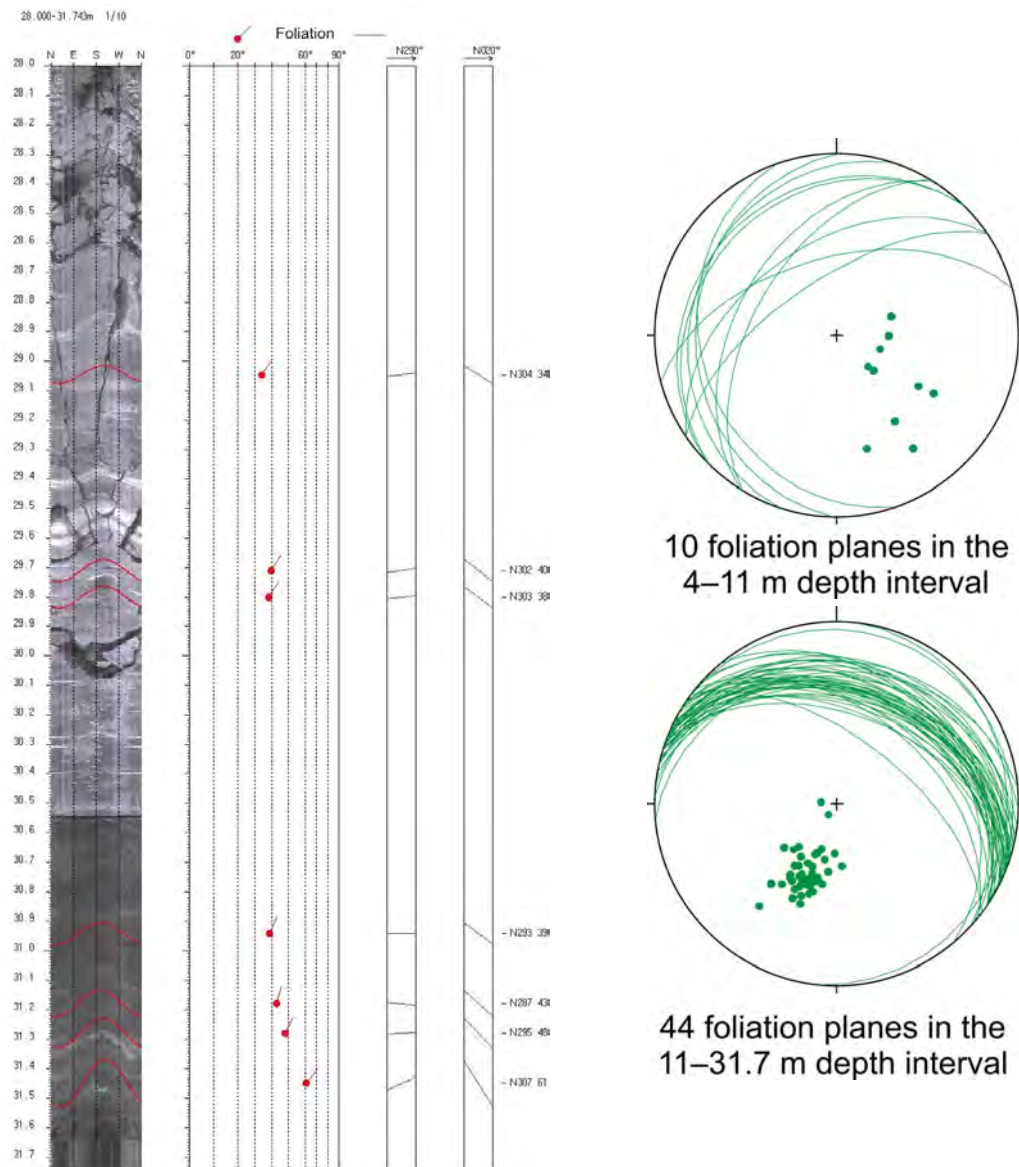
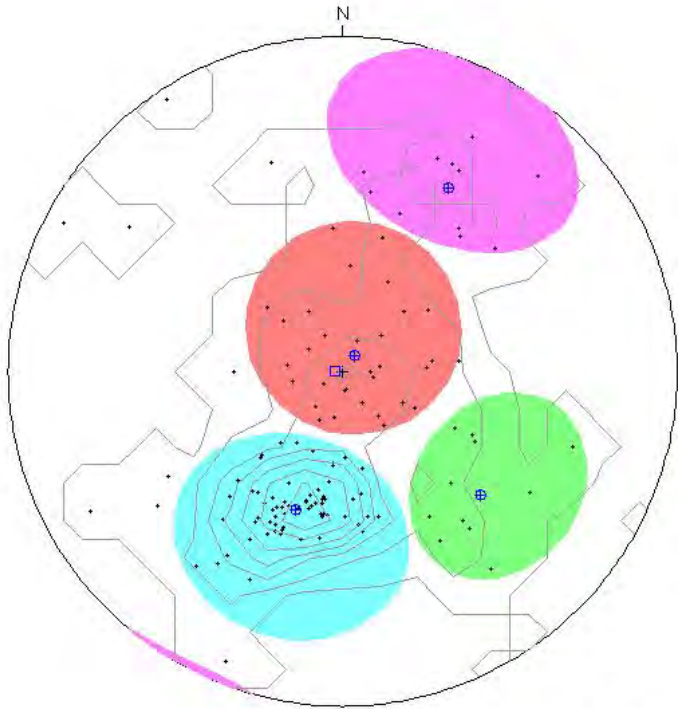


Figure 32. Unwrapped optical images of the wall of Mannen borehole with digitised foliation planes in the 28–31.7 m depth interval (caption as in Figure 30) and stereoplots of the metamorphic foliation (planes and poles) in the 4–11 and 11–31.7 m depth intervals (data listed in Appendix 1).

Zone 0, 2.617 - 31.743m
 Deviation 2.2 N267.0
 Mean dip format: strike and dip
 dip data sets
 OPTV dips

	mean dip	n	f
N289 36	N289 36	65	2.72
N127 5	N127 5	31	1.07
N222 46	N222 46	11	(0.56)
N120 53	N120 53	11	(0.65)



equal-area lower-hemisphere 0-90
 contour-levels 1, 3, 6, 10, 15, 21, 28,
 □ well axis
 ⊕ mean dip

intersections

	N289 36	N127 5	N222 46	N120 53
N289 36	X	1 N291	35 N000	5 N296
N127 5	1 N291	X	5 N227	1 N300
N222 46	35 N000	5 N227	X	36 N267
N120 53	5 N296	1 N300	36 N267	X

Figure 33. Contour plots with poles of fractures providing four main fracture sets (marked by different colours) in the c. 3–32 m depth interval. The prominent fracture set is the blue coloured set with dip direction/dip angle 019°/36°.

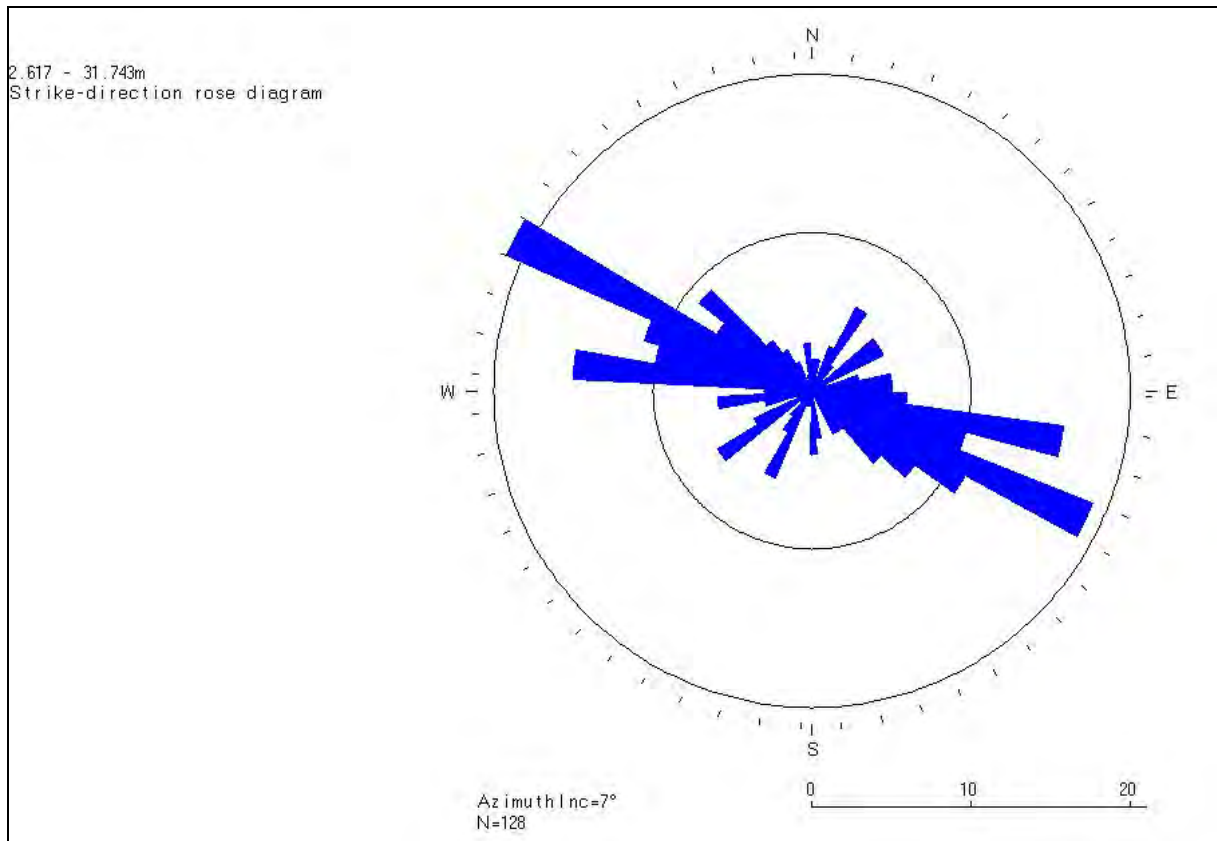


Figure 34. Rose diagram of the fractures in the 3–32 m depth interval.

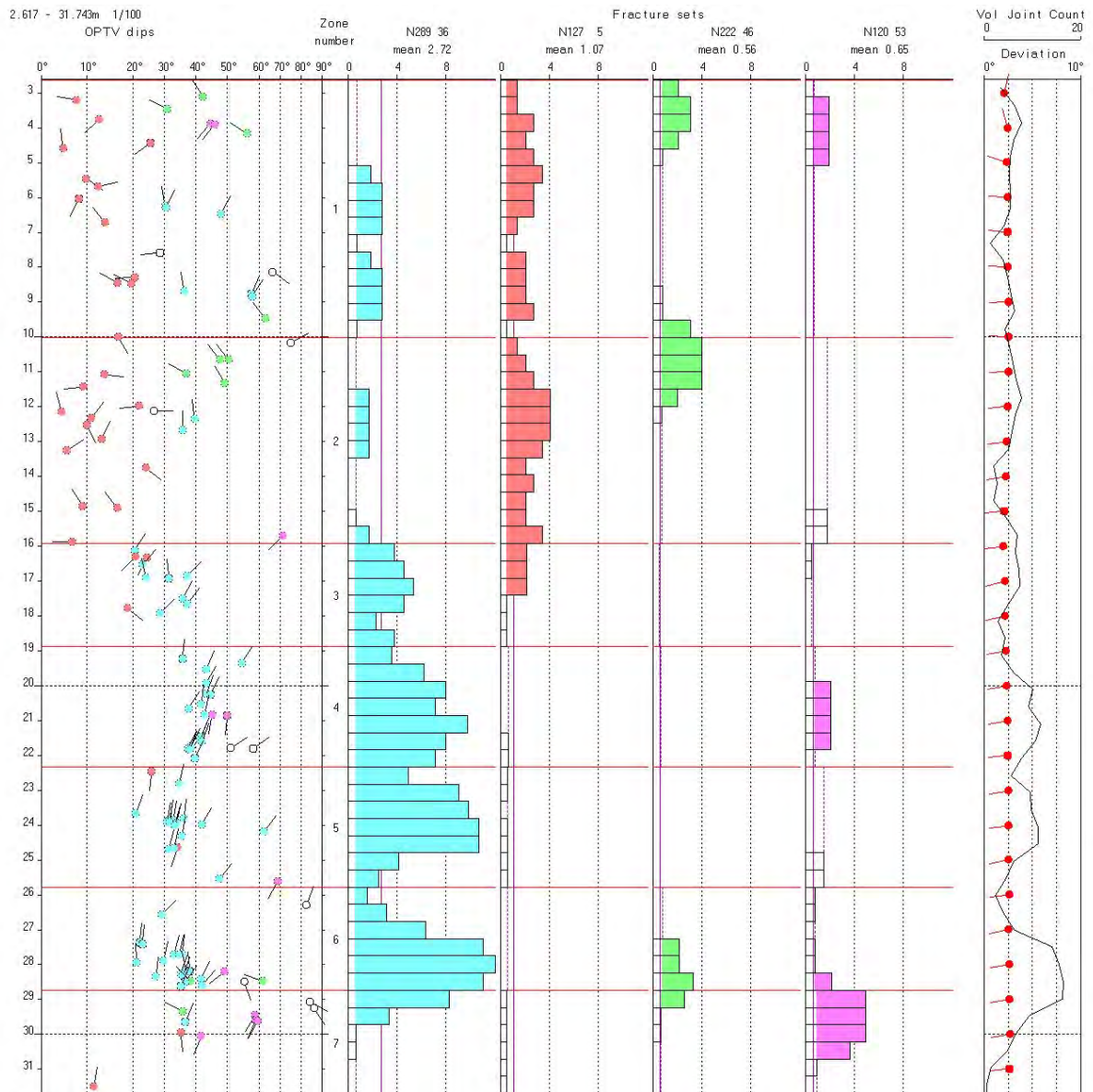
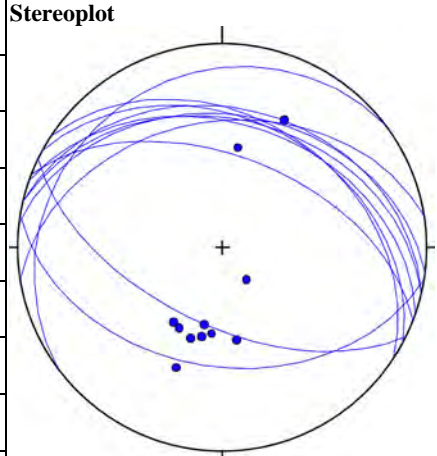


Figure 35. Arrow plots (N up) of the 128 fractures in the c. 3–32 m depth interval, frequency histograms of the four fractures sets as defined by the statistical analysis (see Figure 33; with identical colours representing the fracture sets). The deviation of the borehole (arrow plot; N up) is shown in the right.

Table 4. Observation in the 3.4–31.7 m depth interval of crushed and fractured zones, open fractures, orientation and stereoplot. Mean dip angles and dip angles at the bottom of the fractured zone are shown.

Depth [m]	Dip direction [°]	Dip angle [°]	Thickness [m]	Comments	Stereoplot
14.9	323	13 (mean) 16 (bottom)	0.03	Open fracture (see Figure 38)	
17.6	033	36	0.12	Open fracture, crushed zone (see Figure 39)	
19.3	021	44 (mean) 53 (bottom)	0.09	Open fracture, crushed zone (see Figure 39)	
20.6	019	39	0.09	Open fracture, fractured zone (see Figure 40)	
23.7	013	28 (mean) 37 (bottom)	0.13	Open fracture, fractured zone (see Figure 40, Figure 43)	
27.5	007	29 (mean) 35 (bottom)	0.23	Crushed zone with clays (see Figure 41, Figure 43)	
27.8	013	32	0.15	Crushed zone (see Figure 41, Figure 43)	
28.0	351	29 (mean) 38 (bottom)	0.20	Crushed zone with clays (see Figure 41, Figure 43)	
28.2–28.7	028 (mean)	37 (mean)	0.50	Severely crushed zone (see Figure 42, Figure 43)	
29.5	206	59	0.02	Open fracture (see Figure 42)	
30.0	189	38 (mean) 41 (bottom)	0.07	Open fracture, crushed zone (see Figure 42)	



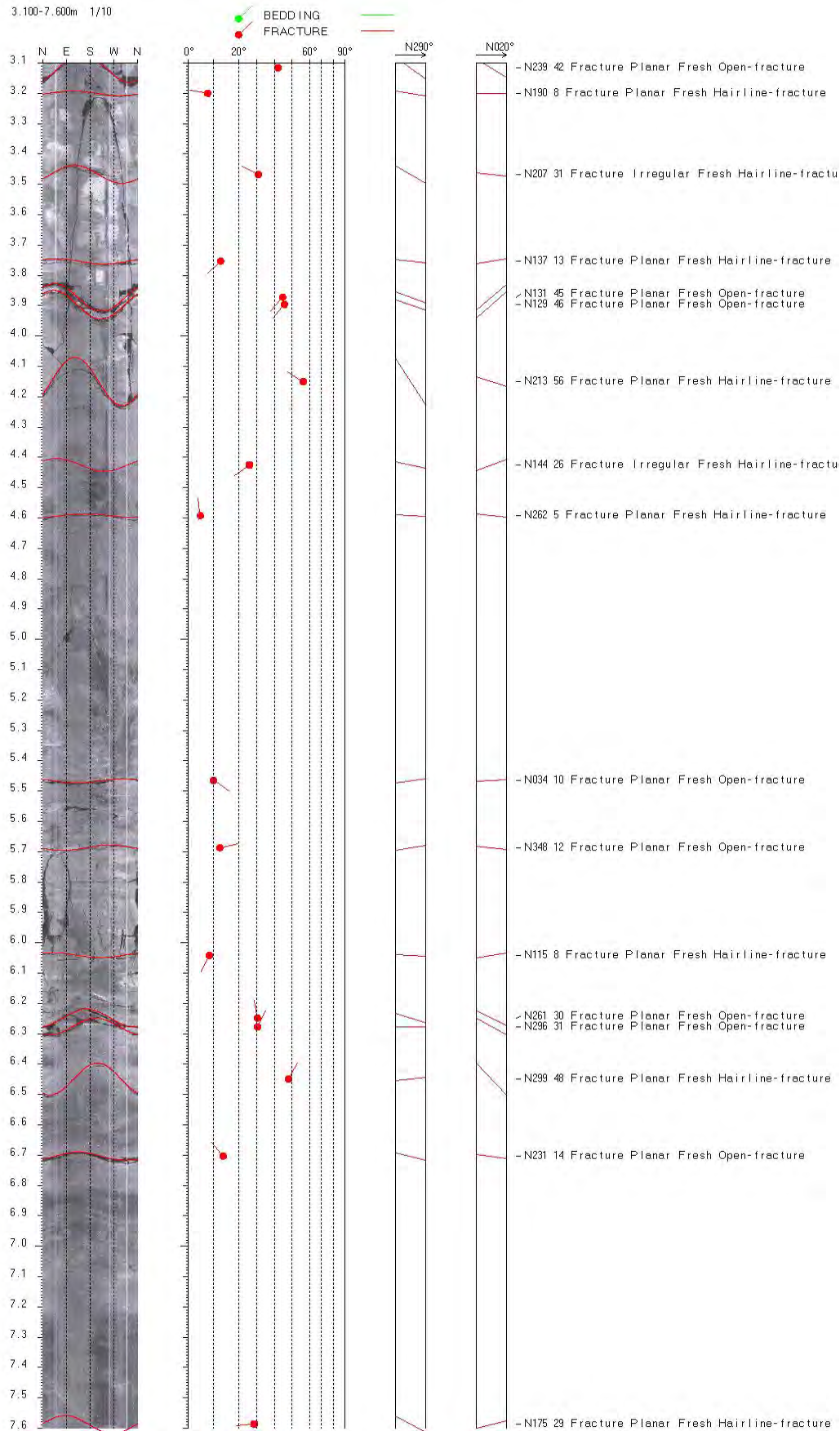


Figure 36. Optical televiwer synthetic images with digitised planar fractures in the 3.1–7.6 m depth interval (left); arrow plots of the fracture orientation (N up; centre); attitude of the fracture from two different view angles (to N290 and N020 herein) and strike/dip angle of the fracture with main characteristics (right).

8.000-12.000m 1/10

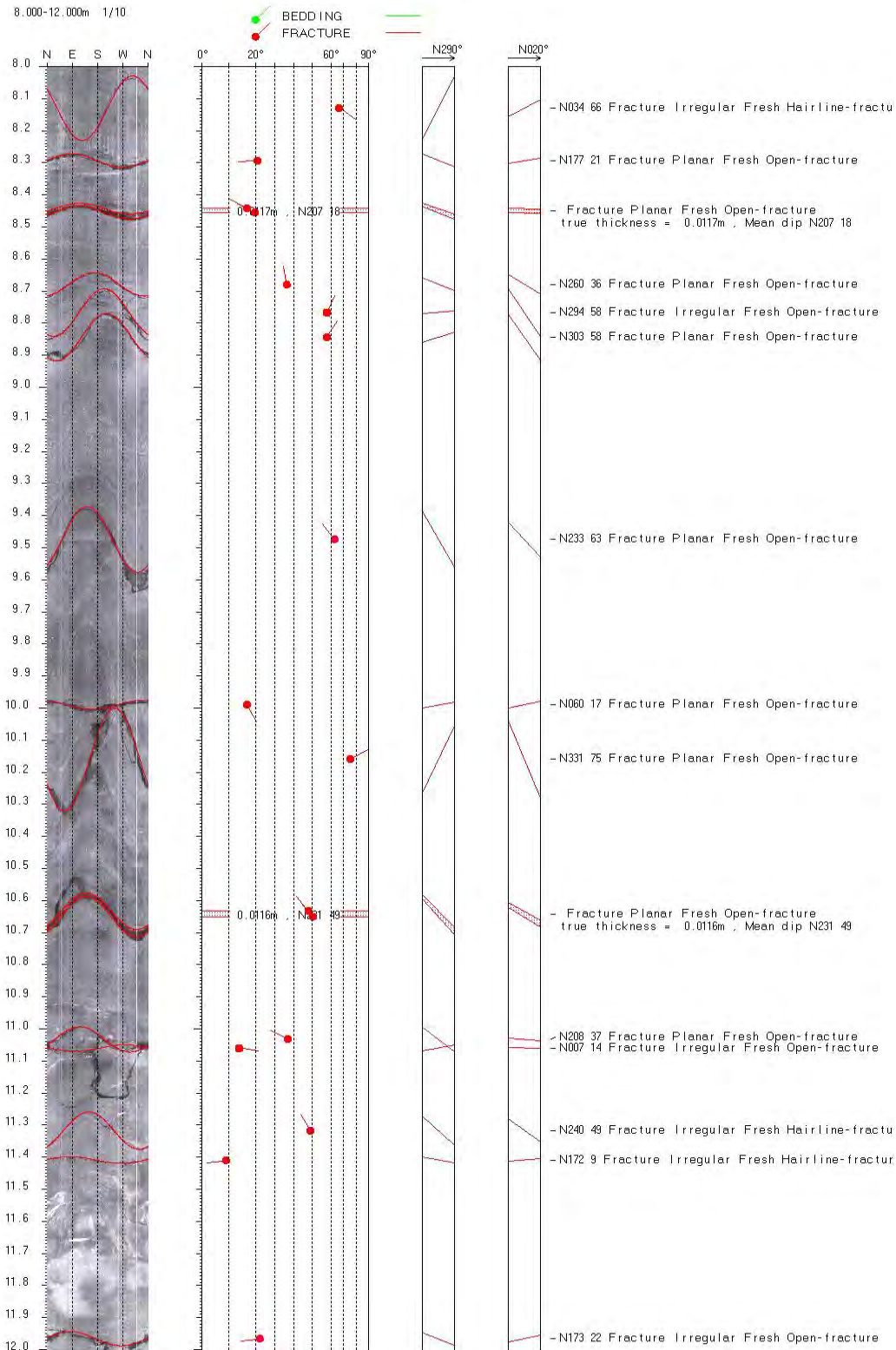


Figure 37. Optical televiewer synthetic images with digitised planar fractures in the 8–12 m depth interval (caption as on Figure 36).

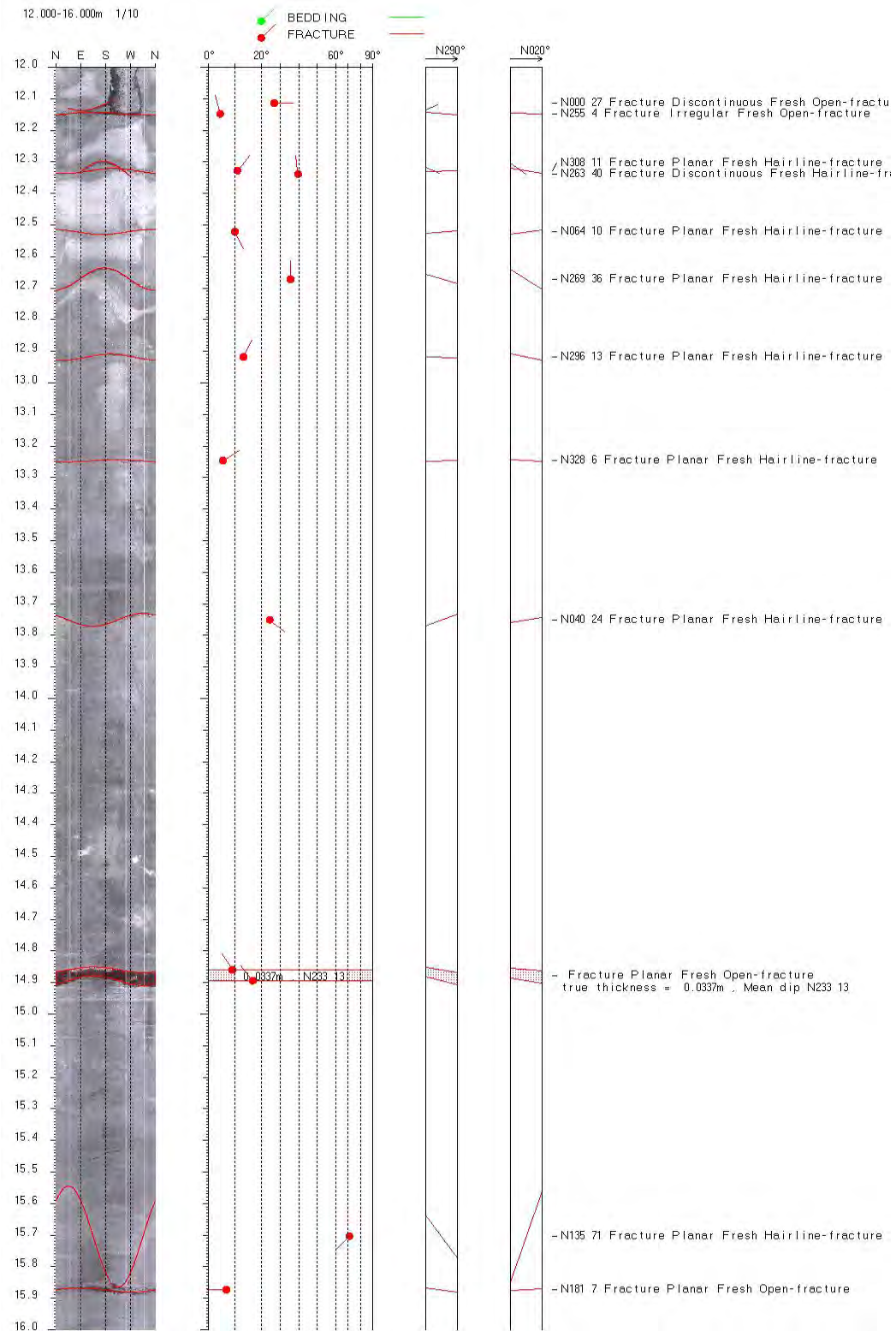


Figure 38. Optical televiewer synthetic images with digitised planar fractures in the 12–16 m depth interval (caption as on Figure 36).

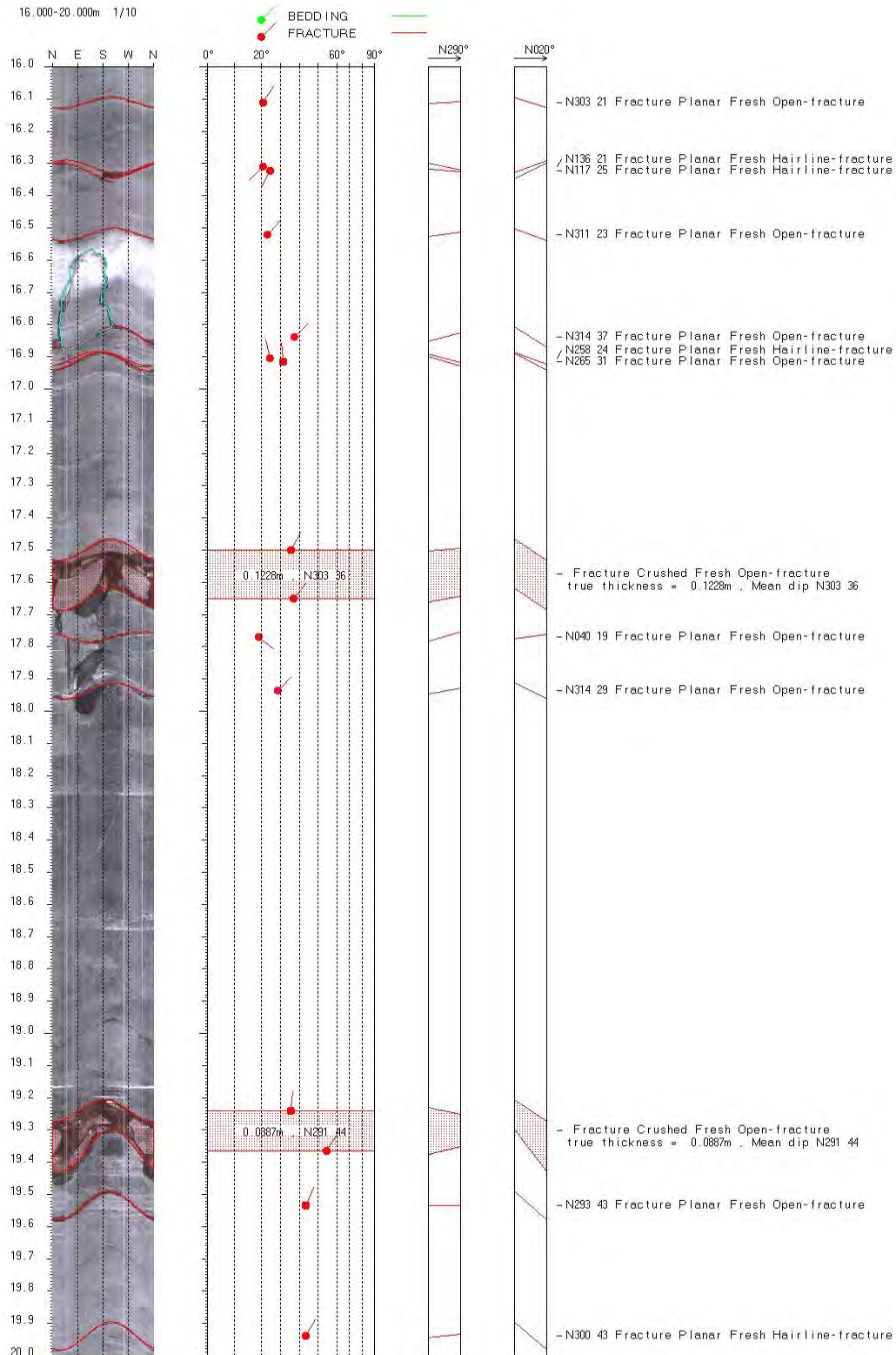


Figure 39. Optical televiwer synthetic images with digitised planar fractures in the 16–20 m depth interval (caption as on Figure 36).

20.000-24.000m 1/10

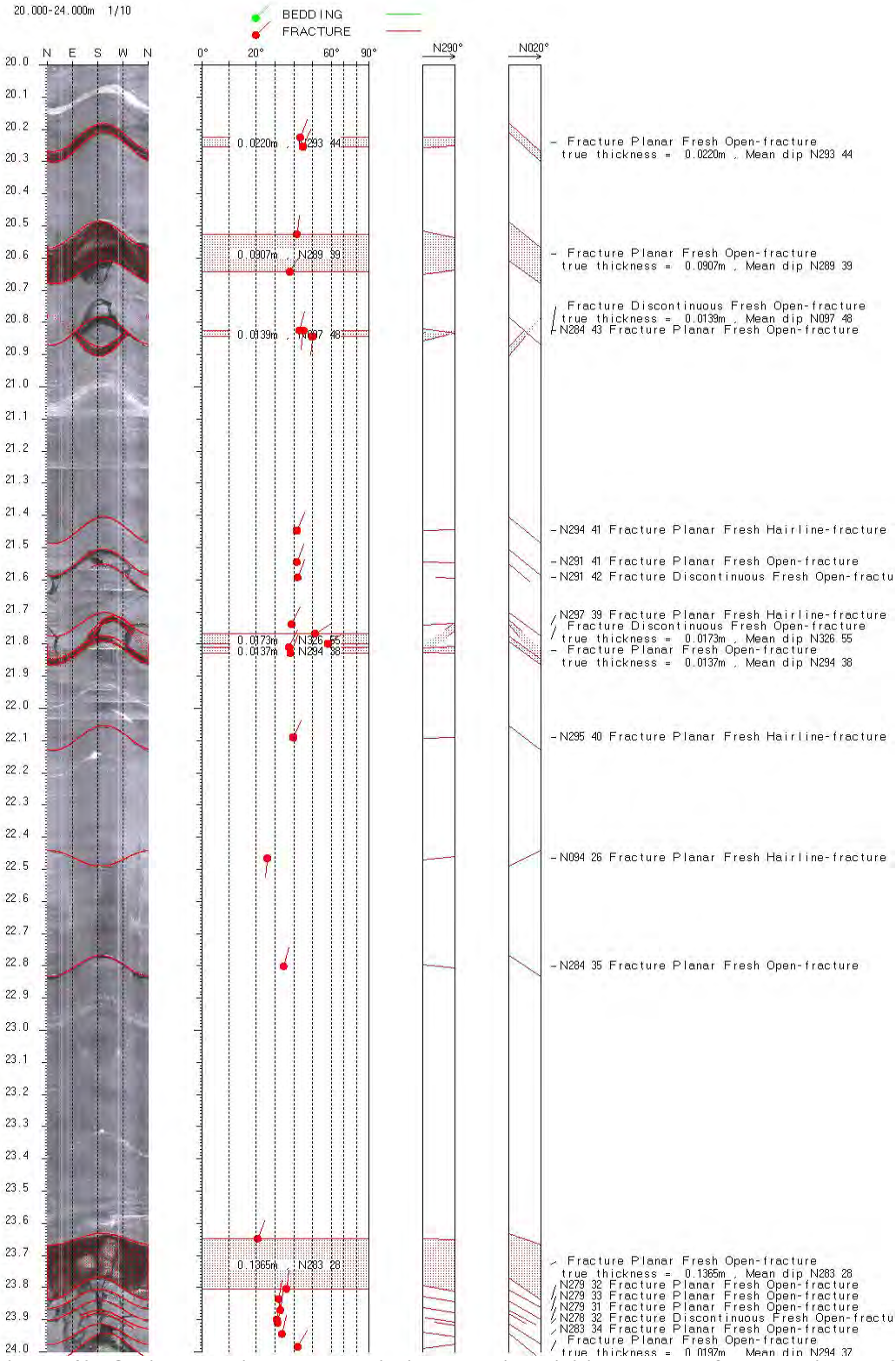


Figure 40. Optical televiwer synthetic images with digitised planar fractures in the 20–24 m depth interval (caption as on Figure 36).

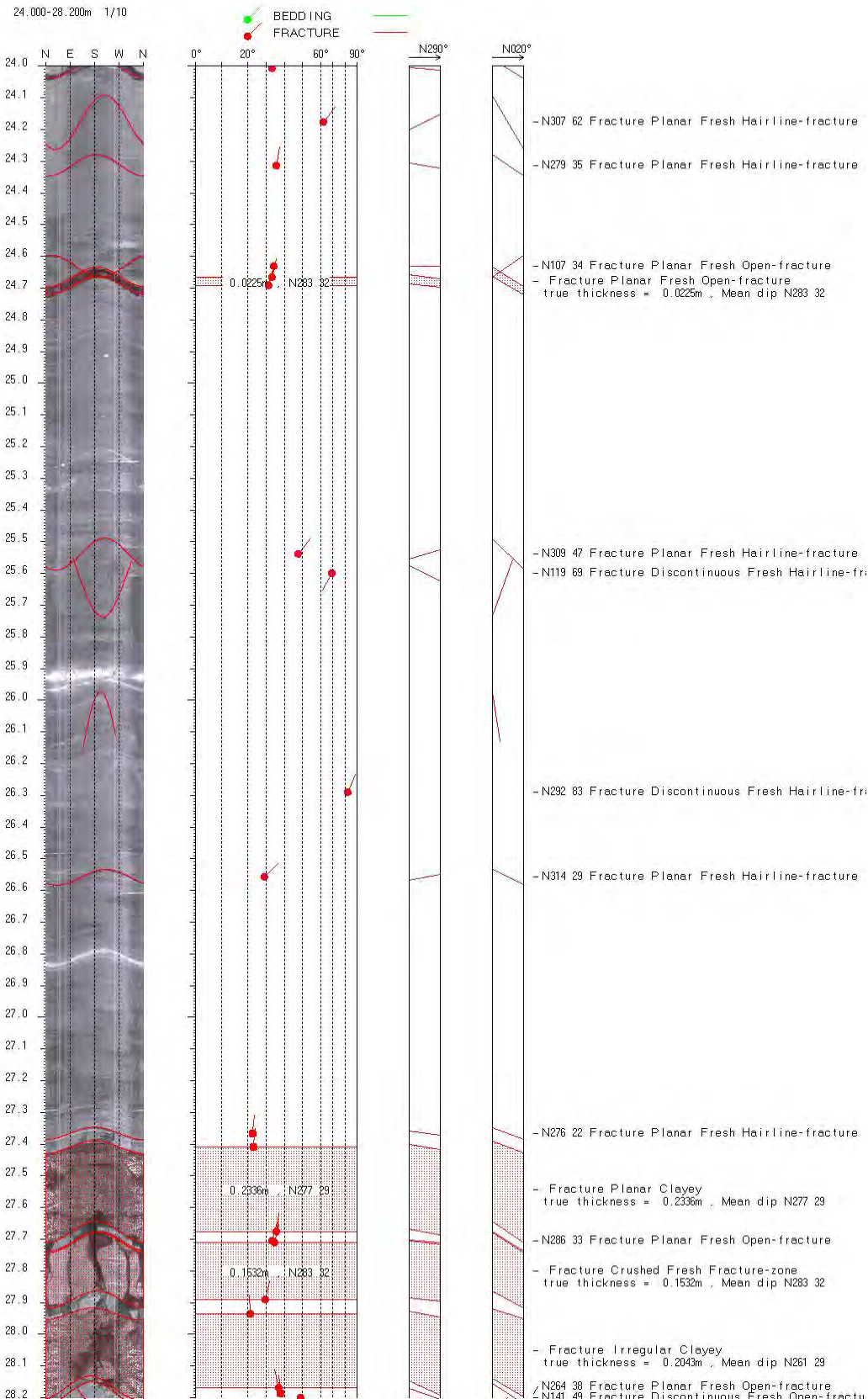


Figure 41. Optical televiewer synthetic images with digitised planar fractures in the 24–28.2 m depth interval (caption as on Figure 36).

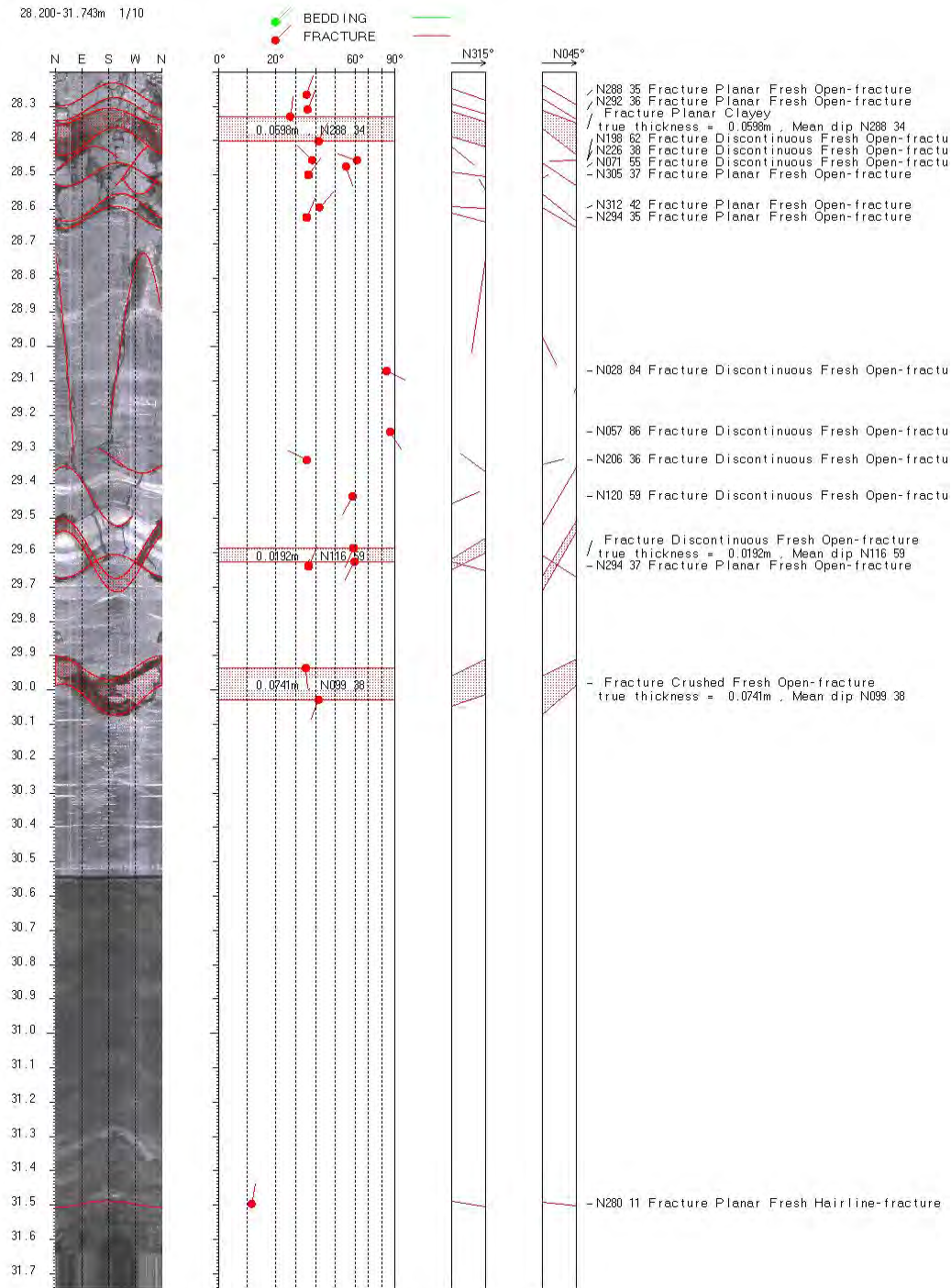


Figure 42. Optical televiwer synthetic images with digitised planar fractures in the 28.2–31.7 m depth interval (caption as on Figure 36).

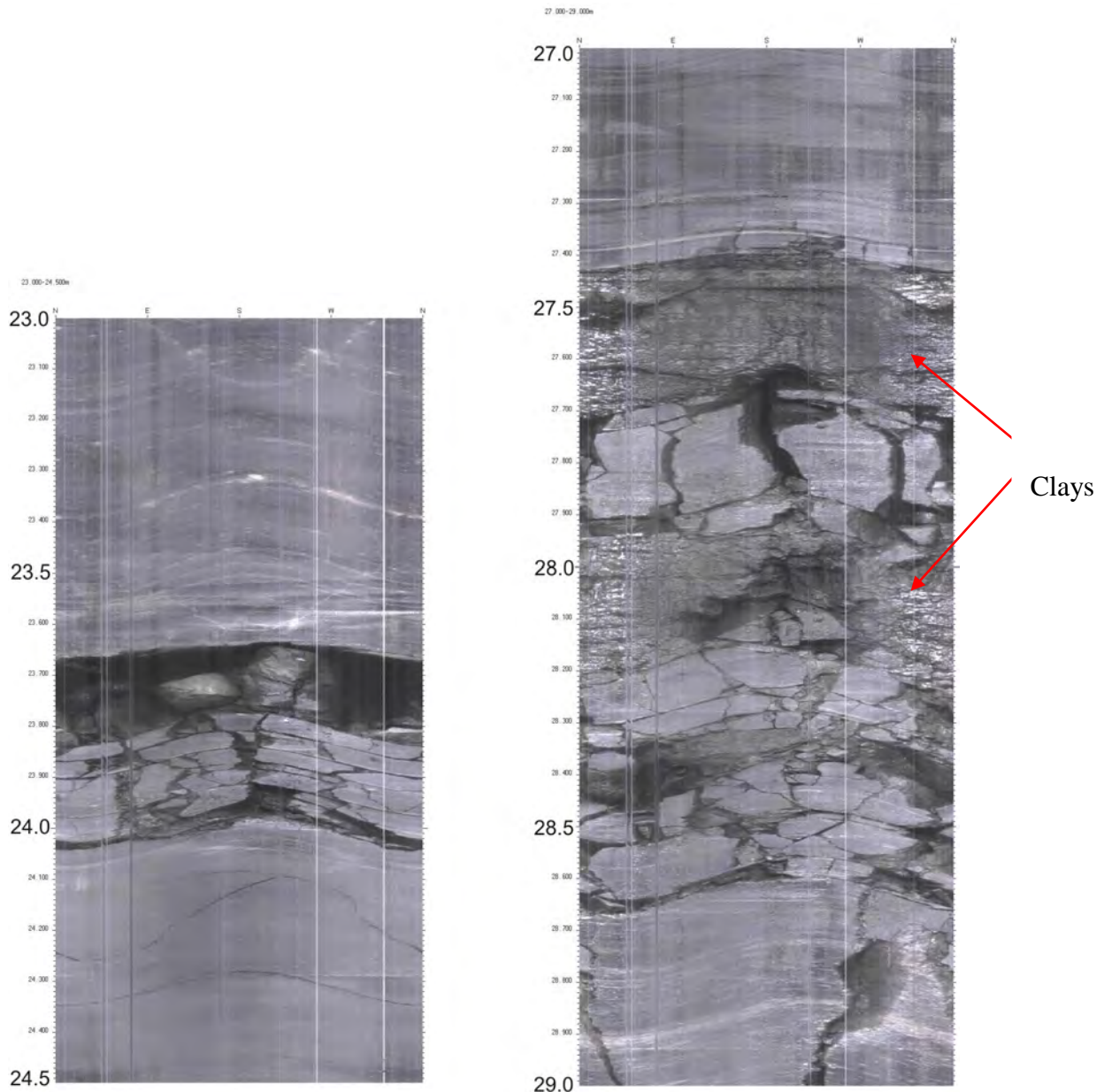


Figure 43. Optical televiewer images showing crushed zones in the two 23–24.5 m (left) and 27–29 m (right) depth intervals. The two layers of clay-rich gouges are well observed in the 27–29 m depth interval.

3.2.3 Structural data in the 32–58 m depth interval

3.2.3.1 Metamorphic foliation in the 33–58 m depth interval

The foliation was measured at 47 different depths along the 33–58 m interval (Figure 44–Figure 46 and Appendix 1). The average dip angle is of 33° . Compared to the bottom of the previous analysed interval, there is a clear clock-wise rotation of the dip direction of the foliation. In the 33.5–38 m depth interval the foliation is dipping eastwards (Figure 44, Figure 46), while in the c. 38–42 m depth interval the dip of the foliation is directed toward the NNE and NE with dip angles steepening up to 58° (Figure 44, Figure 46). A large anti-clockwise rotation of the dip direction of the foliation is observed until the bottom of the 33–58 m depth interval with at c. 58 m depth a S-dipping foliation (Figure 46). In detail, the dip direction is towards the N between 42 and 47 m depths (Figure 44–Figure 46), westward between 47 and 55 m depths (Figure 45 and Figure 46), and towards the SW, between 55 and 57 m depths (Figure 45 and Figure 46).

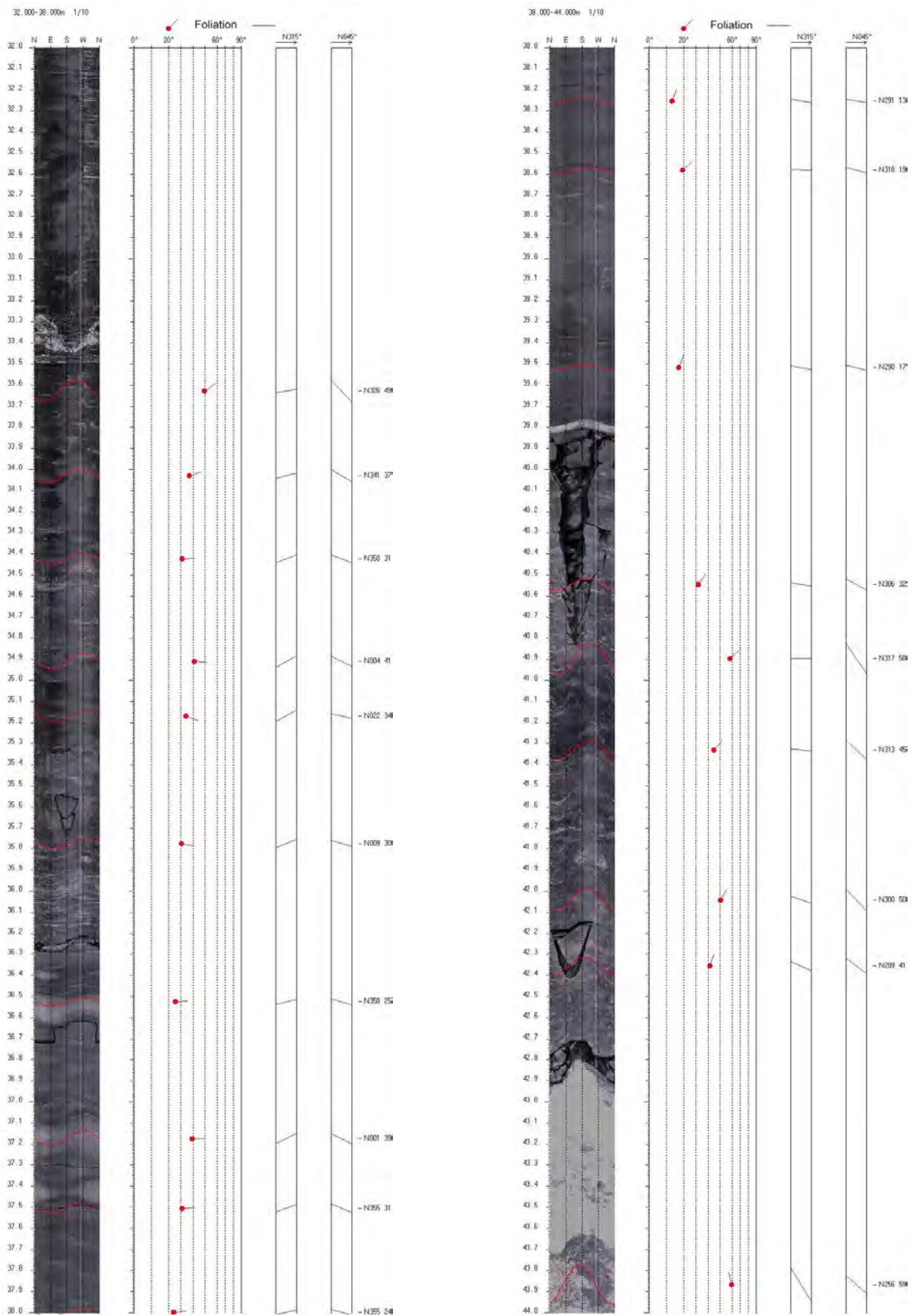


Figure 44. Unwrapped optical images of the wall of Mannen borehole with digitised foliation planes in the 32–44 m depth interval (caption as in Figure 30).

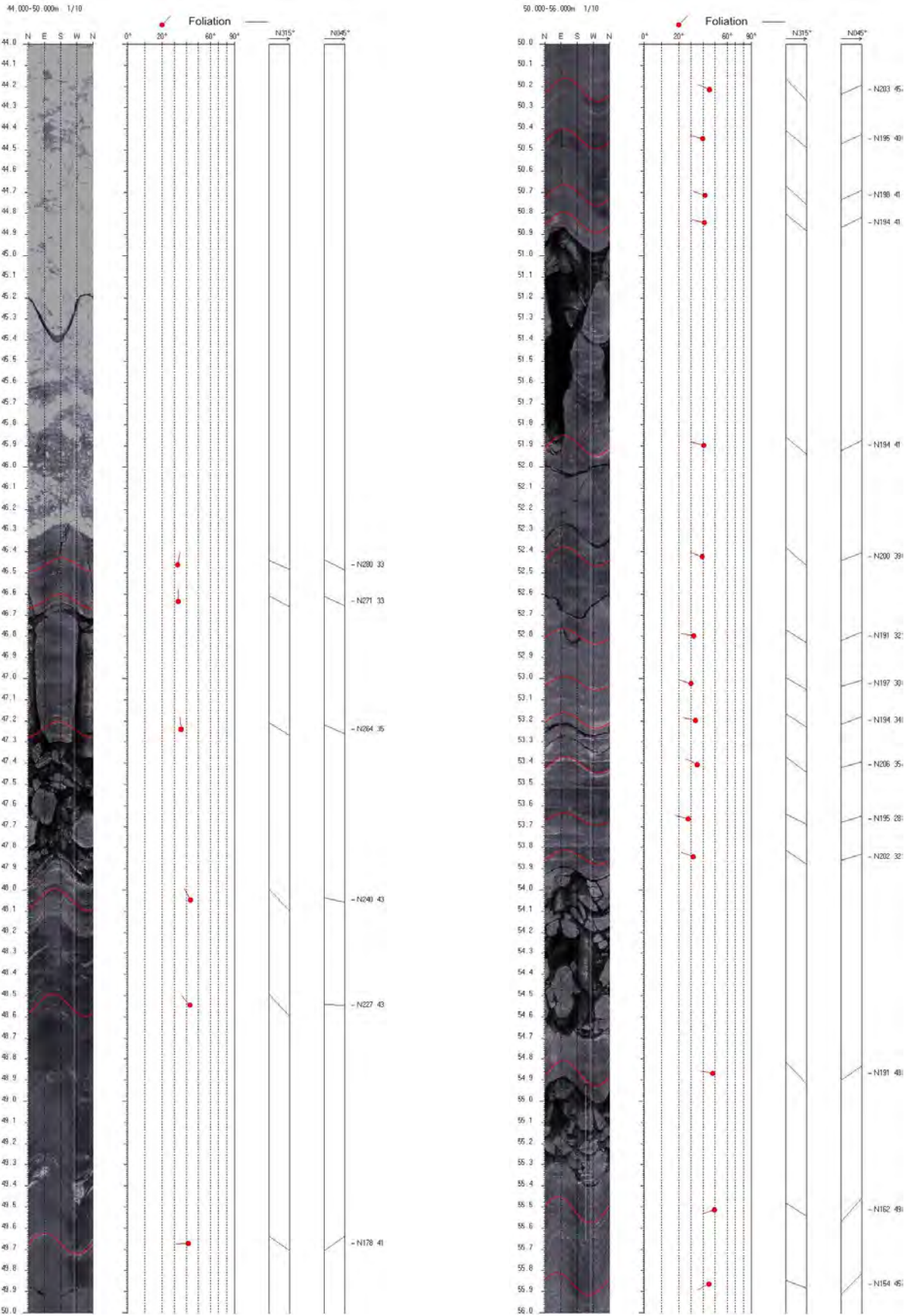


Figure 45. Unwrapped optical images of the wall of Mannen borehole with digitised foliation planes in the 44–56 m depth interval (caption as in Figure 30).

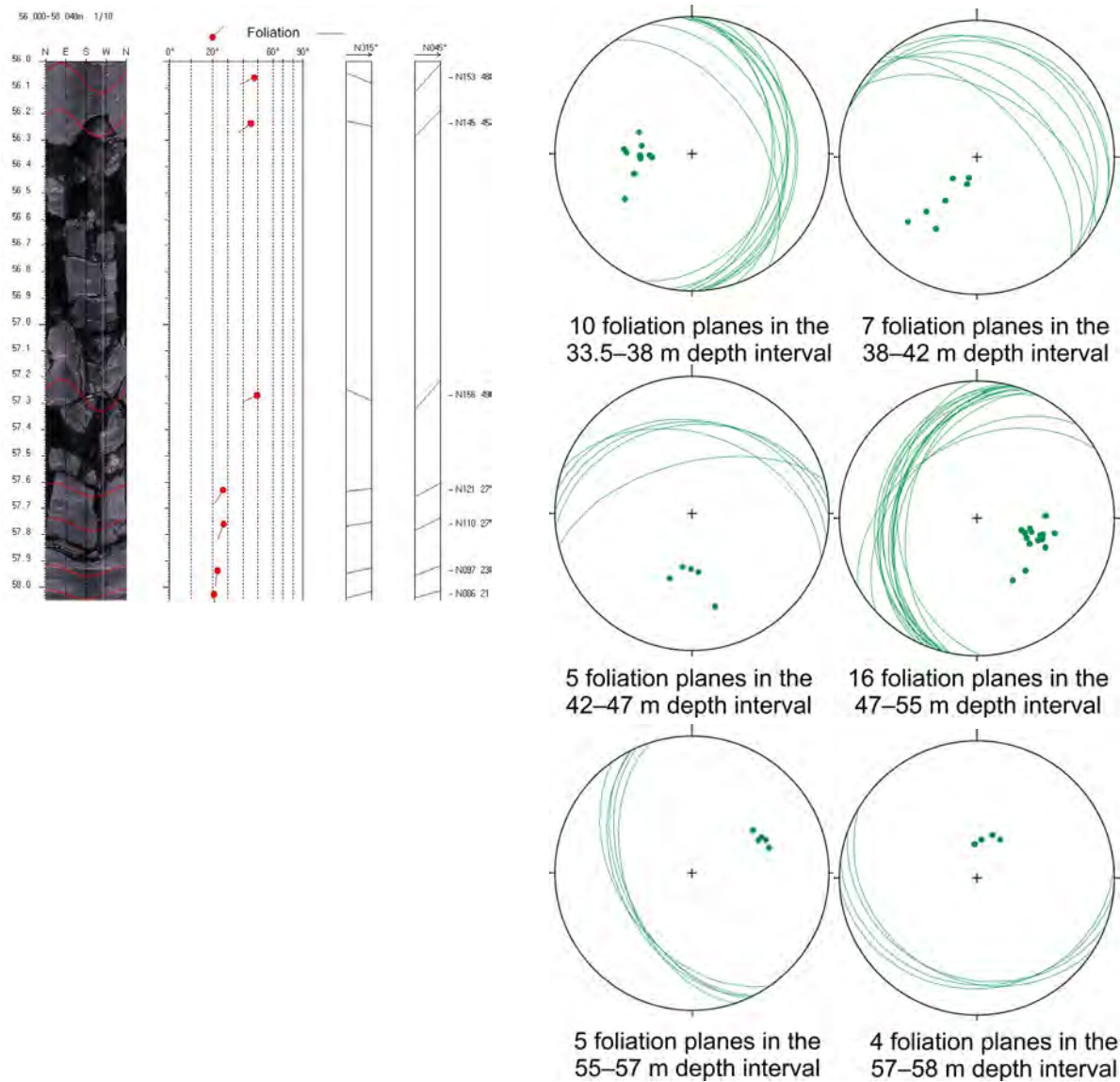


Figure 46. Unwrapped optical images of the wall of Mannen borehole with digitised foliation planes in the 56–58 m depth interval (caption as in Figure 30) and stereoplot of the metamorphic foliation (planes and poles) in the 33.5–38, 38–42, 42–47, 47–55, 55–57 and 57–58 m depth intervals (data listed in Appendix 1).

3.2.3.2 Fractures in the 32–58 m depth interval

The analysis of the 71 fracture orientations in the 32–58 m depth interval reveals five different well-defined fracture sets (Figure 47). The rose diagram of Figure 48 well displays the dispersion of fractures in this interval. The main set is however largely represented by 35 very shallow NE-dipping fractures.

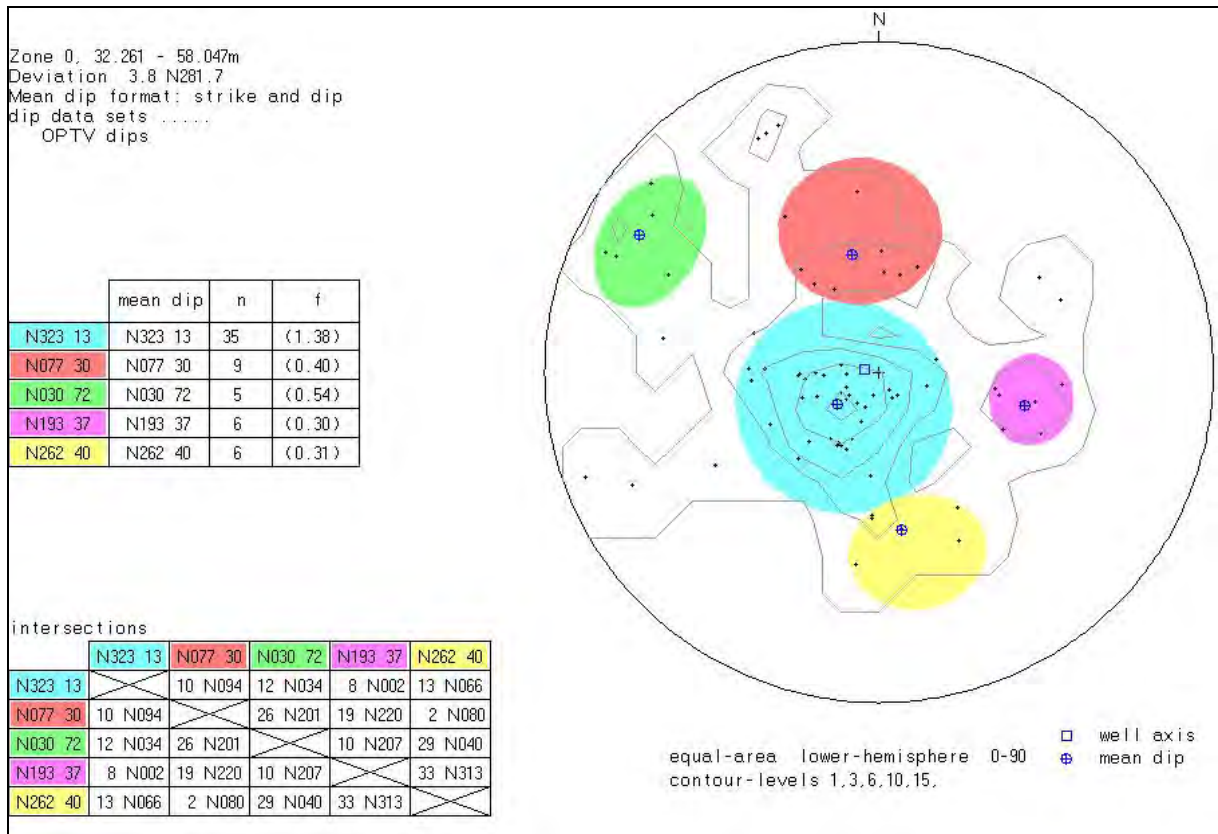


Figure 47. Contour plots, with poles of fractures, providing four main fracture sets in the c. 32–58 m depth interval.

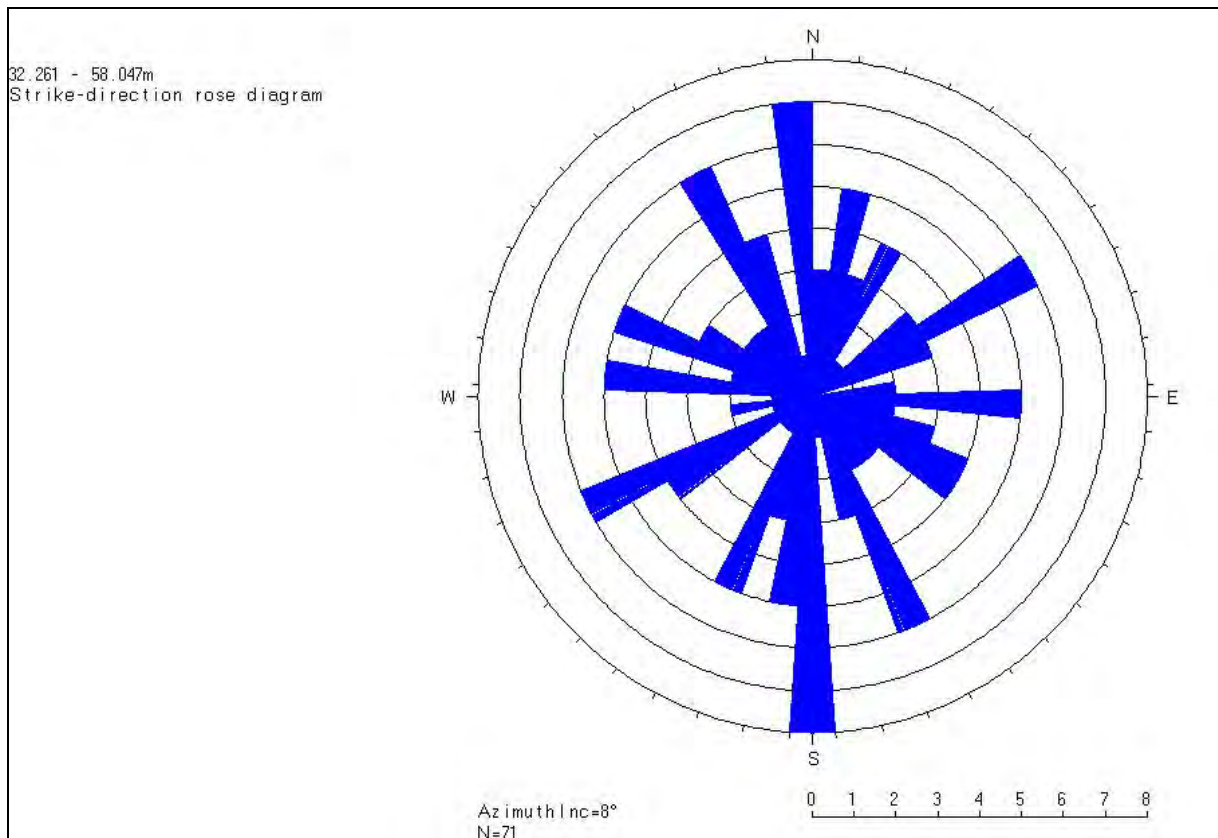


Figure 48. Rose diagram of the fractures in the 32–58 m depth interval.

The fracture frequency is quite high between 35 m and 41 m depth. This is due to the presence of the main set of NE-dipping fractures which are, because of their very shallow dipping angles, probably not of relevance in terms of slope stability (mean dip direction/dip angle: 053°/13°, blue set on Figure 47 and Figure 49). The steeply SE-dipping fractures are localised in the 40–43 m depth interval (mean dip direction/dip angle: 120°/72°, green set on Figure 47 and Figure 49).

The inspection of the detailed pictured fracture logs in the 32–58 m depth interval (Figure 50–Figure 56) reveals that many fractures are foliation-parallel, explaining thereby the large dispersion in fracture orientations due to the changes of the foliation dip direction (see previous section). The foliation-parallel fractures are specifically well observed in the bottom part of the studied interval (Figure 53–Figure 56). In the 51–54.5 m interval, the westward shallow-dipping set of fractures (dip direction/dip angle: 283°/37°; pink set on Figure 47 and Figure 49) is an example of foliation-parallel set as observed on Figure 55.

The c. 32–58 m depth interval was divided in 4 zones with regards to the fracture frequency (Figure 49) during the numerical calculation and according to the results listed in Appendix 3.

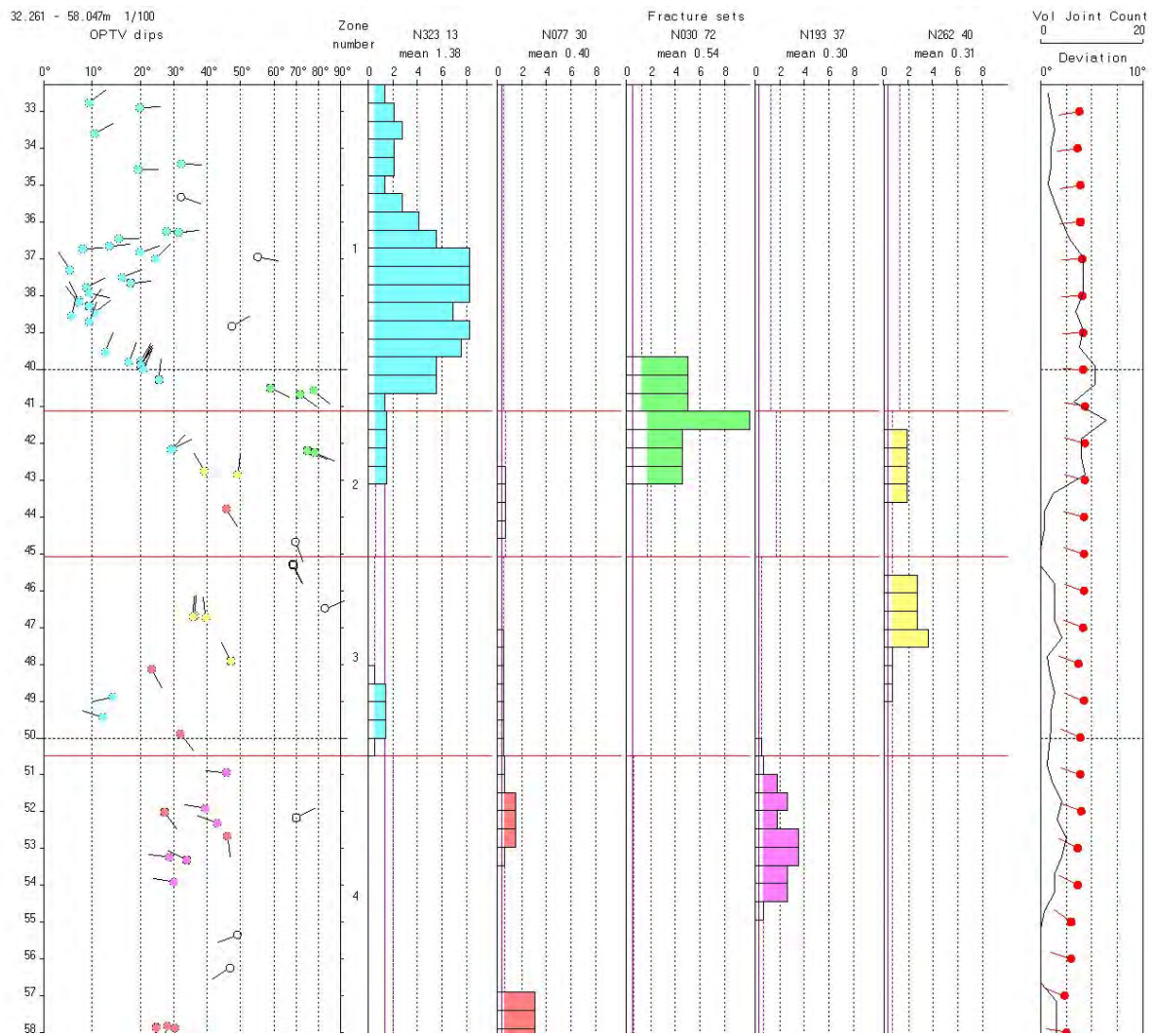


Figure 49. Arrow plots (N up) of the 71 fractures in the c. 32–58 m depth interval, frequency histograms of the five fractures sets as defined by the statistical analysis (see Figure 47). The deviation of the borehole (arrow plot; N up) is shown in the right.

In the 32–58 m depth interval, five crushed zones and opened fractures are extracted from the detailed analysis of the logs as displayed in Figure 50–Figure 56 and listed in Table 5. They are located between 39.8 m and 56.3 m depth. The thickness of crushed zones varies from 0.1–1.2 m. Figure 57 illustrates two of these zones at 46.7 m and 56.3 m depth. All the zones developed along the metamorphic foliation.

Table 5. Observation in the 39.8–56.3 m depth interval of crushed and fractured zones, open fractures, orientation and stereoplot. Mean dip angles and dip angles at the bottom of the fractured zone are shown.

Depth [m]	Dip direction [°]	Dip angle [°]	Thickness [m]	Comments	Stereoplot
39.8	030	20	0.12	Crushed zone, vertical fracture (see Figure 51)	
46.7	343	43 (mean) 46 (bottom)	0.86	Crushed zone, vertical fracture (see Figure 53, Figure 57)	
50.9	277	43	0.72	Vertical open zone (see Figure 54)	
53.9	261	38 (mean) 49 (bottom)	1.11	Crushed zone (see Figure 55)	
56.3	224	36(mean) 28 (bottom)	1.28	Crushed zone (see Figure 56, Figure 57)	

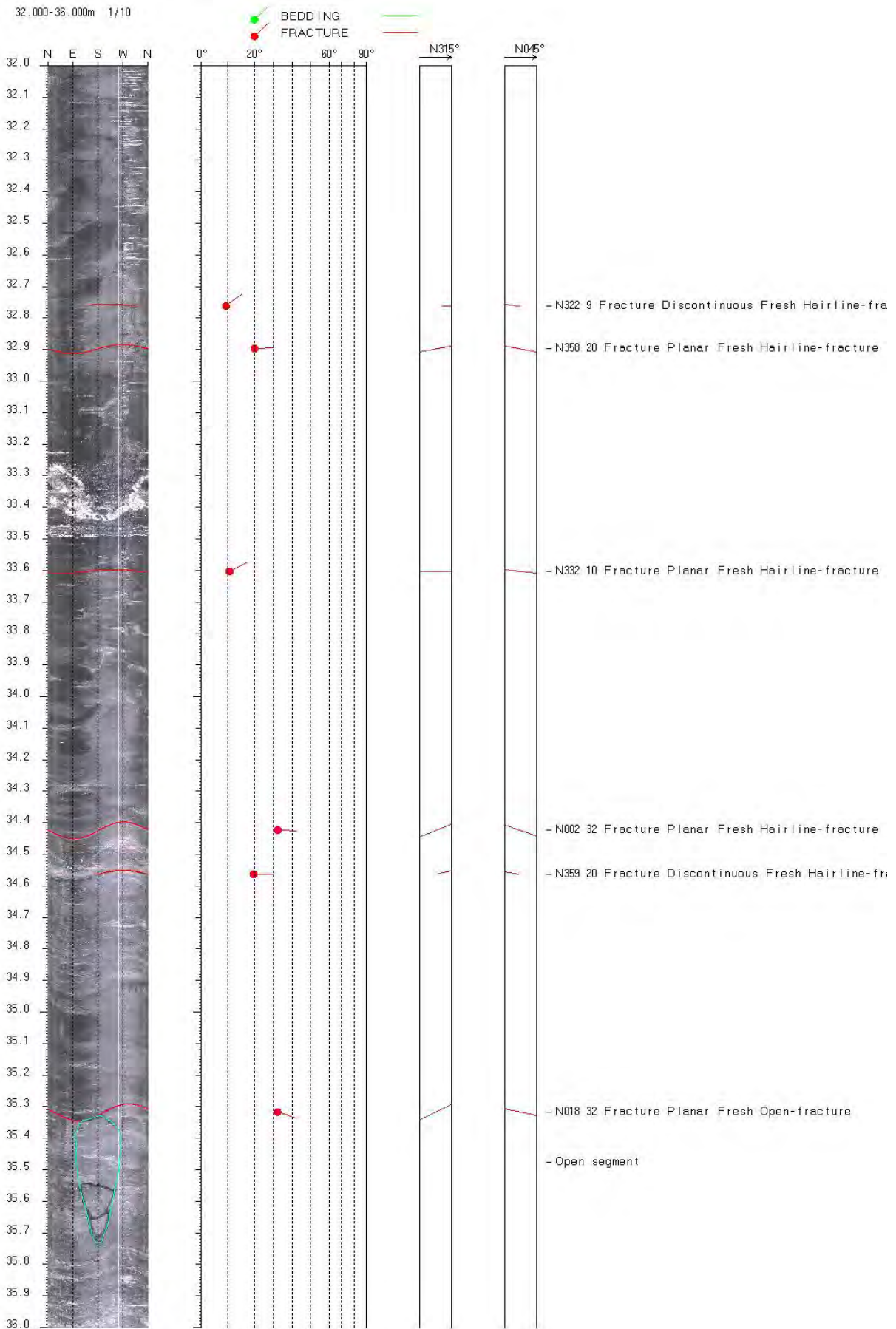


Figure 50. Optical televiewer synthetic images with digitised planar fractures in the 32–36 m depth interval (caption as on Figure 36).

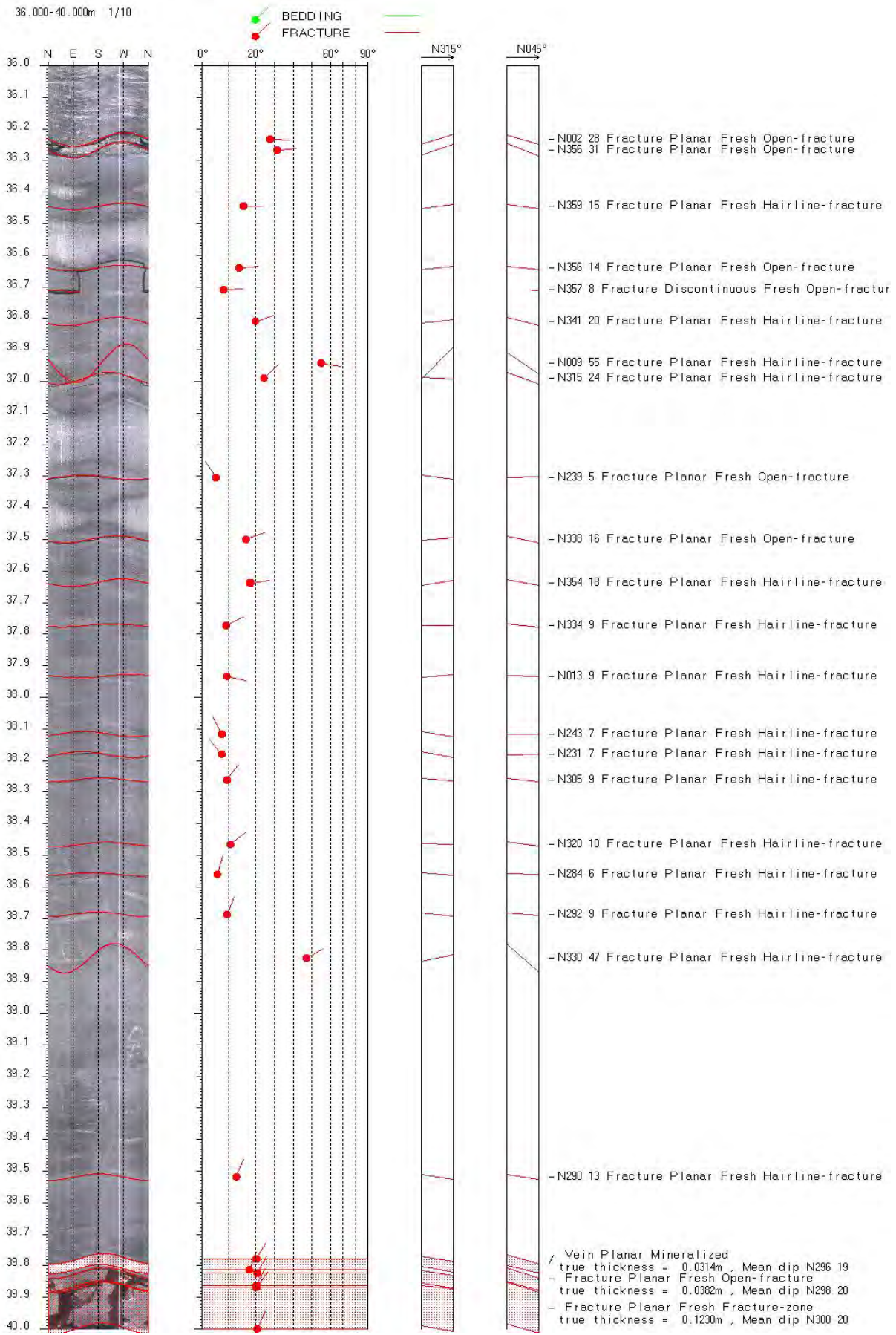


Figure 51. Optical televiewer synthetic images with digitised planar fractures in the 36–40 m depth interval (caption as on Figure 36).

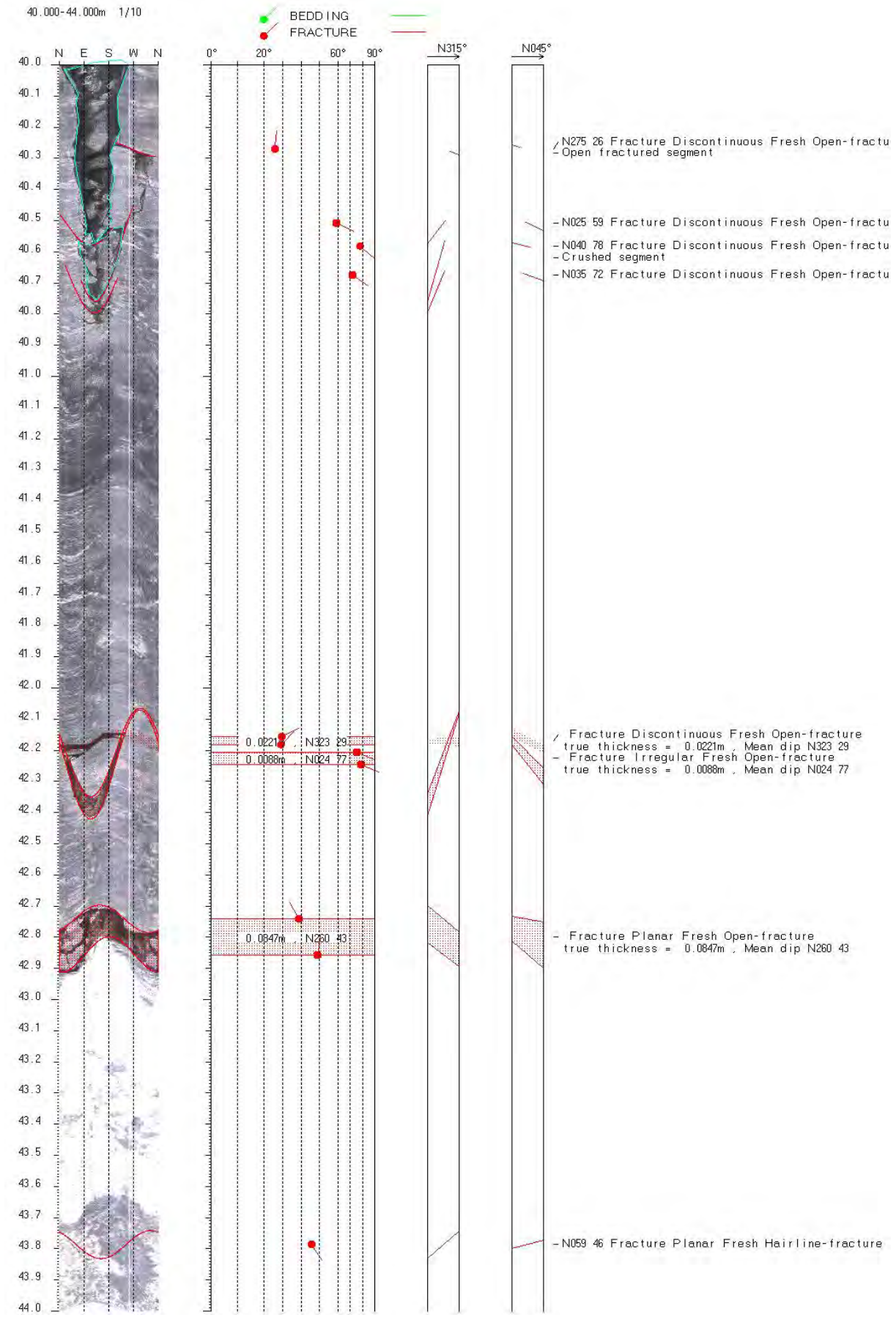


Figure 52. Optical televiewer synthetic images with digitised planar fractures in the 40–44 m depth interval (caption as on Figure 36).

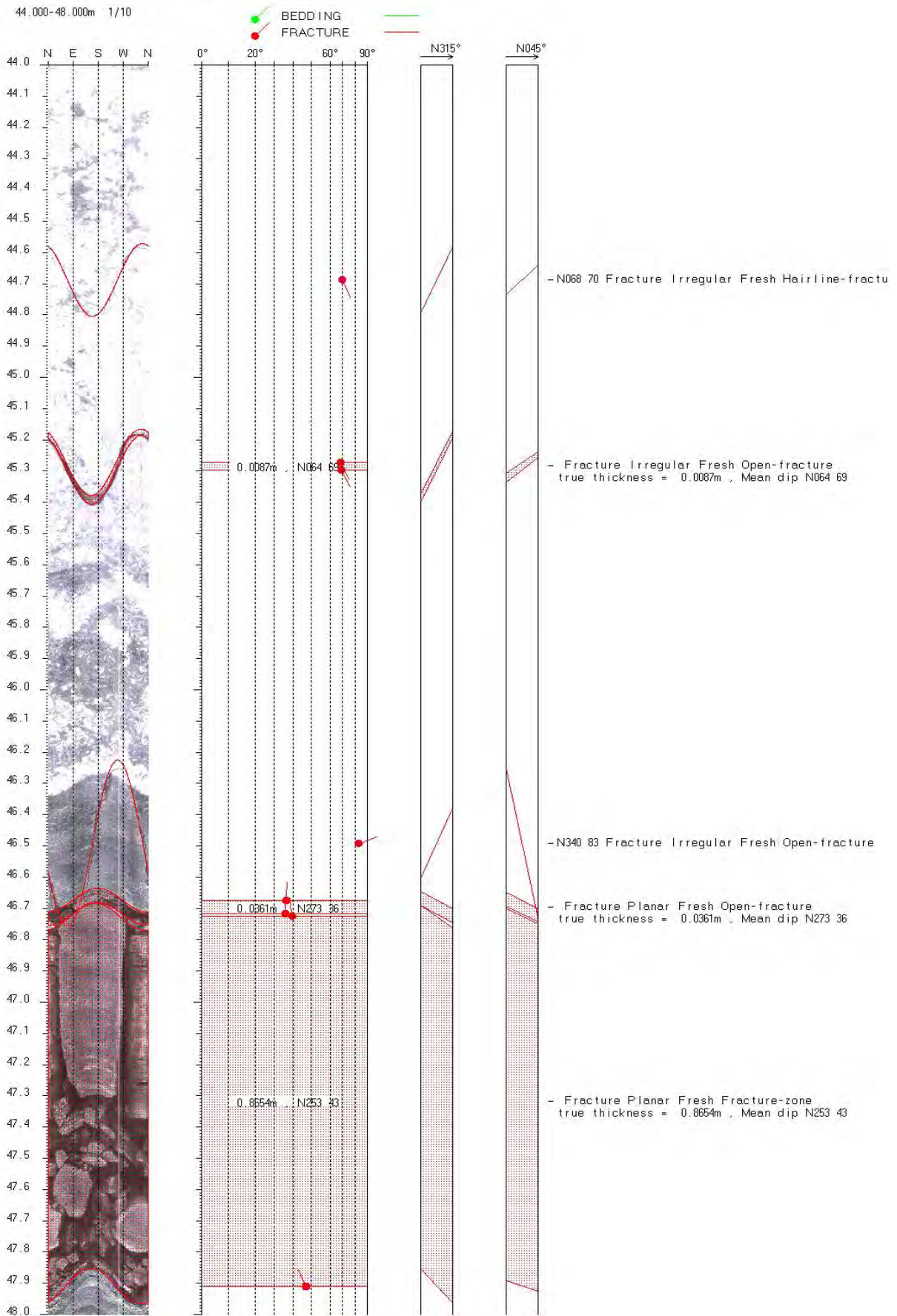


Figure 53. Optical televiwer synthetic images with digitised planar fractures in the 44–48 m depth interval (caption as on Figure 36).

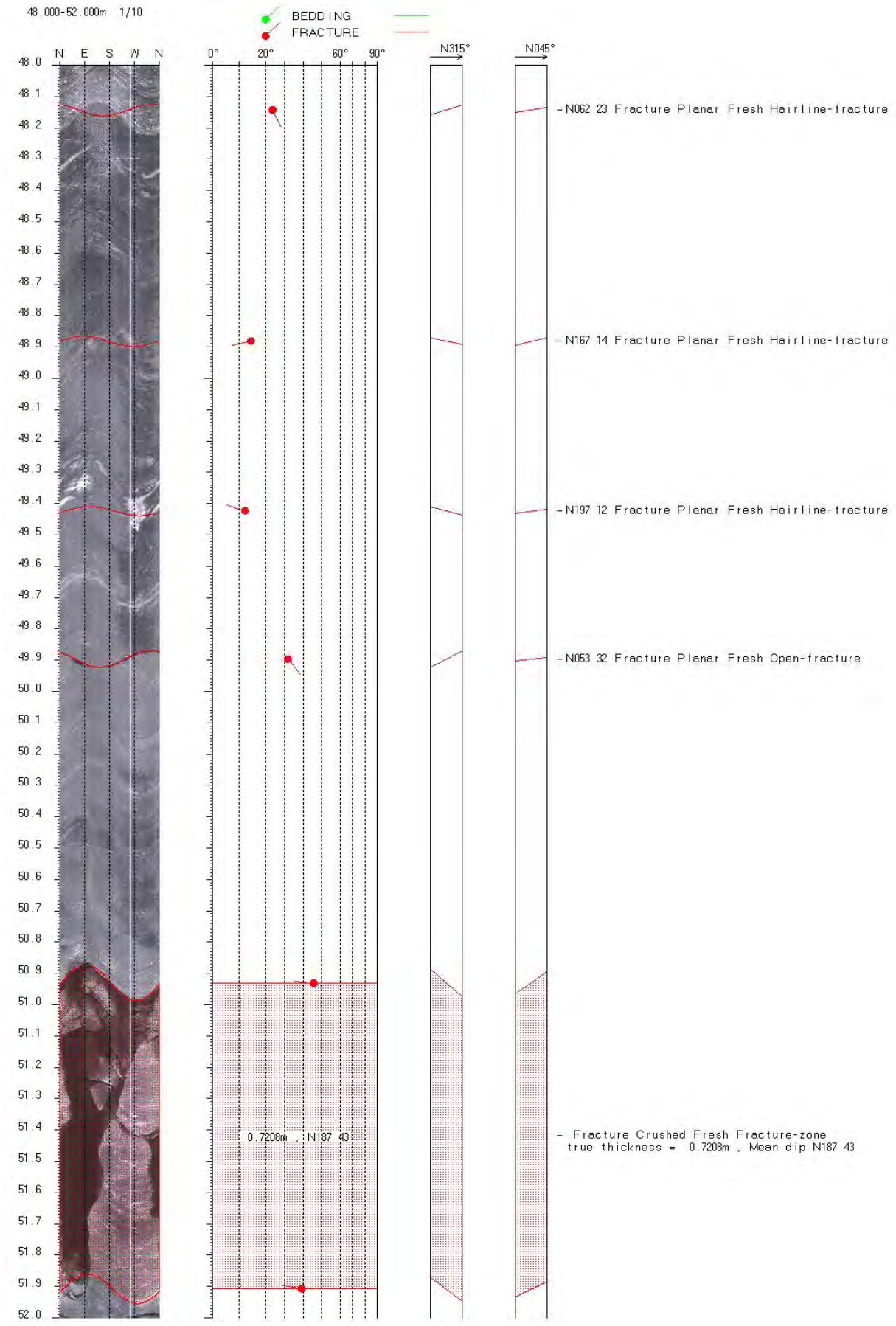


Figure 54. Optical televiwer synthetic images with digitised planar fractures in the 48–52 m depth interval (caption as on Figure 36).

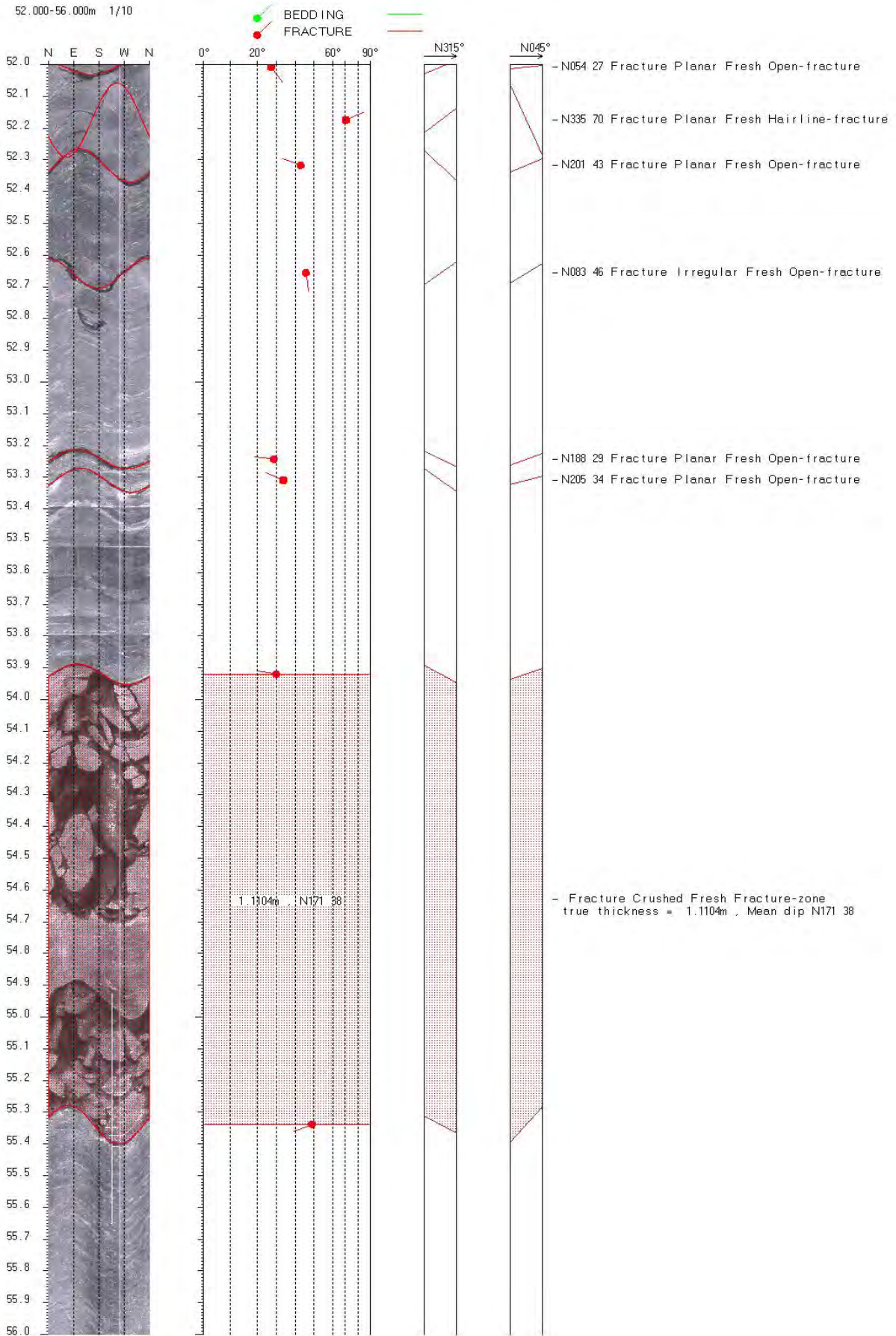


Figure 55. Optical televiwer synthetic images with digitised planar fractures in the 52–56 m depth interval (caption as on Figure 36).

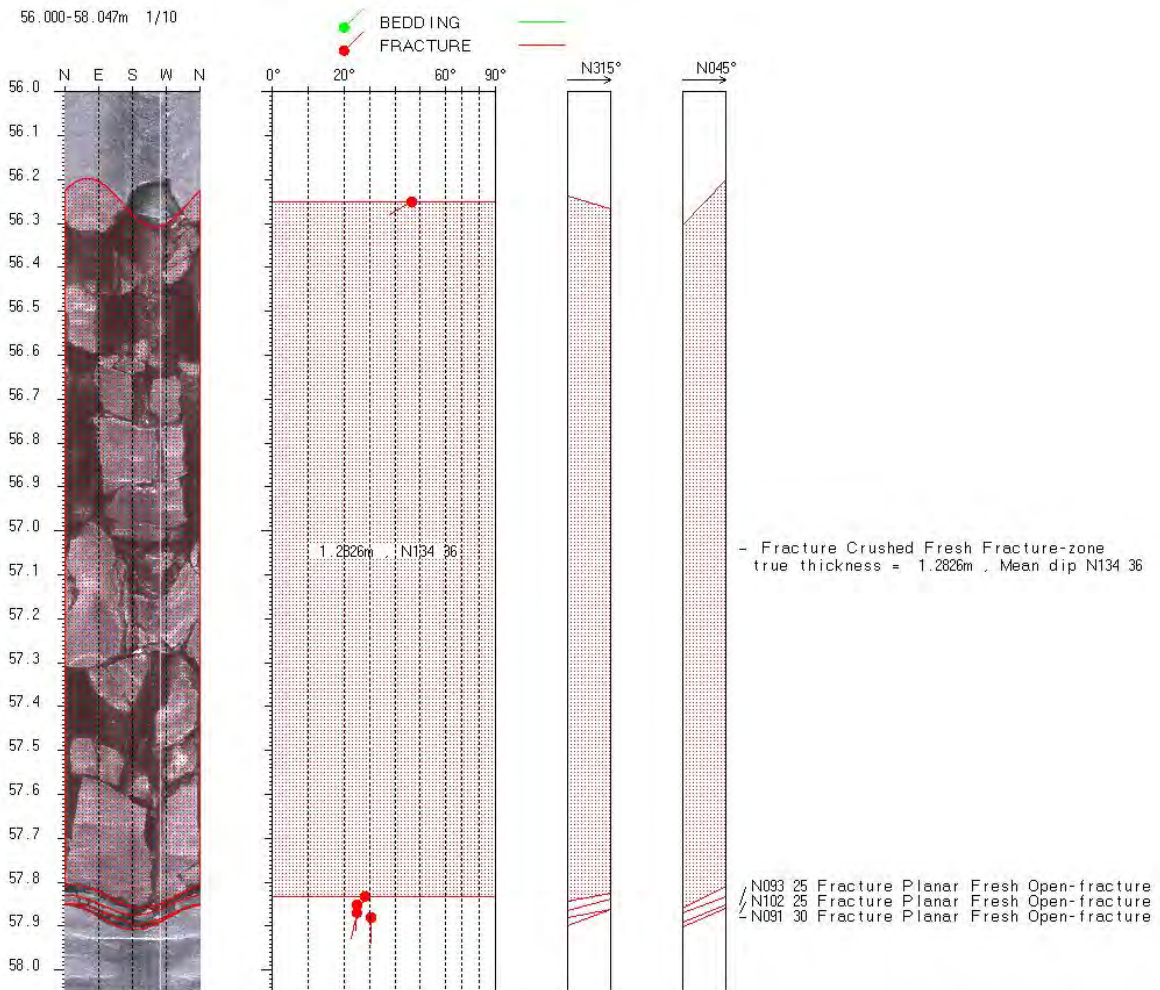


Figure 56. Optical televiewer synthetic images with digitised planar fractures in the 56–58 m depth interval (caption as on Figure 36).

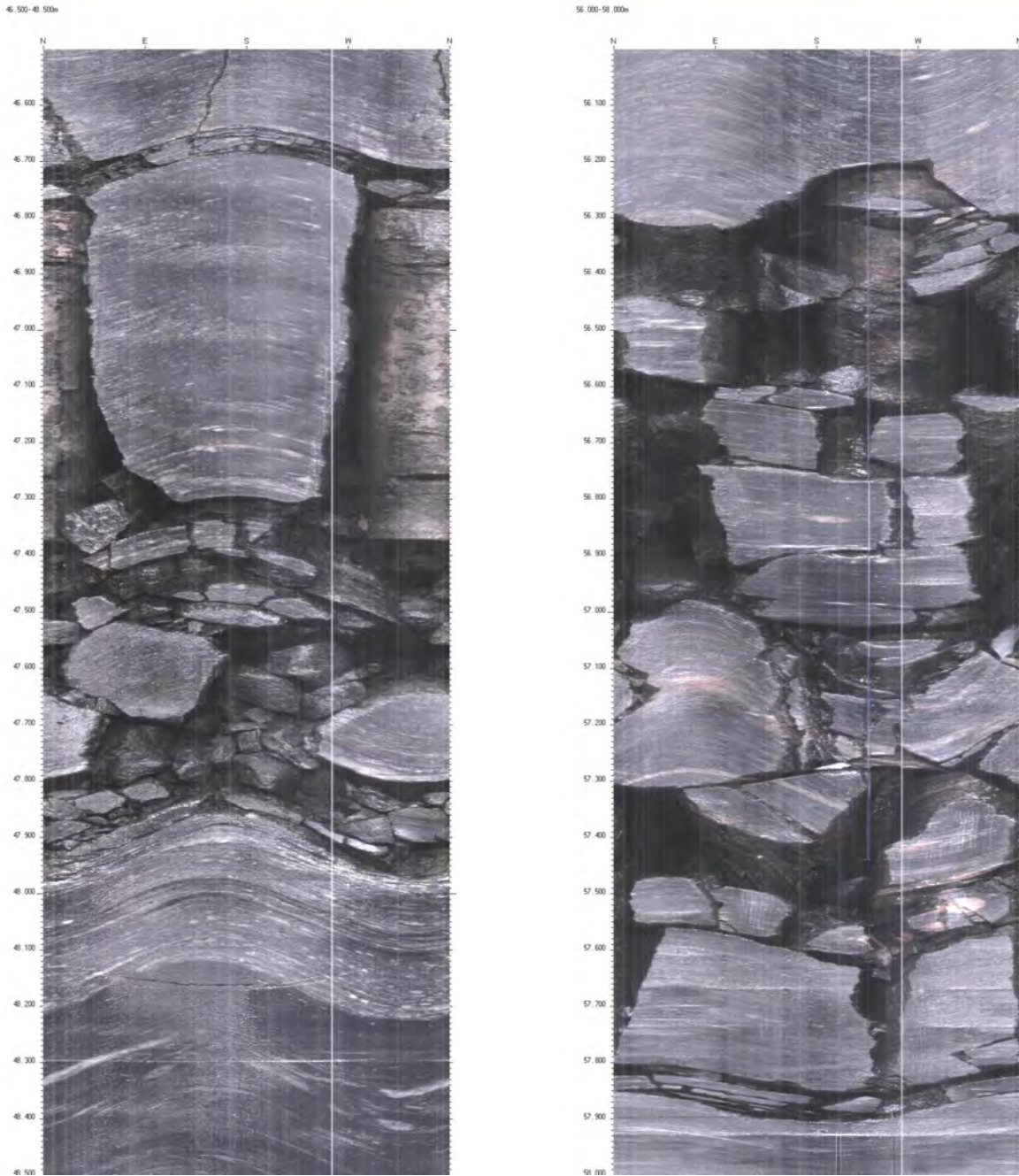


Figure 57. Optical televiewer images showing crushed zones at 46.7 m (left) and 56.3 m (right) depths.

3.2.4 Structural data in depth interval: 57–77 m

3.2.4.1 Metamorphic foliation in the 57–77 m depth interval

The dip direction of the 27 measured foliation planes strongly varies in the 57–77 m depth interval (Figure 58, Figure 59 and Appendix 1). In the 58–59.5 m depth interval, the foliation dips to the SSE (Figure 58, Figure 59), in the 61–64.5 m interval to the east (Figure 58, Figure 59) and in the 64.5–71 m interval roughly to the N and NE (Figure 58 and Figure 59). From 71 to 77 m depth the foliation is directed to the WNW and to the SW in the bottom meter of this logged interval (Figure 59). The average dip angle value equals 39° between 58 and 64 m depth (Figure 58 and Figure 59), 21° between 64 and 71 m depth (Figure 58 and Figure 59) and 35° between 71 and 76 m depth (Figure 59).

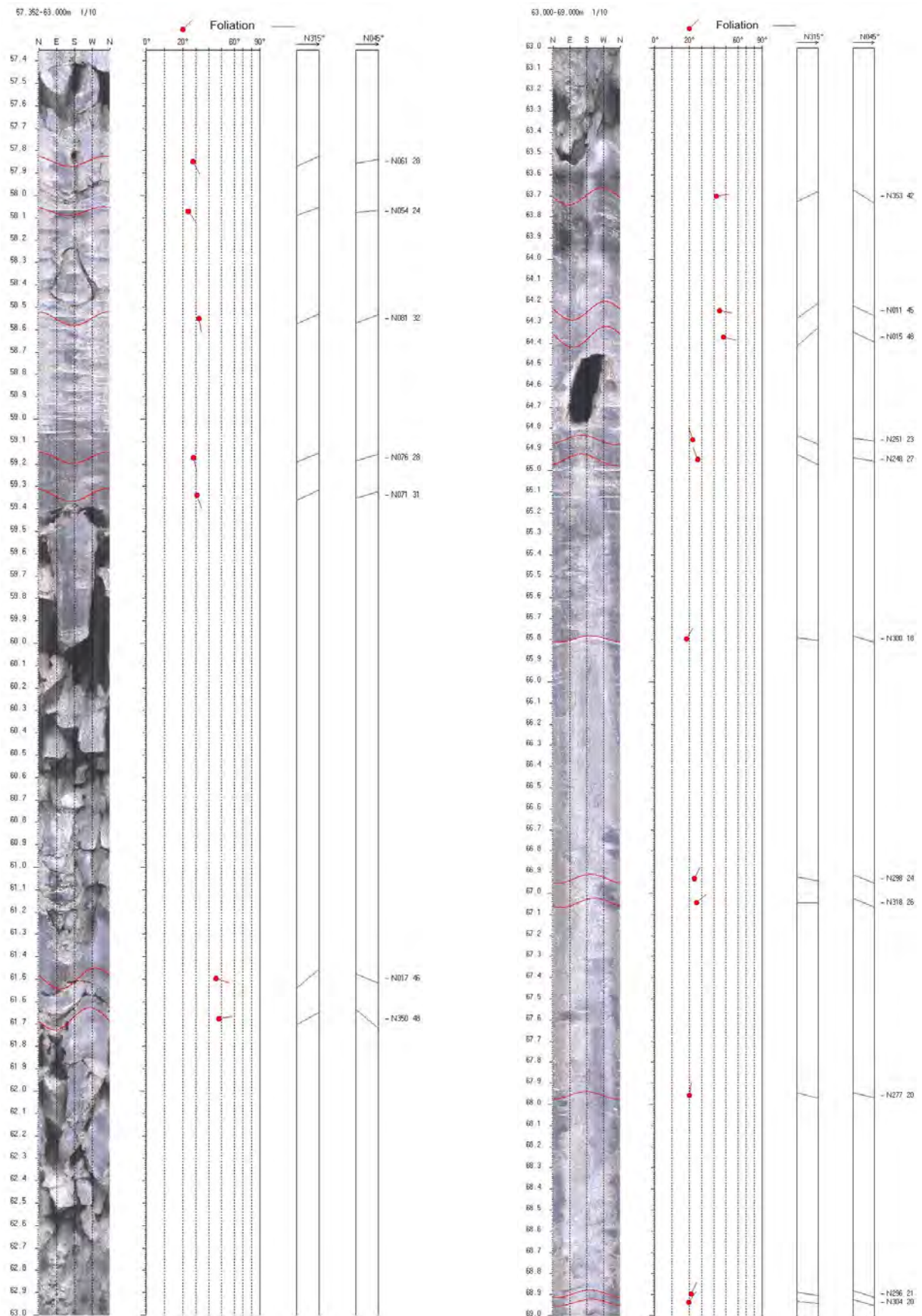


Figure 58. Unwrapped optical images of the wall of Mannen borehole with digitised foliation planes in the 57.4–69 m depth interval (caption as in Figure 30).

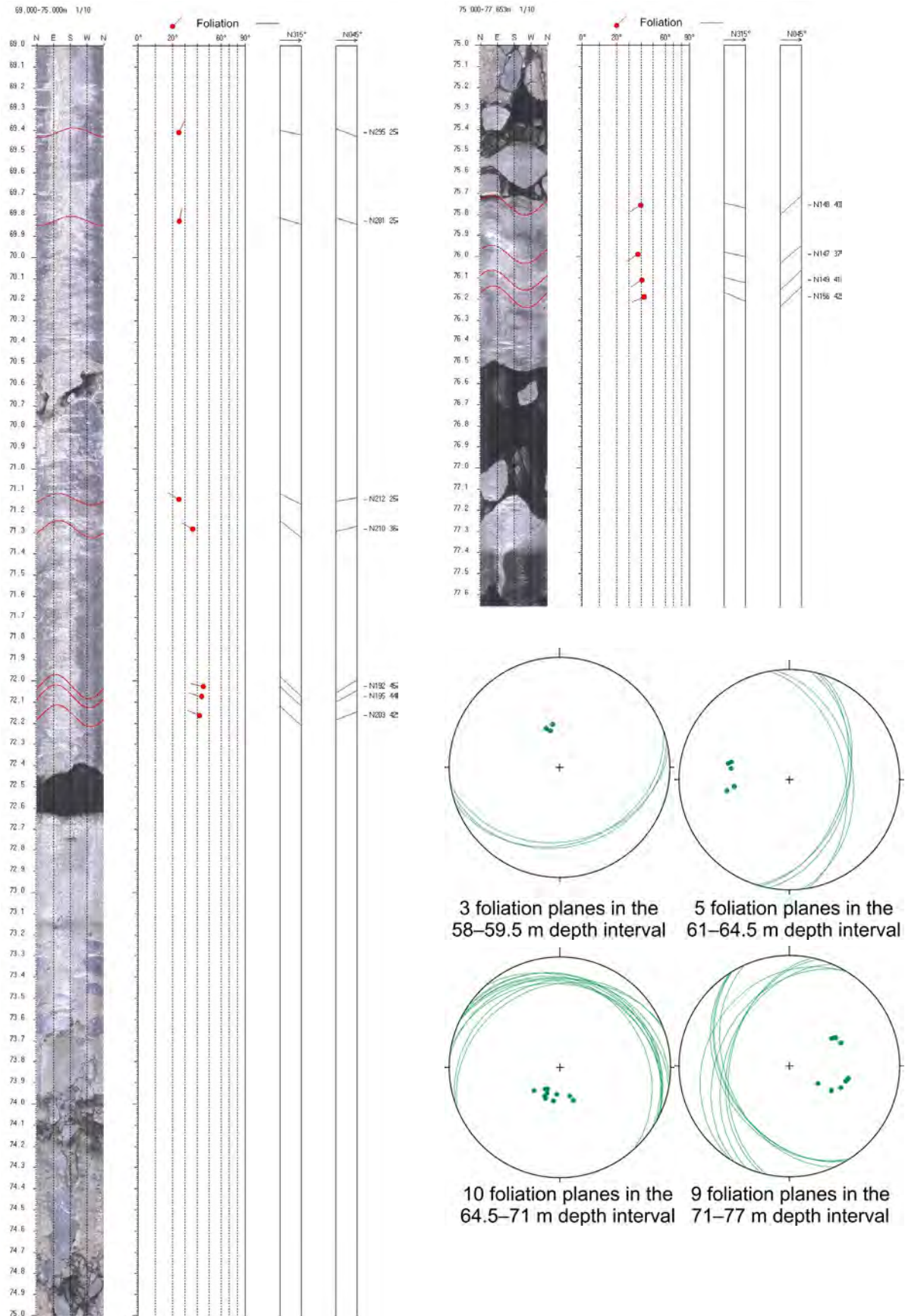


Figure 59. Unwrapped optical images of the wall of Mannen borehole with digitised foliation planes in the 69–77.6 m depth interval (caption as in Figure 30) and stereoplots of the metamorphic foliation (planes and poles) in the 58–59.5, 61–64.5, 64.5–71 and 71–77 m depth interval (data listed in Appendix 1).

3.2.4.2 Fractures in the 57–77 m depth interval

Eighteen fractures are recorded along the 57–77 m depth interval. A statistic analysis is of low significance because of the large dispersion of the dip direction of the fracture orientations (Figure 60). The dispersion in dip direction is also well displayed by the rose diagram of the fracture sets (Figure 61).

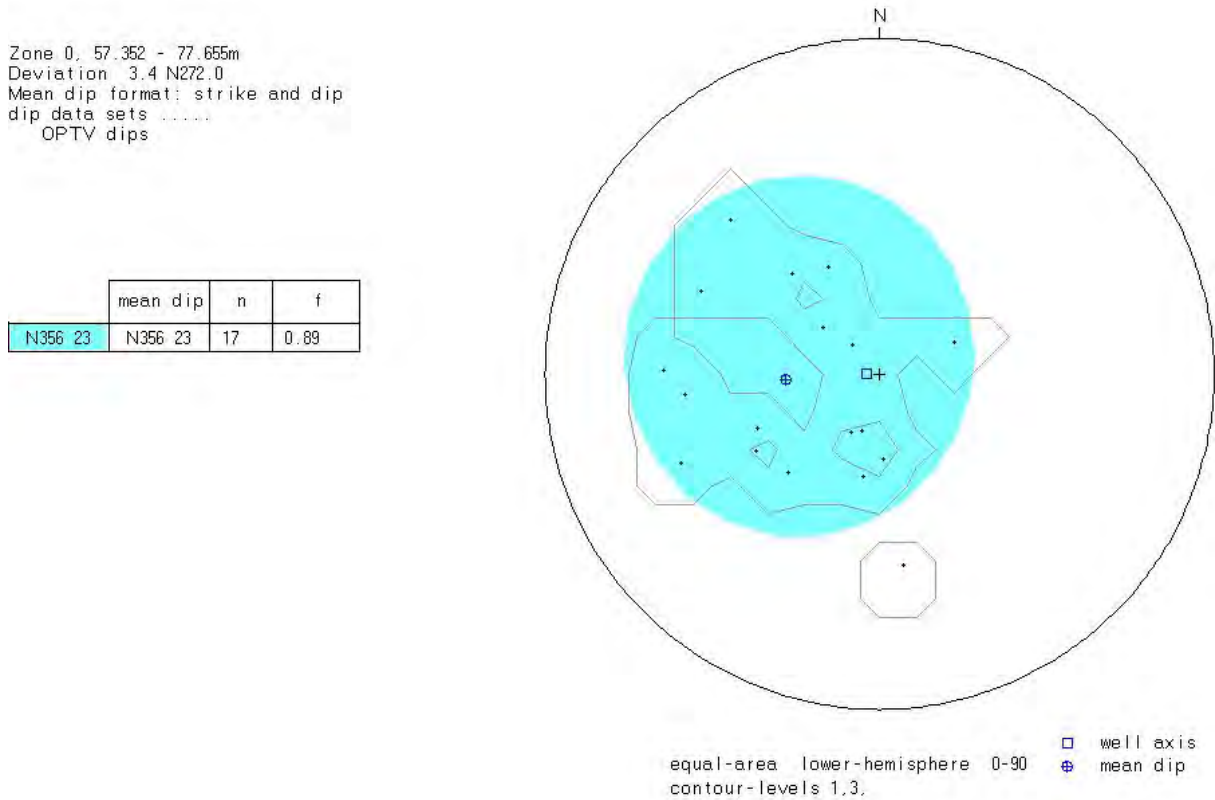


Figure 60. Contour plots, with poles of fractures, providing one main fracture set in the c. 57–77 m depth interval. Note that the strong dispersion of the 18 fractures provides a statistic analysis of low significance.

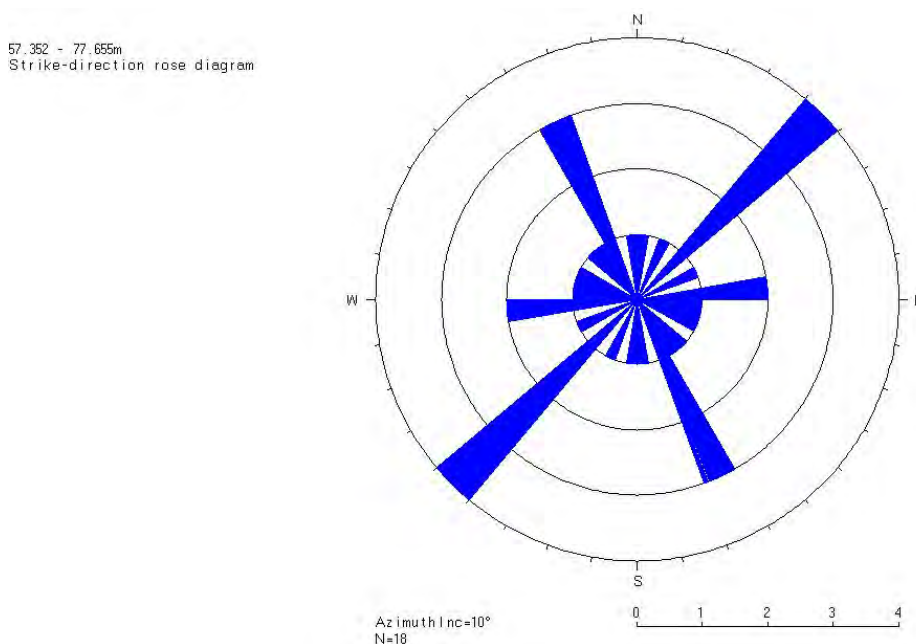


Figure 61. Rose diagram of the fractures in the 57–77 m depth interval.

The fracture frequency is not particularly important in the 57–77 m depth interval and no fracture is observed between 64–70 m depth (Figure 62). The 57–77 m depth interval was divided in 3 zones with regards to the fracture frequency (Figure 62) during the numerical calculation and according to the results listed in Appendix 3.

The inspection of the detailed pictured fracture logs in the 57–77 m depth interval (Figure 63–Figure 67) actually reveals that the 64–70 m depth interval consists of intact rock but that the overlying and underlying intervals are characterised by a large amount of crushed zones (Table 6). Two examples of 1–2.5 m thick crushed zones with an obvious fine-grained matrix are illustrated on Figure 68 and are found at the 59.4–61.2 and 73.2–75.7 m depth intervals. The core logging in these intervals has revealed the presence of clays within the crushed zones (see section 2.3). Large open holes and vertical fractures are also observed at for example at 64.5 m depth (Figure 64). The borders of the crushed zones are in general shallow dipping and not systematically well orientated with regards to the slope to favour gravitational deformation (Table 6).

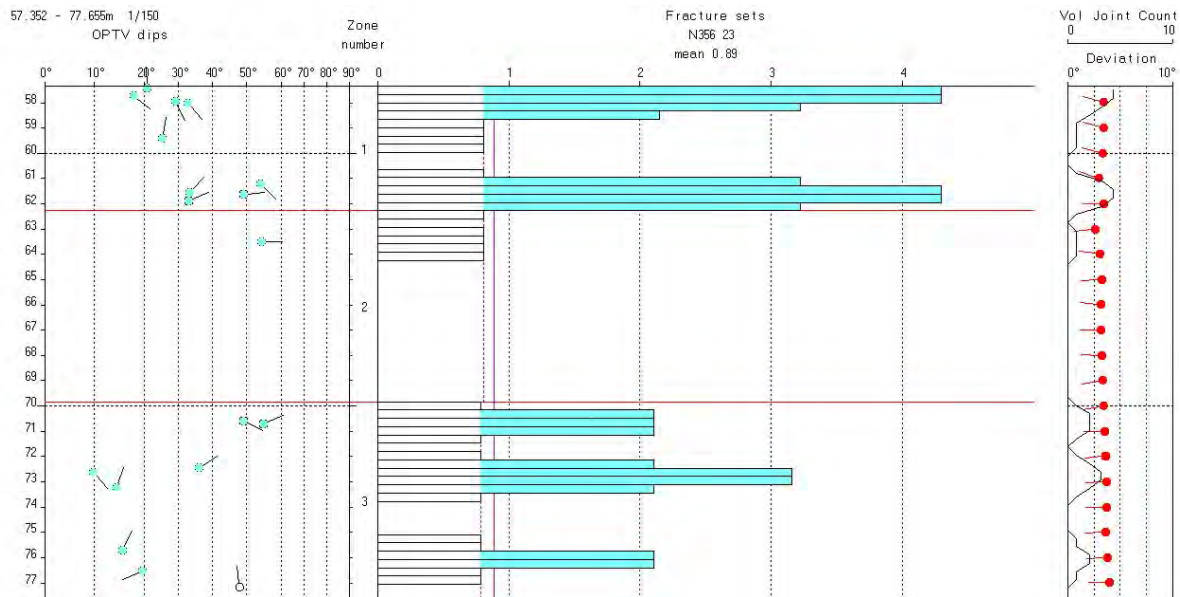


Figure 62. Arrow plots (N up) of the 18 fractures in the c. 57–77 m depth interval, frequency histograms of the single fracture set as defined by the statistical analysis (see Figure 60). The deviation of the borehole (arrow plot; N up) is shown in the right.

Table 6. Observation in the 57.4–77.6 m depth interval of crushed and fractured zones, open fractures, orientation and stereoplot. Mean dip angles and dip angles at the bottom of the fractured zone are shown. (* = uncertain dip direction).

Depth [m]	Dip direction [°]	Dip angle [°]	Thickness [m]	Comments	Stereoplot
57.5–57.7	054 *	8	0.28	Partially open fracture (see Figure 63)	
59.4–61.2	104 (mean) * 130 (bottom)	23 (mean) 53 (bottom)	1.66	Crushed zone (see Figure 63, Figure 68)	
61.9–63.5	081 (mean) 090 (bottom)	43 (mean) 52 (bottom)	1.17	Crushed zone (see Figure 64)	
70.6–70.7	090	49	0.07	Partially open fracture (see Figure 66)	
72.4–72.6	073 (mean) * 135(bottom)	20 (mean) 10 (bottom)	0.18	Hole, fracture (see Figure 66)	
73.2–75.7	023	15	2.41	Crushed zone (see Figure 67 , Figure 68)	
76.5–77.2	326 (mean) 350 (bottom)	24(mean) 49(bottom border)	0.6	Crushed zone (see Figure 67)	

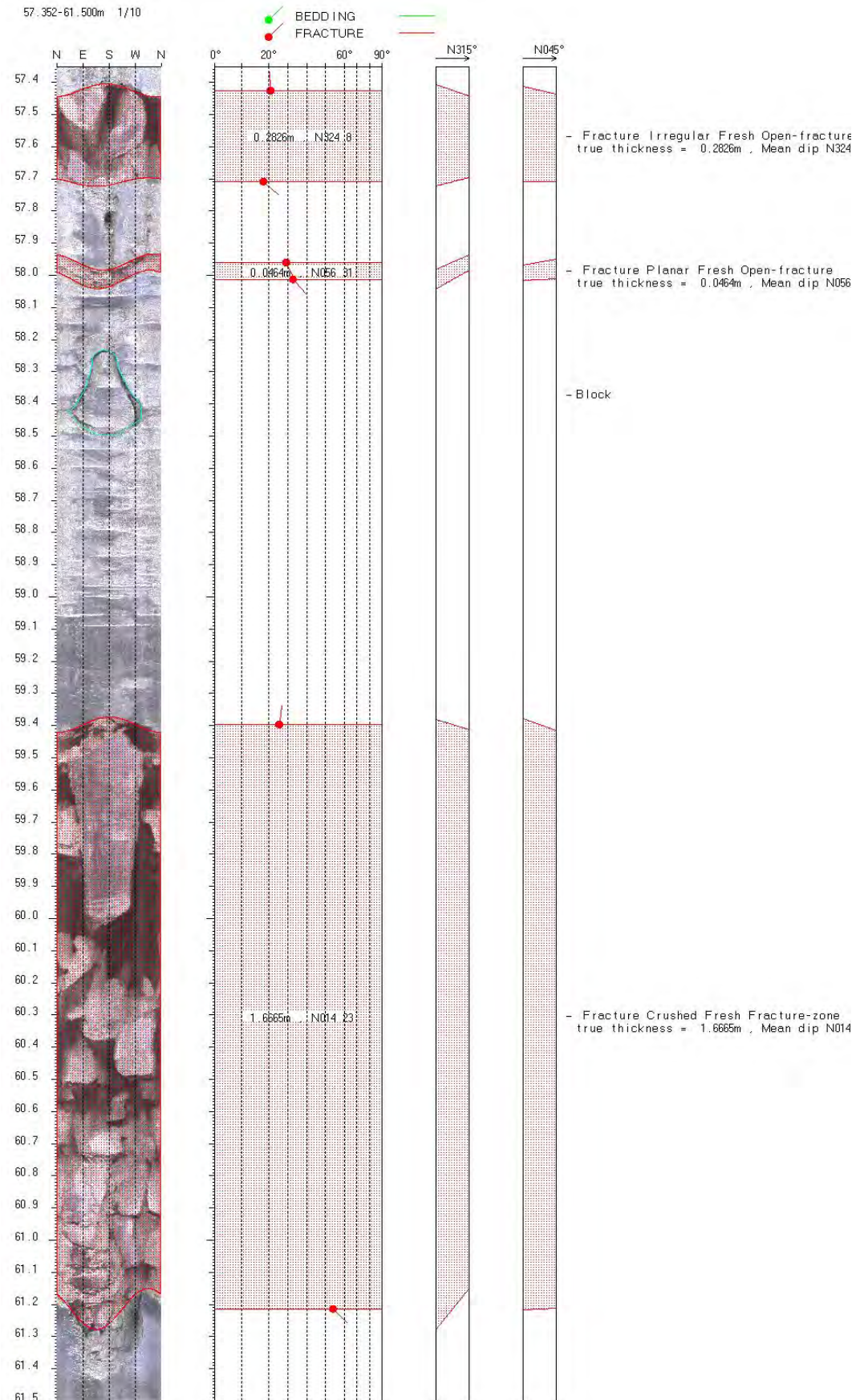


Figure 63. Optical televiwer synthetic images with digitised planar fractures in the 57.4–61.5 m depth interval (caption as on Figure 36).

61.500-65.500m 1/10

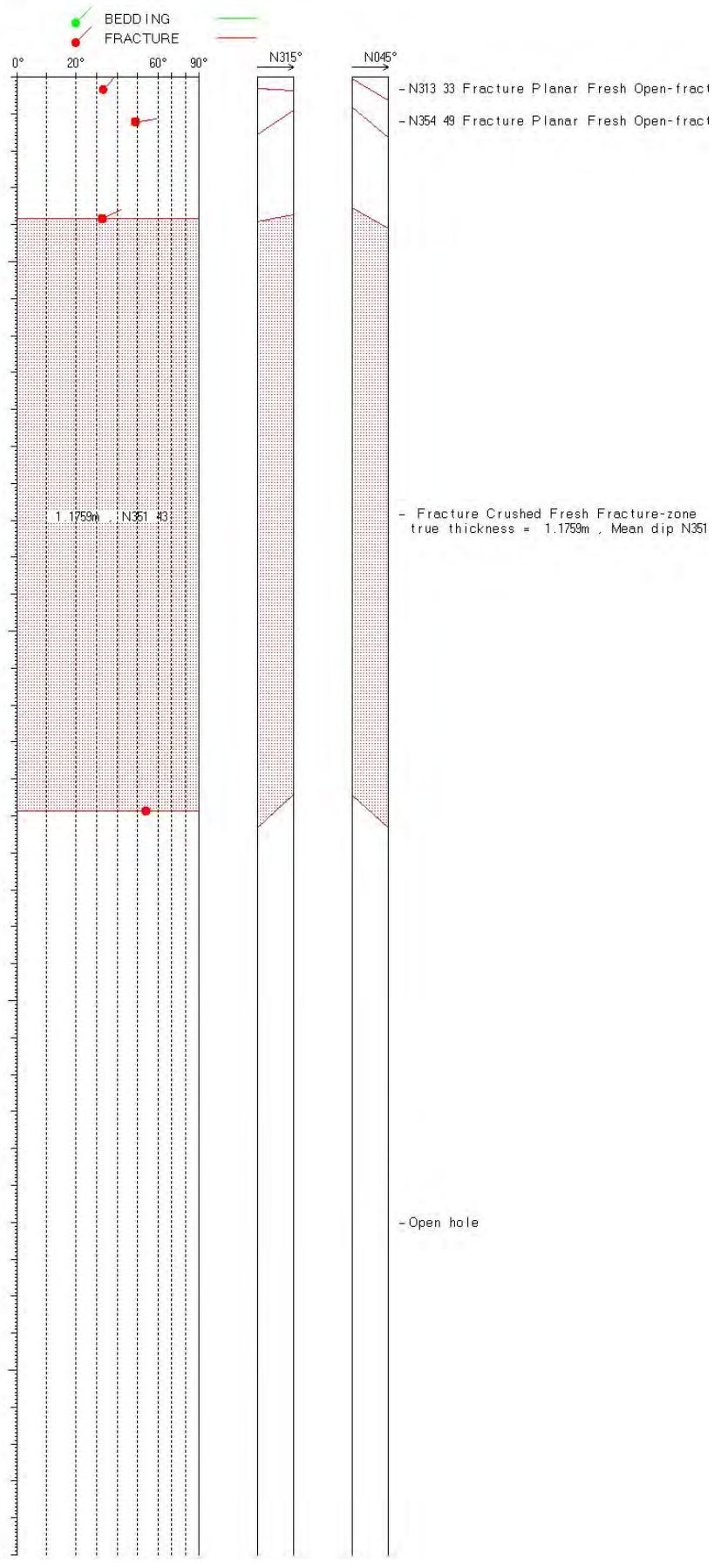
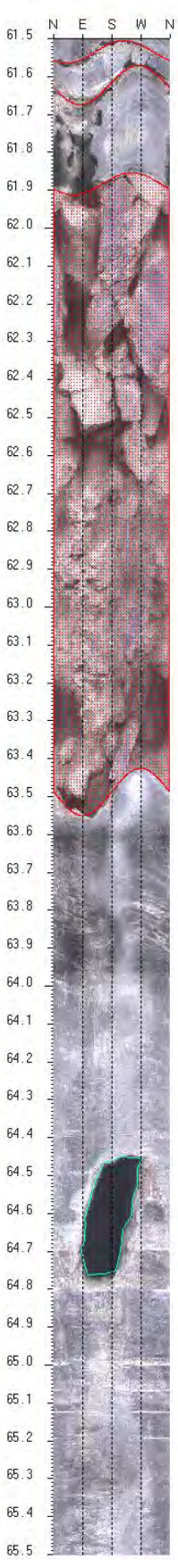


Figure 64. Optical televiewer synthetic images with digitised planar fractures in the 61.5–65.5 m depth interval (caption as on Figure 36).

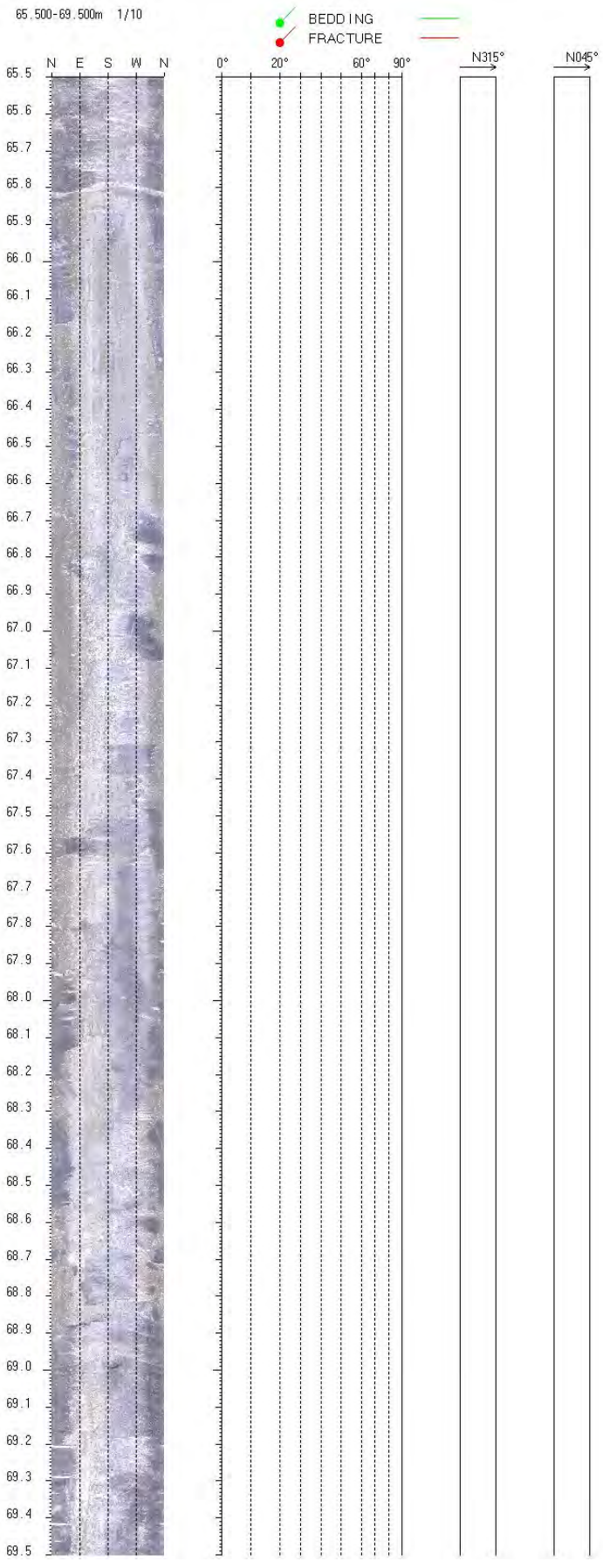


Figure 65. Optical televiewer synthetic images with digitised planar fractures in the 65.5–69.5 m depth interval (caption as on Figure 36).

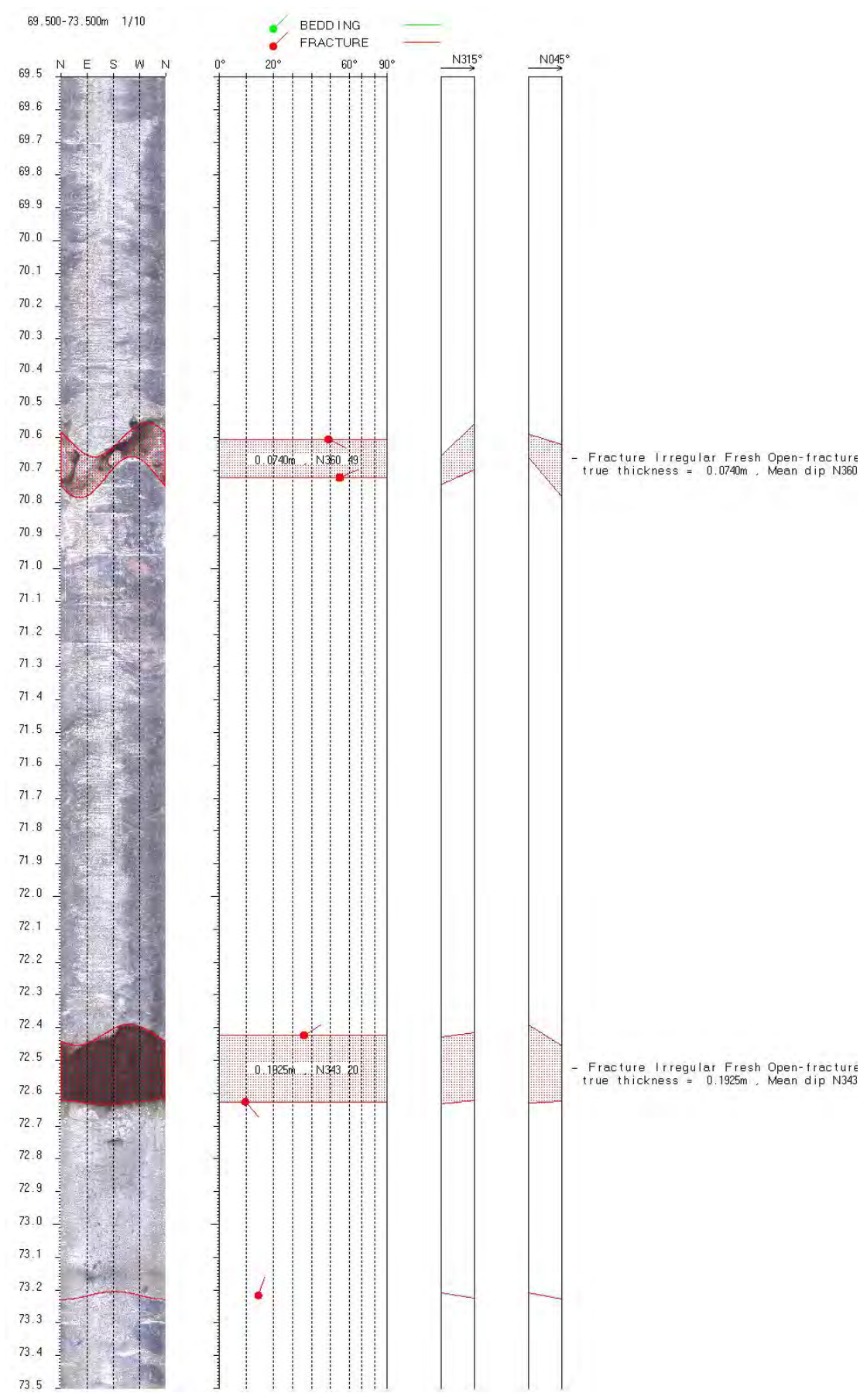


Figure 66. Optical televiwer synthetic images with digitised planar fractures in the 69.5–73.5 m depth interval (caption as on Figure 36).

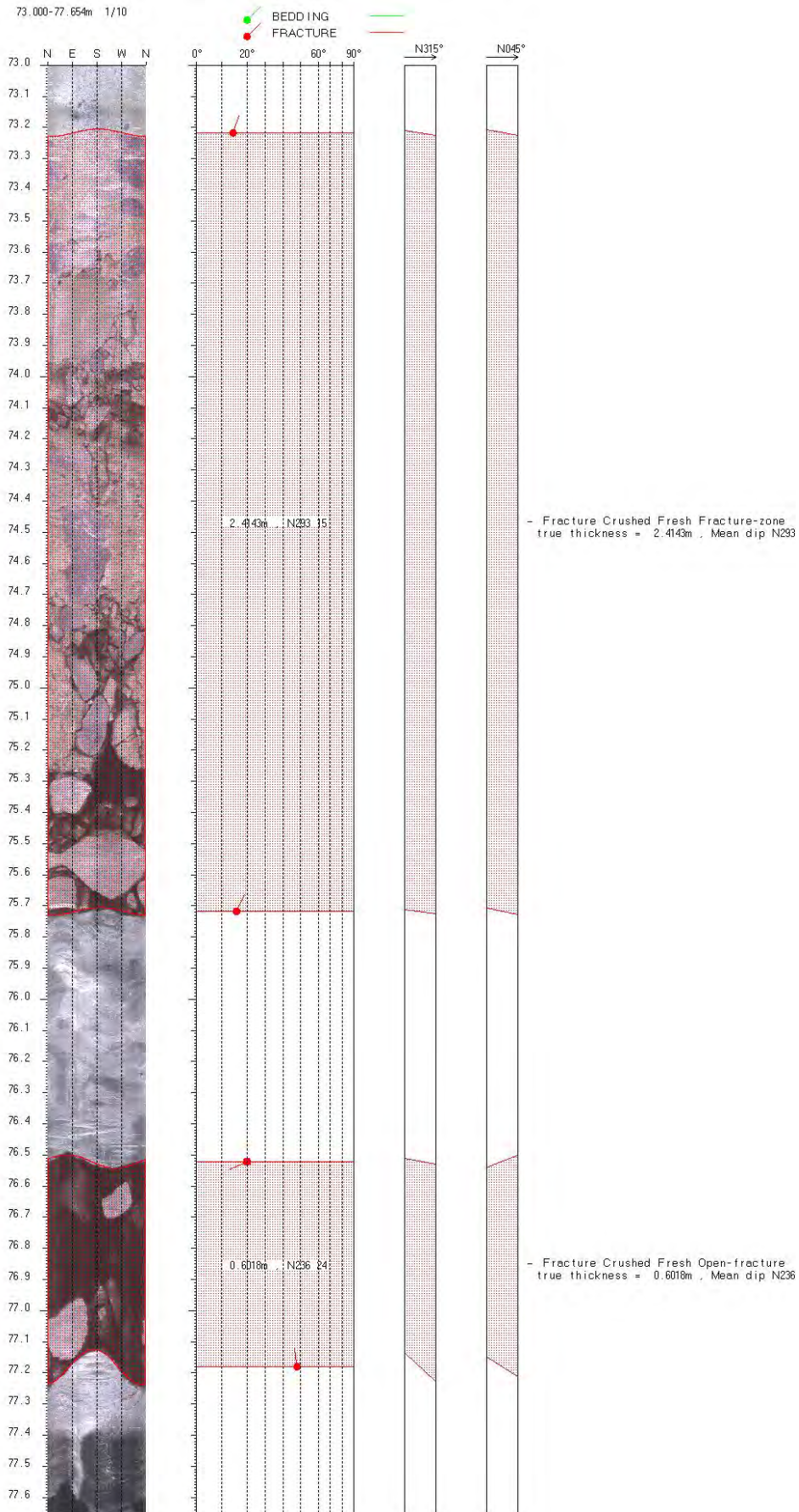


Figure 67. Optical televiewer synthetic images with digitised planar fractures in the 73.0–77.6 m depth interval (caption as on Figure 36).

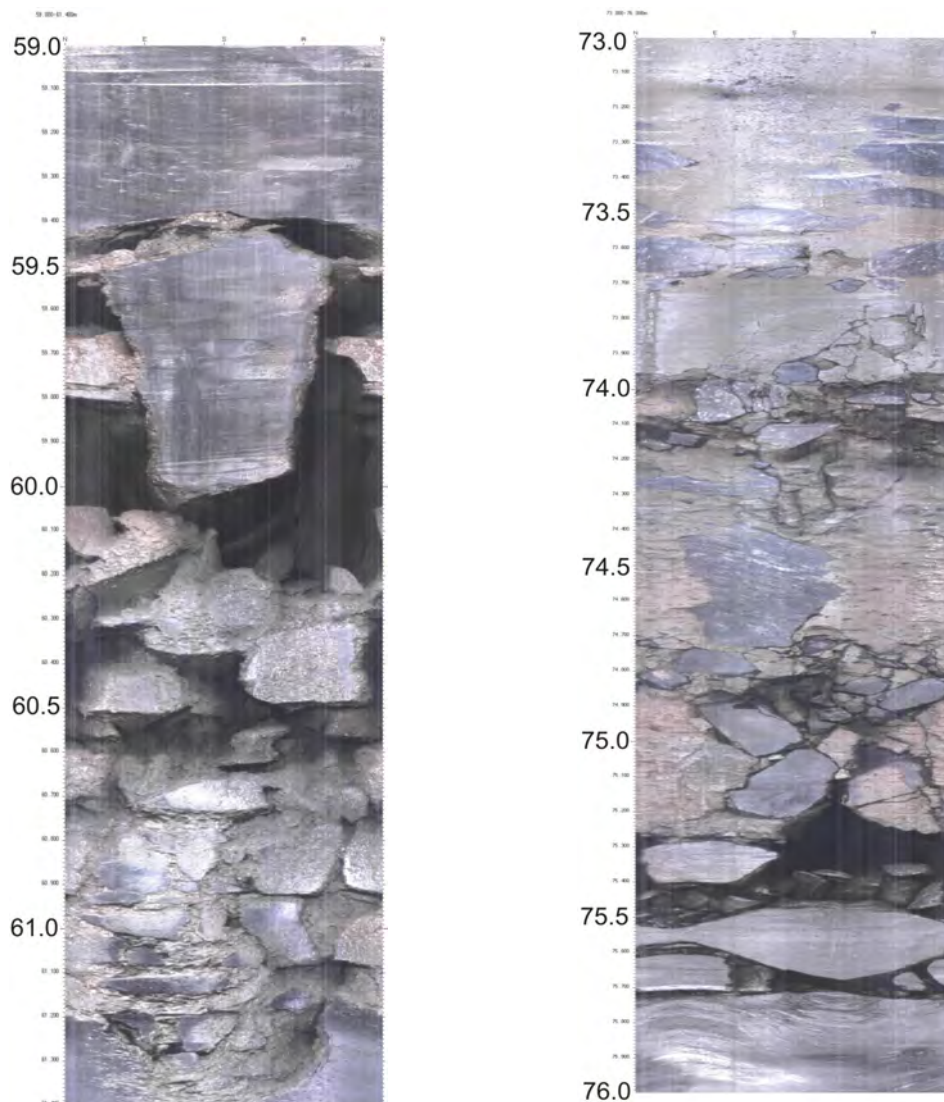


Figure 68. Optical televiewer images showing crushed zones at 59.4 m (left) and 73.2 m (right) depths. The filling of the fractures is partly cement, which was injected to stabilise the borehole. The cement is especially visible in the picture to the right as a grey mass.

3.2.5 Structural data in depth interval: 89–133 m

3.2.5.1 Metamorphic foliation in the 89–133 m depth interval

Sixty-six measurements of foliation were extracted from the optical televiewer images in the 89–133 m depth interval (Figure 69–Figure 72 and Appendix 1). The dip direction of the foliation varies in the interval. However, a NNE to NNW dip direction which predominates from the depth of 116 m down to the bottom of the borehole. At c. 90 m depth, the foliation gently dips to the SW and SSW (Figure 69). From 92 m to 110.2 m depths, the foliation gently to moderately dips to the SE whereas from 110.9 to 111.4 m depth the foliation gently dips to the NNE (Figure 69, Figure 70 and Figure 72). The change of foliation attitude between the 110.2 and 110.9 m depths (Figure 70 and Figure 72) reveals a fold that was not detected during the core logging (see section 2.2). In the depth interval 110.9–112 m the foliation gently dips to the NE (Figure 70 and Figure 72). It has a moderate to steep dip to the east between 113.5 and 116.2 m depth (Figure 71 and Figure 72), a quite steep dip to the NNE and N between 116.4 and 122.3 m depth (Figure 71 and Figure 72) and a moderate to steep dip to the NW from 124 to 126.6 m depth (Figure 71 and Figure 72). Two E–W fold hinges are observed between 127 and 132 m depths (Figure 72).

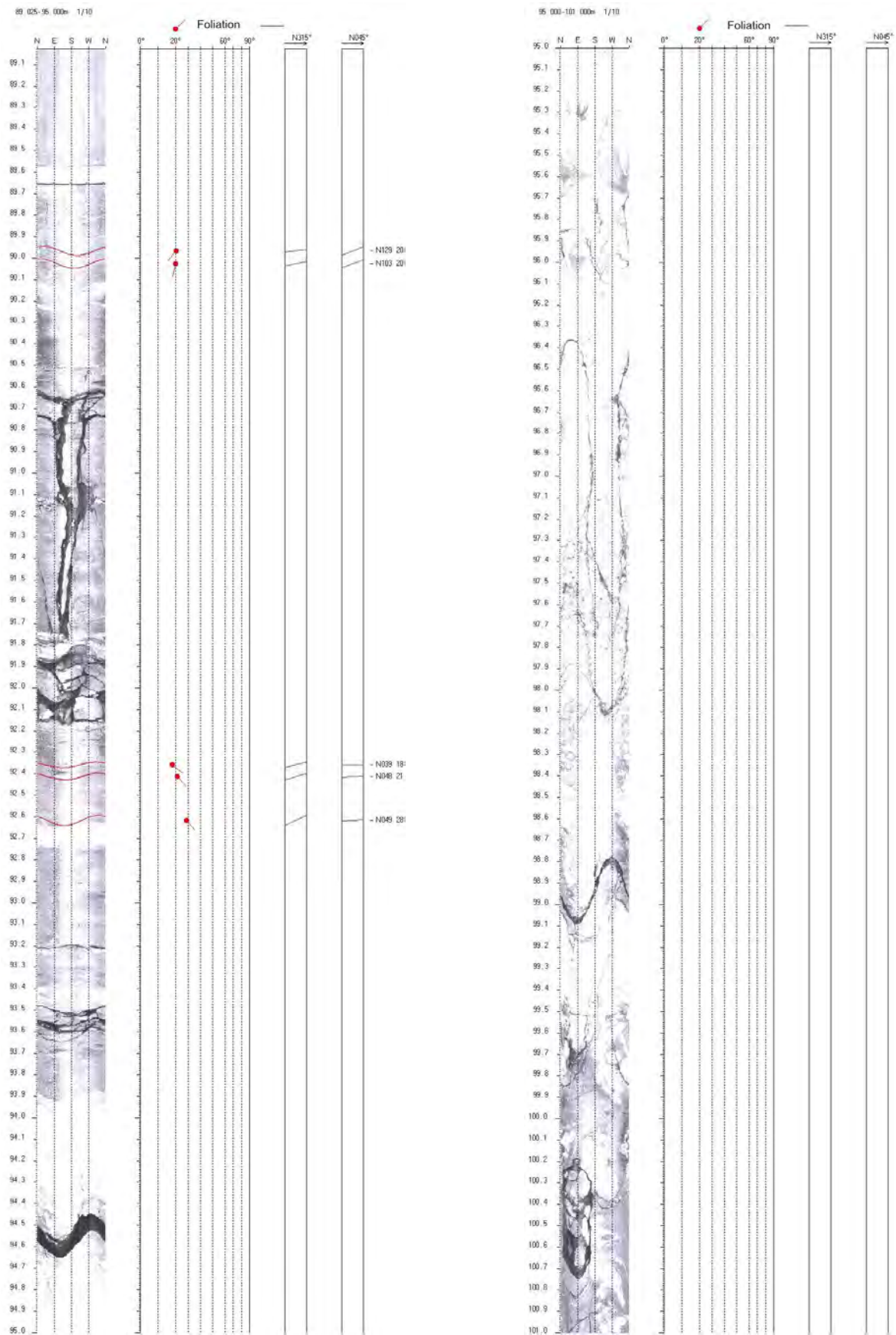


Figure 69. Unwrapped optical images of the wall of Mannen borehole with digitised foliation planes in the 89–101 m depth interval (caption as in Figure 30).

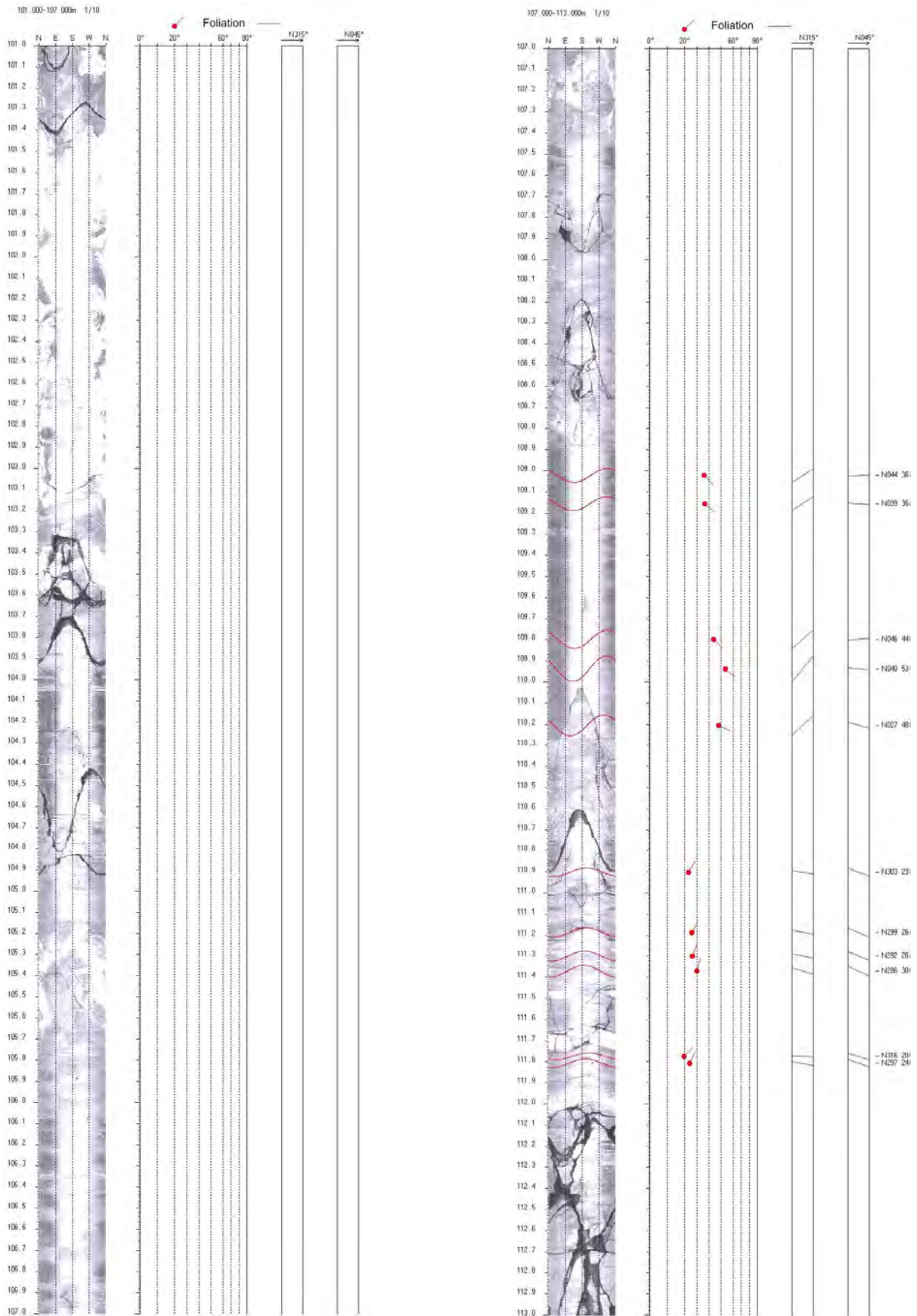


Figure 70. Unwrapped optical images of the wall of Mannen borehole with digitised foliation planes in the 101–113 m depth interval (caption as in Figure 30).

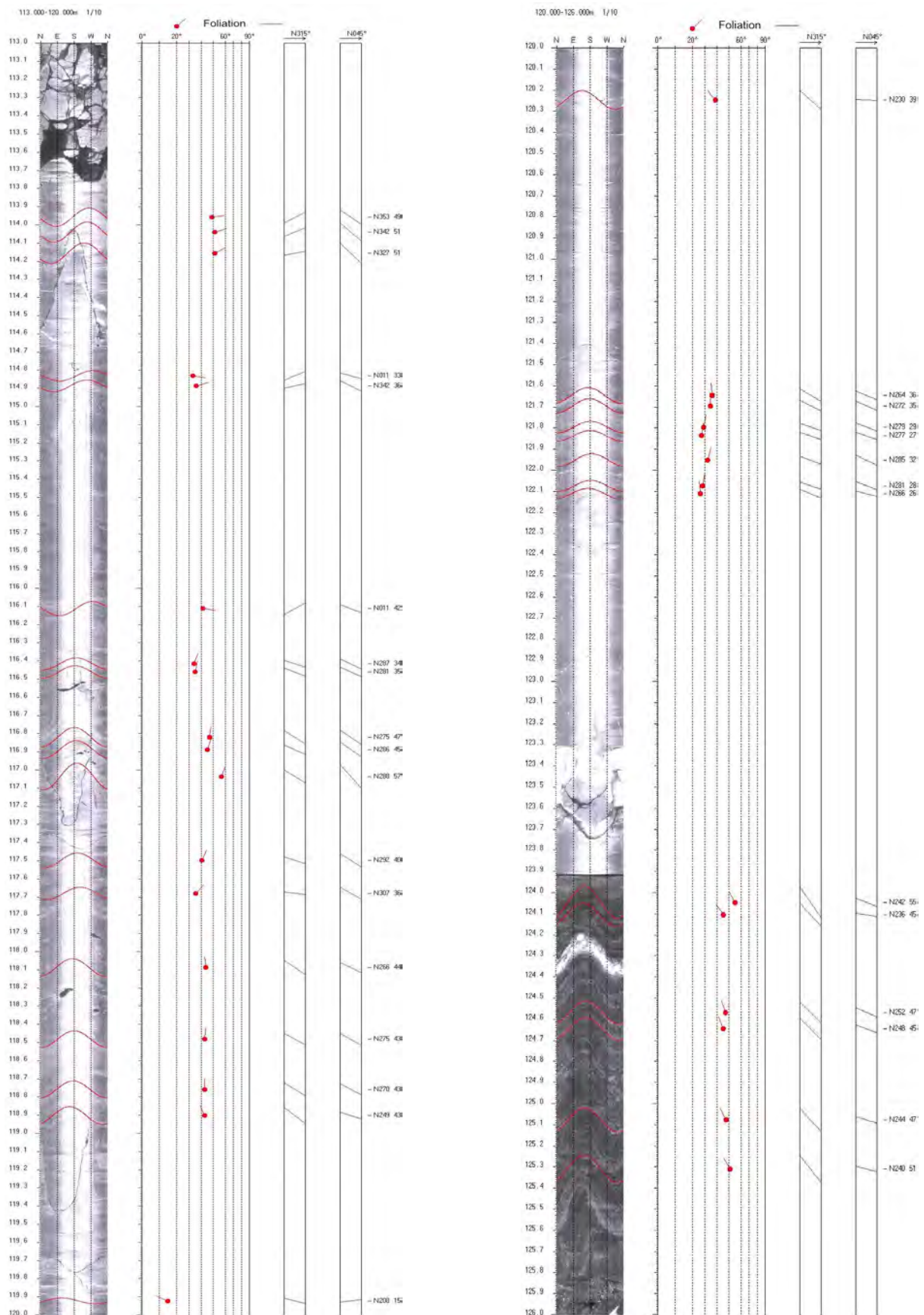


Figure 71. Unwrapped optical images of the wall of Mannen borehole with digitised foliation planes in the 113–126 m depth interval (caption as in Figure 30).

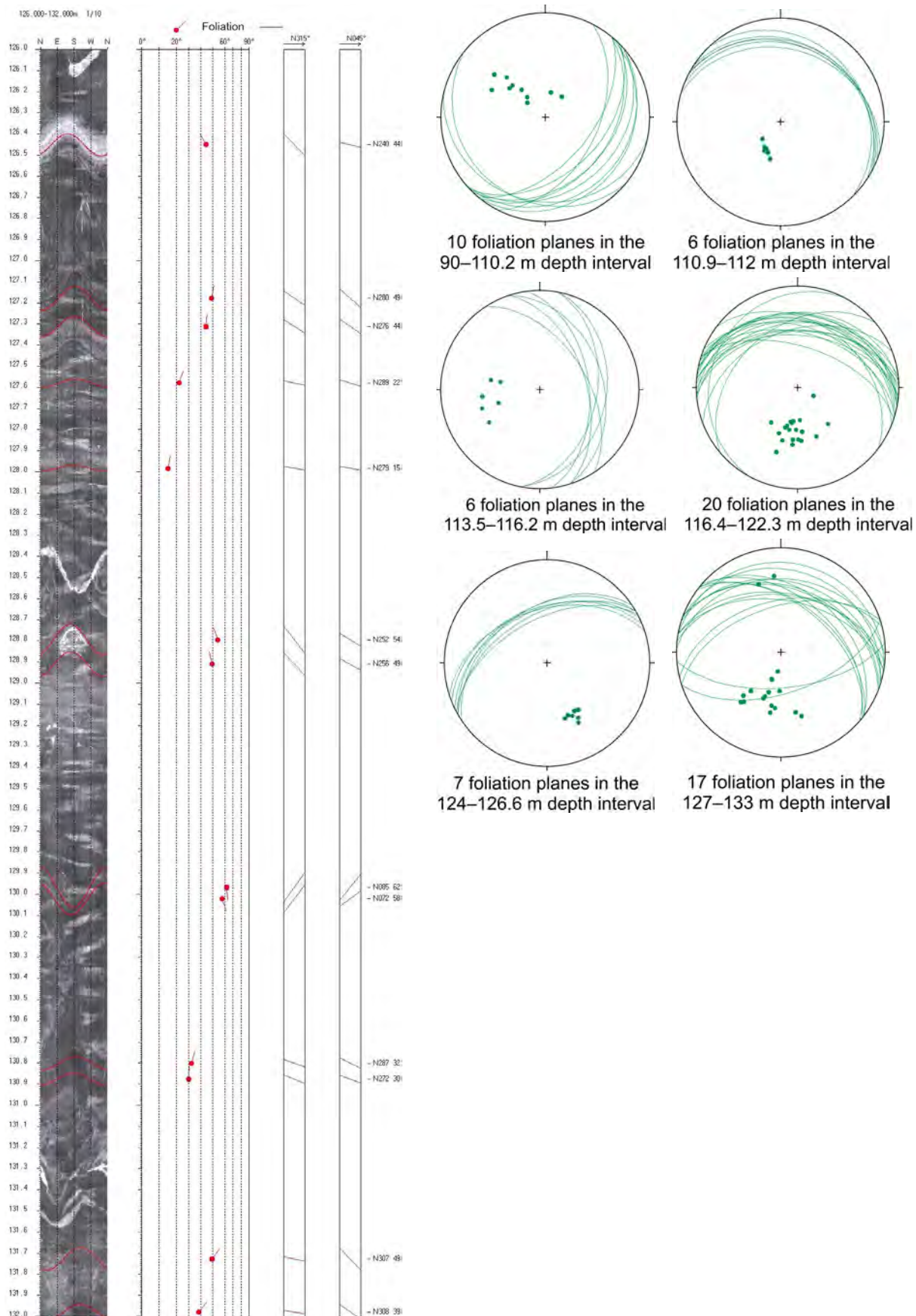


Figure 72. Unwrapped optical images of the wall of Mannen borehole with digitised foliation planes in the 126–132 m depth interval (caption as in Figure 30) and stereoplots of the metamorphic foliation (planes and poles) in the 90–110.2, 110.9–112, 113.5–116.2, 116.4–122.3, 124–126.6 and 127–133 m depth interval (data listed in Appendix 1).

3.2.5.2 Fractures in the 89–133 m depth interval

The 90 fractures measured in the 89–133 m depth interval can be divided into 4 fracture sets (Figure 73). A shallow NE-dipping set (dip direction/dip angle: 122°/19°) of 31 fractures seems to predominate (Figure 73). However, a strong dispersion exists in the data orientation and the set is not represented as predominant by a rose diagram (Figure 74). Another steep NNW-dipping set (dip direction/dip angle: 344°/62°) is conspicuous in the interval (Figure 73) and is well confined to its mean orientation so that it is the best represented fracture set in the rose diagram (Figure 74).

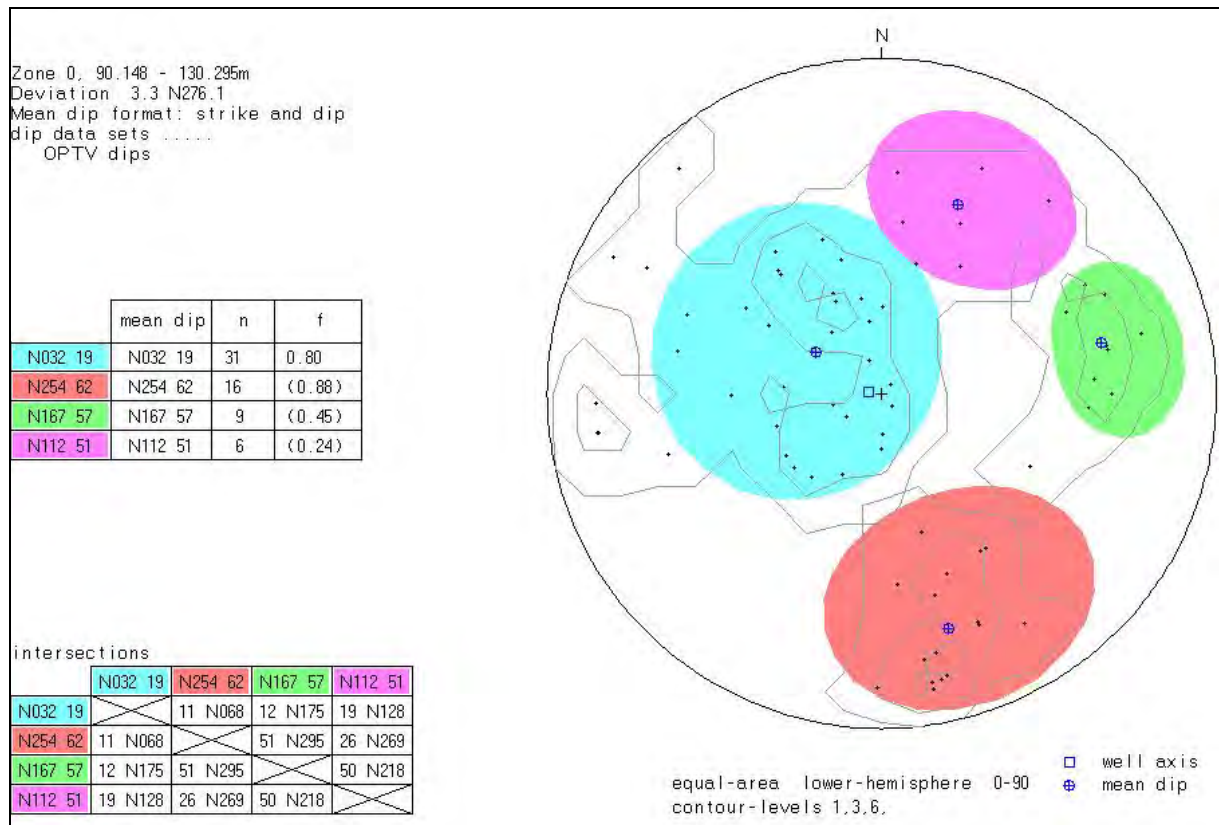


Figure 73. Contour plots, with poles of fractures, providing four main fracture sets in the c. 89–133 m depth interval.

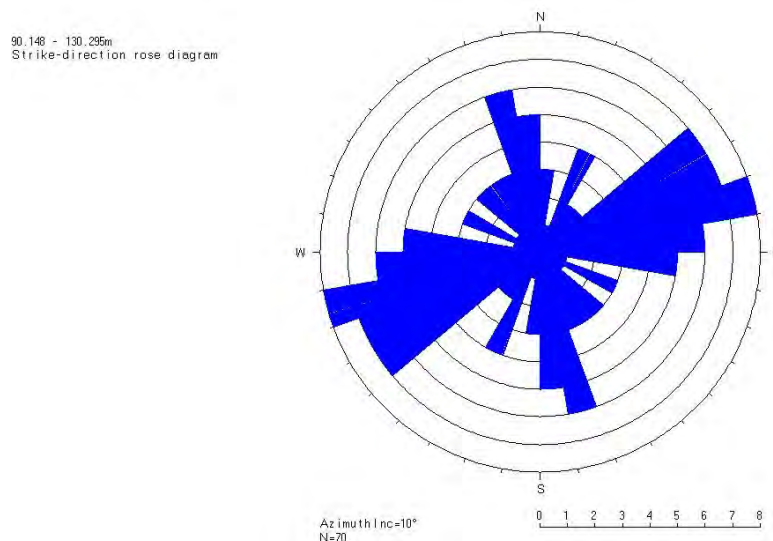


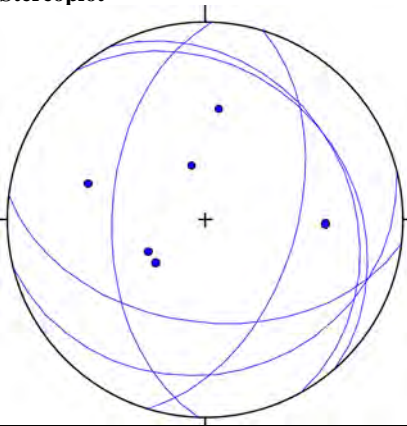
Figure 74. Rose diagram of the fractures in the 90–131 m depth interval.

The spatial distribution of the fractures in the 90–133 m depth interval shows two peaks in the fracture frequency reaching up to 10 fractures/m in the 96–112 m depth interval (Figure 75) mainly due to the high amount of steep NNW-directed fractures (in red on Figure 73 and Figure 75). The overlying 89–96 m depth interval is also fractured and characterised by the dispersion in the orientation of fractures (set in blue on Figure 73 and Figure 75). The underlying 112–130 m depth interval does not contain a significant amount of fractures (Figure 75).

The 90–133 m depth interval was divided into these 3 zones during the numerical calculation of the fracture frequency (Figure 75) and according to the results listed in Appendix 3. However, the fracture frequency analysis only does not reflect the occurrence of crushed zones (as the measurement of plane orientations is not possible in these damaged intervals) while a direct survey of the image log does (Figure 76–Figure 85). As such, the upper and lower of the 3 depth intervals that are defined from fracture frequency values (89–96 m depth and 112–130 m depth, respectively) contain each 3 crushed zones (Table 7). The thickest crushed zone in the 90–133 m depth interval reaches 1.12 m. It is located at 112.1 m and downward (Figure 86). The crushed zones are in general not favourably orientated to have resulted from gravity-induced deformation (Table 7).

Table 7. Observation in the 89–133 m depth interval of crushed and fractured zones, open fractures, orientation and stereoplot. Mean dip angles and dip angles at the bottom of the fractured zone are shown.

Depth [m]	Dip direction [°]	Dip angle [°]	Thickness [m]	Comments	Stereoplot
91.9	061	27	0.17	Crushed zone (see Figure 76)	
93.5	166	23	0.08	Crushed zone (see Figure 77)	
94.5	107	52	0.06	Open fracture (see Figure 77)	
111.7	049	27	0.07	Partially crushed zone (see Figure 80)	
112.1	284 (mean) 272 (bottom)	46 (mean) 51 (bottom)	1.12	Crushed zone (see Figure 80 and Figure 86)	
123.3	187 (mean)	39 (mean) 47 (bottom)	0.27	Partially crushed zone (see Figure 83)	



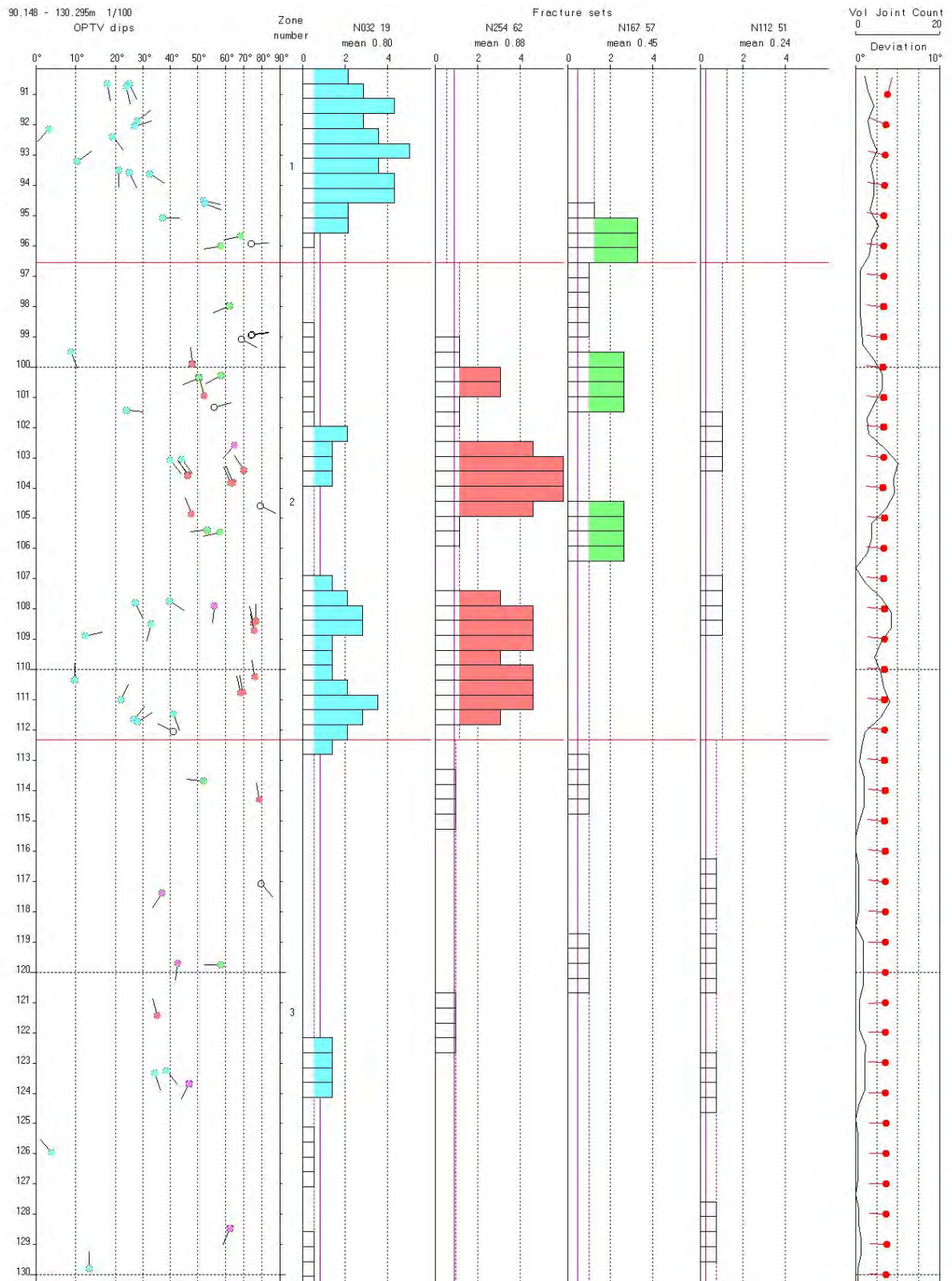


Figure 75. Arrow plots (N up) of the 90 fractures in the c. 89–133 m depth interval, frequency histograms of the four fractures sets as defined by the statistical analysis (see Figure 73). The deviation of the borehole (arrow plot; N up) is shown in the right.

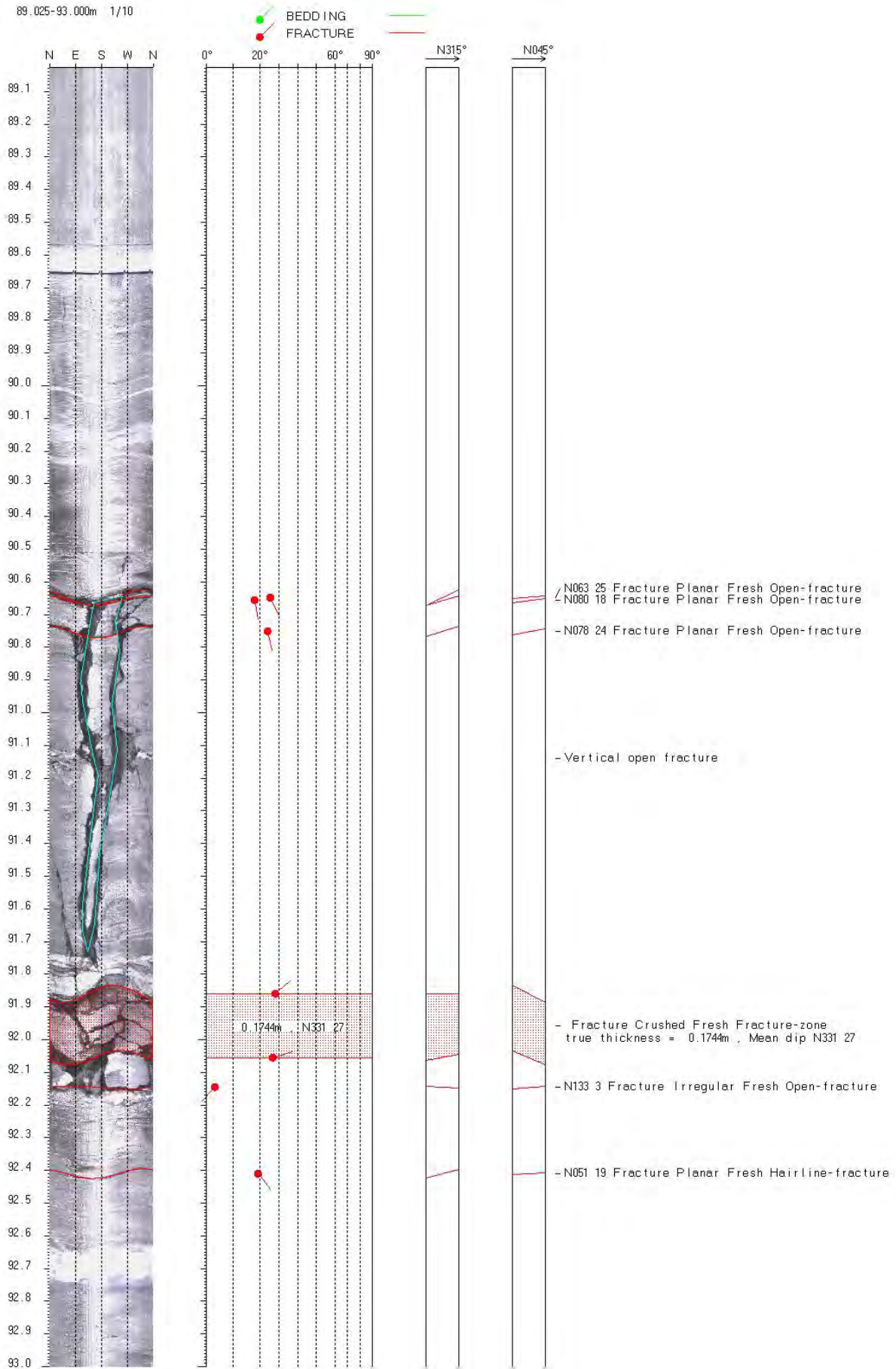


Figure 76. Optical televiwer synthetic images with digitised planar fractures in the 89–93 m depth interval (caption as on Figure 36).

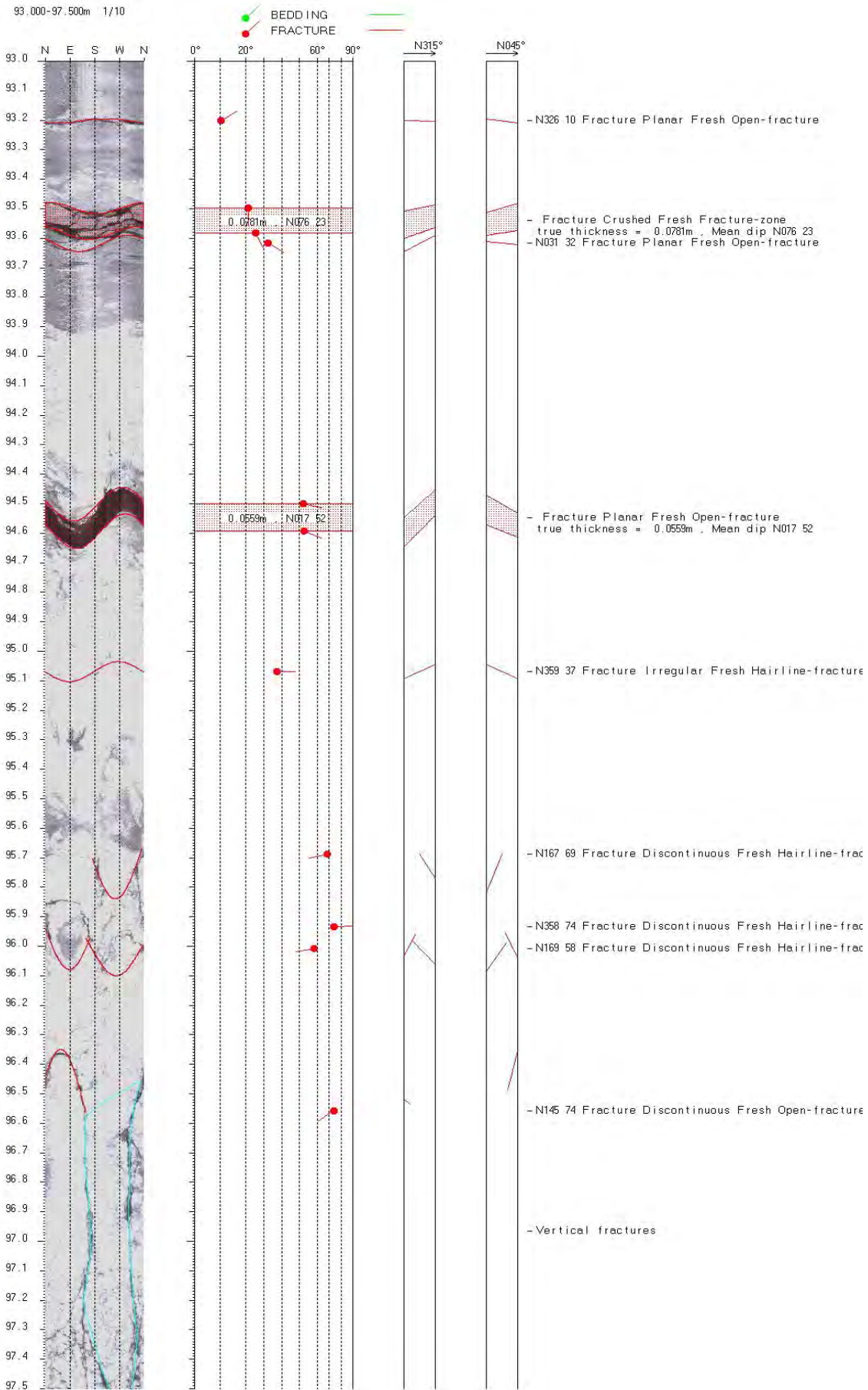


Figure 77. Optical televiwer synthetic images with digitised planar fractures in the 93–97 m depth interval (caption as on Figure 36).

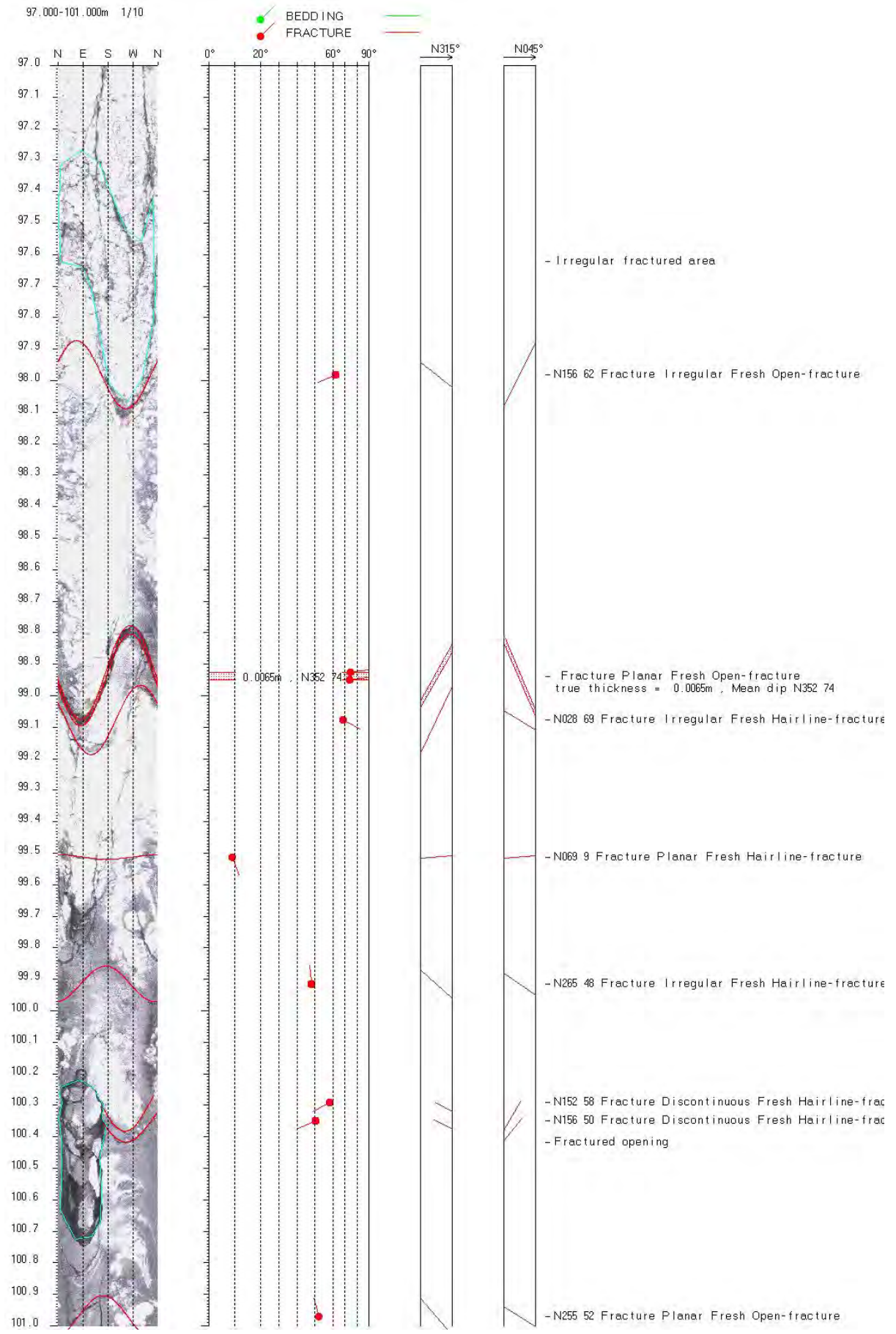


Figure 78. Optical televiwer synthetic images with digitised planar fractures in the 97–101 m depth interval (caption as on Figure 36).

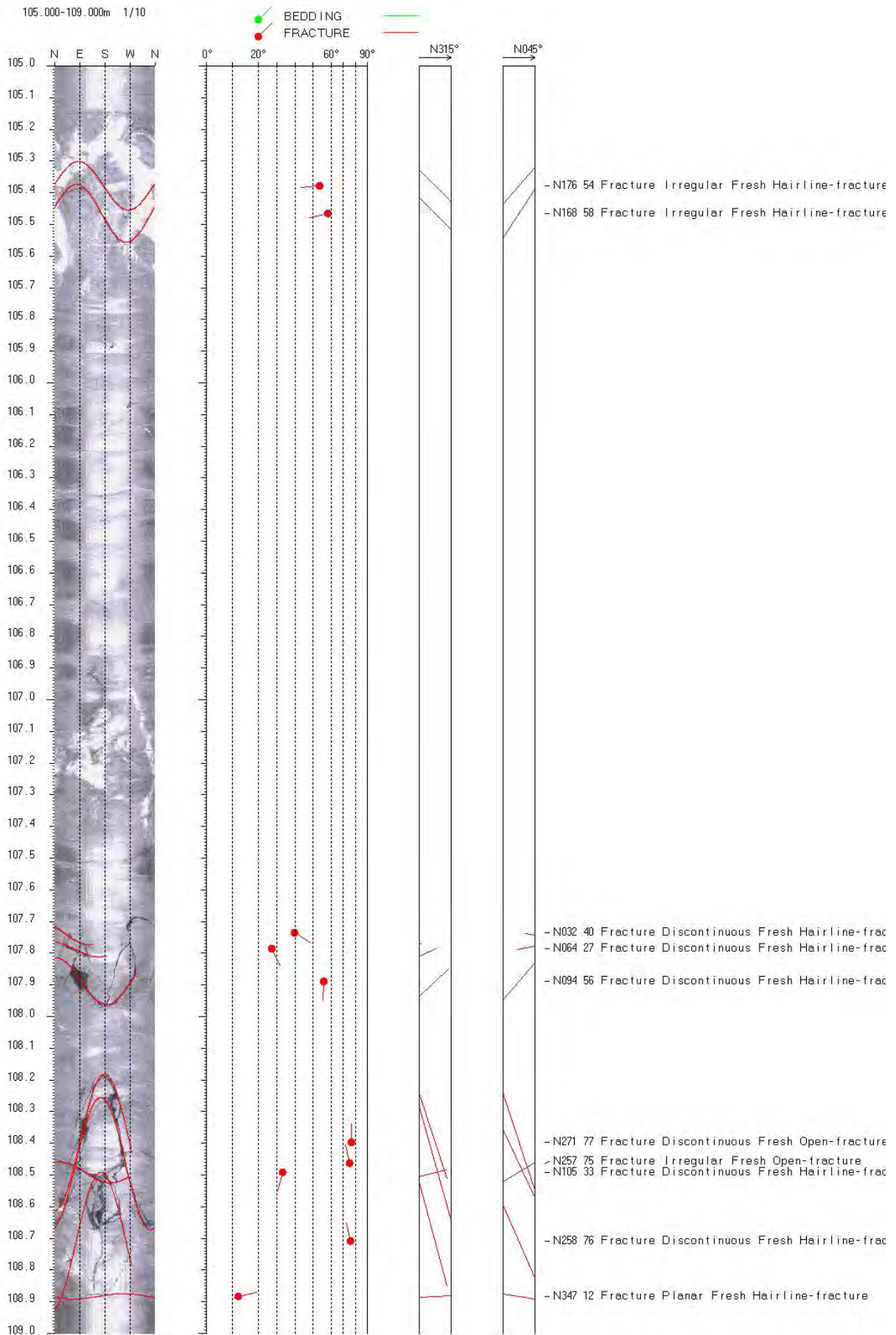


Figure 79. Optical televiewer synthetic images with digitised planar fractures in the 105–109 m depth interval (caption as on Figure 36).

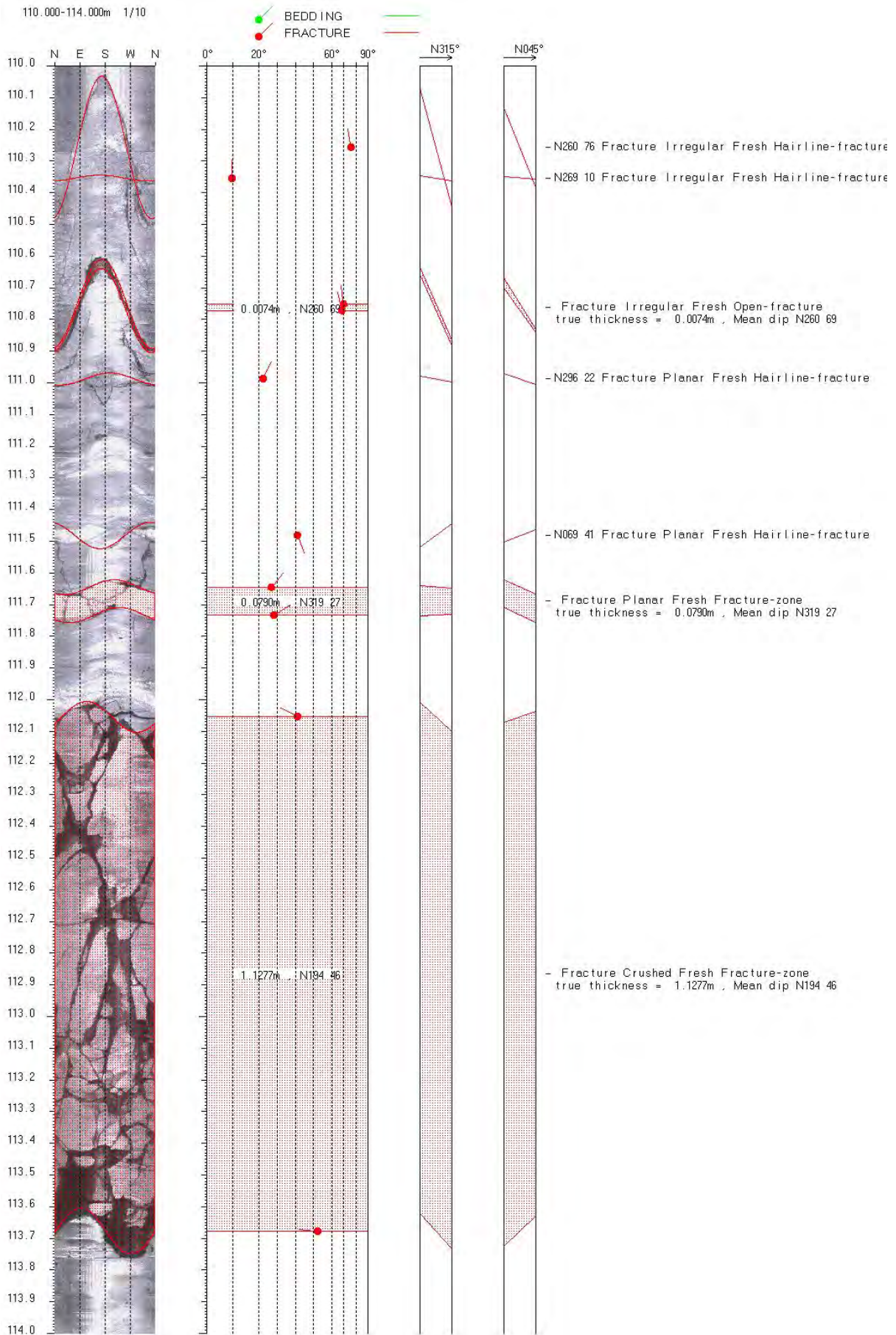


Figure 80. Optical televiwer synthetic images with digitised planar fractures in the 110–114 m depth interval (caption as on Figure 36).

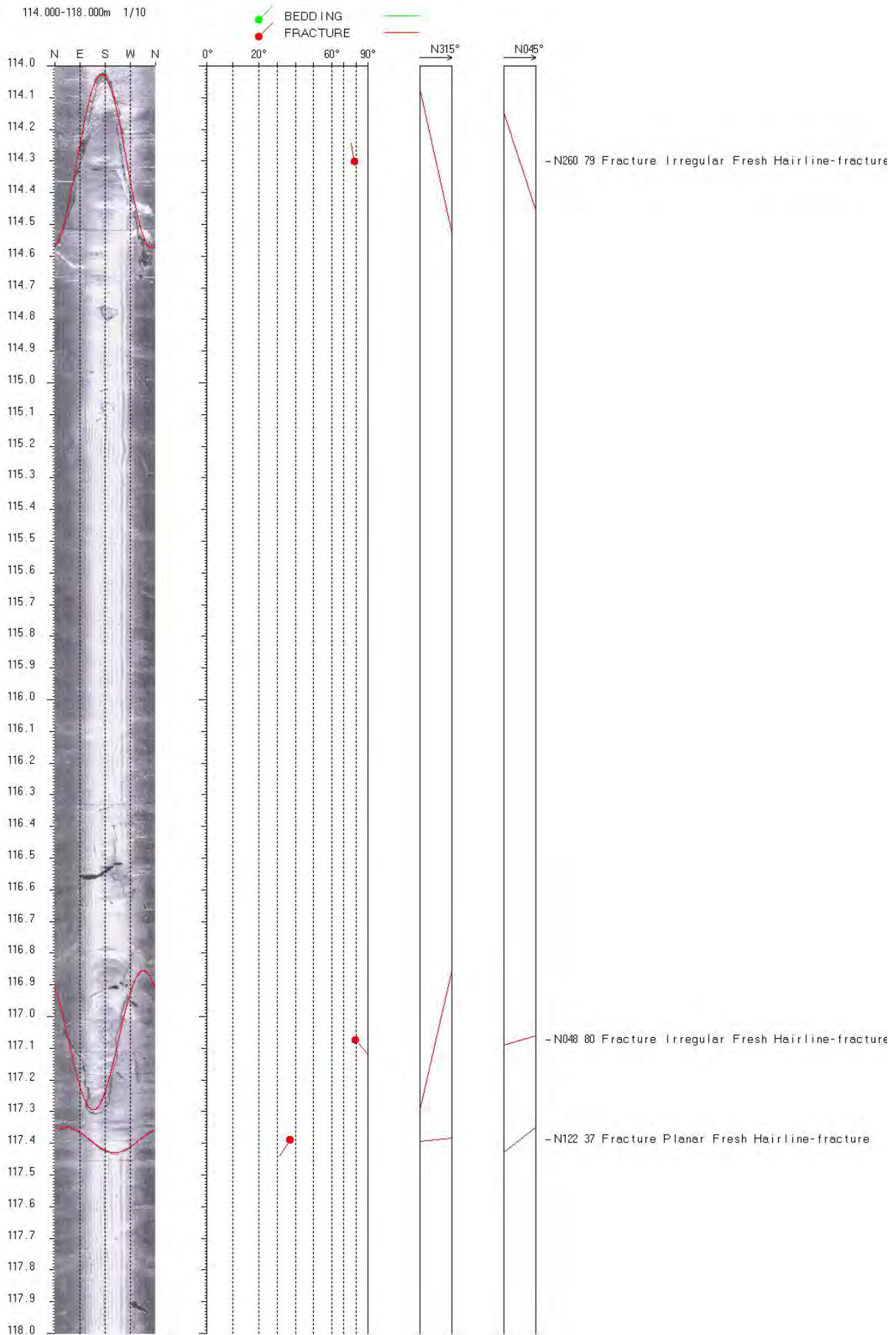


Figure 81. Optical televiewer synthetic images with digitised planar fractures in the 114–118 m depth interval (caption as on Figure 36).

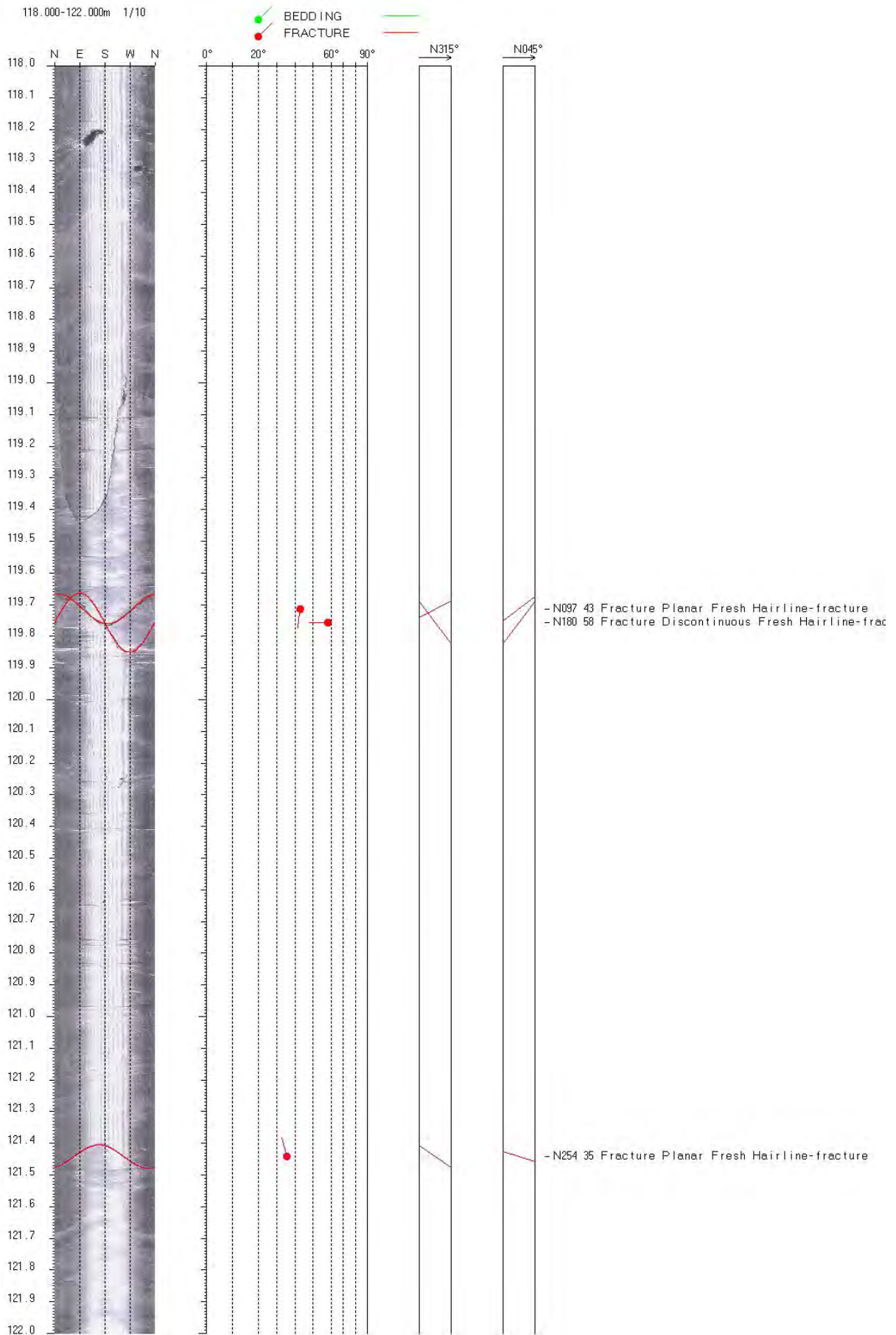


Figure 82. Optical televiewer synthetic images with digitised planar fractures in the 118–122 m depth interval (caption as on Figure 36).

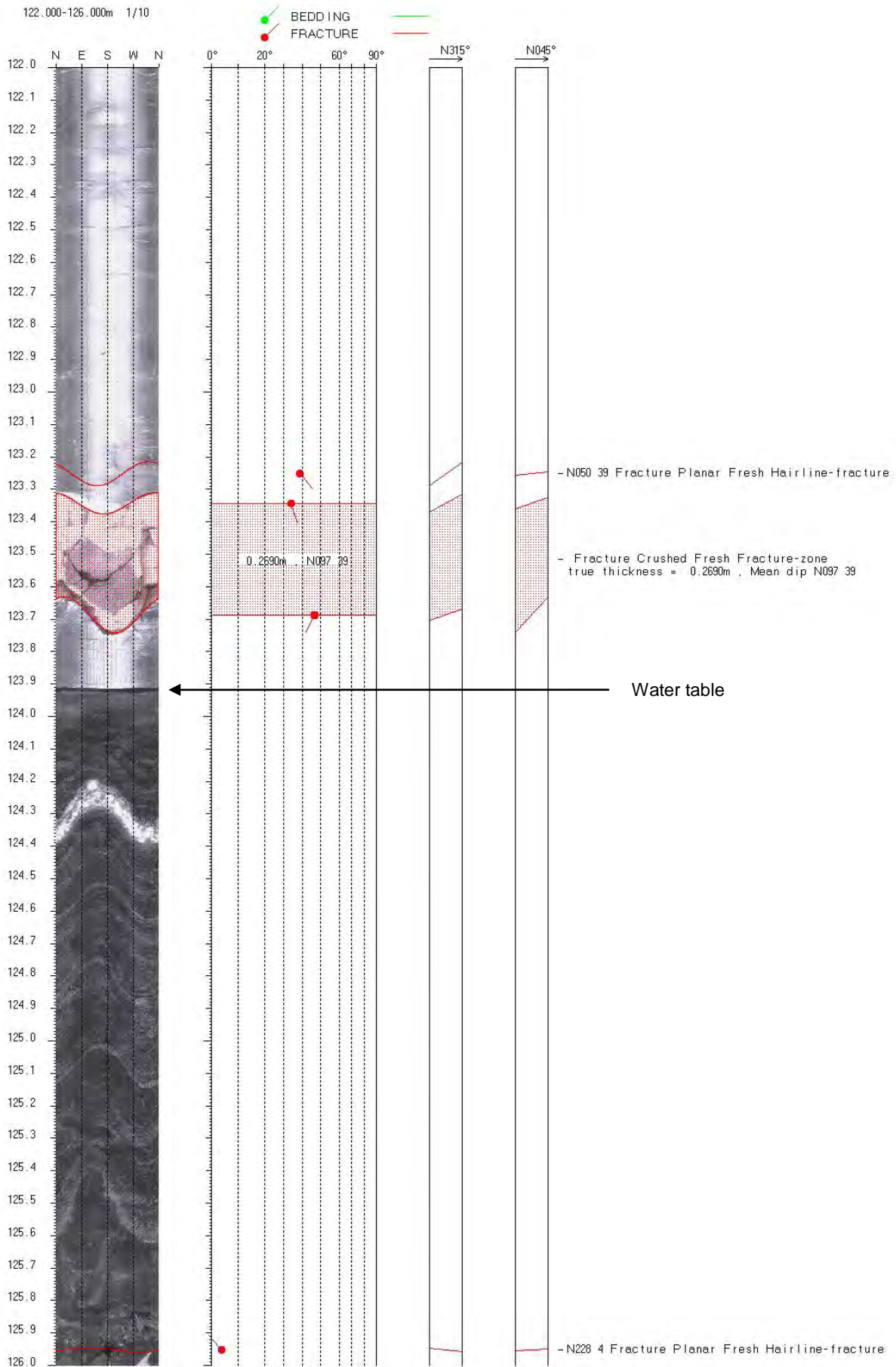


Figure 83. Optical televiewer synthetic images with digitised planar fractures in the 122–126 m depth interval (caption as on Figure 36).

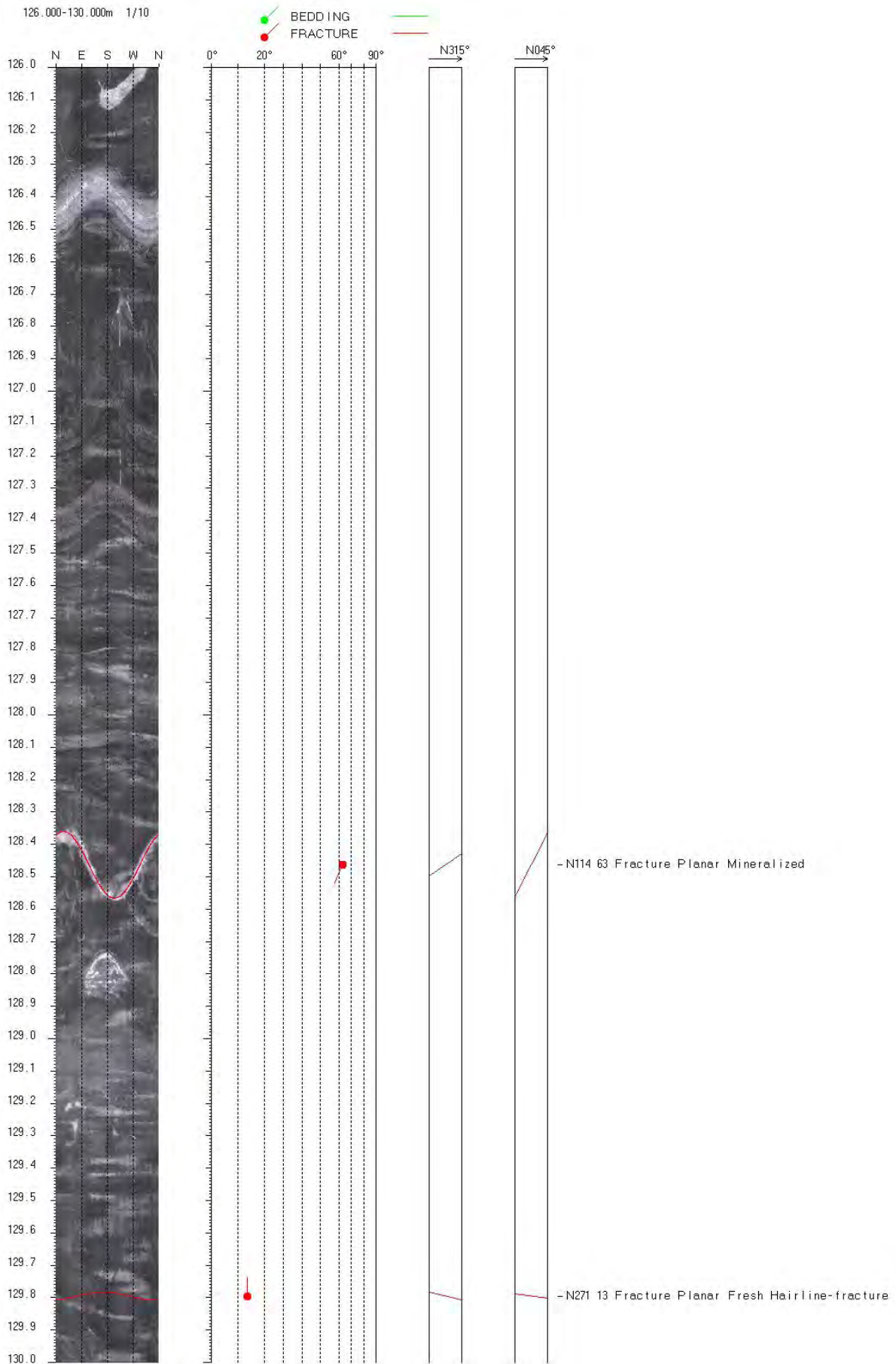


Figure 84. Optical televiewer synthetic images with digitised planar fractures in the 126–130 m depth interval (caption as on Figure 36).

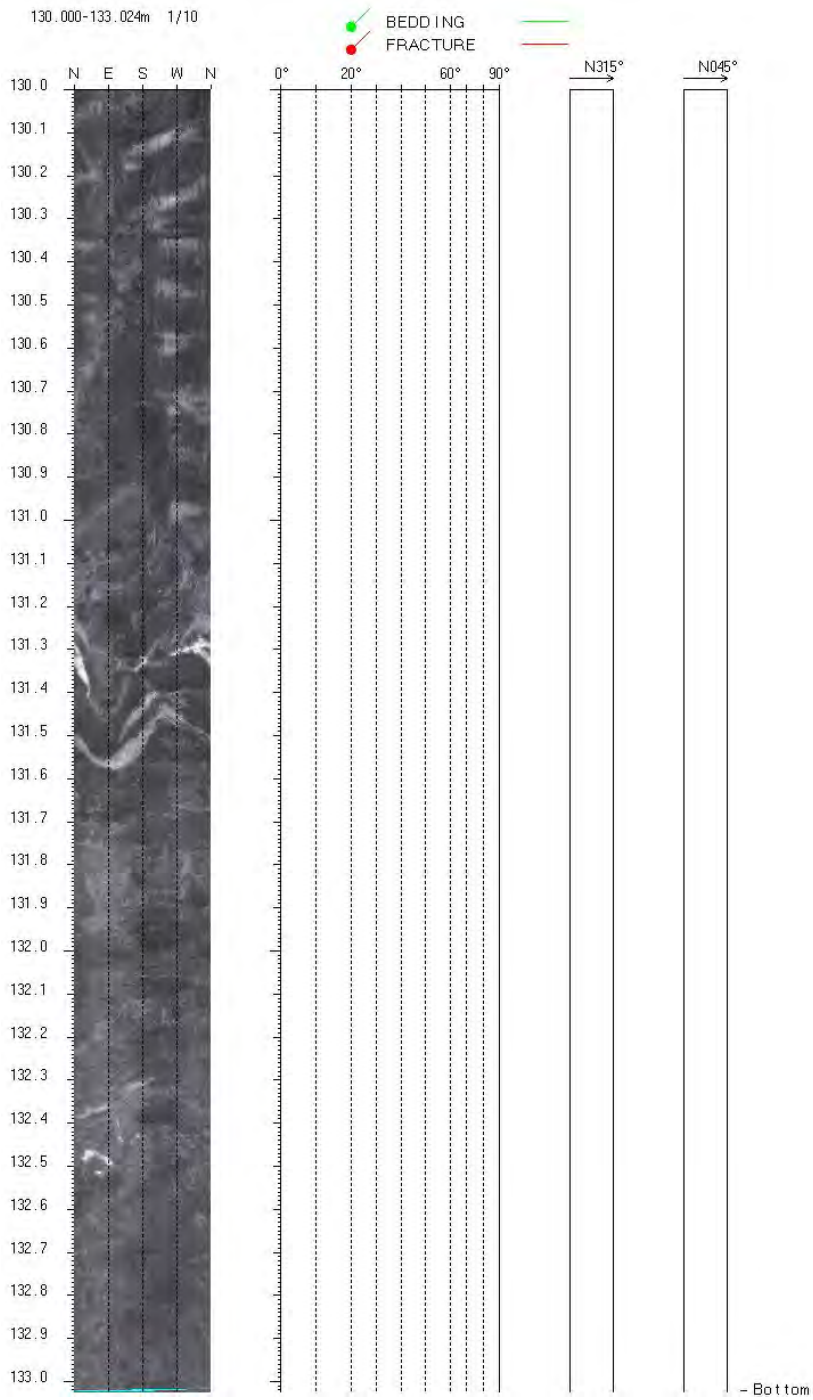


Figure 85. Optical televiewer synthetic images with digitised planar fractures in the 130–133 m depth interval (caption as on Figure 36).

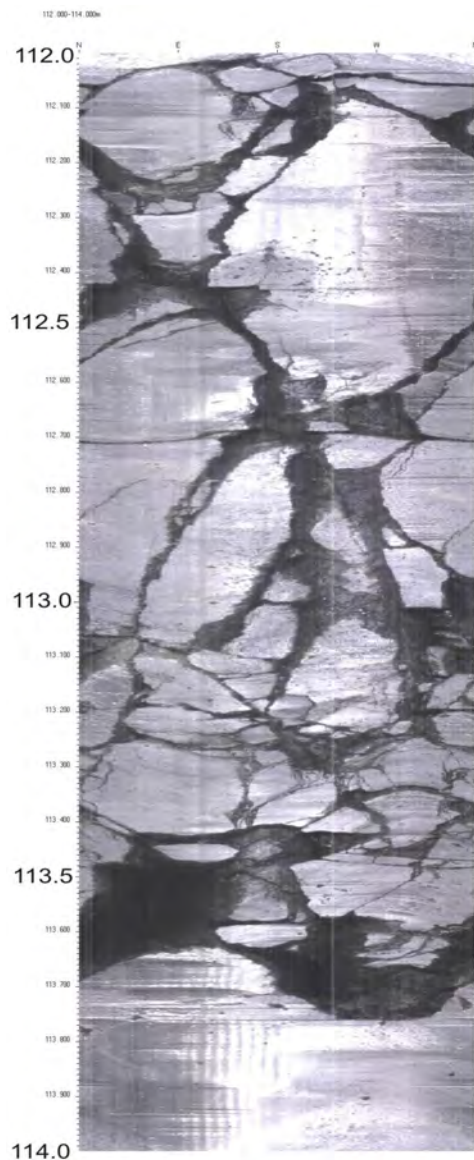


Figure 86. Optical televiewer images showing a crushed zone in the 112–114 m depth interval.

3.3 SUMMARY OF THE ATTITUDE OF THE METAMORPHIC FOLIATION AND FRACTURES ALONG THE ENTIRE BOREHOLE OF MANNEN

The survey of the borehole with the optical televiewer has provided valuable information about foliation directions and angles. The analysis of synthetic log images has also shown that the mountain slope of Mannen is very fractured and crushed with the detection of several cm thick clay-rich shear zones.

The foliation largely varies in the borehole with however a prominent dip direction towards the NNE observed between 15 and 35 m, between 65–70 m and between 110–135 m depth (Figure 87). Foliation dipping to the NW and N are also common. All these trends are compatible with structures along which gravity-induced destabilisation may occur with regards of the slope orientation.

Another important result is that the fractures are commonly found parallel to the foliation (Figure 87, Figure 88 and Figure 89). The foliation-parallel fractures are well represented for example in the 20–30 m (with a dip direction to the NNE) and 50–60 m (with a dip direction to the WNW) depth intervals (Figure 87, Figure 88 and Figure 89).

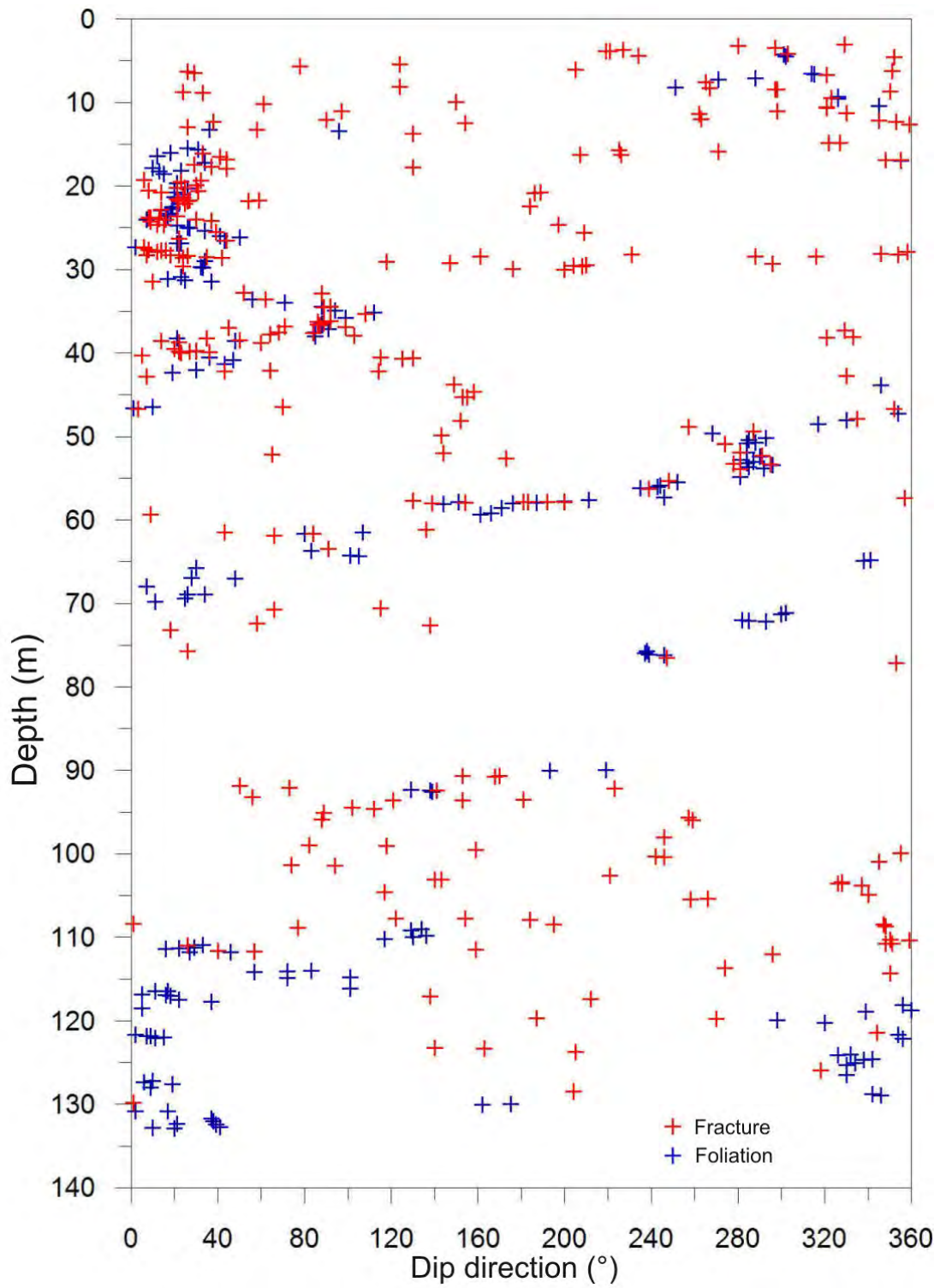


Figure 87. Dip direction of fractures and foliation in function to depth.

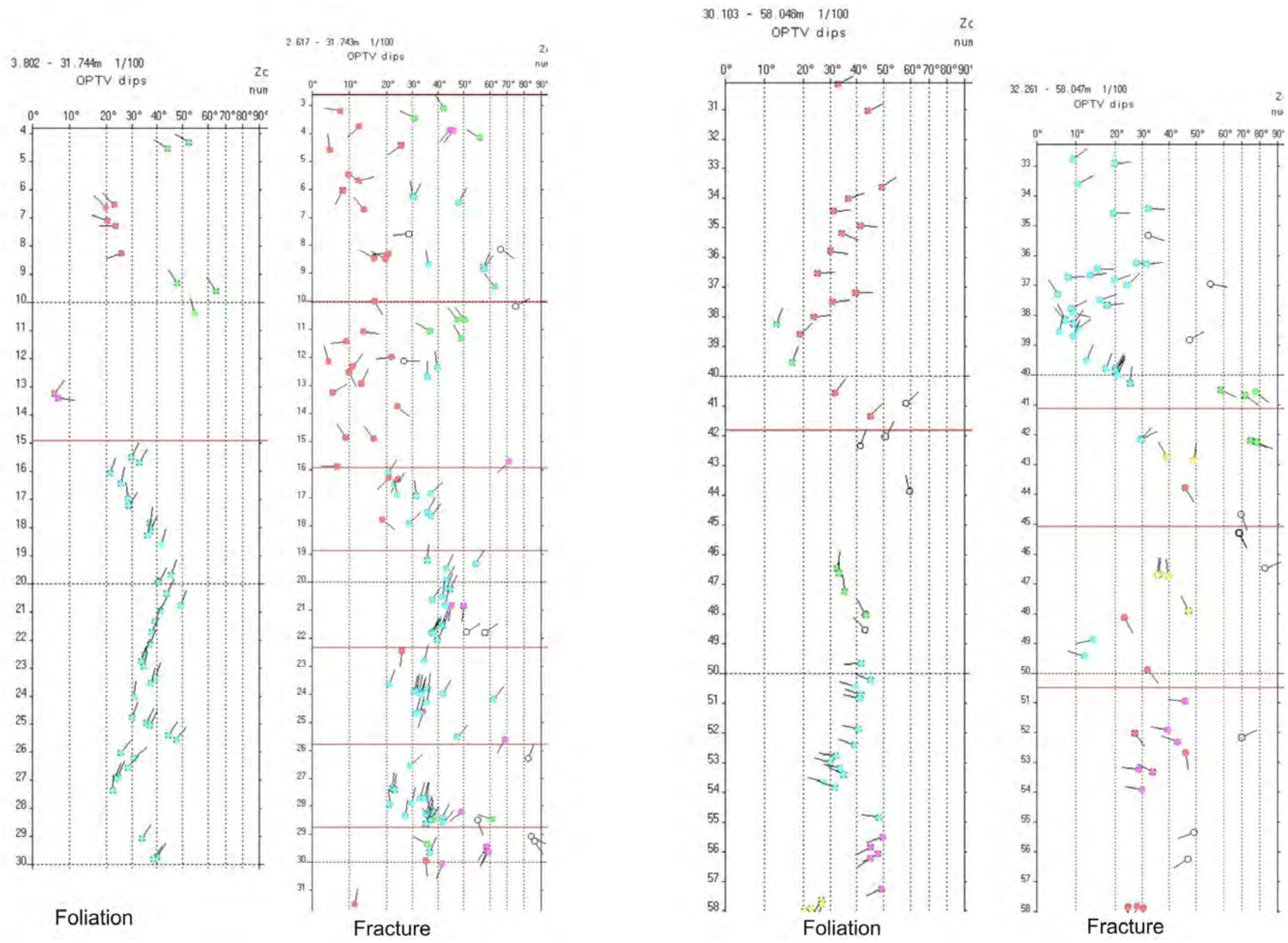


Figure 88. Arrow plots of the foliation and fractures planes in the 4–58 m depth interval.

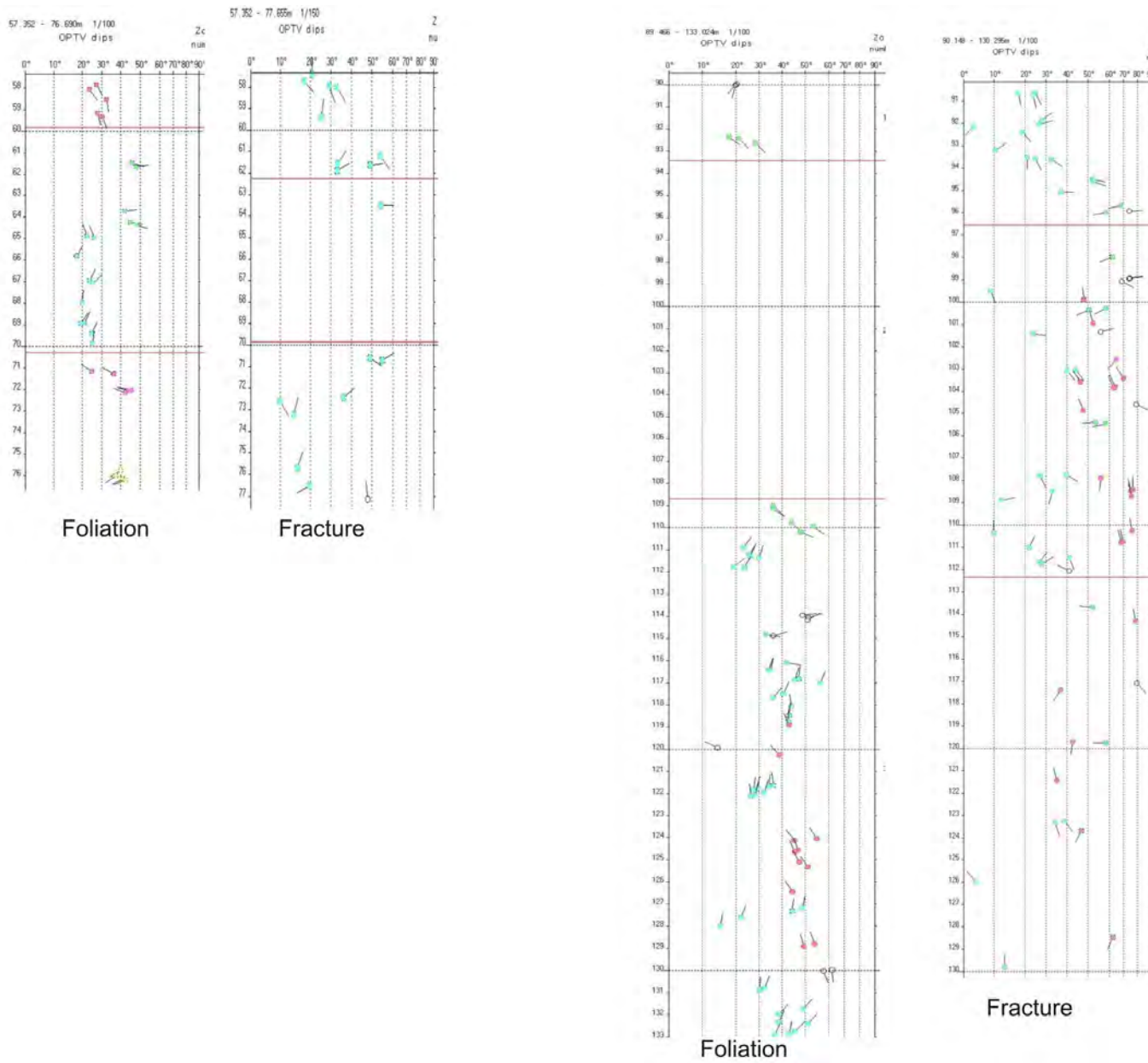


Figure 89. Arrow plots of the foliation and fractures planes in the 58–133 m depth interval.

4. GEOMORPHOLOGIC ANALYSIS OF DIGITAL ELEVATION MODEL AND COMBINAISON WITH DRILL CORE AND BOREHOLE DATA

The 3D view of Mannen instabilities built on the 1 m resolution DEM allows defining the limits of the instabilities and three scenarios are postulated (Figure 90). The orientations of quasi-planar surfaces observed on the rock slope are extracted from the slope gradient and slope direction, which were derived from the 1 m resolution DEM.

Scenario A (Figure 90a,b) comprises the uppermost part of the unstable slope (including the drilling site) and has an estimated volume of 2–3.5 Mm³. Based on the DEM analysis of surface outcrops of possible basal sliding surfaces (Figure 90c), a wedge failure mechanism is inferred for scenario A (Farsund et al. 2011). At the northern limit of scenario A a surface marked by frequent rockfalls satisfies the geometry of a sliding surface (dip direction/dip angle: 102°/41°; Figure 90b,c; Saintot et al. 2011). This quasi-planar surface may intersect the borehole at one of the severely damaged rock intervals from c. 60 to 80 m depth (see Table 2). The southern limit of scenario A corresponds to the cliff dipping 59° towards 017° (Figure 90b,c; Dahle et al., 2010). The intersection of the two planes, i.e. the direction of wedge failure, perfectly fits with the displacement vector determined by the dGPS measurement (Figure 90c; Dahle et al., 2010). The three-dimensional continuity of this wedge remains however open. The presence of folds observed at the surface and in the borehole makes the geometry of fractures more complicated.

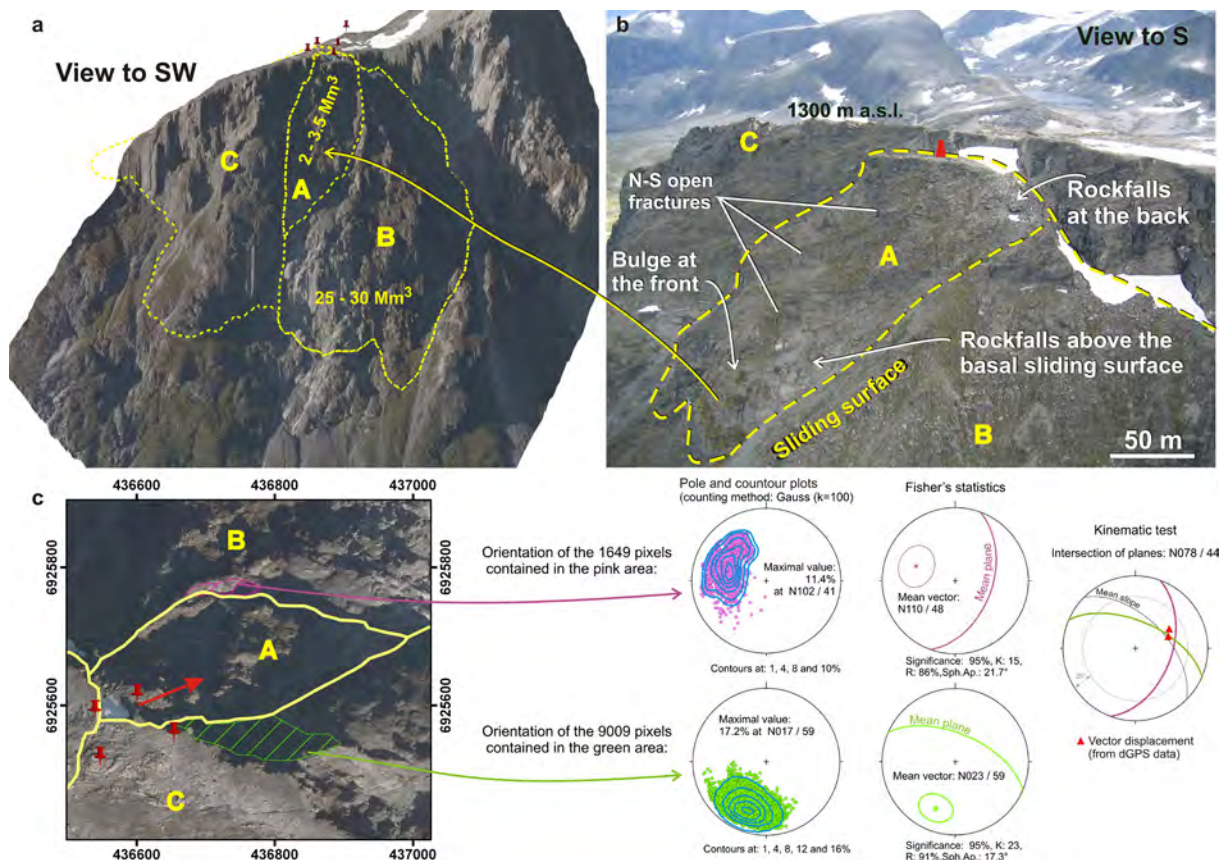


Figure 90. (a), Aerial photograph draped on a meter-scale resolution DEM of the Mannen rock slope with the inferred limits of scenarios A, B and C (yellow lines); red pins mark the location of the dGPS antennas. (b), Photograph from helicopter of the unstable rock slope of Mannen (scenario A) with an important set of N–S trending opened fractures, a bulge at the front and a sliding surface underlined by rockfall events. The red cone is the location of the drilling site on the top of the unstable slope. (c), determination of a wedge failure on two outcropping surfaces at the limits of scenario A. Note the good fit between the wedge intersection line and the displacement vector obtained from dGPS measurements (the red arrow on the map indicates the direction of the vector displacement).

Scenario B includes scenario A and represents a deformed maximum volume of 25–30 Mm^3 and is considered to be less active (Figure 90; Dahle et al., 2010). Its upper limits coincide with the ones of the 2–3.5 Mm^3 block, but its basal limits are not obvious and its kinematics are not fully understood.

The total volume (scenario C, including scenarios A and B) affected by gravity-induced deformation far inward the plateau may reach 80–100 Mm^3 (Figure 90). The basal limits are not clearly visible at the surface and this scenario C is expected to be inactive (Dahle et al., 2010).

5. MAP OF DISPLACEMENT BY TERRESTRIAL LASER SCAN ANALYSIS

5.1 METHODOLOGY

Terrestrial laser scanning (TLS) is based on the reflectorless and contactless acquisition of a point cloud of the topography using the time-of-flight distance measurement of an infrared laser pulse. The Optech ILRIS-3D used for this study has a wavelength of 1500 nm and a range in practice of about 800 to 1200 m on rock slopes, depending on the reflectivity of the object. See Oppikofer et al. (2009) for a detailed description of the instrument.

The high-resolution point clouds of the topography provided by TLS can be used for the structural analysis of rock slopes and for displacement measurements using sequential (multi-temporal) TLS data. The detailed methodology is described by Oppikofer et al. (2009) and includes several steps:

1. Co-registration (alignment) of individual scans of the same epoch
2. Co-registration of sequential TLS scans using only the (supposed) stable area, i.e. the surroundings of the rock slope instability
3. Georeferencing of the entire dataset using the high-resolution DEM obtained from aerial laser scanning (ALS)
4. Structural analysis by plane-fitting on the point cloud or using Coltop3D software (Jaboyedoff et al., 2007)
5. Construction of basal failure surface and volume computation (see Oppikofer, 2009 for details)
6. Shortest distance comparison between sequential scans for the visualisation and a preliminary quantification of displacements
7. Division of the moving area in individual blocks based on the morphology and/or different displacement velocities observed on the shortest distance comparison
8. Detailed displacement analysis of these blocks using the roto-translation matrix technique

The TLS data treatment in this report focused on steps 1–3 and 6–8. The structural analysis and the construction of basal failure surfaces and volume computations will be included in a future report.

5.1.1 TLS data acquisition

The analysis of structures and displacements of the Mannen rock slope uses two TLS datasets acquired on 25 August 2008 and 1 July 2010 (1.85 years interval). Due to limited site accessibility the TLS point clouds cover only the uppermost part of the unstable rock slope, which correspond to the top of scenario A presented in Chapter 4 (Figure 91, Figure 92). The lower part can neither be scanned from stable positions on the top (no direct line-of-sight) nor from the valley bottom (range limitation). For technical and meteorological reasons the 2008 point cloud covers only parts of the upper moving block (Figure 91a).

The 2008 point cloud has 3.6 million points in total with a mean resolution (point spacing) of 3.8 cm (at a mean distance of 87 m). In June 2010 the uppermost part of Mannen was scanned again from the same viewpoint as in 2008 (Figure 91b) and from a second location above the stable cliff in the NW (Figure 91c, d). The 2010 dataset is composed of 5.1 million points and has a mean resolution of 4.4 cm (at a distance of 125 m).

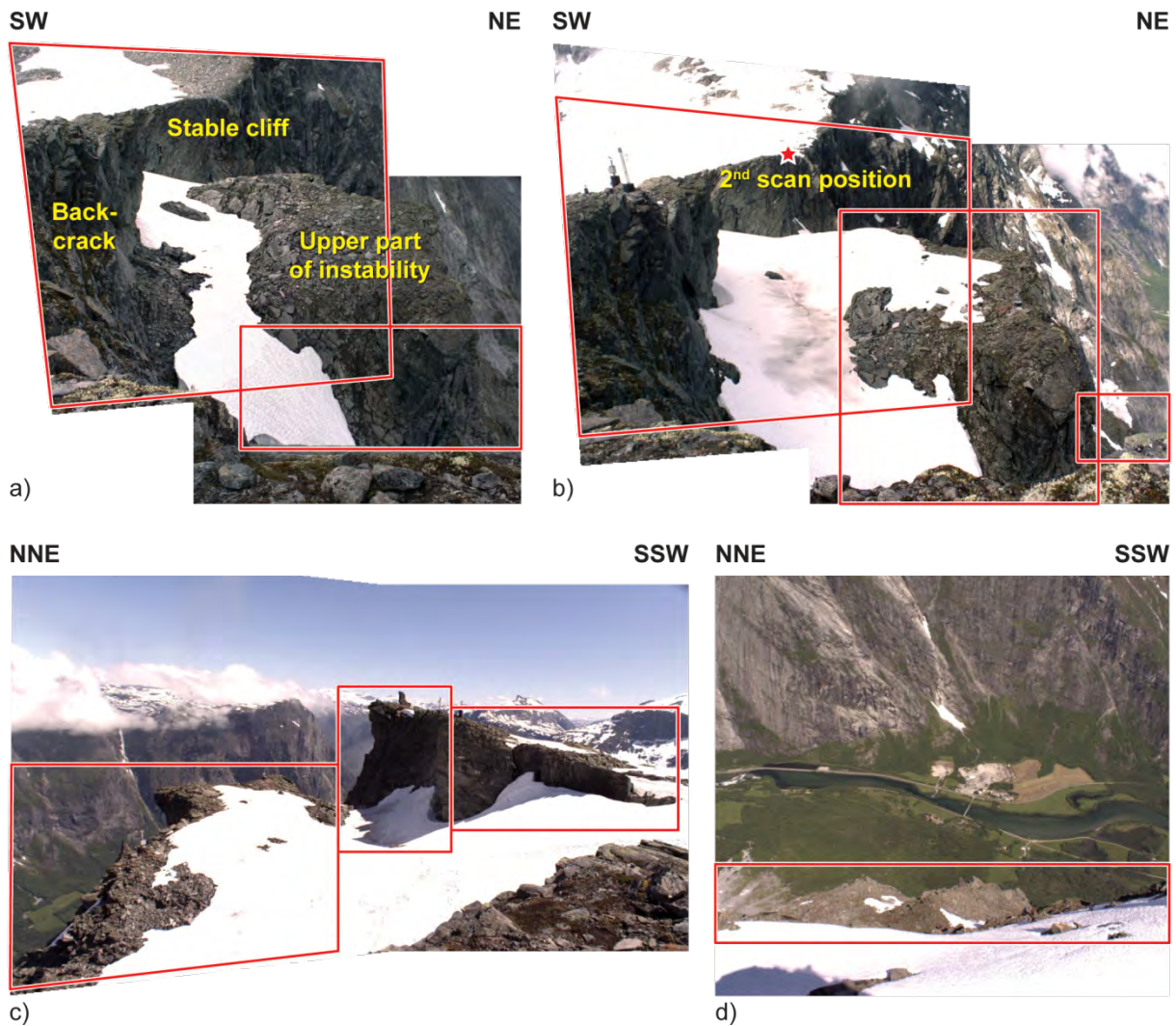


Figure 91: Pictures of the scan extents in a) August 2008 from viewpoint A; b) June 2010 from viewpoint A; c) and d) June 2010 from viewpoint B.

5.1.2 Error assessment

In order to assess the accuracy of the roto-translation matrix technique (step 7) with the given datasets, the stable cliff in the W, which does not show displacements between 2008 and 2010, was divided into 5 areas that served as reference blocks.

For each of the 5 stable reference blocks the computed displacement vectors and rotational angles should be equal to 0. The difference between the computed and theoretical values gives an estimate of the accuracy of the roto-translation matrix technique. For the TLS datasets acquired at Mannen, the accuracy of the translation length varies between 0.24 and 0.60 cm with an average of 0.43 cm (Table 8). The error on rotational components ranges from 0.005° to 0.029° with a mean error of 0.018° for the toppling angle and from 0.002° to 0.017° with an average of 0.011° for the tilt angle (Table 8).

These accuracies are similar to values obtained by Oppikofer et al. (2009) for the Åknes rockslide. The accuracy of the translation length is even better, probably due to the higher point density at Mannen (approx. 4 cm) compared to Åknes (approx. 8–10 cm).

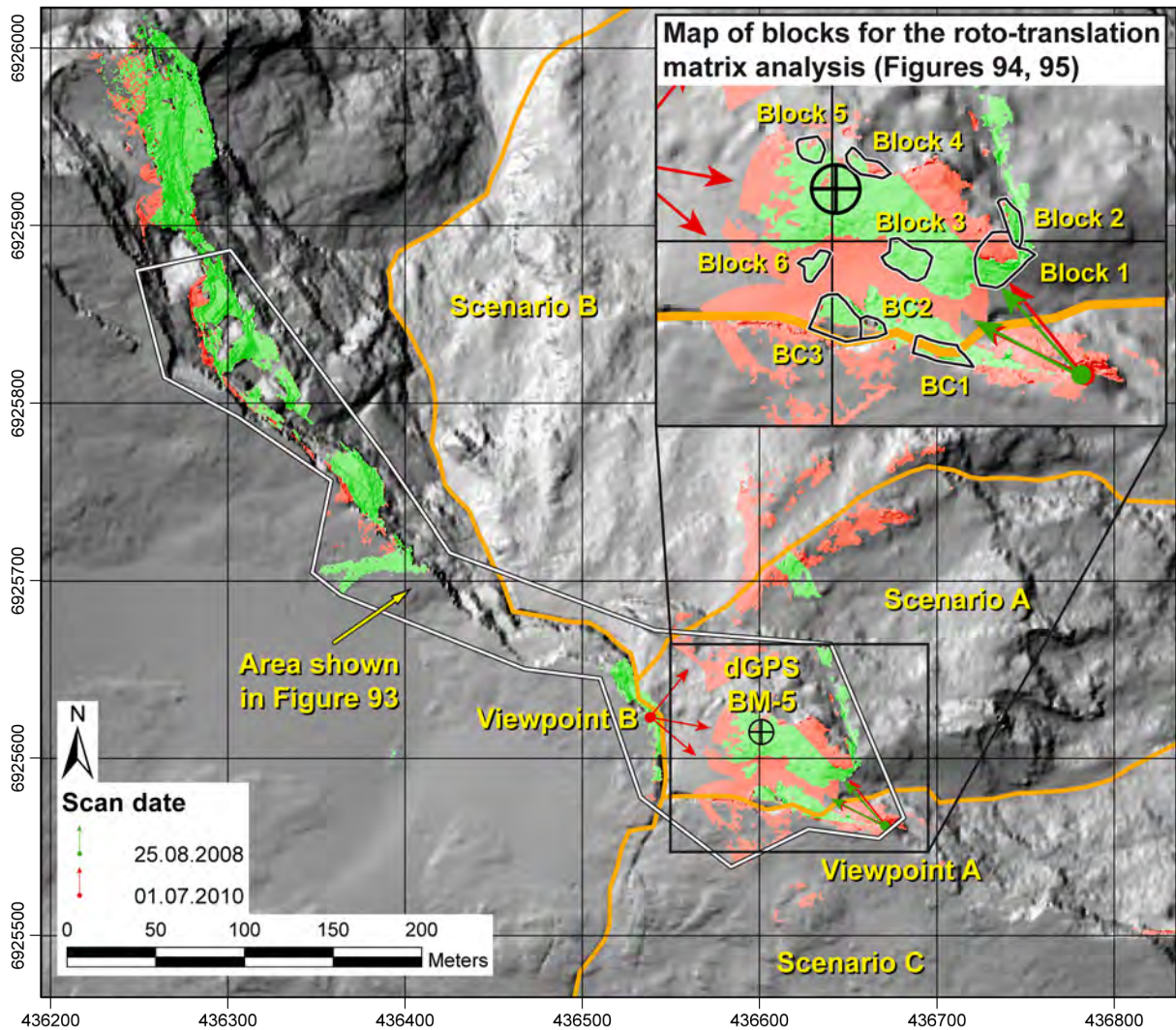


Figure 92: Hillshade maps of 25 cm cell size DEMs created on the TLS point clouds from 2008 (in green) and 2010 (in red). The scan positions and directions are shown. The inset shows a map of the blocks used for the roto-translation matrix technique.

Table 8: Accuracy assessment of the roto-translation matrix technique for 5 stable reference blocks at Mannen.

Block	Years	Translation			Toppling		Tilt
		Length [cm]	Azimuth [°]	Dip [°]	Azimuth [°]	Angle [°]	Angle [°]
Reference 1	2008–2010	0.28	152.9	-16.7	221.1	0.010	0.002
Reference 2	2008–2010	0.24	93.9	65.0	215.1	0.026	0.006
Reference 3	2008–2010	0.59	47.1	-75.6	216.2	0.021	0.016
Reference 4	2008–2010	0.60	214.5	-40.8	207.9	0.029	0.016
Reference 5	2008–2010	0.42	213.4	31.5	268.7	0.005	0.017
Average accuracy		0.43	-	-	-	0.018	0.011
Maximum error		0.60	-	-	-	0.029	0.017

5.2 TLS DISPLACEMENT ANALYSIS

5.2.1 Shortest distance comparison

The shortest distance comparison image between the 2008 and 2010 dataset reveals significant displacements of the uppermost part of the unstable rock slope and of several blocks along the back-crack (up to 25 cm in two years), as well as significant rockfalls (Figure 93). The vertical cliffs in the west of the instability were used as reference for the alignment of the sequential scans and for the shortest distance comparison. Figure 93 reveals that these cliffs are indeed stable, since there are no differential movements over the entire cliff.

The detailed comparison image shows sliding and subsidence by up to 12 cm between 2008 and 2010 (Figure 94). Blocks 1 and 2 slide towards the SSE (Figure 94a), while blocks 3–5 appear essentially to subside. Subsidence of block 3 and other loose blocks in the opened graben is likely to fill voids opened by the downslope sliding of the rock slope (Figure 94a). The apparent subsidence movement of blocks 4 and 5 is probably also related to sliding along a steeply inclined sliding surface (Figure 94b).

The shortest distance comparison of the blocks along the back-crack (Figure 95) shows high displacement rates for two columns that are detached from the stable rock mass behind and that are free to move. These columns are moving by up to 15 cm towards the ENE. The top of the middle column (BC2b) is even moving by up to 25 cm. Block BC1 with the webcam and one of the laser distance meters shows little to no significant displacements on the shortest distance comparison.

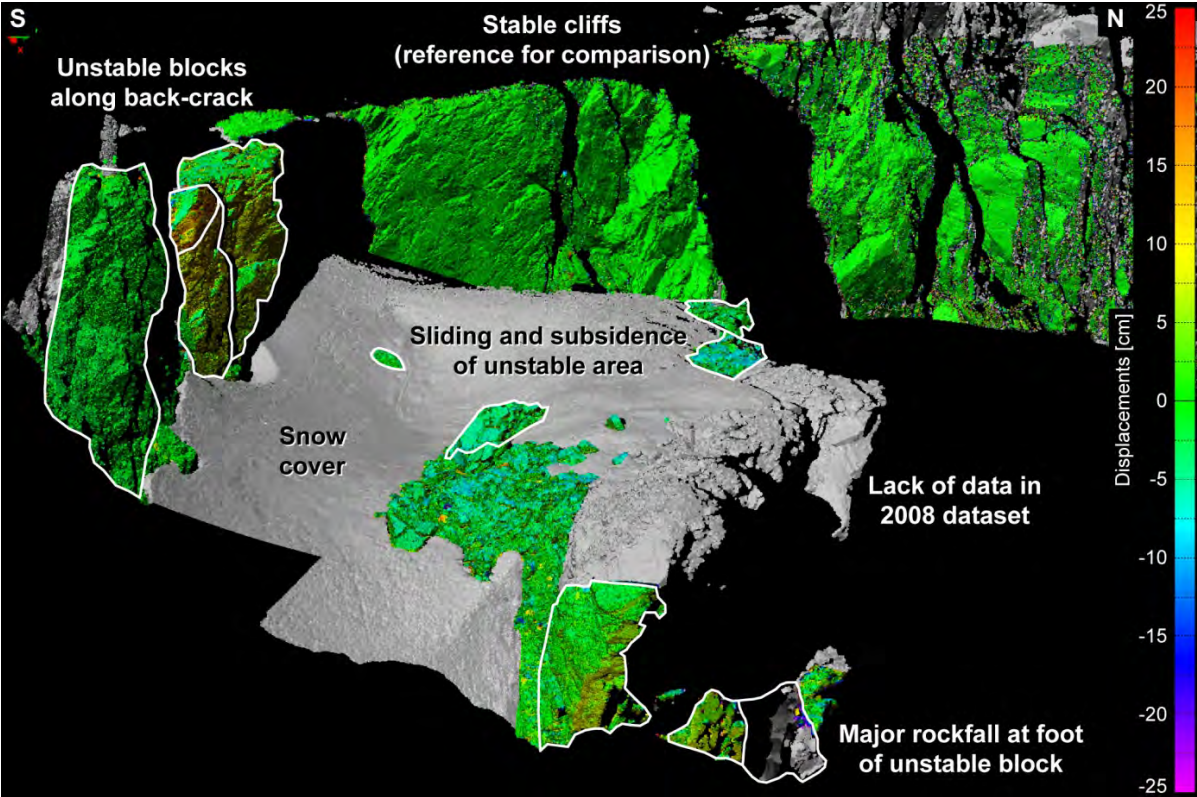


Figure 93: Shortest distance comparison between the 2008 and 2010 TLS point clouds (view to the W). Positive differences up to +25 cm are shown in yellow to red colours and negative differences up to -25 cm in blue to violet colours. The 6 compartments on the instability and 4 blocks along the back-crack used for the detailed displacement analysis using the roto-translation matrix technique are outlined. A major rockfall occurred at the foot of the investigated area. Snow covered areas in 2010 and areas not covered by the 2008 dataset were excluded from the shortest distance comparison (grey areas).

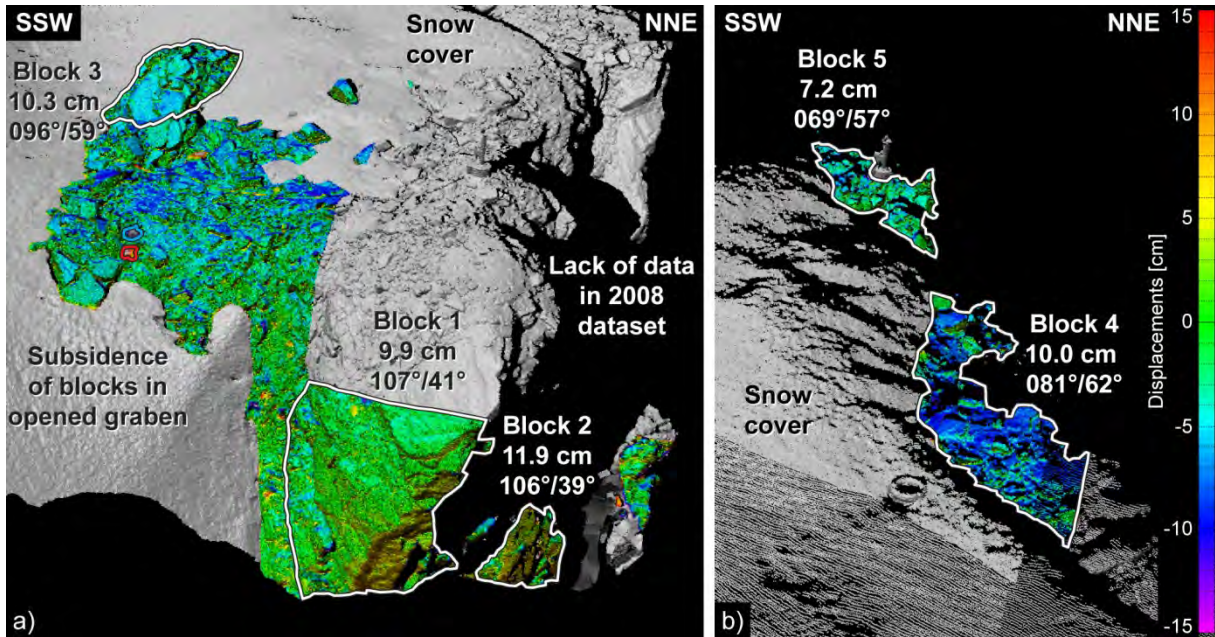


Figure 94: Shortest distance comparison of the Mannen instability (view to the WNW): a) eastern part with blocks 1 and 2 sliding towards the SSE by -10 cm and block 3 and loose blocks in the graben essentially showing subsidence by 5–12 cm; b) western part with blocks 4 and 5 that also move downward by 5–10 cm. The computed translation vectors of each block are indicated by the displacement length and the trend and plunge of the vector orientation.

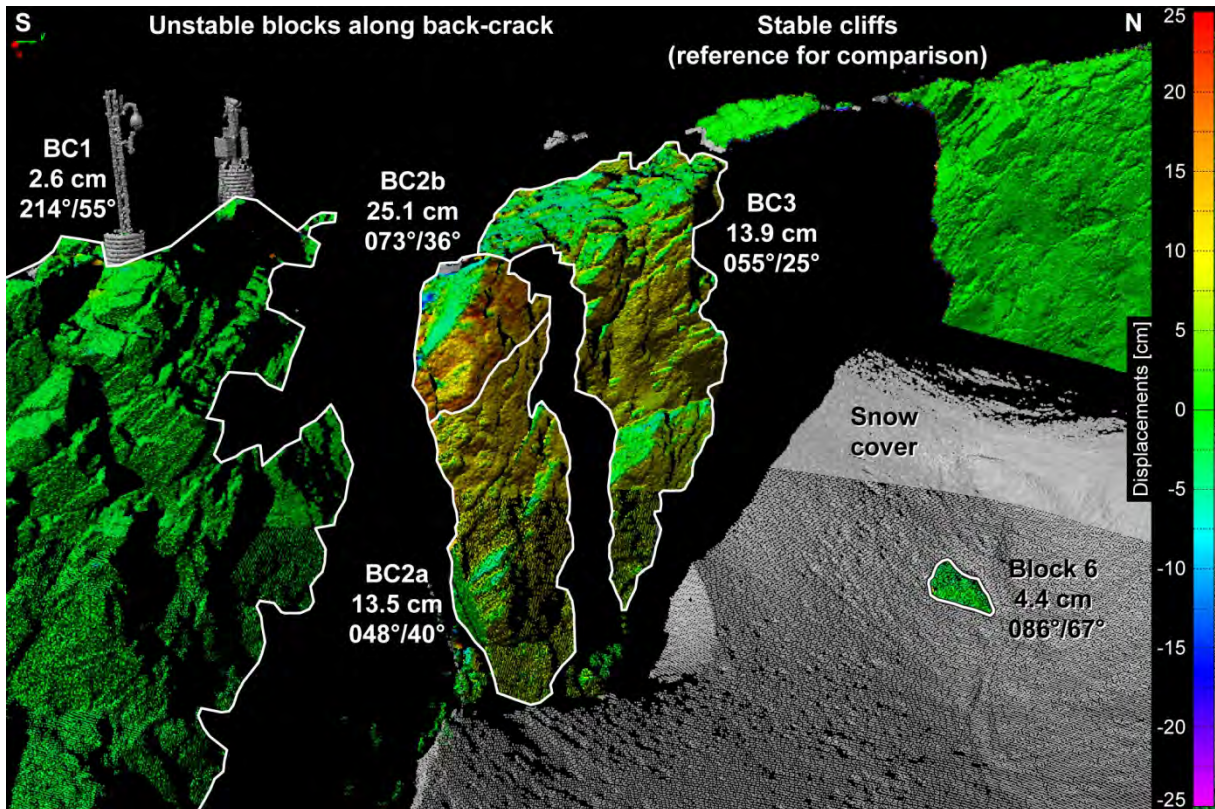


Figure 95: Shortest distance comparison for the 4 blocks along the back-crack (view to the W). The three columns are detached from the stable rock mass behind. The middle column can be divided into two parts BC2a and BC2b with high displacement rates (25 cm) for the latter.

5.2.2 Roto-translation matrix analysis

The uppermost part of the unstable rock slope (top of scenario A) was divided into five blocks based on the morphology and differential displacements. A sixth block is situated in the graben (surrounded by snow in 2010) and displays less displacement between 2008 and 2010 than the other blocks. Four blocks along the back-crack were also delimited based on the shortest distance comparison. The translational and rotational components of the displacements between August 2008 and June 2010 at Mannen are summarized in Table 9.

5.2.2.1 Uppermost part of the Mannen instability

Translation vectors on the instability blocks (blocks 1–5) have a relatively constant trend and plunge (average of blocks between 2008 and 2010: $094^{\circ}/52^{\circ} \pm 16^{\circ}$) with only little variations between the different blocks (trend: $[069^{\circ}; 107^{\circ}]$; plunge: $[39^{\circ}; 62^{\circ}]$; error on trend and plunge: $[2^{\circ}; 3^{\circ}]$). The translation lengths between August 2008 and June 2010 range from 7.2 cm (3.9 cm/year) to 11.9 cm (6.4 cm/year) with an average length of 9.9 cm (5.3 cm/year) (Table 9). These displacements are similar to differential GPS measurements for the 2008–2010 period reported by Eiken (2010): 7.9 cm towards $071^{\circ}/56^{\circ}$.

The detailed three-dimensional displacement analysis also reveals some rotational movements of the blocks. These movements can be interpreted as toppling movement (Oppikofer et al., 2009). All of the measured toppling angles on the uppermost part of the Mannen instability are significant with toppling angles varying between 0.033° ($0.018^{\circ}/\text{year}$) and 0.204° ($0.110^{\circ}/\text{year}$) and toppling directions ranging from 304°N to 096°N (Table 9). Three distinct toppling behaviours can be identified. Blocks 1 and 2 rotate backwards towards the graben (mean: 0.195° towards $305^{\circ}\text{N} \pm 5^{\circ}$), i.e. in the direction opposite to the translation direction; blocks 3 and 5 topple in the sliding direction (mean: 0.071° towards $085^{\circ}\text{N} \pm 15^{\circ}$); and block 4 is essentially subsiding with little toppling towards the North (0.033° towards $007^{\circ}\text{N} \pm 32^{\circ}$) (Table 9). The measured tilt angles, i.e. the clockwise or counter-clockwise rotation around a vertical axis, are often not significant and their interpretation in terms of landslide displacement or landslide mechanism remains open (Table 9).

The toppling movements measured on the frontal blocks on the top of scenario A may not be representative for the deep-seated sliding displacements of the unstable rock slope. The toppling movements are more likely related to local accommodation of deformation of individual blocks forming the unstable rock slope.

Table 9: Displacement analysis of the Mannen instability using the roto-translation matrix technique for 4 unstable blocks along the back-crack and 6 compartments in the uppermost part of the unstable area. Grey-shaded values are not significant given the mean errors measured on the stable reference compartments (Table 8). Errors on the translation orientation and the toppling azimuth depend on the translation length and toppling angle, respectively.

Block	Years	Translation		Toppling		Tilt
		Length [cm]	Trend/plunge	Azimuth	Angle [$^{\circ}$]	Angle [$^{\circ}$]
BC1	2008–2010	2.56	$214^{\circ}/55^{\circ} \pm 10^{\circ}$	$076^{\circ}\text{N} \pm 65^{\circ}$	0.017	-0.023
BC2a	2008–2010	13.53	$048^{\circ}/40^{\circ} \pm 02^{\circ}$	$064^{\circ}\text{N} \pm 02^{\circ}$	0.451	-0.282
BC2b	2008–2010	25.05	$073^{\circ}/36^{\circ} \pm 01^{\circ}$	$072^{\circ}\text{N} \pm 05^{\circ}$	0.194	-0.429
BC3	2008–2010	13.85	$055^{\circ}/25^{\circ} \pm 02^{\circ}$	$062^{\circ}\text{N} \pm 03^{\circ}$	0.310	0.110
Block 1	2008–2010	9.90	$107^{\circ}/41^{\circ} \pm 02^{\circ}$	$304^{\circ}\text{N} \pm 05^{\circ}$	0.204	-0.011
Block 2	2008–2010	11.89	$106^{\circ}/39^{\circ} \pm 02^{\circ}$	$306^{\circ}\text{N} \pm 06^{\circ}$	0.186	-0.089
Block 3	2008–2010	10.33	$096^{\circ}/59^{\circ} \pm 02^{\circ}$	$096^{\circ}\text{N} \pm 13^{\circ}$	0.079	0.007
Block 4	2008–2010	10.03	$081^{\circ}/62^{\circ} \pm 02^{\circ}$	$007^{\circ}\text{N} \pm 32^{\circ}$	0.033	-0.008
Block 5	2008–2010	7.23	$069^{\circ}/57^{\circ} \pm 03^{\circ}$	$073^{\circ}\text{N} \pm 16^{\circ}$	0.064	0.053
Block 6	2008–2010	4.44	$086^{\circ}/67^{\circ} \pm 06^{\circ}$	$108^{\circ}\text{N} \pm 20^{\circ}$	0.053	0.013
Average of blocks 1–5		9.88	$094^{\circ}/52^{\circ} \pm 16^{\circ}$			-0.010

5.2.2.2 Unstable blocks along the back-crack

As already observed on the shortest distance comparison, the unstable blocks along the back-crack move independently with different velocities and directions (Table 9). The block BC1 with the webcam and laser distancemeter shows small displacements (2.6 cm; 1.4 cm/year) towards the SSW. This movement opposite to the general slope direction lets suppose that it is due to small alignment errors between the sequential scans and that this block is indeed stable. The very low toppling angles also support this hypothesis.

In contrast, the other blocks along the back-crack are clearly moving with high displacement rates (13.5 to 25.1 cm; 7.3 to 13.5 cm/year) in NE to ENE direction. The top part of the middle column (BC2b) has significantly higher displacement rates than the lower part (BC2a). The toppling angles and directions for blocks BC2a, BC2b and BC3 are fairly constant. These freestanding columns slide and topple in downslope direction.

The volume of the blocks along the back-crack being limited to few hundreds cubicmeters, their eventual collapse will neither significantly affect the stability of the unstable rock slope nor pose a threat to the settlements in the valley.

6. CONCLUSION AND PERSPECTIVES

The geological logging of a vertically drilled core at the top of the Mannen rock slope instability has allowed identifying several zones of damaged rocks. Some of these zones contain highly deformed rocks or crushed rocks, such as fine-grained breccias and/or clay-rich gouges. However, the relationship with the gravitational slope deformation is not clearly determined for all of the zones. The highly deformed zones logged in the drill core were confirmed by optical televiewer from the borehole, including fracture frequency, opening of fractures and occurrence of clay-rich zones.

The geomorphological analysis of the DEM of the slope confirmed the different scenarios of slope deformation at Mannen. Scenario A has a volume of 2.5–3 Mm³ and shows highest displacements rates of several cm/year. Scenario B has an estimated volume of 25–30 Mm³ and includes scenario A. The unstable rock slope in scenario B shows presently no signs of activity related to its motion. The entire gravitationally deformed rock slope corresponding to scenario C has a volume of 80–100 Mm³, but displays no signs of activity and its basal limits are not clearly developed.

A wedge failure mechanism is inferred for scenario A based on the orientation of quasi-planar structures delimiting scenario A. One of these basal surfaces would correspond to one of the four intervals of highly deformed rock encountered between 57 and 81 m along the core and characterised by severely crushed rocks. These intervals are expected to be very weak and will not support the load of the moving volume for long due to the inherent fatigue of the material, but until now the rate of deformation measured by the dGPS datasets is in agreement with a steady-state deformation (i.e. no acceleration of sliding is detected).

The orientation of the wedge intersection line formed by the two basal surfaces is parallel to the displacement vector determined by periodic dGPS measurement. This orientation is also consistent with the direction of movement obtained by processed successive acquisitions of terrestrial laser scans of the uppermost part of scenario A. Small toppling movements measured by sequential terrestrial laser scanning are interpreted to be the local accommodation of deformation and are likely not representative for the entire unstable rock slope.

A more detailed analysis of the processed 1 m resolution DEM will be described in a separate report. Future work will focus to integrate borehole data, geophysical data, surface observations, DEM interpretation and displacements measurements to create a complete geological model of the instabilities. The results of the numerical slope stability modelling for scenarios A and B will also be presented in this future report.

7. REFERENCES

- Bieniawski, Z. (1975). The point-load test in geotechnical practice, *Engineering Geology* 9(1), 1–11.
- Deere, D.U. (1964). Technical description of rock cores for engineering purposes, *Rock Mechanics Engineering Geology*, 1, 16–22.
- Eiken, T. (2010). GNSS-måling fjellskred Møre og Romsdal 2010. Technical report, University of Oslo, unpublished.
- Farsund, T.Ø. (2010). Geology, DEM analysis and geohazard assessment of the Romsdalen valley. Project thesis, Norwegian University of Science and Technology, Trondheim, unpublished, 56 pp.
- Farsund, T.Ø. (2011). Geological and numerical stability modelling of Mannen, Romsdalen. MSc thesis, Norwegian University of Science and Technology, Trondheim, unpublished, 119 pp.
- IGRF (2011). <http://www.ngdc.noaa.gov/IAGA/vmod/igrf.html>
- ISRM (1978). International Society for Rock Mechanics Commission on standardization of laboratory and field tests: Suggested methods for the quantitative description of discontinuities in rock masses. *International Journal of Rock Mechanics and Mining Sciences & Geomechanics, Abstracts*, 15(6), 319–368.
- Jaboyedoff, M., Metzger, R., Oppikofer, T., Couture, R., Derron, M., Locat, J. & Turmel, D. (2007). New insight techniques to analyze rock slope relief using DEM and 3D-imaging cloud points: COLTOP-3D software. In: *Rock mechanics: Meeting Society's challenges and demands. Proceedings of the 1st Canada - U.S. Rock Mechanics Symposium*, Vancouver, Canada, 27–31 May 2007, eds. E. Eberhardt, D. Stead & T. Morrison, Taylor & Francis, London, pp. 61–68.
- Oppikofer, T. (2009). Detection, analysis and monitoring of slope movements by high-resolution digital elevation models. PhD thesis, Institute of Geomatics and Analysis of Risk, University of Lausanne, Switzerland.
- Oppikofer, T., Jaboyedoff, M., Blikra, L.H. & Derron, M. (2009). Characterization and monitoring of the Åknes rockslide using terrestrial laser scanning. *Natural Hazards and Earth System Sciences*, 9(3), 1003–1019.
- Saintot, A., Henderson, I. & Derron, M.-H. (2011). Inheritance of ductile and brittle structures in the development of large rock slope instabilities: examples from Western Norway. *Geological Society, London, Special Publication*, 351, 27–78.

8. APPENDIX

Appendix 1

Table of the orientation of the metamorphic foliation in the 4–31.7 m depth interval

Depth	Dip direction	Strike	Dip Angle
4.302	N301	N211	52.2
4.523	N302	N212	44.2
6.517	N314	N224	23.1
6.631	N315	N225	20
7.092	N288	N198	20.5
7.282	N271	N181	23.5
8.232	N251	N161	26
9.311	N326	N236	47.8
9.583	N326	N236	64.4
10.416	N345	N255	54.6
13.247	N036	N306	6
13.423	N096	N006	6.9
15.516	N026	N296	29.8
15.679	N031	N301	32.8
16.077	N018	N288	21.4
16.453	N012	N282	25.7
16.976	N355	N265	28.3
17.232	N034	N304	28.7
17.844	N010	N280	37.1
18.139	N023	N293	37.5
18.288	N013	N283	36.2
18.599	N015	N285	41.6
19.698	N021	N291	45.3
19.939	N030	N300	40.6
20.347	N026	N296	43.6
20.778	N020	N290	49.1
20.996	N024	N294	41.2
21.366	N020	N290	39.3
21.739	N025	N295	37.8
22.174	N022	N292	37
22.528	N019	N289	35.2
22.752	N019	N289	33.6
22.961	N014	N284	34.6
23.354	N018	N288	39.1
23.536	N017	N287	37.6
24.061	N007	N277	31
24.772	N021	N291	30.3
24.944	N026	N296	35.6
25.062	N027	N297	37.1
25.378	N034	N304	44.4
25.541	N039	N309	47.4
26.009	N041	N311	25.6
26.195	N050	N320	30.9
26.558	N043	N313	28.3
26.874	N023	N293	24.7
26.921	N021	N291	23.7
27.365	N002	N272	22.5
29.046	N034	N304	33.9
29.711	N032	N302	39.7
29.801	N033	N303	38.5

30.942	N023	N293	38.9
31.179	N017	N287	43.1
31.281	N025	N295	47.9
31.451	N037	N307	60.

Table of the orientation of the metamorphic foliation in the 33–58 m depth interval

Depth	Dip direction	Strike	Dip angle
33.626	N056	N326	49.3
34.03	N071	N341	36.8
34.423	N088	N358	31.1
34.911	N094	N004	41.1
35.169	N112	N022	34.2
35.775	N099	N009	30.3
36.525	N088	N358	25.2
37.174	N091	N001	39.4
37.504	N085	N355	30.8
37.997	N085	N355	23.8
38.251	N021	N291	13.2
38.579	N048	N318	19.1
39.517	N020	N290	17.1
40.545	N036	N306	31.9
40.897	N047	N317	58.1
41.331	N043	N313	45
42.042	N030	N300	50.4
42.355	N019	N289	41.4
43.867	N346	N256	59.4
46.463	N010	N280	32.5
46.634	N001	N271	33.3
47.24	N354	N264	35.3
48.048	N330	N240	43.2
48.544	N317	N227	43
49.673	N268	N178	41.4
50.214	N293	N203	45
50.448	N285	N195	39.6
50.714	N288	N198	41.4
50.843	N284	N194	41
51.898	N284	N194	40.6
52.423	N290	N200	39.3
52.8	N281	N191	32.2
53.023	N287	N197	30.1
53.198	N284	N194	33.7
53.408	N296	N206	35
53.665	N285	N195	27.6
53.845	N292	N202	32
54.867	N281	N191	48.1
55.513	N252	N162	49.4
55.864	N244	N154	44.9
56.062	N243	N153	47.7
56.235	N235	N145	45.2
57.269	N246	N156	49.3
57.63	N211	N121	26.7
57.76	N200	N110	27.1
57.937	N187	N097	22.9
58.027	N176	N086	20

Table of the orientation of the metamorphic foliation in the 58–76 m depth interval

Depth	Dip direction	Strike	Dip angle
58.551	N171	N081	32.5
59.171	N166	N076	28.1
59.338	N161	N071	30.7
61.497	N107	N017	45.7
61.677	N080	N350	47.9
63.702	N083	N353	41.8
64.243	N101	N011	44.6
64.367	N105	N015	47.9
64.854	N341	N251	22.5
64.948	N338	N248	26.5
65.797	N030	N300	18.2
66.932	N028	N298	24
67.045	N048	N318	25.7
67.957	N007	N277	20
68.896	N026	N296	21.2
68.937	N034	N304	19.5
69.41	N025	N295	25.1
69.828	N011	N281	25.3
71.142	N302	N212	24.8
71.283	N300	N210	36.3
72.027	N282	N192	45.4
72.073	N285	N195	44
72.165	N293	N203	42.1
75.757	N238	N148	39.9
75.989	N237	N147	37.5
76.111	N239	N149	40.7
76.19	N246	N156	42.3

Table of the orientation of the metamorphic foliation in the 89–133 m depth interval

Depth	Dip direction	Strike	Dip angle
89.966	N219	N129	20.4
90.026	N193	N103	19.9
92.358	N129	N039	17.9
92.412	N138	N048	21.1
92.617	N139	N049	28.4
109.022	N134	N044	36.1
109.156	N129	N039	36.3
109.798	N136	N046	44.1
109.938	N130	N040	53.4
110.206	N117	N027	47.9
110.902	N033	N303	23.3
111.187	N029	N299	25.9
111.299	N022	N292	26.1
111.371	N016	N286	30.1
111.774	N046	N316	19.6
111.807	N027	N297	23.7
113.958	N083	N353	48.8
114.04	N072	N342	51.2
114.156	N057	N327	51
114.831	N101	N011	33.1
114.886	N072	N342	36.1

116.112	N101	N011	41.7
116.416	N017	N287	34
116.461	N011	N281	35.1
116.82	N005	N275	47.2
116.888	N016	N286	45.3
117.036	N018	N288	56.6
117.498	N022	N292	40.4
117.679	N037	N307	35.7
118.088	N356	N266	43.9
118.482	N005	N275	43
118.758	N360	N270	42.7
118.902	N339	N249	42.9
119.922	N298	N208	14.6
120.246	N320	N230	38.9
121.645	N354	N264	36.2
121.695	N002	N272	34.5
121.795	N009	N279	29.1
121.837	N007	N277	27.4
121.952	N015	N285	32.3
122.074	N011	N281	28.3
122.111	N356	N266	26.5
124.047	N332	N242	54.8
124.105	N326	N236	45.1
124.568	N342	N252	46.9
124.645	N338	N248	45.3
125.077	N334	N244	47.3
125.309	N330	N240	50.9
126.451	N330	N240	44.4
127.177	N010	N280	48.8
127.312	N006	N276	44.4
127.58	N019	N289	22.2
127.983	N009	N279	15.2
128.795	N342	N252	53.9
128.911	N346	N256	49.2
129.967	N175	N085	62.3
130.022	N162	N072	57.9
130.801	N017	N287	32.5
130.876	N002	N272	30.2
131.727	N037	N307	49.2
131.979	N038	N308	38.5
132.314	N021	N291	38.6
132.398	N039	N309	51.1
132.747	N041	N311	45.4
132.843	N010	N280	42.9
132.904	N020	N290	36.8

Appendix 2

Fracture orientation and characterisation from televiewer logging of Mannen borehole 3–32 m depth interval.

Fracture №	Depth	Azimuth	Strike	Dip angle	Upper Depth	Lower Depth	Borehole Diameter	Borehole Azimuth	Borehole Deviation	Fracture Thickness	Comments			
1	3.117	N329	N239	42.1	3.07	3.164	0.098	6.51	2.09	0	Fracture	Planar	Fresh	Open fracture
2	3.2	N280	N190	7.6	3.193	3.208	0.098	341.63	2.11	0	Fracture	Planar	Fresh	Hairline fracture
3	3.467	N297	N207	30.7	3.437	3.497	0.098	12.31	2.16	0	Fracture	Irregular	Fresh	Hairline fracture
4	3.754	N227	N137	12.7	3.745	3.763	0.098	28.39	2.37	0	Fracture	Planar	Fresh	Hairline fracture
5	3.873	N221	N131	44.6	3.827	3.918	0.098	0.53	2.4	0	Fracture	Planar	Fresh	Open fracture
6	3.897	N219	N129	45.9	3.85	3.945	0.098	1.03	2.4	0	Fracture	Planar	Fresh	Open fracture
7	4.15	N303	N213	56.3	4.07	4.229	0.098	268.99	2.43	0	Fracture	Planar	Fresh	Hairline fracture
8	4.425	N234	N144	25.7	4.404	4.446	0.098	62.26	2.48	0	Fracture	Irregular	Fresh	Hairline fracture
9	4.592	N352	N262	4.7	4.586	4.598	0.098	322.51	2.4	0	Fracture	Planar	Fresh	Hairline fracture
10	5.466	N124	N034	9.8	5.459	5.473	0.098	275.6	2.31	0	Fracture	Planar	Fresh	Open fracture
11	5.687	N078	N348	12.4	5.678	5.696	0.098	272.18	2.35	0	Fracture	Planar	Fresh	Open fracture
12	6.041	N205	N115	8.3	6.032	6.049	0.098	274.78	2.4	0	Fracture	Planar	Fresh	Hairline fracture
13	6.248	N351	N261	30.3	6.218	6.277	0.098	275.04	2.43	0	Fracture	Planar	Fresh	Open fracture
14	6.277	N026	N296	30.5	6.249	6.305	0.098	275.61	2.44	0	Fracture	Planar	Fresh	Open fracture
15	6.449	N029	N299	47.9	6.397	6.502	0.098	276.07	2.43	0	Fracture	Planar	Fresh	Hairline fracture
16	6.704	N321	N231	13.9	6.691	6.718	0.098	277	2.4	0	Fracture	Planar	Fresh	Open fracture
17	7.588	N265	N175	28.7	7.558	7.617	0.098	271.17	2.43	0	Fracture	Planar	Fresh	Hairline fracture
18	8.13	N124	N034	66.1	8.029	8.231	0.098	273	2.43	0	Fracture	Irregular	Fresh	Hairline fracture
19	8.293	N267	N177	20.6	8.273	8.314	0.098	273	2.45	0	Fracture	Planar	Fresh	Open fracture
20	8.443	N298	N208	16.6	8.427	8.46	0.098	272	2.45	0	Fracture	Planar	Fresh	Open fracture
21	8.456	N297	N207	19.6	8.436	8.475	0.098	272.19	2.45	0.0117	Fracture	Planar	Fresh	Open fracture
22	8.679	N350	N260	36.3	8.642	8.715	0.098	270.31	2.45	0	Fracture	Planar	Fresh	Open fracture
23	8.767	N024	N294	57.5	8.693	8.841	0.098	270.58	2.47	0	Fracture	Irregular	Fresh	Open fracture
24	8.844	N033	N303	57.9	8.77	8.918	0.098	268.08	2.46	0	Fracture	Planar	Fresh	Open fracture
25	9.474	N323	N233	62.9	9.371	9.576	0.098	269	2.52	0	Fracture	Planar	Fresh	Open fracture
26	9.99	N150	N060	16.7	9.976	10.003	0.098	272	2.53	0	Fracture	Planar	Fresh	Open fracture
27	10.16	N061	N331	75.2	9.999	10.321	0.098	272	2.54	0	Fracture	Planar	Fresh	Open fracture
28	10.633	N321	N231	47.8	10.576	10.69	0.098	270	2.48	0	Fracture	Planar	Fresh	Open fracture
29	10.651	N321	N231	50.4	10.588	10.713	0.098	270	2.48	0.0116	Fracture	Planar	Fresh	Open fracture
30	11.033	N298	N208	37	10.994	11.073	0.098	266.25	2.48	0	Fracture	Planar	Fresh	Open fracture
31	11.06	N097	N007	13.7	11.051	11.07	0.098	265.13	2.48	0	Fracture	Irregular	Fresh	Open fracture
32	11.317	N330	N240	48.9	11.259	11.375	0.098	261.59	2.48	0	Fracture	Irregular	Fresh	Hairline fracture
33	11.409	N262	N172	9.1	11.399	11.419	0.098	262.26	2.47	0	Fracture	Irregular	Fresh	Hairline fracture
34	11.966	N263	N173	22	11.944	11.988	0.098	265.4	2.42	0	Fracture	Irregular	Fresh	Open fracture
35	12.115	N090	N000	26.7	12.107	12.137	0.098	263.49	2.41	0	Fracture	Discontinuous	Fresh	Open fracture
36	12.147	N345	N255	4.4	12.142	12.151	0.098	265.96	2.4	0	Fracture	Irregular	Fresh	Open fracture
37	12.329	N038	N308	10.8	12.321	12.337	0.098	265.34	2.43	0	Fracture	Planar	Fresh	Hairline fracture
38	12.339	N353	N263	39.8	12.298	12.345	0.098	265.14	2.42	0	Fracture	Discontinuous	Fresh	Hairline fracture
39	12.522	N154	N064	9.9	12.514	12.53	0.098	264.58	2.42	0	Fracture	Planar	Fresh	Hairline fracture
40	12.671	N359	N269	35.7	12.636	12.706	0.098	265.5	2.39	0	Fracture	Planar	Fresh	Hairline fracture

41	12.919	N026	N296	13.2	12.909	12.93	0.098	263.93	2.37	0	Fracture	Planar	Fresh	Hairline fracture
42	13.247	N058	N328	5.6	13.244	13.25	0.098	265	2.33	0	Fracture	Planar	Fresh	Hairline fracture
43	13.751	N130	N040	24.2	13.73	13.772	0.098	261.9	2.29	0	Fracture	Planar	Fresh	Hairline fracture
44	14.859	N327	N237	9	14.851	14.868	0.098	264.21	2.1	0	Fracture	Planar	Fresh	Open fracture
45	14.894	N322	N232	16.6	14.878	14.909	0.098	262.13	2.1	0.0337	Fracture	Planar	Fresh	Open fracture
46	15.705	N225	N135	71.4	15.544	15.865	0.098	262.83	1.98	0	Fracture	Planar	Fresh	Hairline fracture
47	15.874	N271	N181	6.7	15.866	15.881	0.098	262.45	1.99	0	Fracture	Planar	Fresh	Open fracture
48	16.111	N033	N303	20.7	16.094	16.128	0.098	260.7	2.02	0	Fracture	Planar	Fresh	Open fracture
49	16.31	N226	N136	20.9	16.29	16.33	0.098	261.28	2.03	0	Fracture	Planar	Fresh	Hairline fracture
50	16.322	N207	N117	24.6	16.298	16.346	0.098	261.52	2.04	0	Fracture	Planar	Fresh	Hairline fracture
51	16.52	N041	N311	23.2	16.5	16.539	0.098	260	2.11	0	Fracture	Planar	Fresh	Open fracture
52	16.839	N044	N314	37.2	16.804	16.874	0.098	254	2.16	0	Fracture	Planar	Fresh	Open fracture
53	16.905	N348	N258	24.3	16.883	16.928	0.098	256.44	2.15	0	Fracture	Planar	Fresh	Hairline fracture
54	16.915	N355	N265	31.4	16.886	16.945	0.098	255.84	2.15	0	Fracture	Planar	Fresh	Open fracture
55	17.499	N029	N299	35.7	17.466	17.533	0.098	259.61	2.18	0	Fracture	Crushed	Fresh	Open fracture
56	17.652	N037	N307	37.1	17.617	17.687	0.098	256.34	2.16	0.1228	Fracture	Crushed	Fresh	Open fracture
57	17.769	N130	N040	19	17.753	17.784	0.098	259.1	2.17	0	Fracture	Planar	Fresh	Open fracture
58	17.937	N044	N314	28.5	17.913	17.962	0.098	260.17	2.16	0	Fracture	Planar	Fresh	Open fracture
59	19.24	N006	N276	35.7	19.205	19.274	0.098	263	2.25	0	Fracture	Crushed	Fresh	Open fracture
60	19.364	N032	N302	54.7	19.298	19.43	0.098	261.36	2.22	0.0887	Fracture	Crushed	Fresh	Open fracture
61	19.534	N023	N293	43.2	19.49	19.578	0.098	262	2.29	0	Fracture	Planar	Fresh	Open fracture
62	19.939	N030	N300	43.2	19.895	19.983	0.098	262	2.31	0	Fracture	Planar	Fresh	Hairline fracture
63	20.225	N021	N291	43.2	20.181	20.269	0.098	258.13	2.37	0	Fracture	Planar	Fresh	Open fracture
64	20.255	N025	N295	44.8	20.209	20.302	0.098	256.19	2.38	0.022	Fracture	Planar	Fresh	Open fracture
65	20.527	N008	N278	41.6	20.485	20.569	0.098	251.13	2.41	0	Fracture	Planar	Fresh	Open fracture
66	20.644	N031	N301	37.7	20.608	20.68	0.098	257.92	2.42	0.0907	Fracture	Planar	Fresh	Open fracture
67	20.825	N189	N099	45.1	20.823	20.876	0.098	258.3	2.46	0	Fracture	Discontinuous	Fresh	Open fracture
68	20.826	N014	N284	42.8	20.782	20.87	0.098	258.39	2.46	0	Fracture	Planar	Fresh	Open fracture
69	20.845	N186	N096	50	20.832	20.905	0.098	259.94	2.47	0.0139	Fracture	Discontinuous	Fresh	Open fracture
70	21.446	N024	N294	41.5	21.404	21.488	0.098	265	2.46	0	Fracture	Planar	Fresh	Hairline fracture
71	21.546	N021	N291	41.4	21.505	21.588	0.098	264	2.45	0	Fracture	Planar	Fresh	Open fracture
72	21.593	N021	N291	41.9	21.551	21.632	0.098	264	2.44	0	Fracture	Discontinuous	Fresh	Open fracture
73	21.739	N027	N297	38.5	21.702	21.777	0.098	264	2.45	0	Fracture	Planar	Fresh	Hairline fracture
74	21.768	N059	N329	51.1	21.712	21.77	0.098	263.55	2.46	0	Fracture	Discontinuous	Fresh	Open fracture
75	21.798	N054	N324	58.1	21.726	21.781	0.098	262.96	2.48	0.0173	Fracture	Discontinuous	Fresh	Open fracture
76	21.81	N026	N296	37.4	21.774	21.846	0.098	262.72	2.47	0	Fracture	Planar	Fresh	Open fracture
77	21.827	N022	N292	38.1	21.79	21.864	0.098	262.37	2.47	0.0137	Fracture	Planar	Fresh	Open fracture
78	22.091	N025	N295	39.7	22.052	22.13	0.098	264.1	2.45	0	Fracture	Planar	Fresh	Hairline fracture
79	22.466	N184	N094	25.9	22.441	22.49	0.098	264.61	2.48	0	Fracture	Planar	Fresh	Hairline fracture
80	22.801	N014	N284	34.7	22.768	22.834	0.098	265	2.5	0	Fracture	Planar	Fresh	Open fracture
81	23.649	N021	N291	20.8	23.632	23.667	0.098	264.07	2.5	0	Fracture	Planar	Fresh	Open fracture
82	23.804	N008	N278	36.1	23.769	23.839	0.098	265	2.51	0.1365	Fracture	Planar	Fresh	Open fracture
83	23.835	N009	N279	31.7	23.806	23.865	0.098	265	2.49	0	Fracture	Planar	Fresh	Open fracture
84	23.87	N009	N279	32.8	23.839	23.901	0.098	265	2.5	0	Fracture	Planar	Fresh	Open fracture
85	23.899	N009	N279	30.9	23.87	23.927	0.098	264.8	2.52	0	Fracture	Planar	Fresh	Open fracture

86	23.91	N008	N278	31.6	23.881	23.925	0.098	263.85	2.52	0	Fracture	Discontinuous	Fresh	Open fracture
87	23.945	N013	N283	33.8	23.913	23.977	0.098	261.08	2.51	0	Fracture	Planar	Fresh	Open fracture
88	23.983	N030	N300	41.8	23.942	24.025	0.098	262.49	2.52	0	Fracture	Planar	Fresh	Open fracture
89	24.008	N016	N286	33.4	23.977	24.039	0.098	262.52	2.53	0.0197	Fracture	Planar	Fresh	Open fracture
90	24.177	N037	N307	62.1	24.091	24.263	0.098	261.62	2.51	0	Fracture	Planar	Fresh	Hairline fracture
91	24.313	N009	N279	35.4	24.279	24.347	0.098	261.65	2.49	0	Fracture	Planar	Fresh	Hairline fracture
92	24.631	N197	N107	34.2	24.596	24.666	0.098	257.9	2.47	0	Fracture	Planar	Fresh	Open fracture
93	24.665	N012	N282	33	24.634	24.696	0.098	257.38	2.48	0	Fracture	Planar	Fresh	Open fracture
94	24.692	N015	N285	31.3	24.663	24.72	0.098	257.91	2.5	0.0225	Fracture	Planar	Fresh	Open fracture
95	25.539	N039	N309	47.5	25.489	25.59	0.098	262.26	2.58	0	Fracture	Planar	Fresh	Hairline fracture
96	25.6	N209	N119	68.9	25.555	25.737	0.098	263.85	2.57	0	Fracture	Discontinuous	Fresh	Hairline fracture
97	26.29	N022	N292	82.5	25.974	26.146	0.098	260.25	2.54	0	Fracture	Discontinuous	Fresh	Hairline fracture
98	26.558	N044	N314	29.2	26.533	26.584	0.098	261.5	2.55	0	Fracture	Planar	Fresh	Hairline fracture
99	27.366	N006	N276	22.4	27.347	27.385	0.098	257	2.56	0	Fracture	Planar	Fresh	Hairline fracture
100	27.409	N006	N276	23	27.389	27.429	0.098	257.26	2.57	0	Fracture	Planar	Clayey	
101	27.677	N008	N278	35.4	27.643	27.711	0.098	259	2.59	0.2336	Fracture	Planar	Clayey	
102	27.706	N016	N286	33.1	27.675	27.737	0.098	259	2.6	0	Fracture	Planar	Fresh	Open fracture
103	27.71	N014	N284	34.7	27.677	27.743	0.098	259	2.59	0	Fracture	Crushed	Fresh	Fracture zone
104	27.891	N012	N282	29.7	27.864	27.918	0.098	258.2	2.59	0.1532	Fracture	Crushed	Fresh	Fracture zone
105	27.936	N358	N268	21.1	27.917	27.954	0.098	258.8	2.59	0	Fracture	Irregular	Clayey	
106	28.169	N346	N256	36.9	28.132	28.206	0.098	257.46	2.56	0.2043	Fracture	Irregular	Clayey	
107	28.188	N354	N264	37.9	28.15	28.225	0.098	257.83	2.55	0	Fracture	Planar	Fresh	Open fracture
108	28.2	N231	N141	49	28.177	28.261	0.098	258	2.55	0	Fracture	Discontinuous	Fresh	Open fracture
109	28.266	N018	N288	35.4	28.233	28.299	0.098	258	2.56	0	Fracture	Planar	Fresh	Open fracture
110	28.308	N022	N292	35.8	28.274	28.342	0.098	257.76	2.57	0	Fracture	Planar	Fresh	Open fracture
111	28.33	N007	N277	27.2	28.306	28.355	0.098	257.32	2.57	0	Fracture	Planar	Clayey	
112	28.402	N026	N296	41.5	28.361	28.443	0.098	256.13	2.57	0.0598	Fracture	Planar	Clayey	
113	28.456	N288	N198	61.7	28.511	28.556	0.098	256.59	2.6	0	Fracture	Discontinuous	Fresh	Open fracture
114	28.458	N316	N226	38.4	28.417	28.485	0.098	256.53	2.6	0	Fracture	Discontinuous	Fresh	Open fracture
115	28.477	N161	N071	55.5	28.416	28.53	0.098	255.77	2.6	0	Fracture	Discontinuous	Fresh	Open fracture
116	28.499	N035	N305	36.6	28.465	28.533	0.098	255.05	2.6	0	Fracture	Planar	Fresh	Open fracture
117	28.595	N042	N312	41.8	28.554	28.636	0.098	257.97	2.6	0	Fracture	Planar	Fresh	Open fracture
118	28.624	N024	N294	35.3	28.591	28.657	0.098	261.94	2.63	0	Fracture	Planar	Fresh	Open fracture
119	29.072	N118	N028	84.1	28.728	29.196	0.098	260.57	2.7	0	Fracture	Discontinuous	Fresh	Open fracture
120	29.248	N147	N057	86.4	28.746	29.308	0.098	257.08	2.69	0	Fracture	Discontinuous	Fresh	Open fracture
121	29.33	N296	N206	35.7	29.299	29.368	0.098	257.65	2.69	0	Fracture	Discontinuous	Fresh	Open fracture
122	29.436	N210	N120	58.8	29.349	29.522	0.098	261.58	2.72	0	Fracture	Discontinuous	Fresh	Open fracture
123	29.588	N204	N114	59	29.501	29.675	0.098	259.48	2.72	0	Fracture	Discontinuous	Fresh	Open fracture
124	29.626	N208	N118	59.5	29.536	29.715	0.098	260.18	2.74	0.0192	Fracture	Discontinuous	Fresh	Open fracture
125	29.64	N024	N294	36.6	29.606	29.675	0.098	260.78	2.75	0	Fracture	Planar	Fresh	Open fracture
126	29.935	N176	N086	35.2	29.9	29.97	0.098	265.1	2.72	0	Fracture	Crushed	Fresh	Open fracture
127	30.029	N200	N110	41.7	29.983	30.074	0.098	260	2.71	0.0741	Fracture	Crushed	Fresh	Open fracture
128	31.497	N010	N280	11.5	31.488	31.507	0.098	260.1	2.7	0	Fracture	Planar	Fresh	Hairline fracture

Fracture orientation and characterisation from televiewer logging of Mannen borehole 32–58 m depth interval.

Depth	Azimuth	Strike	Dip angle	Upper Depth	Lower Depth	Borehole Diameter	Borehole Azimuth	Borehole Deviation	Fracture Thickness	Comments			
32.761	N052	N322	9.3	32.756	32.761	0.098	259.3	3.74	0	Fracture	Discontinuous	Fresh	Hairline fracture
32.898	N088	N358	19.8	32.884	32.912	0.098	261	3.74	0	Fracture	Planar	Fresh	Hairline fracture
33.603	N062	N332	10.5	33.597	33.609	0.098	261.14	3.64	0	Fracture	Planar	Fresh	Hairline fracture
34.424	N092	N002	32.1	34.398	34.451	0.098	259.14	3.77	0	Fracture	Planar	Fresh	Hairline fracture
34.564	N089	N359	19.5	34.55	34.563	0.098	261	3.79	0	Fracture	Discontinuous	Fresh	Hairline fracture
35.318	N108	N018	32.3	35.291	35.345	0.098	265.13	3.87	0	Fracture	Planar	Fresh	Open fracture
36.233	N092	N002	27.9	36.211	36.254	0.098	265	3.94	0	Fracture	Planar	Fresh	Open fracture
36.266	N086	N356	31.3	36.24	36.291	0.098	265.39	3.96	0	Fracture	Planar	Fresh	Open fracture
36.445	N089	N359	15.5	36.435	36.455	0.098	265.97	3.99	0	Fracture	Planar	Fresh	Hairline fracture
36.64	N086	N356	13.6	36.631	36.648	0.098	265.12	4	0	Fracture	Planar	Fresh	Open fracture
36.71	N087	N357	8	36.71	36.713	0.098	266.72	4.02	0	Fracture	Discontinuous	Fresh	Open fracture
36.81	N071	N341	19.8	36.796	36.824	0.098	266.27	4	0	Fracture	Planar	Fresh	Hairline fracture
36.942	N099	N009	55.1	36.881	37.003	0.098	266.92	4.02	0	Fracture	Planar	Fresh	Hairline fracture
36.99	N045	N315	24.4	36.97	37.009	0.098	267.87	4.01	0	Fracture	Planar	Fresh	Hairline fracture
37.303	N329	N239	5.3	37.296	37.31	0.098	269.74	4.01	0	Fracture	Planar	Fresh	Open fracture
37.499	N068	N338	16.3	37.488	37.51	0.098	267.05	3.98	0	Fracture	Planar	Fresh	Open fracture
37.637	N084	N354	18	37.625	37.65	0.098	269	4.01	0	Fracture	Planar	Fresh	Hairline fracture
37.772	N064	N334	8.9	37.768	37.777	0.098	267.58	4.01	0	Fracture	Planar	Fresh	Hairline fracture
37.933	N103	N013	9.3	37.928	37.938	0.098	268.52	4.03	0	Fracture	Planar	Fresh	Hairline fracture
38.116	N333	N243	7.2	38.107	38.124	0.098	265.39	4.04	0	Fracture	Planar	Fresh	Hairline fracture
38.181	N321	N231	7.3	38.172	38.19	0.098	266	4.06	0	Fracture	Planar	Fresh	Hairline fracture
38.261	N035	N305	9.3	38.255	38.268	0.098	266	4.06	0	Fracture	Planar	Fresh	Hairline fracture
38.465	N050	N320	10.5	38.459	38.472	0.098	265.61	4.08	0	Fracture	Planar	Fresh	Hairline fracture
38.56	N014	N284	5.7	38.555	38.565	0.098	266	4.1	0	Fracture	Planar	Fresh	Hairline fracture
38.687	N022	N292	9.4	38.68	38.694	0.098	266.64	4.1	0	Fracture	Planar	Fresh	Hairline fracture
38.826	N060	N330	47.3	38.78	38.873	0.098	267	4.1	0	Fracture	Planar	Fresh	Hairline fracture
39.519	N020	N290	12.8	39.508	39.529	0.098	268.45	4.14	0	Fracture	Planar	Fresh	Hairline fracture
39.778	N030	N300	20.1	39.761	39.794	0.098	271.27	4.15	0	Vein	Planar		Mineralized
39.811	N022	N292	17.6	39.796	39.826	0.098	272	4.15	0.0314	Vein	Planar		Quartz-vein
39.822	N030	N300	20.7	39.805	39.839	0.098	272	4.14	0	Fractur	Planar	Fresh	Open fracture
39.863	N027	N297	20.3	39.846	39.879	0.098	272.33	4.14	0.0382	Fracture	Planar	Fresh	Open fracture
39.868	N036	N306	20.2	39.852	39.884	0.098	272.44	4.14	0	Fracture	Planar	Fresh	Fracture zone
39.999	N023	N293	20.8	39.981	40.017	0.098	273	4.14	0.123	Fracture	Planar	Fresh	Open fracture
40.271	N005	N275	25.6	40.248	40.294	0.098	273.49	4.16	0	Fracture	Discontinuous	Fresh	Open fracture
40.509	N115	N025	58.9	40.484	40.579	0.098	276.26	4.16	0	Fracture	Discontinuous	Fresh	Open fracture
40.583	N130	N040	77.9	40.452	40.759	0.098	277	4.16	0	Fracture	Discontinuous	Fresh	Open fracture
40.675	N125	N035	71.6	40.645	40.796	0.098	276.57	4.19	0	Fracture	Discontinuous	Fresh	Open fracture
42.156	N064	N334	29.6	42.167	42.168	0.098	285	4.28	0	Fracture	Discontinuous	Fresh	Open fracture
42.182	N043	N313	29.2	42.2	42.201	0.098	285	4.27	0.0221	Fracture	Discontinuous	Fresh	Open fracture
42.207	N114	N024	75.1	42.065	42.349	0.098	285	4.27	0	Fracture	Irregular	Fresh	Open fracture
42.246	N114	N024	78.6	42.071	42.421	0.098	285	4.25	0.0088	Fracture	Irregular	Fresh	Open fracture

42.741	N330	N240	39	42.696	42.785	0.098	285.11	4.3	0	Fracture	Planar	Fresh	Open fracture
42.856	N007	N277	48.9	42.798	42.913	0.098	286	4.3	0.0847	Fracture	Planar	Fresh	Open fracture
43.787	N149	N059	45.8	43.742	43.832	0.098	287.83	4.32	0	Fracture	Planar	Fresh	Hairline fracture
44.688	N158	N068	69.8	44.572	44.804	0.098	286.83	4.26	0	Fracture	Irregular	Fresh	Hairline fracture
45.272	N153	N063	68.3	45.166	45.379	0.098	288	4.25	0	Fracture	Irregular	Fresh	Open fracture
45.296	N155	N065	69	45.186	45.407	0.098	288	4.25	0.0087	Fracture	Irregular	Fresh	Open fracture
46.491	N070	N340	82.8	46.225	46.756	0.098	290	4.2	0	Fracture	Irregular	Fresh	Open fracture
46.674	N003	N273	36.4	46.636	46.712	0.098	290	4.18	0	Fracture	Planar	Fresh	Open fracture
46.718	N003	N273	35.8	46.681	46.755	0.098	290	4.18	0.0361	Fracture	Planar	Fresh	Open fracture
46.726	N352	N262	39.6	46.682	46.769	0.098	290	4.18	0	Fracture	Planar	Fresh	Fracture zone
47.909	N335	N245	47	47.851	47.966	0.098	289	3.82	0.8654	Fracture	Planar	Fresh	Fracture zone
48.143	N152	N062	23.5	48.125	48.162	0.098	292.94	3.88	0	Fracture	Planar	Fresh	Hairline fracture
48.882	N257	N167	14.4	48.866	48.898	0.098	294	4.68	0	Fracture	Planar	Fresh	Hairline fracture
49.424	N287	N197	12.1	49.41	49.438	0.098	294.56	3.99	0	Fracture	Planar	Fresh	Hairline fracture
49.896	N143	N053	32	49.87	49.923	0.098	295.99	3.93	0	Fracture	Planar	Fresh	Open fracture
50.93	N274	N184	45.8	50.873	50.987	0.098	290.68	3.82	0	Fracture	Crushed	Fresh	Fracture zone
51.908	N281	N191	39.4	51.862	51.954	0.098	291.24	4.04	0.7208	Fracture	Crushed	Fresh	Fracture zone
52.009	N144	N054	27.2	51.987	52.031	0.098	289.95	3.99	0	Fracture	Planar	Fresh	Open fracture
52.175	N065	N335	70.2	52.059	52.292	0.098	288.59	4.05	0	Fracture	Planar	Fresh	Hairline fracture
52.318	N291	N201	43.1	52.265	52.371	0.098	290.23	4.02	0	Fracture	Planar	Fresh	Open fracture
52.657	N173	N083	45.9	52.61	52.704	0.098	296.21	3.91	0	Fracture	Irregular	Fresh	Open fracture
53.243	N278	N188	28.7	53.212	53.274	0.098	297	3.63	0	Fracture	Planar	Fresh	Open fracture
53.31	N295	N205	33.8	53.272	53.347	0.098	297	3.65	0	Fracture	Planar	Fresh	Open fracture
53.92	N281	N191	30.1	53.888	53.953	0.098	295.52	3.61	0	Fracture	Crushed	Fresh	Fracture zone
55.339	N248	N158	49.1	55.277	55.4	0.098	293.85	3.16	1.1104	Fracture	Crushed	Fresh	Fracture zone
56.252	N239	N149	46.7	56.197	56.306	0.098	291.11	2.33	0	Fracture	Crushed	Fresh	Fracture zone
57.833	N200	N110	28	57.807	57.86	0.098	283.75	2.5	1.2826	Fracture	Crushed	Fresh	Fracture zone
57.852	N183	N093	24.7	57.83	57.875	0.098	283.74	2.53	0	Fracture	Planar	Fresh	Open fracture
57.871	N192	N102	24.8	57.848	57.894	0.098	283	2.58	0	Fracture	Planar	Fresh	Open fracture
57.88	N181	N091	30.3	57.851	57.908	0.098	282.66	2.6	0	Fracture	Planar	Fresh	Open fracture

Fracture orientation and characterisation from televiewer logging of Mannen borehole 57–77 m depth interval.

Depth	Azimuth	Strike	Dip angle	Upper Depth	Lower Depth	Borehole Diameter	Borehole Azimuth	Borehole Deviation	Fracture Thickness	Comments			
57.425	N357	N267	20.9	57.405	57.445	0.98	284	3.48	0	Fracture Irregular	Fresh	Open fracture	
57.71	N130	N040	17.9	57.697	57.724	0.98	283.85	3.46	0.2826	Fracture Irregular	Fresh	Open fracture	
57.959	N154	N064	29.1	57.934	57.985	0.98	286	3.39	0	Fracture Planar	Fresh	Open fracture	
58.013	N139	N049	32.7	57.985	58.042	0.98	286.35	3.37	0.0464	Fracture Planar	Fresh	Open fracture	
59.397	N009	N279	25.3	59.372	59.421	0.98	285.01	3.31	0	Fracture Crushed	Fresh	Fracture zone	
61.214	N136	N046	53.9	61.15	61.277	0.98	277.65	2.68	1.6665	Fracture Crushed	Fresh	Fracture zone	
61.535	N043	N313	33.2	61.505	61.565	0.98	260	3.23	0	Fracture Planar	Fresh	Open fracture	
61.623	N084	N354	49	61.571	61.675	0.98	275.95	3.05	0	Fracture Planar	Fresh	Open fracture	
61.883	N066	N336	32.9	61.854	61.912	0.98	275.48	3.05	0	Fracture Crushed	Fresh	Fracture zone	
63.488	N091	N001	54.2	63.425	63.55	0.98	273.68	2.91	1.1759	Fracture Crushed	Fresh	Fracture zone	
70.607	N115	N025	49.1	70.556	70.659	0.98	268	3.5	0	Fracture Irregular	Fresh	Open fracture	
70.721	N066	N336	54.7	70.658	70.784	0.98	270.99	3.51	0.074	Fracture Irregular	Fresh	Open fracture	
72.422	N058	N328	35.9	72.39	72.455	0.98	267.53	3.66	0	Fracture Irregular	Fresh	Open fracture	
72.627	N138	N048	9.8	72.62	72.634	0.98	268	3.66	0.1925	Fracture Irregular	Fresh	Open fracture	
73.217	N018	N288	14.6	73.205	73.229	0.98	266.42	3.47	0	Fracture Crushed	Fresh	Fracture zone	
75.718	N026	N296	15.7	75.705	75.731	0.98	270	3.83	2.4143	Fracture Crushed	Fresh	Fracture zone	
76.521	N247	N157	19.8	76.499	76.543	0.98	268.5	4	0	Fracture Crushed	Fresh	Open fracture	
77.181	N353	N263	48	77.125	77.238	0.98	267.59	4.01	0.6018	Fracture Crushed	Fresh	Open fracture	

Fracture orientation and characterisation from televiewer logging of Mannen borehole 90–130 m depth interval.

Depth	Azimuth	Strike	Dip angle	Upper Depth	Lower Depth	Borehole Diameter	Borehole Azimuth	Borehole Deviation	Fracture Thickness	Comments			
90.648	N153	N063	25.2	90.624	90.671	0.1	59.95	3.81	0	Fracture Planar	Fresh	Open fracture	
90.657	N170	N080	17.9	90.643	90.672	0.1	53.43	3.81	0	Fracture Planar	Fresh	Open fracture	
90.752	N168	N078	23.8	90.734	90.77	0.1	356.5	3.83	0	Fracture Planar	Fresh	Open fracture	
91.86	N050	N320	28.2	91.834	91.885	0.1	298.27	3.66	0	Fracture Crushed	Fresh	Fracture zone	
92.055	N073	N343	26.9	92.033	92.078	0.1	291.81	3.6	0.1744	Fracture Crushed	Fresh	Fracture zone	
92.146	N223	N133	3.2	92.142	92.151	0.1	291.99	3.58	0	Fracture Irregular	Fresh	Open fracture	
92.41	N141	N051	19.3	92.395	92.424	0.1	287.46	3.55	0	Fracture Planar	Fresh	Hairline fracture	
93.202	N056	N326	10.3	93.195	93.209	0.1	282	3.49	0	Fracture Planar	Fresh	Open fracture	
93.497	N181	N091	21.2	93.478	93.517	0.1	281.06	3.47	0	Fracture Crushed	Fresh	Fracture zone	
93.582	N153	N063	25.2	93.561	93.603	0.1	281.56	3.46	0.0781	Fracture Crushed	Fresh	Fracture zone	
93.617	N121	N031	32.4	93.589	93.645	0.1	281	3.45	0	Fracture Planar	Fresh	Open fracture	
94.501	N102	N012	52.2	94.444	94.558	0.1	281.79	3.39	0	Fracture Planar	Fresh	Open fracture	
94.593	N112	N022	52.5	94.535	94.651	0.1	280.93	3.37	0.0559	Fracture Planar	Fresh	Open fracture	
95.069	N089	N359	37.2	95.035	95.102	0.1	278	3.35	0	Fracture Irregular	Fresh	Hairline fracture	
95.689	N257	N167	68.5	95.669	95.839	0.1	278.15	3.3	0	Fracture Discontinuous	Fresh	Hairline fracture	
95.934	N088	N358	74.2	95.944	96.078	0.1	278.24	3.32	0	Fracture Discontinuous	Fresh	Hairline fracture	
96.008	N259	N169	58.3	95.977	96.1	0.1	277.75	3.3	0	Fracture Discontinuous	Fresh	Hairline fracture	

97.981	N246	N156	62.3	97.873	98.089	0.1	276	3.3	0	Fracture	Irregular	Fresh	Open fracture
98.926	N082	N352	74.6	98.777	99.075	0.1	276.4	3.31	0	Fracture	Planar	Fresh	Open fracture
98.95	N082	N352	74.3	98.805	99.096	0.1	276	3.29	0.0065	Fracture	Planar	Fresh	Open fracture
99.077	N118	N028	68.6	98.967	99.187	0.1	276.37	3.31	0	Fracture	Irregular	Fresh	Hairline fracture
99.512	N159	N069	8.9	99.505	99.519	0.1	275.32	3.26	0	Fracture	Planar	Fresh	Hairline fracture
99.915	N355	N265	47.8	99.859	99.972	0.1	276	3.24	0	Fracture	Irregular	Fresh	Hairline fracture
100.292	N242	N152	58.3	100.268	100.383	0.1	276	3.24	0	Fracture	Discontinuous	Fresh	Hairline fracture
100.35	N246	N156	50.4	100.325	100.417	0.1	276	3.22	0	Fracture	Discontinuous	Fresh	Hairline fracture
100.971	N345	N255	52.3	100.903	101.038	0.1	275	3.29	0	Fracture	Planar	Fresh	Open fracture
101.337	N074	N344	56	101.27	101.403	0.1	274.19	3.3	0	Fracture	Planar	Fresh	Open fracture
101.444	N094	N004	23.9	101.425	101.463	0.1	274	3.28	0	Fracture	Planar	Fresh	Hairline fracture
102.576	N221	N131	65.2	102.457	102.694	0.1	274.6	3.3	0	Fracture	Irregular	Fresh	Hairline fracture
103.072	N143	N053	44.1	103.027	103.117	0.1	275	3.29	0	Fracture	Planar	Fresh	Open fracture
103.081	N140	N050	39.8	103.042	103.119	0.1	275	3.29	0	Fracture	Planar	Fresh	Hairline fracture
103.415	N328	N238	70	103.261	103.569	0.1	274	3.29	0	Fracture	Planar	Fresh	Open fracture
103.571	N326	N236	46.3	103.515	103.627	0.1	275	3.29	0	Fracture	Planar	Fresh	Open fracture
103.587	N328	N238	46.3	103.53	103.643	0.1	275	3.3	0	Fracture	Planar	Fresh	Open fracture
103.803	N337	N247	64.1	103.693	103.913	0.1	274.14	3.31	0	Fracture	Irregular	Fresh	Open fracture
103.83	N337	N247	63.2	103.724	103.936	0.1	274.69	3.33	0.0123	Fracture	Irregular	Fresh	Open fracture
104.598	N117	N027	79.2	104.396	104.8	0.1	276	3.33	0	Fracture	Irregular	Fresh	Open fracture
104.86	N340	N250	47.7	104.802	104.918	0.1	277	3.35	0	Fracture	Irregular	Fresh	Open fracture
105.378	N266	N176	53.6	105.301	105.454	0.1	274.1	3.34	0	Fracture	Irregular	Fresh	Hairline fracture
105.465	N258	N168	58	105.374	105.556	0.1	272	3.34	0	Fracture	Irregular	Fresh	Hairline fracture
107.736	N122	N032	39.7	107.716	107.773	0.1	275.8	3.37	0	Fracture	Discontinuous	Fresh	Hairline fracture
107.787	N154	N064	27.4	107.766	107.811	0.1	276	3.36	0	Fracture	Discontinuous	Fresh	Hairline fracture
107.889	N184	N094	55.8	107.815	107.963	0.1	274.86	3.37	0	Fracture	Discontinuous	Fresh	Hairline fracture
108.396	N001	N271	76.6	108.181	108.61	0.1	275	3.39	0	Fracture	Discontinuous	Fresh	Open fracture
108.464	N347	N257	75.4	108.256	108.672	0.1	275	3.37	0	Fracture	Irregular	Fresh	Open fracture
108.492	N195	N105	33.2	108.458	108.525	0.1	275	3.37	0	Fracture	Discontinuous	Fresh	Hairline fracture
108.71	N348	N258	76.1	108.492	108.923	0.1	275	3.41	0	Fracture	Discontinuous	Fresh	Hairline fracture
108.883	N077	N347	12.3	108.875	108.891	0.1	278.74	3.39	0	Fracture	Planar	Fresh	Hairline fracture
110.257	N350	N260	76.4	110.032	110.482	0.1	277	3.42	0	Fracture	Irregular	Fresh	Hairline fracture
110.354	N359	N269	9.7	110.344	110.363	0.1	277	3.43	0	Fracture	Irregular	Fresh	Hairline fracture
110.751	N351	N261	69.5	110.61	110.892	0.1	276.9	3.41	0	Fracture	Irregular	Fresh	Open fracture
110.772	N348	N258	68.2	110.639	110.904	0.1	276.49	3.42	0.0074	Fracture	Irregular	Fresh	Open fracture
110.989	N026	N296	21.9	110.969	111.008	0.1	276	3.41	0	Fracture	Planar	Fresh	Hairline fracture
111.482	N159	N069	41	111.44	111.523	0.1	276.29	3.42	0	Fracture	Planar	Fresh	Hairline fracture
111.645	N040	N310	26.6	111.622	111.668	0.1	276.03	3.44	0	Fracture	Planar	Fresh	Fracture zone
111.733	N057	N327	28.1	111.71	111.757	0.1	276.75	3.42	0.079	Fracture	Planar	Fresh	Fracture zone
112.054	N296	N206	41	112.005	112.103	0.1	276.84	3.42	0	Fracture	Crushed	Fresh	Fracture zone
113.677	N274	N184	52.1	113.604	113.749	0.1	274	3.42	1.1277	Fracture	Crushed	Fresh	Fracture zone
114.301	N350	N260	78.8	114.028	114.575	0.1	274	3.41	0	Fracture	Irregular	Fresh	Hairline fracture
117.075	N138	N048	79.6	116.855	117.295	0.1	273.42	3.5	0	Fracture	Irregular	Fresh	Hairline fracture
117.389	N212	N122	37	117.349	117.429	0.1	272	3.5	0	Fracture	Planar	Fresh	Hairline fracture
119.713	N187	N097	42.8	119.666	119.761	0.1	269.04	3.51	0	Fracture	Planar	Fresh	Hairline fracture

119.757	N270	N180	58.3	119.663	119.85	0.1	271	3.53	0	Fracture	Discontinuous	Fresh	Hairline fracture
121.442	N344	N254	35.3	121.405	121.478	0.1	268.91	3.52	0	Fracture	Planar	Fresh	Hairline fracture
123.252	N140	N050	38.6	123.215	123.288	0.1	271	3.58	0	Fracture	Planar	Fresh	Hairline fracture
123.343	N163	N073	34.3	123.31	123.376	0.1	271.95	3.55	0	Fracture	Crushed	Fresh	Fracture zone
123.687	N205	N115	46.7	123.631	123.743	0.1	271	3.55	0.269	Fracture	Crushed	Fresh	Fracture zone
125.952	N318	N228	3.9	125.946	125.958	0.1	270	3.64	0	Fracture	Planar	Fresh	Hairline fracture
128.463	N204	N114	62.6	128.361	128.566	0.1	271.65	3.65	0	Fracture	Planar	Mineralized	
129.795	N001	N271	13.4	129.783	129.808	0.1	272.02	3.67	0	Fracture	Planar	Fresh	Hairline fracture

Appendix 3

Fracture frequency calculation parameters

RGLDIPv6.2 DIP DATA INTERPRETATION: FRACTURE ANALYSIS

borehole Mannen Upper 1

zone from 2.000 to 31.000 m

North ref is magnetic

07 Sep 2010

Data is classed into 1 types

5 OPTV_dips

Quality cut-off level: *

Mean well deviation: 2.2°deg to N267.0°

4 small-circles defined

	SEARCH AREA			MEAN DIP		n	f
	azim	pl	cone	strike	dip		
1	197.3°	45.8°	27.0°	289°	36°	65	2.72
2	14.0°	78.8°	26.3°	127°	5°	31	1.07
3	126.4°	40.7°	22.0°	222°	46°	11	0.56
4	26.6°	24.6°	27.3°	120°	53°	11	0.65

Total number of data = 118

Number of data unaccounted for = 10

ZONE No.	DEVIATION		DEPTHS m		No. DATA	MEAN DIPS and FREQUENCIES															
	Dev	Azim	TOP	BASE		Str	Dip	n	f	Str	Dip	n	f	Str	Dip	n	f	Str	Dip	n	f
1	1.7	290.3	2.63	10.02	26	288	42	6	1.10	168	6	12	1.64	224	47	4	0.82	130	45	2	0.39
2	2.3	264.3	10.02	15.93	21	266	38	2	0.43	269	2	12	2.03	229	45	4	0.99	135	71	1	0.58
3	2.1	258.9	15.93	18.88	11	298	28	8	3.04	103	17	3	1.07	0	0	0	0.00	0	0	0	0.00
4	2.4	261.2	18.88	22.33	20	292	41	16	6.07	0	0	0	0.00	0	0	0	0.00	97	48	2	0.87
5	2.5	262.0	22.33	25.78	18	288	35	15	5.26	101	30	2	0.68	0	0	0	0.00	119	69	1	0.87
6	2.6	259.5	25.78	28.74	22	286	32	17	6.69	0	0	0	0.00	210	49	2	1.08	141	49	1	0.54
7	2.7	261.6	28.74	31.74	10	294	37	1	0.41	79	12	2	0.68	206	36	1	0.42	116	55	4	2.39

RGLDIPv6.2 DIP DATA INTERPRETATION: FRACTURE ANALYSIS

borehole Mannen Upper

zone from 32.000 to 58.000 m

North ref is magnetic

17 Sep 2010

Data is classed into 1 types

5 OPTV_dips

Quality cut-off level: *

Mean well deviation: 3.8°deg to N281.7°

5 small-circles defined

	SEARCH AREA			MEAN DIP		n	f
	azim	pl	cone	strike	dip		
1	225.0°	77.6°	26.5°	323°	13°	35	1.38
2	352.3°	54.0°	19.0°	77°	30°	9	0.40
3	300.0°	21.2°	14.5°	30°	72°	5	0.54
4	100.3°	51.5°	10.7°	193°	37°	6	0.31
5	168.0°	43.1°	15.4°	262°	40°	6	0.31

Total number of data = 61

Number of data unaccounted for = 10

ZONE No.	DEVIATION		DEPTHS m		No. DATA	MEAN DIPS and FREQUENCIES																							
	Dev	Azim	TOP	BASE		Str	Dip	n	f	Str	Dip	n	f	Str	Dip	n	f	Str	Dip	n	f	Str	Dip	n	f				
1	3.9	266.4	32.27	41.14	37	325	13	31	3.55	0	0	0	0.00	34	69	3	0.84	0	0	0	0.00	0	0	0	0.00				
2	4.3	284.6	41.14	45.08	8	324	29	2	0.57	59	46	1	0.35	24	77	2	1.70	0	0	0	0.00	260	42	2	0.71				
3	4.1	291.5	45.08	50.50	11	181	13	2	0.39	57	28	2	0.41	0	0	0	0.00	0	0	0	0.00	262	39	4	0.98				
4	3.3	291.9	50.50	58.05	15	0	0	0	0.00	88	29	6	0.90	0	0	0	0.00	193	37	6	1.04	0	0	0	0.00				

RGLDIPv6.2 DIP DATA INTERPRETATION: FRACTURE ANALYSIS

borehole Mannen Upper

zone from 57.000 to 77.000 m

North ref is magnetic

02 Feb 2011

Data is classed into 1 types

5 OPTV_dips

Quality cut-off level: *

Mean well deviation: 3.4°deg to N272.0°

1 small-circles defined

	SEARCH AREA			MEAN DIP		n	f
	azim	pl	cone	strike	dip		
1	282.7°	68.4°	44.1°	356°	23°	17	0.89

Total number of data = 17

Number of data unaccounted for = 1

ZONE No.	DEVIATION		DEPTHS m		No. DATA	Str Dip n			f
	Dev	Azim	TOP	BASE		Str	Dip	n	
1	3.3	282.7	57.35	62.28	9	3	22	9	1.93
2	3.1	270.3	62.28	69.83	1	0	0	0	0.00
3	3.7	267.6	69.83	77.65	8	344	19	7	0.93

RGLDIPv6.2 DIP DATA INTERPRETATION: FRACTURE ANALYSIS

borehole Mannen Upper

zone from 90.000 to 130.000 m

North ref is magnetic

18 Feb 2011

Data is classed into 1 types

5 OPTV_dips

Quality cut-off level: *

Mean well deviation: 3.3°deg to N276.1°

4 small-circles defined

	SEARCH AREA			MEAN DIP		n	f
	azim	pl	cone	strike	dip		
1	309.0°	71.7°	40.0°	40°	19°	33	0.86
2	161.6°	32.0°	28.5°	254°	62°	16	0.88
3	75.3°	28.5°	24.1°	167°	57°	9	0.46
4	21.5°	21.4°	24.1°	114°	57°	4	0.19

Total number of data = 62

Number of data unaccounted for = 8

ZONE No.	DEVIATION		DEPTHS m		No. DATA	MEAN DIPS and FREQUENCIES															
	Dev	Azim	TOP	BASE		Str	Dip	n	f	Str	Dip	n	f	Str	Dip	n	f				
1	2.8	293.9	90.15	97.04	17	29	21	14	2.14	0	0	0	0.00	168	63	2	0.70	0	0	0	0.00
2	3.3	275.4	97.04	112.81	40	32	18	13	0.86	253	63	14	2.01	161	56	5	0.62	113	59	2	0.26
3	3.5	271.3	112.81	130.05	13	86	21	6	0.37	258	57	2	0.22	182	55	2	0.22	114	55	2	0.21
4	3.7	271.0	130.05	130.29	13	40	19	33	139.88	254	62	16	143.39	167	57	9	75.30	114	57	4	31.06